

**Intricacies of 3D printing with freeze casting in microgravity**

by

Abrar Ahmed

A thesis submitted in partial fulfillment of the requirements for the degree of

Doctor of Philosophy

Department of Mechanical Engineering  
University of Alberta

© Abrar Ahmed, 2024

# Abstract

The burgeoning demand for advancements in space technology and the relentless pursuit of exploring uncharted celestial frontiers necessitate a comprehensive grasp of the multifaceted aspects underpinning the sustainability of space missions. In this context, additive manufacturing (AM) has emerged as an enticing proposition for inclusion in the tool-kit of every space mission, primarily owing to its capacity to fabricate components on-demand.

The overarching objective of this doctoral thesis is to engineer a compact laboratory platform, herein referred to as FrizCast<sup>™</sup>, dedicated to unraveling the intricate intricacies of various processes integral to conventional additive manufacturing. These processes encompass material deposition, additive layering, solidification, and post-processing procedures. In the austere environment of space, characterized by the absence of gravitational forces, interfacial forces wield significant influence over the outcomes at each stage of the additive manufacturing process.

The research endeavors in this thesis will scrutinize the three dimensional (3D) printing process, both within terrestrial conditions and within reduced-gravity settings, with a keen focus on elucidating the fundamental principles governing colloidal material delivery, drop-based material accretion, multilayer mass accumulation via colloidal droplet coalescence, and the subsequent solidification processes. Given the prevalence of lower temperatures in space, our investigations have led us to adopt freeze casting as an integral facet of the additive manufacturing process. During material solidification, external body forces will be harnessed to facilitate the manipulation of the final shape of the solidified material. Consequently, the widely employed

electromagnetic field will be subjected to a rigorous examination to discern its impact on the aforementioned facets of the additive manufacturing process.

The ultimate aim of this project is to propose a jet-based 3D printing mechanism, which has the potential of being used in space and to study how surface and body forces affect the 3D printing process on a printer bed. Furthermore, we have also establish a prototypical instrument that could serve as a blueprint for future space missions necessitating recurrent measurements of surface tension, surface energy, as well as 3D printing of metallic and biomaterials. Thus, this research initiative holds the potential to become an invaluable asset for the future of space exploration.

# Preface

This thesis is an original work by Abrar Ahmed. All of the research conducted for this thesis is directly supervised by Professor Dr. Prashant R. Waghmare, while Professor Dr. Alexandra Komrakova and Professor Dr. Andrew Martin, as a supervising committee members, were advising and commenting on the progress of the research.

Chapter 2 of this thesis has been published as Abrar Ahmed, Raymond Sanedrin, Thomas Willers, and Prashant R. Waghmare, “The effect of dynamic wetting pressure on contact angle measurements”, *Journal of Colloid and Interface Science*, Volume 608, issue 1, Pages 1086-1093, 2022. I was responsible for the data collection, analysis as well as the manuscript composition. Raymond Sanedrin, and Thomas Willers assisted in Data collection and Prashant R Waghmare was the primary supervisor for the research.

Chapter 3 of this thesis has been published as Aleksey Baldygin (A.B), Abrar Ahmed (A.A.), Ryan Baily (R.B.), Md Farhad Ismail (M.F.I.), Muhammed Khan (M.K.), Nigel Rodrigues (N.R.), Ali-Reza Salehi (A.R.S.), Megnath Ramesh (M.R.), Sanjay Bhattacharya (S.B.), Thomas Willers (T.W.), Derek Gowanlock (D.G.), and Prashant R. Waghmare (P.R.W.), “Effect of gravity on the spreading of a droplet deposited by liquid needle deposition technique”, *npj Microgravity*, Volume 9, issue 1, Pages 49, 2023. A.B. and A.A. have equally contributed to the manuscript as first authors. A.B. lead the devising of experimental setup in support of R.B. and A.A. where M.K. was assisting with preliminary FEA analysis. M.F.I, M.K., N.R., A.R.S.,

and M.R. carried out ground experiments. During CAN-RGX campaign, as primary mission specialists, R.B. and M.F.I. were on the parabolic flight, where R.B. carried out all the microgravity experiments. The experimental set-up was redesigned to accommodate other components and tested its functionality for FAST grant campaign. A.B. led re-designing and testing with support from R.B. A.A. and R.B. redesigned the set-up that was needed due to additional instrumentation and rearrangements of the previously used. D.G. was involved in the redesigning and training for flight campaign, as well as facilitated the approval of flights, payload and other security details, he also sequenced the parabolas in flight and monitored the safety of every mission specialist on board. A.A., A.B., R.B., and P.R.W. collected microgravity experimental data used in this manuscript during the FAST grant campaign. P.R.W. conceptualized the theoretical model, M.F.I. developed it along with the initial literature review and parametric studies. A.A. performed the theoretical analysis and detailed parametric studies to compare the results from both flight campaigns. S.B. developed third-party software for drop shape analysis which was used during the CAN-RGX campaign. A.A. led the writing and editing of the manuscript which was supported by A.B., and R.B. T.W. provided valuable inputs during different stages of this project. Project idea was conceptualized by P.R.W., for CAN-RGX and FAST grant, secured the funding to develop the experimental set-up. P.R.W. was mentoring, monitoring, and advising for all the above-mentioned activities.

Chapter 4 will be submitted in Journal of Fluid Mechanics. I was responsible for mathematical modelling, data collection, analysis as well as the manuscript composition. Prashant R. Waghmare was the primary supervisor for the research.

Chapter 5 will be submitted in journal of microgravity science and technology. I was responsible for mathematical modelling, data collection, analysis as well as the manuscript composition. Prashant R. Waghmare was the primary supervisor for the

research.

Chapter 6 will be submitted in Applied physics letters where I was leading the project with mathematical modelling, data collection, analysis as well as the manuscript composition. Ganesh Prabhu and Md Farhad Ismail were assisting in data collection and manuscript writing. Prashant R. Waghmare was the primary supervisor for the research.

Chapter 7 will be submitted in Physical Review letters. I was responsible for mathematical modelling, data collection, analysis as well as the manuscript composition. Prashant R. Waghmare was the primary supervisor for the research.

My supervisor, Dr. Prashant R. Waghmare was responsible for conceptualisation and overall supervision of all the projects mentioned above.

# Acknowledgements

I express my deepest gratitude to Almighty Allah, the Most Merciful and Compassionate, for providing me with the strength, guidance, and perseverance throughout my doctoral journey.

I extend heartfelt appreciation to my late father, whose unwavering belief in my abilities continues to resonate within me. His memory serves as a guiding light, and I am profoundly grateful to both of my father and mother for the values, wisdom, and encouragement they instilled in me.

My sincere thanks go to my wife, whose boundless support, patience, and understanding have been my pillars of strength. Her unwavering belief in my pursuit of knowledge has been a source of motivation, and her sacrifices have been invaluable. To my newborn, who brought an added dimension of joy and purpose to my life during this challenging academic endeavor, I am grateful for the love and inspiration you have provided.

I am indebted to my supervisor, Professor Dr Prashant Waghmare, for his exceptional guidance, expertise, and mentorship. His insightful feedback, encouragement, and commitment to excellence have been instrumental in shaping the outcome of this research. Under Dr. Waghmare's supervision I realised how a high quality research should be performed while maintaining a healthy work life balance. If it was not Dr. Waghmare's motivation I would not have been pursuing my PhD degree.

I would also like to express my heartfelt gratitude to my supervisory committee members Dr. Alexandra Komrakova and Dr. Andrew Martin, whose constant support and feedback help me a lot to organise my thesis as well as to meet the goal.

I also extend my gratitude to Dr. Aleksey Baldygin who trained me on how to perform error free experiments and he also played a significant role in helping me on designing my experimental setup. I would also like to thank Ryan Baily for his dedicated effort on helping me on developing and designing the experimental setup suitable for parabolic flight condition.

At the end I would like to specially thank Canadian Space Agency (CSA) for providing fund for my thesis project, which is on intricacies of 3D printing with freeze casting in microgravity. This thesis is a culmination of the collective efforts, encouragement, and blessings bestowed upon me. I am thankful for the presence of these significant individuals in my life, and their impact will forever be etched in my academic and personal journey.

# Table of Contents

<b>1</b>	<b>Introduction</b>	<b>1</b>
1.1	Motivation . . . . .	1
1.2	Objectives . . . . .	4
1.3	Thesis outlines . . . . .	6
1.3.1	First Milestone . . . . .	8
1.3.2	Second Milestone . . . . .	8
1.3.3	Third Milestone . . . . .	9
	References . . . . .	10
<b>2</b>	<b>Effect of dynamic wetting pressure on contact angle measurement</b>	<b>11</b>
2.1	Introduction . . . . .	12
2.2	Materials and methods . . . . .	15
2.3	Results and discussion . . . . .	18
2.3.1	Contact angle as a function of volume . . . . .	18
2.3.2	High speed recordings of drop deposition processes . . . . .	18
2.3.3	Dynamic wetting pressure . . . . .	24
2.3.4	Comparison with literature data . . . . .	26
2.4	Conclusions . . . . .	28
	References . . . . .	30
<b>3</b>	<b>Effect of gravity on the spreading of a droplet deposited by liquid needle deposition technique</b>	<b>35</b>
3.1	Introduction . . . . .	36
3.2	Results and Discussion . . . . .	40
3.2.1	Drop Deposition in $\mu g$ . . . . .	40
3.2.2	Dynamics of Drop Spreading . . . . .	44
3.3	Methods . . . . .	51
3.3.1	Experimental Constraints and Requirements . . . . .	51
3.3.2	Prototype Components . . . . .	51

3.4	Experimental Procedure . . . . .	54
3.4.1	Experimental Trails . . . . .	56
3.5	Mathematical Model . . . . .	57
3.6	Conclusion . . . . .	61
	References . . . . .	62
<b>4</b>	<b>Dynamics of jet breakup and subsequent drop formation dynamics as a function of gravity</b>	<b>66</b>
4.1	Introduction . . . . .	67
4.2	Experimental Procedure . . . . .	72
4.3	Theoretical Model . . . . .	72
4.4	Results and Discussion . . . . .	81
4.5	Conclusion . . . . .	89
	References . . . . .	91
<b>5</b>	<b>Measurement of surface free energy in microgravity</b>	<b>93</b>
5.1	Introduction . . . . .	94
5.2	Experimental procedure . . . . .	99
5.3	Theoretical Model . . . . .	99
5.4	Discussion . . . . .	108
5.5	Results . . . . .	116
5.6	Conclusions . . . . .	120
	References . . . . .	122
<b>6</b>	<b>Geometric similarities in asymmetric droplet freezing under reduced gravity environment</b>	<b>124</b>
6.1	Introduction . . . . .	125
6.2	Experimental Procedure . . . . .	127
6.3	Theoretical Model . . . . .	129
6.4	Results and discussion . . . . .	135
6.5	Conclusion . . . . .	138
	References . . . . .	140
<b>7</b>	<b>Freezing of a magnetic liquid under the effect of magnetic field</b>	<b>142</b>
7.1	Introduction . . . . .	143
7.2	Theoretical modelling . . . . .	144
7.3	Results and discussion . . . . .	157
7.4	Conclusion . . . . .	159

References . . . . .	161
<b>8 Conclusions, Recommendations, &amp; Future Work</b>	<b>163</b>
8.1 Concluding remarks . . . . .	163
8.2 Future work and recommendations . . . . .	165
<b>Bibliography</b>	<b>169</b>
<b>Appendix A: Chapter 2</b>	<b>182</b>
A.1 Supplementary figure for Chapter 2 . . . . .	182
<b>Appendix B: Chapter4</b>	<b>185</b>
B.1 Derivation of mathematical model for spreading of a drop deposited by liquid needle drop deposition technique . . . . .	185
B.2 How parabolic flight works . . . . .	191
B.3 Treatment of copper substrate . . . . .	192
<b>Appendix C: Nomenclature</b>	<b>194</b>
C.1 Chapter 2 . . . . .	194
C.2 Chapter 3 . . . . .	194
C.3 Chapter 4 . . . . .	195
C.4 Chapter 5 . . . . .	196
C.5 Chapter 6 . . . . .	197
C.6 Chapter 7 . . . . .	198

# List of Tables

2.1	Static contact angle data for DIM on Aqua Regia treated glass substrate deposited by pendant drop and liquid needle technique. . . . .	26
2.2	Contact angle data for deionised water on untreated PDMS substrate deposited by needle dosing or pendant drop technique. . . . .	27
B.1	Table depicting the water contact angle (W-CA), diiodomethane contact angle (DIIM-CA), surface free energy (SFE), polar and dispersive part of variously treated copper substrate. . . . .	192

# List of Figures

1.1	Process diagram for the proposed research . . . . .	7
2.1	Equilibrium contact angle variation with respect to volume for various substrate-liquid combinations . . . . .	17
2.2	Variation in wetting of Aqua regia treated glass slides with Diiodomethane drop due to two different deposition method: pendant drop and liquid needle. . . . .	19
2.3	Transient variation of dynamic wetting pressure for pendant drop deposition technique and liquid needle deposition technique . . . . .	23
3.1	Snapshots representing the formation of a droplet through liquid needle drop deposition technique. . . . .	43
3.2	Variation of geometrical parameter of drop in $\mu g$ and $1g$ . . . . .	50
3.3	Description for experimental setup developed for investigating instabilities of freeze casting with 3D printing in reduce gravity. . . . .	53
3.4	Transient variation of droplet shape and wetting properties with respect to different levels of gravity . . . . .	54
3.5	Gravitational acceleration profile in parabolic flight. . . . .	57
3.6	Validation of theoretical model with experimental observation for spreading of drop deposited via jet based deposition. . . . .	60
4.1	Graphical representation of breakup of a liquid jet, emanating from a nozzle, and subsequent drop formation in gravity. . . . .	72
4.2	Snapshot of jet break up dynamics and subsequent drop formation in $\mu g$ and $1g$ . . . . .	82
4.3	Experimental observations of break up length and time as a function of jet velocity, gravitational acceleration and surface forces. . . . .	84
4.4	Parametric study for the effect of Bond number number , modified Ohnesorge number and modified Froude number on the non dimensional drop size, generated from the laminar jet break up. . . . .	85

4.5	Accuracy of the prediction of non dimensional microdrop diameter from the developed model with the experimental observation . . . . .	89
5.1	Metastable state of a drop in different gravity level which can be utilised to measure the surface free energy of a solid by Sessile Drop Accelerometry method. . . . .	106
5.2	Probable droplet shape profile while the droplet is not effected by the gravity and effected by the gravity. . . . .	109
5.3	Change in interfacial areas as a function of droplet base radius, from the hypothetical configuration $o$ to the configuration $\kappa'$ , by assuming $\kappa = \kappa'$ . . . . .	109
5.4	Variation of Helmholtz free energy of the system during the spontaneous wetting of droplet on a solid surface without the effect of gravity. . . . .	111
5.5	Sensitivity analysis of the non dimensional governing equation. . . . .	112
5.6	Phase plot of the non dimensional governing equation showing the variation of non dimensional surface energy with represent to $B_o$ and $\kappa$ . 114	
5.7	Simulated results of droplet shape under different gravity conditions. All the droplet shapes have been generated by solving the Adam-Bashforth equation through a fourth order Runge-Kutta scheme. . . . .	115
5.8	Experimental evidence of drop profile change on Superhydrophobic (chemically functionalised )copper substrate as a function of gravity. . . . .	117
5.9	Experimental evidence of drop profile change on hydrophilic copper substrate as a function of gravity. . . . .	119
5.10	Comparison of surface free energy of solid surfaces measured by SDAcc model and classical Two component (OWRK) method. . . . .	120
6.1	Graphical representation of drop freezing dynamics via liquid needle drop deposition techniques. . . . .	127
6.2	Asymmetric drop maximum height ( $h_i$ ) prediction: We compare the two triangle approach and heat transfer model with our experimental results. . . . .	129
6.3	Geometric parameter, involved in maximum height measurement of asymmetric drop, required for theoretical modelling. . . . .	132
6.4	Universality in ice ( $h_s$ ) to water $h_l$ height ratio for symmetric and asymmetric drop with respect to Bond number. . . . .	136
6.5	Solid-liquid height ratio for different density ratio predicted by Two-triangle and symmetric drop approach. . . . .	137

7.1	Water based ferrofluid drop freezing on a copper substrate at $-20^{\circ}C$	146
7.2	Log-log plot representing the relation between the nondimensional freezing height and the nondimensional time. . . . .	156
7.3	Freezing time vs magnetic Bond number . . . . .	158
7.4	Response of concentration of particles to the applies magnetic field strength. . . . .	159
8.1	Effect of magnetic field on the interparticle spacing of a freeze dried ferrofluid film. . . . .	166
8.2	Printed iron dome. . . . .	167
8.3	Proposed design of 3D printer unit jetting unit with thermal unit and freeze drying unit. . . . .	168
A.1	Center of gravity detection method for the (a)pendant drop and (b) liquid needle drop deposition technique. . . . .	182
A.2	Transient variation of contact angle (left axis)and volume (right axis) for $2\mu l$ , $5\mu l$ and $10\mu l$ DIM drop on aqua regia treated glass substrate deposited via liquid needle drop deposition system. . . . .	183
A.3	Supplementary figure for variation of dynamic wetting pressure with respect to center of gravity in case of pendant drop deposition technique.	184

# Abbreviations

**2D** Two Dimensional.

**3D** Three Dimensional.

**AM** Additive Manufacturing.

**AR** Aqua Regia.

**CA** Contact Angle.

**DI** Deionised.

**DIM** Diiodomethane.

**FDM** Fused Deposition Modelling.

**PDMS** Polydimethylsiloxane.

**PEEK** Polyether Ether Ketone.

**SDAcc** Sessile Drop Accelerometry.

**TM** Trade Mark.

# Chapter 1

## Introduction

### 1.1 Motivation

The realm of outer space has always been a frontier of human exploration and discovery, pushing the boundaries of our knowledge and capabilities. As we continue to reach for the stars, our need for innovative solutions to address the challenges of space exploration becomes increasingly apparent. One such ground breaking technology that has emerged in recent years is 3D printing, and its application in the extraterrestrial environment has ignited a new era in space manufacturing. This remarkable fusion of cutting-edge technology and space exploration has given birth to the concept of 3D printing in space, a transformative approach that holds the potential to revolutionize how we manufacture and maintain essential equipment, structures, and even habitats in the harsh and unforgiving vacuum of space.

The successful deployment of the remote shuttle manipulator system (Canadarm) serves as a catalyst, inspiring numerous researchers across the world to embark on the career in space industry. Since then research groups worldwide have dedicated their efforts in advancing emerging technologies relevant to space research and development[1, 2]. This collective pursuit of exploring vast mysteries of space and providing astronauts with cutting-edge research tools for efficient space exploration has opened up new avenues of research. One such recent addition to this field is 3D printing during space

mission.

Additive manufacturing (AM) has transformed the manufacturing industry, and space organizations are actively striving to integrate this technology into their missions[3]. Some space missions have already directly or indirectly benefited from 3D printing technology. For instance, Audi’s ”Lunar Quattro” rover[3], designed for lunar exploration, was 3D printed using aluminium and titanium, resulting in an extremely lightweight yet robust vehicle. The European Space Agency (ESA) has developed miniaturized 3D-printed satellites using cost-effective and lightweight polyether ether ketone (PEEK) materials[3].

However, these examples involve 3D printing carried out under terrestrial conditions before deployment in space applications. There is a pressing need for the capability to perform 3D printing directly in space, as current circumstances demand. NASA, with a long-term goal before 2040, aims to establish a multi-material fabrication laboratory in space to support future lunar and Mars exploration missions. Additionally, for critical missions such as Mars exploration[4], the presence of on-board 3D printers is imperative, given the challenges of resupply missions.

Nonetheless, due to minimal convection and the prevalence of interfacial forces, the adaptation of 3D printing processes for space applications necessitates special attention. While there has been some progress, such as the development of a 3D printer by “Made in Space” [5] that successfully printed a polymeric object aboard the International Space Station (ISS) in July 2014, the challenge of achieving metal and bio 3D printing in space persists. Metal components are indispensable for ensuring structural integrity and long-term viability, particularly in extended missions. Most metal 3D printing technologies on Earth are rooted in either powder-based methods like Selective Laser Sintering [6, 7] or fused deposition modeling (FDM) [8, 9]. Powder-based

printing relies on a flat bed of powder [6, 7], but in microgravity, this would result in a dispersed cloud of powder, rendering it infeasible to manufacture objects using this method. Managing powder in microgravity is exceptionally challenging due to containment concerns, as releasing the powder could pose hazards to crew members and spacecraft ventilation systems. Consequently, FDM is regarded as the most suitable method for 3D printing in space. Nevertheless, metal FDM presents its own set of challenges. In terrestrial gravity, metal FDM consists of three consecutive steps [10]: deposition, de-binding, and furnacing. During de-binding, a liquid bath is employed to remove base materials from the printed object. In microgravity, maintaining the stability of the liquid bath interface becomes a formidable task, as dominant surface forces prevent the formation of a flat interface, and withdrawing the part from the liquid bath becomes infeasible. Furthermore, in microgravity condition the material deposited via FDM encounters deadhesion from the printer bed due to the dominance of surface forces and the lack of convection in space. Due to the deadhesion the breakage and warping of 3D printed part from the printer bed take place.

Furthermore, we believe that the study presented in this thesis can be applied, albeit not within the scope of this research, to address challenges encountered in material handling during bioprinting. It is worth noting that the 3D printing of biological products[11] faces additional difficulties under Earth's gravity. Printing tissue-like materials on Earth often results in structural collapse due to their weight. Moreover, maintaining the desired porosity of printed biomaterials is challenging in terrestrial gravity, as pore closure can occur due to fusion between adjacent layers[12, 13]. The desired porosity in bioprinted materials can be controlled by freezing the bioink at a specific rate.

In order to address the challenges faced by both metal and bio 3D printing in microgravity this thesis aims to investigate the principles of surface science that govern

the various stages of 3D printing on a printer bed in space environments. To achieve this goal, we have developed a payload to validate our hypotheses.

## 1.2 Objectives

To fully leverage the advantages of 3D printing or Additive Manufacturing (AM) in space missions, it is imperative to gain a deep understanding of each individual phenomenon inherent to AM, especially those dominated by interfacial forces. This proposed project is meticulously designed to comprehensively investigate various fundamental aspects, ranging from the delivery and deposition of colloidal solutions to the freezing mechanisms of these colloidal suspensions in microgravity.

To facilitate material delivery for 3D printing in space, we propose a jet-based material delivery method within this study. Furthermore, we investigate the impact of gravity and surface tension on the physics of this jet-based material delivery method, particularly in relation to the wetting properties of a liquid droplet. Quantifying these wetting parameters, including drop base diameter, drop height, and dynamic contact angle, will enable us to optimize the position of the 3D printer nozzle and the timing of nozzle opening for multilayer material deposition.

A comprehensive theoretical and experimental investigation is also conducted to explore the influence of gravity and liquid properties on the dynamics of jet breakup and the subsequent formation of droplets. The outcomes of this investigation hold the potential to enhance the optimization of jetting parameters for space-based 3D printing processes. This optimization is crucial for addressing issues such as liquid splashes and the formation of bubbles within the deposited material, which could otherwise compromise the structural integrity of the printed objects.

Solidification represents the final stage of a 3D printing process that occurs on the printer bed. In microgravity ( $\mu g$ ) conditions, the solidification stage encounters numerous challenges[5, 14], including de-adhesion, unwanted adhesion to the base plate causing damage to the printed parts, non-uniform porosity, and variations in material properties.

To address these challenges in space conditions, we propose a mathematical model related to the solidification of objects via the freezing of colloidal solutions in the presence or absence of a magnetic field. This model is developed based on the principles of mass, momentum, and energy conservation, eventually leading to an equation resembling the lubrication equation. It accounts for phase changes and solidification velocity as functions of magnetic field strength. We identify a mechanism for controlling the solidification rate of materials infused with metal nanoparticles, with the operating parameters determined through modelling exercises.

This study is pivotal for freeze casting and additive manufacturing of metallic and organic objects containing magnetic nanoparticles. In such processes, the solidification rate of a colloidal droplet dictates the pore morphology, which in turn influences the strength of the green body. It's worth noting that our long-term objective is to 3D print irregularly shaped metallic objects where solidification and shaping are achieved through freezing and externally triggered magnetic fields. Hence, we are currently employing a water-based magnetic liquid, which is responsive to magnetic fields, as a proof of concept. Conversely, this study does not encompass the discussion of the physical properties of thermoplastic and biological materials and their applications; such topics fall outside the scope of this research.

In short, main goal of this proposed research is to conduct a comprehensive examination of the complex phenomena governed by surface tension in 3D printing within

a microgravity ( $\mu$ -gravity) environment. The specific objectives of this study are as follows:

- Develop a theoretical framework for understanding material deposition via jetting and validate the proposed model.
- Propose measurement techniques for interfacial tension, a dominant force in reduced gravity, and validate the proposed model.
- Quantify the spacing between successive material depositions in 3D printing by predicting the spreading of deposited material through the jet-based deposition technique.
- Establish a comprehensive understanding of the dynamics involved in jet breakup and subsequent drop formation in reduced gravity, with the aim of preventing undesired bubble formation and splashing in such an environment.
- Investigate the solidification process of deposited material through the freezing of drops.
- Formulate a model for magnetic field assisted freezing of colloidal metallic object and validation of the proposed model
- Provide a proof of concept demonstrating the viability of freeze casting as an effective additive manufacturing process.

### **1.3 Thesis outlines**

During this PhD program, we are diligently working on establishing a foundational platform to comprehend the intricacies of the additive manufacturing process in microgravity ( $\mu$ -gravity). Our research endeavors not only aim to elucidate the underlying physics behind interfacial and surface tension-driven phenomena in the 3D

printing process but also seek to provide innovative solutions to the challenges encountered in 3D printing under reduced gravity conditions.

In pursuit of these objectives, we have organized the goals of the Ph.D. thesis into three distinct categories or milestones, denoted as M1 (Material Delivery), M2 (Multilayer Mass Addition), and M3 (Solidification) of the deposited material. The successful completion of these three milestones will culminate in the realization of a laboratory-scale 3D printed object. A comprehensive process flow chart, encompassing all key research milestones, is visually depicted in Figure 1.1.

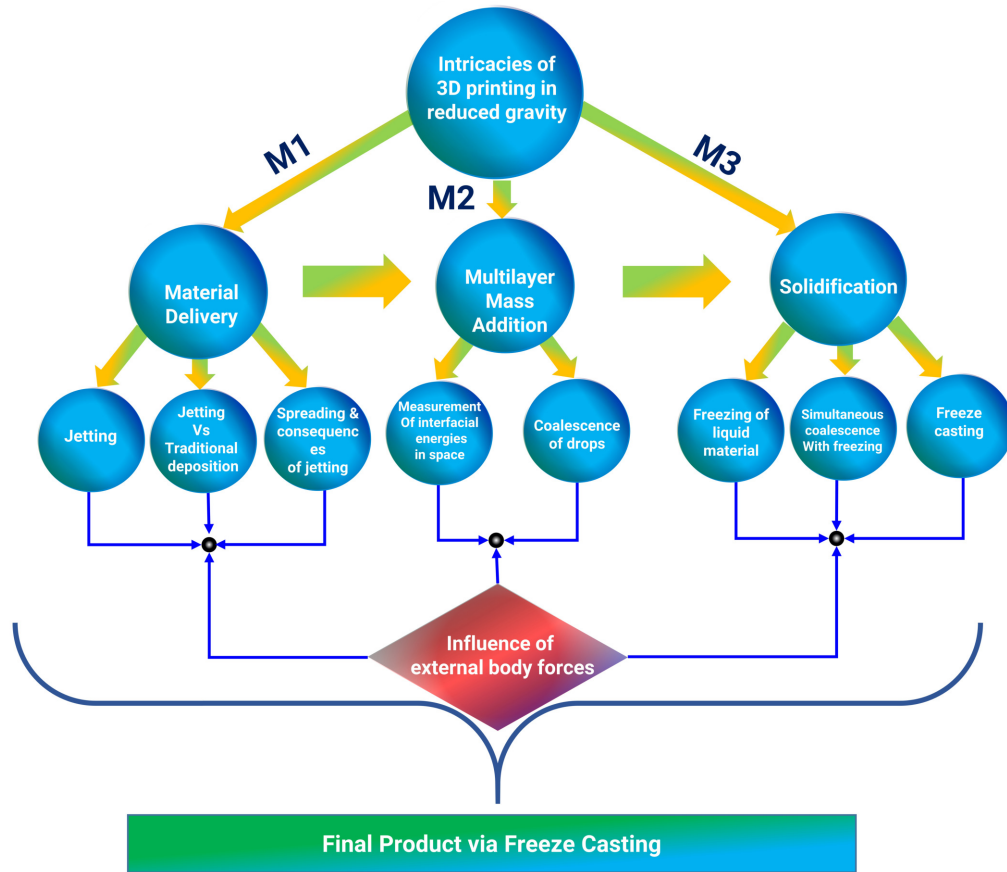


Figure 1.1: Process diagram for the proposed research

In pursuit of the aforementioned milestones, this thesis is structured into eight chapters (including introduction and conclusion), with each milestone being allocated

two dedicated chapters. The overall arrangement of chapters in this thesis is as follows:

### **1.3.1 First Milestone**

Chapter 2 provides a comprehensive exploration of our proposed material delivery method, jet-based deposition, and highlights its superiority over traditional deposition techniques in reduced gravity conditions. Within this chapter, we offer both theoretical arguments and experimental evidence to emphasize the critical importance of achieving well-controlled drop deposition with minimal wetting pressure. This control is essential to ensure that contact angle data and the characteristics of the deposited material remain independent of the chosen material delivery technique.

Chapter 3 introduces a model grounded in the overall energy balance equation, designed to predict the growth and spreading rate of deposited material from a single pulsating jet. This model serves a dual purpose: it enables us to anticipate the size of the deposited material in a microgravity environment and provides a means to quantify the minimum distance required between successive depositions to facilitate material coalescence on the 3D printer bed.

### **1.3.2 Second Milestone**

Moving on to Chapter 4, we delve into the investigation of liquid jet breakup as it relates to the influence of gravity. Within this chapter, we introduce a mathematical model designed to predict the size of microdroplets, originated from liquid jet breakup. The mathematical model takes into account factors such as the Rayleigh Plateau instability and a modified Navier Stokes equation. The final form of the equation is a function of Bond number, Ohnesorge number, and Froude number.

In Chapter 5, we present a model founded on the modified sessile droplet accelerometry technique. This model possesses the unique ability to concurrently measure the surface energy of the solid material and the surface tension at the liquid-solid interface. The significance of this study lies in its capacity to characterize the surface properties of in-situ materials collected during Mars or Lunar missions.

### **1.3.3 Third Milestone**

Chapter 6 explores the concept of universality in solid-liquid height through a novel two-triangle approach. This approach not only offers insights into predicting the size of solidified deposited material but does so irrespective of density differences and gravitational variations.

Moving on to Chapter 7, we delve into a model rooted in the principles of mass, momentum, and energy conservation equations. This model can be derived to resemble the lubrication equation and accounts for phase change and solidification velocity as influenced by magnetic field strength. This study holds great significance in the fields of freeze casting and additive manufacturing, especially concerning metallic and organic objects containing magnetic nanoparticles. The solidification rate of a colloidal droplet plays a pivotal role in determining pore morphology, thereby influencing the overall strength of the green body.

Finally, Chapter 8 encapsulates the research findings and offers insights into future directions and recommendations based on the outcomes of the conducted research.

## References

- [1] A. A. Siddiqi, *Beyond Earth: A chronicle of deep space exploration, 1958-2016*. National Aeronautics & Space Administration, 2018, vol. 4041.
- [2] N. NASA, “Strategic plan,” *National Aeronautics and Space Administration*, 2018.
- [3] A. Barton, N. Wong, and D. Webber, “The google lunar xprize—past, present and future,” in *Proceedings of the 13th Reinventing Space Conference*, Springer, 2018, pp. 75–82.
- [4] T. Prater *et al.*, “Summary report on phase i results from the 3d printing in zero g technology demonstration mission, volume i,” 2016.
- [5] T. Prater, N. Werkheiser, F. Ledbetter, D. Timucin, K. Wheeler, and M. Snyder, “3d printing in zero g technology demonstration mission: Complete experimental results and summary of related material modeling efforts,” *The International Journal of Advanced Manufacturing Technology*, vol. 101, pp. 391–417, 2019.
- [6] C. Buchanan and L. Gardner, “Metal 3d printing in construction: A review of methods, research, applications, opportunities and challenges,” *Engineering Structures*, vol. 180, pp. 332–348, 2019.
- [7] S. Das, D. L. Bourell, and S. Babu, “Metallic materials for 3d printing,” *Mrs Bulletin*, vol. 41, no. 10, pp. 729–741, 2016.
- [8] A. Ambrosi and M. Pumera, “3d-printing technologies for electrochemical applications,” *Chemical society reviews*, vol. 45, no. 10, pp. 2740–2755, 2016.
- [9] S. H. Ko, J. Chung, N. Hotz, K. H. Nam, and C. P. Grigoropoulos, “Metal nanoparticle direct inkjet printing for low-temperature 3d micro metal structure fabrication,” *Journal of Micromechanics and Microengineering*, vol. 20, no. 12, p. 125 010, 2010.
- [10] S. Hong, C. Sanchez, H. Du, and N. Kim, “Fabrication of 3d printed metal structures by use of high-viscosity cu paste and a screw extruder,” *Journal of electronic materials*, vol. 44, pp. 836–841, 2015.
- [11] S. V. Murphy and A. Atala, “3d bioprinting of tissues and organs,” *Nature biotechnology*, vol. 32, no. 8, pp. 773–785, 2014.
- [12] A. Ribeiro *et al.*, “Assessing bioink shape fidelity to aid material development in 3d bioprinting,” *Biofabrication*, vol. 10, no. 1, p. 014 102, 2017.
- [13] J. H. Chung *et al.*, “Bio-ink properties and printability for extrusion printing living cells,” *Biomaterials Science*, vol. 1, no. 7, pp. 763–773, 2013.
- [14] T. Prater *et al.*, “Analysis of specimens from phase i of the 3d printing in zero g technology demonstration mission,” *Rapid Prototyping Journal*, vol. 23, no. 6, pp. 1212–1225, 2017.

# Chapter 2

## Effect of dynamic wetting pressure on contact angle measurement<sup>1</sup>

### Abstract

#### Hypothesis:

The drop deposition technique can impact contact angle measurements. We hypothesized that the drop pinch-off, during the traditionally used pendant drop technique, significantly alters the static contact angle. The capillary waves and dynamic wetting pressure generated during the pendant drop deposition are the source for forced spreading which can be circumvented by alternative liquid-needle drop deposition techniques.

#### Experiments:

To compare the role of drop-pinch off and resultant dynamic wetting pressure, we meticulously observed and quantified the entire drop deposition process using high speed imaging until the drop attains the static contact angle in both cases, namely pendant drop and liquid needle deposition technique. Conventionally used standard substrates are compared using both techniques and further compared using literature data. The capillary waves and corresponding drop shape variations are analysed for

---

<sup>1</sup>A version of this thesis chapter has been published as Abrar Ahmed, Raymond Sanedrin, Thomas Willers, and Prashant R Waghmare, “The effect of dynamic wetting pressure on contact angle measurements”, *Journal of Colloid and Interface Science*, Volume 608, issue 1, Pages 1086-1093, 2022.

quantifying the dynamic wetting pressure by measuring drop base diameter, contact angle and centre of mass.

### **Findings:**

We compared three parameters - drop pinch-off, spreading behaviour and respective static contact angles along with the resultant dynamic wetting pressure for both the techniques, i.e., pendant drop and liquid-needle. For the pendant drop technique we observed a pronounced drop volume dependency of these parameters even though the corresponding Bond numbers are less than unity. In contrast, for the liquid needle there is no such dependency. With a theoretical argument corroborating experimental observations, this work highlights the importance of a well controlled drop deposition, with a minimum wetting pressure, in order to guarantee contact angle data is independent of drop deposition effects, thereby only reflecting the substrate properties.

## **2.1 Introduction**

Optical contact angle (CA) measurements are significantly relevant to numerous scientific research fields as well as to a vast field of industrial applications. Precise measurement of contact angle is the most crucial parameter in many industrial processes, such as oil recovery[15], lubrication [16] , liquid coating[17] and printing [18, 19]. In recent years, there has been an increasing interest in the study of superhydrophobic surfaces, due to their potential applications in, for example, self-cleaning [20], nanofluidics [21], and electrowetting [22, 23]. The meticulous determination of contact angle is required in droplet based additive manufacturing as the spreading of complex colloidal liquid ink directly affect the footprint and resolution of 3D printed materials [24]. It has already been reported that Electrowetting on Dielectric (EWOD) based chips [25] and biomedical microelectromechanical processes are hindered by inaccessibility to precise contact angle measurement techniques [26]. Moreover, a suitable contact angle measurement technology will contribute a lot in the future of space

science and technology because an error free drop deposition technique is inevitable in the field of additive manufacturing and materials research in reduced gravity[4, 27, 28].

The direct optical determination of the contact angle of a resting drop on a substrate, known as a sessile drop, is probably the most widely used method owing to its versatility and ease-of-use[29]. There are at least four different CA assessments: advancing CA, receding CA, most stable, and static CA[30, 31]. There are pertinent experimental procedures and quantification processes for each of these assessments and respective techniques. Each of these techniques, however, comes with rather different advantages and disadvantages in terms of scientific and industry related usability, reproducibility irrespective of users or lab conditions, experimental ease-of-use (i.e. complexity of experimental protocols to be followed), degree of possible automation, and time required to perform the experiments[31–37].

In this work, we focus on two drop deposition techniques that allow measurement of the static CA of deposited drops: Static CA with pendant drop and liquid needle drop deposition. The static CA is probably the most popular one [30] and quiet often measured with the pendant drop deposition method. This method is experimentally well controlled [34–36] and the dominating method in industry applications as referred in industrial standards [38–41]. This technique, however, is prone to user dependence and drop deposition related experimental inaccuracies. The liquid needle was recently introduced as a properly controlled way of drop deposition[36] for measuring the dynamic advancing and the static advancing CA, i.e., the recently advanced CA[42, 43]. In the case of pendant drop deposition, after interacting with the solid-air interface, drops experience an energetically punishing process[44]. While spreading and attaining another minimum energy state configuration, capillary waves are generated that give rise to the dynamic wetting pressure[45]. A simple but elegant

process like contact angle measurement, in particular with the pendant drop deposition, always experiences such a scenario where the capillary waves can be witnessed during the drop detachment from the needle[45] or drop impact[46] or instantaneous drop spreading on a surface[47]. The dynamic wetting pressure witnessed through these capillary waves relies on the interfacial and thermophysical properties of the drop along with the momentum of the drop while it is spreading. If this pressure is not managed appropriately, undesirable and non-intuitive observations are witnessed such as bouncing of water drops on super hydrophilic surfaces[48] and overspreading of the drops [34, 36]. Therefore, as Shuttleworth and Bailey[49] mentioned in one of their classical papers, the manner of drop deposition dictates the final configuration of the drop at rest.

The physics behind the erroneous contact angle data and the proposed measurement technique presented here significantly advances the field of colloids and interface sciences, which relies heavily on the accurate quantification of contact angles and wettability. Such areas are, but not limited to, quantification of surface energy[50–54], coating[17], colloidal drop deposition[24], droplet based additive manufacturing [55, 56], space based research[4, 27, 28] and other industrial applications [56].

Given the significance of wetting properties and contact angle measurements, drop deposition techniques have been thoroughly studied by many researchers but interestingly the role of wetting pressure is overlooked. Herein, we articulate and compare the role of dynamic wetting pressure, via pendant drop and liquid needle drop deposition, on wetting characteristics, i.e. quantifying the difference in static contact angle by altering the wetting pressure.

## 2.2 Materials and methods

The materials and methods used for this study can be segmented into three parts: substrate preparation, high-speed imaging arrangements and contact angle measurements. To maintain the consistency in the surface energy level, we have used an aqua regia (AR) treated microscopic cover slip (Fisher Scientific) as a characterizing substrate. Aqua regia solution was prepared by mixing 3 : 1 ratio of 35% concentrated hydrochloric (HCl) acid and 65% concentrated nitric acid ( $\text{HNO}_3$ ) by volume. The glass substrate is immersed in the aqua regia solution for 30 minutes to assure the cleaning of the surfaces. The treated slides were then washed with distilled water and dried with pressurized air. The drop deposition and contact angle measurement was always performed within the first 30 seconds after drying. In addition to aqua regia cleaned glass, polyethylene (PE) and polydimethylsiloxane (PDMS) substrates were also used. The PDMS samples were prepared using Sylgard 184 (Dow Corning). Both samples were cleaned with detergent and subsequently rinsed with hot water, cold water and isopropanol.

The capillary wave dynamics of drops spreading on the AR substrates were captured with CMOS high-speed camera (Vision research, Phantom V711) fitted with an extended macro lens assembly. In order to maintain the frame capturing frequency within the same order of spreading time scale, the frame rate was selected between 5000Hz to 10000Hz. In addition,  $10\mu\text{s}$  exposure time was maintained for a resolution of  $800 \times 800$  pixels. The front view of the drop was recorded with optimized magnification where more than two-thirds of the sensor was occupied by the drop image. A needle with a known diameter (0.51 mm) was used as a reference for image calibration. A backlit illumination technique was employed using a 150W, 60Hz fibre optic light source (Type MO150, JH Technologies INC). Intermittently, an optical thermometer was used to verify that there was no significant temperature rise in the

surrounding medium and the substrate due to the light source. To maintain smooth and homogeneous illumination, a 70mm $\times$ 70mm square glass diffuser (Thorlab, Inc.) was used between the camera and the light source.

The KRÜSS DSA 100E equipped with software controlled needle dosing system assures constant minimum distance between the substrate and the needle, constant volume and fixed minimal speed ( $\approx$  4mm/s) of the needle moving towards the substrate. A flat tip needle of inner and outer diameter of 0.50 mm and 0.51 mm, respectively was used to generate the pendant drop.

All contact angles and base radii were measured with in-built ADVANCE software with the Drop Shape Analyser DSA 100E (KRÜSS GmbH) instrument. For measuring center of gravity (C.G.) of the drop a commercial image processing software (Image Pro V10, Media Cybernetics) was used. First a region of interest was selected to detect the darker drop from the brighter background, after, which the C.G. of the detected drop could be determined.

For both pendant drop and liquid needle drop deposition techniques, the datum line, i.e. the line from which we started C.G measurement was the top surface of the substrate. In the case of a pendant drop, as shown in supplementary figure A.1, as soon as the drop is in point contact with the substrate, the whole liquid bridge between the needle tip and substrate was considered for the C.G. measurement. It is important to consider the liquid bridge between the substrate and needle tip, so that the sudden fall in C.G., due to the pinch off, can be witnessed and well understood. Moreover, we can neglect the effect of residual liquid on the needle while measuring the C.G., since the magnitude of residual volume at the tip of the needle is comparatively small.

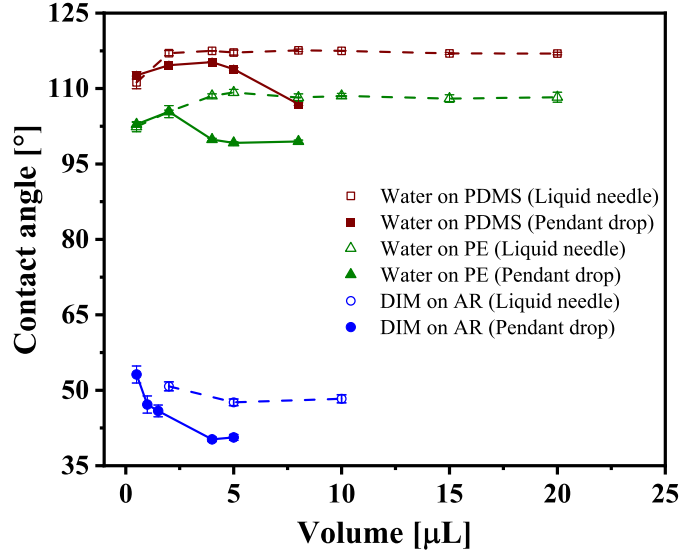


Figure 2.1: Equilibrium contact angle variation with respect to volume for various substrate-liquid combinations. Closed and open symbols represent drop deposited by pendant drop deposition technique and liquid needle drop deposition technique, respectively. The Bond number for 0.5, 1, 1.5, 2, 5, 10, 15 and 20  $\mu\text{l}$  are 0.03, 0.05, 0.06, 0.08, 0.15, 0.24, 0.31 and 0.38, respectively for water and for DIM the Bond number corresponding to 0.5, 1, 1.5, 2, 5 and 10  $\mu\text{l}$  are 0.1, 0.17, 0.23, 0.28, 0.51 and 0.81, respectively.

For liquid needle drop deposition, considering the thin jet diameter of  $\sim 0.1\text{mm}$  (compared to the deposited drop size), the jet attached to the drop was ignored and C.G of the already deposited drop was measured, as shown in the supplementary figure A.1(b).

In the case of jet based drop deposition technique, i.e. liquid needle deposition method, we used the pressure dosing system (DO3252, KRÜSS, GmbH)[57]. It is noteworthy to mention that that a minimum of four to a maximum of six experiments were performed for each data set showcasing the reproducibility of the measured data.

## 2.3 Results and discussion

### 2.3.1 Contact angle as a function of volume

Figure 2.1 illustrates the volume dependence of the static contact angle, which was measured after drop deposition with the pendant drop and liquid needle method. In the case of PE and PDMS, the contact angle of water after pendant drop deposition significantly decreases for volumes larger than  $3\mu L$ . It is important to note that the corresponding Bond number ( $Bo$ ) is less than unity for these volumes, hence the role of gravity can be safely ignored. Next to water, diiodomethane (DIM) is another liquid commonly used for wetting characterization. The relative decrease in contact angle of DIM after pendant drop deposition is larger than for water and starts decreasing at even smaller volumes. This is due to the density of DIM, which is three times larger compared to water. As capillary waves and dynamic wetting pressure strongly depend on the liquid density, it follows that the capillary waves resulting from the drop pinch off are largely responsible for an additional forceful wetting causing overspreading and thereby smaller contact angles. Interestingly, for all investigated liquid-substrate combinations, we observed no such decrease in contact angles with increasing drop volumes after liquid needle drop deposition. This suggests that the generated capillary waves are much less pronounced in liquid needle drop deposition than in the pendant drop deposition method. The comparably larger CAs after liquid needle drop deposition for volumes of  $1\mu L$  and  $3\mu L$  on PDMS and PE agree well with previous investigations and were already discussed therein[36]. In the following paragraphs, we will elucidate the pronounced volume dependence for DIM, analyzing the capillary waves detected with high speed image recordings.

### 2.3.2 High speed recordings of drop deposition processes

The spreading of the pendant drop onto a substrate undergoes several subsequent stages. Figure 2.2 (A) represents the collection of temporal snapshots corresponding

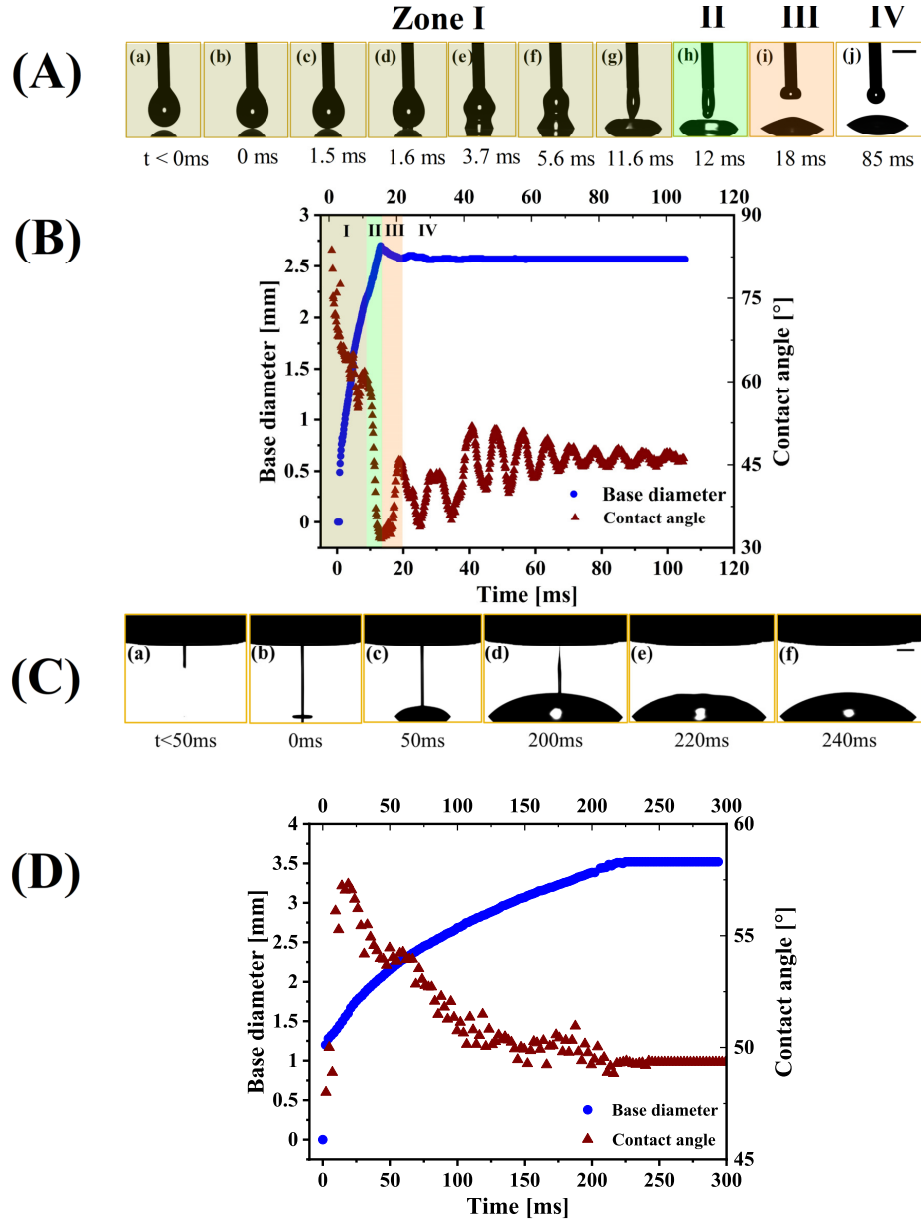


Figure 2.2: (A) Temporal snapshots of pendant drop deposition of DIM drop on aqua regia treated glass substrate. The scale bar is equivalent to 0.5 mm. (B) Variation of base diameter and dynamic contact angle of a  $1.5 \mu\text{L}$  DIM drop, via pendant drop deposition, with respect to time. (C) Temporal snapshots of liquid needle drop deposition of DIM drop on aqua regia treated glass substrate. The scale bar is equivalent to 0.5 mm. (D) Variation of base diameter and dynamic contact angle of a  $1.5 \mu\text{L}$  DIM drop, deposited by liquid needle drop deposition with respect to time.

to the spreading dynamics of a DIM drop on the aqua regia treated glass substrate, whereas the corresponding contact angle and base diameter for the same combination are presented in Figure 2.2 (B). The instant at which the drop contacts the substrate (Figure 2.2(A):(a-c)) is considered as  $t = 0s$ . At  $t=1.6$  ms Figure 2.2(A):(d), instantaneous rapid spreading of the drop is noticed triggering the first capillary wave. The perturbation, which is caused by the capillary wave, propagates from the bottom of the drop to the tip of the needle, which results in a formation of a neck closer to the needle. Eventually this first wave leads to a pinch-off scenario as depicted in Figure 2.2(A):(e-g). The phase from drop generation to the drop pinch-off is categorized as zone I. Finally, at 12 ms, Figure 2.2(A):(h), the pinch-off occurs and the drop detaches from the extended neck and a second generation of waves is triggered. The base diameter of the drop overspreads (Zone II) as soon as this secondary wave reaches the three-phase contact line and the oscillatory motion in the drop continues until the total energy inside the drop is dissipated. During this process, the oscillatory motion is evident at the drop-medium interface, which is reflected in contact angle variations. A small but significant recoiling of the drop base diameter is observed (Zone III and IV). This oscillation of the base diameter equilibrates significantly earlier than the contact angle (Figure 2.2(A):(j)). The recoiling of drops upon impacting is well understood[58–60]. But, the role of this contact line recoiling eventually causes a drop to finally overspread resulting in a difficult to control change in contact angle.

The oscillations observed in Figure 2.2B are the consequence of the capillary wave generated due to drop pinch off. Capillary waves and resulting dynamic wetting pressure can be almost completely avoided if the liquid is pumped to the already equilibrated sessile drop with a minimum possible flow rate. For this, either a needle must be inserted into the drop or drilled through the bottom of the substrate [61, 62], which both have their own limitations. The liquid-needle drop deposition technique circumvents such adverse effects as the liquid is pumped through the drop-air

interface by a thin jet.

For the liquid needle drop deposition technique a continuous laminar and  $100\mu m$  thick liquid jet, emanating from a dosing system above the substrate, generates the drop, as shown in Figure 2.2 (C). As soon as the liquid jet hits the surface, the jet spreads radially outward from the point of contact due to the kinetic or stored inertial energy as shown in Figure 2.2(C):(a-c). Initially when the jet impacts the substrate, the drop takes a splat shape instead of a spherical cap shape. The splat shape due to impact has already been well understood by drop impact studies [58–60]. As shown in Figure 2.2 (D), the drop base diameter increases continuously as the drop volume increases. From  $0 - 25ms$ , the drop base diameter spreading rate is relatively slower compared to the drop volume growth. Hence, a sharp increment in advancing contact angle is observed. In this period of time the kinetic energy imparted by the jet is the dominating force for the drop spreading. However, as a certain drop volume is achieved ( $\sim 25ms$ ), a gradual decrease in contact angle is observed. This reflects the continuously decreasing influence of the jet kinetic energy on the drop spreading, as with rising drop volume the viscous dissipation of the jet’s kinetic energy dominates [63]. At  $125ms$  the contact angle does not change any more within the experimental scattering. The latter originates from the fast forward moving three phase contact lines. Thus, from this point, the kinetic energy of the jet does not have any effect on the dynamic advancing contact angle. This is supported by earlier observations, that the drop shape during the liquid needle dosing phase is well described by the Young-Laplace function usually describing equilibrium drop shapes[36]. This also explains the observation that up to the volume of  $2\mu L$ , the CA measured after liquid needle drop deposition increases until it reaches its maximum plateau value (compare Fig. 2.1). A fundamental lower volume limit exists, below which the liquid needle does not provide the recently advanced CA, independent of the kinetic effect imposed by the jet. From figure 2D a constant contact angle is observed from  $150 - 200ms$  when

the drop volume is closer to  $1.5\mu\text{l}$ . In addition, it is also evident in figure 2.1 that, for liquid needle drop deposition, the contact of the drop is not independent of volume for a drop volume less than  $1.5\mu\text{l}$ . This suggests that after  $2\mu\text{l}$ , the effect of kinetic energy of the jet is completely subdued by the dampening effect inside the drop. This phenomenon is evident in the supplementary figure A.2.

For a fixed jet exit-substrate distance, optimisation of the dosing rate of the liquid jet is a crucial parameter for drop deposition: if the dosing is too low then it can trigger jet break up and conversely jet break up is witnessed with splashing and other undesirable effects[64]. Significantly higher velocity guarantees a continuous jet but at the cost of very high kinetic energy that adversely affect the contact angle measurement. It is reported that if the volume flow rate of the liquid jet is between  $0.1\ \mu\text{l}/\text{s}$  and  $25\ \mu\text{l}/\text{s}$ , and the ratio of the diameter of the jet to the diameter of the drop is 0.2 or less, most preferably 0.01 to 0.1, the adverse effect of kinetic energy on the reproducibility of equilibrium contact angles can be avoided[57]. In this study we have also maintained a 100 micron jet for a millimetric sized drop while maintaining volume flow rate of  $11.5 \pm 2.5\ \mu\text{l}/\text{s}$  and  $16.5 \pm 2\ \mu\text{l}/\text{s}$ , for DIM and water, respectively, which is in between the desired value, while maintaining a constant jet exit-substrate gap of 4mm.

For significantly smaller drop volumes the comparatively large kinetic energy still influences the final drop shape, resulting in smaller contact angles [36]. At  $200\text{ms}$  and  $220\text{ms}$ , jetting is ceased at the dosing valve and all the liquid mass has converged into the drop, respectively. It is interesting to note that the mean value of the dynamic advancing CA phase ( $125\text{ms}$  to  $200\text{ms}$ ) is  $52^\circ \pm 2.5^\circ$ , i.e. very close to the static advancing CA of  $49.5^\circ$  after the drop has come to rest. It is equally important to note that after all the liquid has converged into the drop, no further increase in drop base diameter, nor any recoiling effect of the three phase line is observed. This,

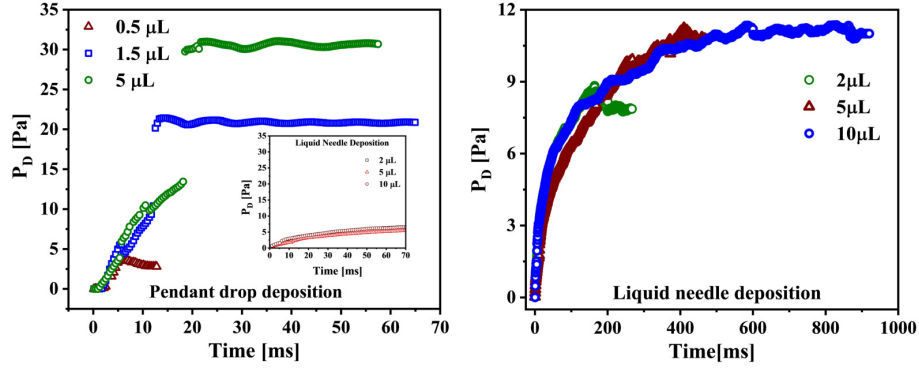


Figure 2.3: Transient variation of dynamic wetting pressure for (a) pendant drop deposition technique and (b) liquid needle deposition technique.

and the observed constant dynamic advancing contact angle during spreading, are in-line with previous results observed after liquid needle dosing of larger ( $> 13\mu L$ ) water and DIM drops onto PDMS [36]. It is noteworthy to mention that, unlike the pendant drop deposition technique, the generation of a primary capillary wave is avoided in liquid needle drop deposition since continuous spreading is achieved instead of instantaneous spreading. The absence of instantaneous spreading circumvents the triggering of the first capillary wave.

As described earlier, in the case of pendant drop deposition, the primary capillary waves force the drop to detach from the needle and during detachment the subsequent pinch-off generates the secondary capillary waves. Similarly, in the case of liquid needle deposition, as the desired volume is delivered ( $\sim 200ms$ ), jetting stops and the perturbation is observed at the drop-medium interface, as shown in Figure 2.2C:(d-e). At the end of the liquid needle drop deposition process, as a consequence of jet discontinuation, a ripple or capillary waves at the drop-medium interface can be witnessed. However, the perturbations marginally affect the drop shape because the mass of the deposited drop is large enough to dampen the capillary waves.

### 2.3.3 Dynamic wetting pressure

The dynamic wetting pressure ( $P_D$ ), acting on the three phase contact line of the drop, can be expressed as  $\frac{1}{2}\rho V_{fall}^2$ , which can be scaled as  $V_{fall}^2$  for a constant density liquid [45]. Here,  $V_{fall}$  is the impinging velocity of the spreading drop. Figure 2.3 depicts the temporal evolution of the dynamic wetting pressure for drops of different volumes for pendant and liquid needle drop deposition. In the case of pendant drop deposition, the center of gravity (C.G.) of the drop is gradually moving towards the solid-liquid interface. Immediately after the pinch-off a sudden fall in the C.G. is observed. This displacement of C.G. gives rise to the falling or impinging velocity,  $V_{fall} = \sqrt{2g\Delta}$ , where  $g$  is the gravitational acceleration and  $\Delta$  is the displacement of the drop's C.G. This  $V_{fall}$  then triggers the secondary capillary waves. Corresponding variations in  $\Delta$ ,  $V_{fall}$ , and  $P_D$ , for pendant drop deposition are presented in Supplementary Figure A.3.

The role of dynamic wetting pressure can be realized from the pressure scaling in the Navier-Stokes (NS) equation. For a smaller drop with low viscosity and Bond number less than unity, we can ignore the viscous and body forces in the NS equation. In the case of a low impact velocity scenario we can ignore the unsteady inertia term, and as a result, the NS equation can be expressed as the following:

$$\rho(u \cdot \Delta)u \sim \Delta P$$

A pressure term can be scaled with the convective inertia term such as  $P_D \sim \rho V_{fall}^2$ , where the  $P \sim P_D$ ,  $\Delta \sim 1/L$ ,  $u \sim V_{fall}$  and  $L$  can be considered as the wavelength of the capillary wave.

When a drop is deposited on a surface, the state of wetting depends on the balance

of wetting and capillary pressure, alternatively known as antiwetting pressure. The capillary pressure is the surface force per unit area. The characteristic length for the capillary pressure depends on the surface morphology or drop geometry. For example, for a micropillar substrate the length is the pillar length whereas for a porous substrate the length is the pore diameter [65]. For a smooth surface with perturbed drop interface the capillary wavelength can be considered as the characteristic length. Similarly, in our case we can consider the capillary pressure as,  $P_c = \frac{2\gamma_{LV}\cos\theta}{\lambda}$ , where  $\gamma_{LV}$  is the liquid-vapor interfacial tension and  $\lambda$  is the capillary wavelength, and as mentioned earlier the dynamic wetting pressure can be expressed as,  $P_D = \frac{1}{2}\rho v_{fall}^2$ . Now balancing  $P_C$  and  $P_D$  and solving for  $\theta$  gives  $\cos\theta \sim \frac{P_D\lambda}{\gamma_{LV}}$ , from which we can clearly observe that contact angle has an inversely proportional relationship to dynamic wetting pressure and capillary wavelength. Increasing either or both the  $P_D$  and  $\lambda$  will decrease contact angle and can cause overspreading of the drop base radius.

As shown in Figure 2.3 (a), two different regimes, caused by two separate capillary waves, can be observed for pendant drop deposition. As the drop detaches from the needle the sudden change in the location of C.G. results in discontinuity in the  $P_D$ . For a smaller volume ( $0.5\mu L$ ), this sudden increase in  $P_D$  is marginal but as the volume increases, the discontinuity is noticeable with larger magnitude of  $P_D$ . The amplitude of the secondary oscillations, after the pinch-off, is a function of drop volume. For larger volumes, the amplitudes are large enough to affect the C.G. of the drop, hence the oscillations in  $P_D$  are also noticed. The inset in Figure 2.3 (a) depicts the  $P_D$  variation for liquid needle drop deposition, and in order to draw a comparison, the inset figure also has same limit for both the axes. The magnified version of the same inset figure is presented in Figure 2.3 (b). The gradual shift in the C.G. results in a linear change in dynamic wetting pressure without any abrupt change and corresponding effects on the spreading dynamics. The larger dynamic wetting pressure in pendant drop deposition due to capillary waves has undesirable

effects on the spreading and contact angle measurements as was shown in Figure 2.1. A decreasing magnitude of the contact angle is witnessed for increasing drop volumes when using pendant drop deposition, whereas such dependency is not observed for the liquid needle deposition technique as shown in table 2.1. Our data shows that increased dynamic wetting pressure ( $P_D$ ) causes additional forceful dynamic wetting or spreading in pendant drop deposition scenario. In contrast, this effect is negligible in the case of liquid needle deposition technique. This further supports our finding that the dynamic wetting pressure ( $P_D$ ) certainly affects the equilibrium contact angle. If we compare both methods of drop deposition, the liquid needle drop deposition clearly outperforms the pendant drop deposition technique, as ignoring the effect of dynamic wetting pressure in pendant drop deposition can lead to an uncontrollable change in static contact angle up to  $10 - 15^\circ$  for the same liquid-solid combination. For the liquid needle drop deposition, this source of error is intrinsically excluded.

Volume ( $\mu L$ )	Contact angle ( $^\circ$ )	Contact angle ( $^\circ$ )
	Pendant drop	Liquid needle
0.5	$52 \pm 1.7$	$50 \pm 1.5$
1	$47 \pm 1.5$	$50 \pm 2$
1.5	$45 \pm 1.25$	$50 \pm 1.5$
4	$40 \pm 0.5$	$49 \pm 1$
5	$40.5 \pm 0.5$	$49 \pm 1$

Table 2.1: Static contact angle data for DIM on Aqua Regia treated glass substrate deposited by pendant drop and liquid needle technique.

### 2.3.4 Comparison with literature data

Table 2.2 represents some examples of contact angle data reported by other studies. In order to demonstrate the significance of this study, we have presented only contact angle data for water on untreated PDMS so that a comparative study can be per-

Volume ( $\mu L$ )	Contact Angle [Ref] ( $^{\circ}$ )
0.5	125 [66]
2	112 $\pm$ 10 [67]
3	112.5 $\pm$ 1.5 [68]
6	113.5 $\pm$ 2 [26]
10	100 $\pm$ 2 [69]
20	99.2 $\pm$ 2 [70]
25	120 $\pm$ 2 [71]

Table 2.2: Contact angle data for deionised water on untreated PDMS substrate deposited by needle dosing or pendant drop technique.

formed. From this table it is evident that a wide range of scattered contact angle data with a higher uncertainty or larger error bar can be observed from various studies, reason for which can be attributed to the different drop deposition approach adopted by different researchers. Though we have presented data from completely different group of researchers, we can also observe a slight decrease in contact angle data with the increment of drop volume for a certain drop-substrate combination. However, an exception to this is the study performed by Wang et al where it is showed that even at  $25\mu l$  contact angle of water on PDMS is still  $120^{\circ}$ . The result from Wong et al.[71], can be considered standard as they have performed very careful and meticulous contact angle measurements. Moreover, in that study, Wong et al.[71], slowly increased drop volume while the needle was immersed inside the drop, avoiding any drop pinch off and thus subsequent appearance of dynamic wetting pressure. As a result of minimizing the effects of dynamic wetting pressure, a contact angle of  $120^{\circ}$  was observed, which is similar to liquid needle drop deposition results presented in this study. Similar to our figure 1 results, from table 1 we can observe that different study reported different contact angle as a function of volume measured after pendant drop deposition technique. However, in case of liquid needle drop deposition we have

observed consistent contact angle of  $120^\circ$ .

## 2.4 Conclusions

This study reports an experimental investigation of contact angle variation with respect to volume of the drop deposited either by the pendant drop or liquid needle drop deposition. From this study, it can be observed that after pendant drop deposition there is an exponential decay in equilibrium contact angle of DIM and water drops on various substrates, with respect to drop volume, although the effective length of the drop is maintained under the capillary length scale. However, this aberrant relationship between the equilibrium contact angle and drop volume can be attributed to strong capillary waves (primary and secondary) generated at the drop-air interface, which originate from the pinch-off of the drop from the needle during pendant drop deposition. During the pinch-off regime of the pendant drop deposition, the abrupt fall of the drop's center of gravity gives rise to a dynamic wetting pressure. Due to the increase in dynamic wetting pressure, the base radius of the drop increases and the contact angle decreases. Interestingly, drops deposited with a liquid needle deposition method show that both dynamic wetting pressure and contact angle are not changing, regardless of the drop volume. This study proves that the liquid needle drop deposition technique has advantage over pendant drop deposition in terms of impeccable contact angle measurements, and can prevent volume dependant contact angle data, such has been encountered by previous studies [26, 66–71], due to adverse effects of drop-needle interactions. During liquid needle dosing, the drop shape can be well described by the equilibrium Young-Laplace function, once the initial phase of dominating kinetic energy effects on the jet has passed. This and the fact that the observed static CA after liquid needle drop deposition is always larger for drop volumes  $\geq 2\mu L$  motivates future studies to strengthen the statement that the CA after liquid needle drop deposition always provides the highest accessible static contact angle, and thereby the best controlled and easiest accessible way to determine the

static advancing CA, *i.e.*, the recently advanced contact angle [31, 42].

## References

- [4] T. Prater *et al.*, “Summary report on phase i results from the 3d printing in zero g technology demonstration mission, volume i,” 2016.
- [15] K. N. Prabhu, P. Fernades, and G. Kumar, “Effect of substrate surface roughness on wetting behaviour of vegetable oils,” *Materials & design*, vol. 30, no. 2, pp. 297–305, 2009.
- [16] A. Eifert, D. Paulssen, S. N. Varanakkottu, T. Baier, and S. Hardt, “Simple fabrication of robust water-repellent surfaces with low contact-angle hysteresis based on impregnation,” *Advanced Materials Interfaces*, vol. 1, no. 3, p. 1300138, 2014.
- [17] M. Sakai, T. Yanagisawa, A. Nakajima, Y. Kameshima, and K. Okada, “Effect of surface structure on the sustainability of an air layer on superhydrophobic coatings in a water- ethanol mixture,” *Langmuir*, vol. 25, no. 1, pp. 13–16, 2009.
- [18] Y. Son, C. Kim, D. H. Yang, and D. J. Ahn, “Spreading of an inkjet droplet on a solid surface with a controlled contact angle at low weber and reynolds numbers,” *Langmuir*, vol. 24, no. 6, pp. 2900–2907, 2008.
- [19] J. Perelaer, C. E. Hendriks, A. W. de Laat, and U. S. Schubert, “One-step inkjet printing of conductive silver tracks on polymer substrates,” *Nanotechnology*, vol. 20, no. 16, p. 165303, 2009.
- [20] H. Yang and P. Jiang, “Self-cleaning diffractive macroporous films by doctor blade coating,” *Langmuir*, vol. 26, no. 15, pp. 12598–12604, 2010.
- [21] M Rauscher and S Dietrich, “Wetting phenomena in nanofluidics,” *Annu. Rev. Mater. Res.*, vol. 38, pp. 143–172, 2008.
- [22] Z. Keshavarz-Motamed, L. Kadem, and A. Dolatabadi, “Effects of dynamic contact angle on numerical modeling of electrowetting in parallel plate microchannels,” *Microfluidics and Nanofluidics*, vol. 8, no. 1, p. 47, 2010.
- [23] J. S. Marin Quintero and P. R. Waghmare, “Sessile drop response to a single wave electrokinetic excitation,” *Physics of Fluids*, vol. 32, no. 12, p. 122102, 2020.
- [24] Y. Guo, H. S. Patanwala, B. Bognet, and A. W. Ma, “Inkjet and inkjet-based 3d printing: Connecting fluid properties and printing performance,” *Rapid Prototyping Journal*, 2017.
- [25] L. Li, W. Kang, and D. Ye, “A contact angle measurement method for the droplets in ewod-based chips,” in *2007 2nd IEEE International Conference on Nano/Micro Engineered and Molecular Systems*, IEEE, 2007, pp. 1071–1075.
- [26] A. Mata, A. J. Fleischman, and S. Roy, “Characterization of polydimethylsiloxane (pdms) properties for biomedical micro/nanosystems,” *Biomedical microdevices*, vol. 7, no. 4, pp. 281–293, 2005.

- [27] A. Passerone, “Twenty years of surface tension measurements in space,” *Microgravity Sci. Technol.*, vol. 23, no. 2, pp. 101–111, 2011.
- [28] A Ababneh, A Amirfazli, and J. Elliott, “Effect of gravity on the macroscopic advancing contact angle of sessile drops,” *Can. J. Chem. Eng.*, vol. 84, no. 1, pp. 39–43, 2006.
- [29] T. Huhtamäki, X. Tian, J. T. Korhonen, and R. H. Ras, “Surface-wetting characterization using contact-angle measurements,” *Nature protocols*, vol. 13, no. 7, pp. 1521–1538, 2018.
- [30] A Marmur, “Measures of wettability of solid surfaces,” *Eur. Phys. J. Special Topics*, vol. 197, no. 1, pp. 193–198, 2011.
- [31] A. Marmur, C. Della Volpe, S. Siboni, A. Amirfazli, and J. W. Drelich, “Contact angles and wettability: Towards common and accurate terminology,” *Surf. Innov.*, vol. 5, no. 1, pp. 3–8, 2017.
- [32] D. Cwikel, Q. Zhao, C. Liu, X. Su, and A. Marmur, “Comparing contact angle measurements and surface tension assessments of solid surfaces,” *Langmuir*, vol. 26, no. 19, pp. 15 289–15 294, 2010.
- [33] G. Wolansky and A. Marmur, “The actual contact angle on a heterogeneous rough surface in three dimensions,” *Langmuir*, vol. 14, no. 18, pp. 5292–5297, 1998.
- [34] P. R. Waghmare, S. Das, and S. K. Mitra, “Drop deposition on under-liquid low energy surfaces,” *Soft Matter*, vol. 9, no. 31, pp. 7437–7447, 2013.
- [35] P. R. Waghmare and S. K. Mitra, “Needle-free drop deposition technique for contact angle measurements of superhydrophobic surfaces,” *J. Appl. Phys.*, vol. 116, no. 11, p. 114 903, 2014.
- [36] M. Jin, R. Sanedrin, D. Frese, C. Scheithauer, and T. Willers, “Replacing the solid needle by a liquid one when measuring static and advancing contact angles,” *Colloid Polym Sci.*, vol. 294, no. 4, pp. 657–665, 2016.
- [37] J. W. Drelich, “Contact angles: From past mistakes to new developments through liquid-solid adhesion measurements,” *Advances in colloid and interface science*, vol. 267, pp. 1–14, 2019.
- [38] R. M. Podhajny, “Material science-astm d-5946-96, an astm-approved water contact angle test method for quantifying the level of corona treated films, is reported to be a more accurate alternative to the dyne,” *Paper Film and Foil Converter*, vol. 71, no. 6, pp. 26–27, 1997.
- [39] A. Designation, “D 724 89: Standard test method for surface wettability of paper (angle of contact method),” *Annual Book of ASTM Standards*, vol. 15, p. 60,
- [40] DIN, “Coating materials — wettability — part 2: Determination of the free surface energy of solid surfaces by measuring the contact angle,” *DIN 55660-2*, 2011.

- [41] E. DIN, *828: Klebstoffe–benetzbarkeit–bestimmung durch messung des kontaktwinkels und der kritischen oberflächenspannung fester oberflächen*, 1997.
- [42] J. Drelich, “Guidelines to measurements of reproducible contact angles using a sessile-drop technique,” *Surface innovations*, vol. 1, no. 4, pp. 248–254, 2013.
- [43] G. F. Teletzke, L. Scriven, and H. T. Davis, “Gradient theory of wetting transitions,” *Journal of Colloid and Interface Science*, vol. 87, no. 2, pp. 550–571, 1982.
- [44] A. Bussonnière, A. Antkowiak, F. Ollivier, M. Baudoin, and R. Wunenburger, “Acoustic sensing of forces driving fast capillary flows,” *Physical Review Letters*, vol. 124, no. 8, p. 084502, 2020.
- [45] H.-M. Kwon, A. T. Paxson, K. K. Varanasi, and N. A. Patankar, “Rapid deceleration-driven wetting transition during pendant drop deposition on superhydrophobic surfaces,” *Physical review letters*, vol. 106, no. 3, p. 036102, 2011.
- [46] J. M. Kolinski, L Mahadevan, and S. M. Rubinstein, “Lift-off instability during the impact of a drop on a solid surface,” *Physical review letters*, vol. 112, no. 13, p. 134501, 2014.
- [47] M. R. Rahman, H. N. Mullagura, B. Kattamalalawadi, and P. R. Waghmare, “Droplet spreading on liquid–fluid interface,” *Colloids and Surfaces A: Physicochemical and Engineering Aspects*, vol. 553, pp. 143–148, 2018.
- [48] J. M. Kolinski, L Mahadevan, and S. Rubinstein, “Drops can bounce from perfectly hydrophilic surfaces,” *EPL (Europhysics Letters)*, vol. 108, no. 2, p. 24001, 2014.
- [49] R Shuttleworth and G. Bailey, “The spreading of a liquid over a rough solid,” *Discussions of the Faraday Society*, vol. 3, pp. 16–22, 1948.
- [50] H. Fox and W. Zisman, “The spreading of liquids on low energy surfaces. i. polytetrafluoroethylene,” *Journal of Colloid Science*, vol. 5, no. 6, pp. 514–531, 1950.
- [51] D. K. Owens and R. Wendt, “Estimation of the surface free energy of polymers,” *Journal of applied polymer science*, vol. 13, no. 8, pp. 1741–1747, 1969.
- [52] S. Wu, “Calculation of interfacial tension in polymer systems,” in *Journal of Polymer Science Part C: Polymer Symposia*, Wiley Online Library, vol. 34, 1971, pp. 19–30.
- [53] C. J. van Oss, M. Chaudhury, and R. J. Good, “Monopolar surfaces,” *Advances in colloid and interface science*, vol. 28, pp. 35–64, 1987.
- [54] D. Kwok, A Leung, C. Lam, A Li, R Wu, and A. Neumann, “Low-rate dynamic contact angles on poly (methyl methacrylate) and the determination of solid surface tensions,” *Journal of colloid and interface science*, vol. 206, no. 1, pp. 44–51, 1998.

- [55] I. Fraunhofer *et al.*, “Droplet-based additive manufacturing of hard metal components by thermoplastic 3d printing (t3dp),” *Journal of Ceramic Science and Technology*, vol. 8, no. 1, pp. 155–160, 2016.
- [56] S. Basu, A. K. Agarwal, A. Mukhopadhyay, and C. Patel, *Droplet and spray transport: paradigms and applications*. Springer, 2018.
- [57] B. Friedrich, F. Weser, and C. Scheithauer, *Contact angle measurement apparatus*, US Patent 9,816,909, 2017.
- [58] M Pasandideh-Fard, Y. Qiao, S. Chandra, and J. Mostaghimi, “Capillary effects during droplet impact on a solid surface,” *Phys. Fluids*, vol. 8, no. 3, pp. 650–659, 1996.
- [59] T. Mao, D. C. Kuhn, and H. Tran, “Spread and rebound of liquid droplets upon impact on flat surfaces,” *AIChE Journal*, vol. 43, no. 9, pp. 2169–2179, 1997.
- [60] A. Ahmed, B. A. Fleck, and P. R. Waghmare, “Maximum spreading of a ferrofluid droplet under the effect of magnetic field,” *Phys. Fluids*, vol. 30, no. 7, p. 077102, 2018.
- [61] D Li, P Cheng, and A. Neumann, “Contact angle measurement by axisymmetric drop shape analysis (adsa),” *Adv. Colloid Interface Sci.*, vol. 39, pp. 347–382, 1992.
- [62] D. Kwok, R. Lin, M Mui, and A. Neumann, “Low-rate dynamic and static contact angles and the determination of solid surface tensions,” *Colloids Surf. A Physicochem. Eng. Asp.*, vol. 116, no. 1-2, pp. 63–77, 1996.
- [63] D. Erickson, B. Blackmore, and D. Li, “An energy balance approach to modeling the hydrodynamically driven spreading of a liquid drop,” *Colloids Surf. A Physicochem. Eng. Asp.*, vol. 182, no. 1-3, pp. 109–122, 2001.
- [64] B. Bonhoeffer, A. Kwade, and M. Juhnke, “Impact of formulation properties and process parameters on the dispensing and deposition of drug nanosuspensions using micro-valve technology,” *J. Pharm. Sci.*, vol. 106, no. 4, pp. 1102–1110, 2017.
- [65] T. Deng *et al.*, “Nonwetting of impinging droplets on textured surfaces,” *Applied Physics Letters*, vol. 94, no. 13, p. 133109, 2009.
- [66] P. Goel, S. Kumar, J. Sarkar, and J. P. Singh, “Mechanical strain induced tunable anisotropic wetting on buckled pdms silver nanorods arrays,” *ACS applied materials & interfaces*, vol. 7, no. 16, pp. 8419–8426, 2015.
- [67] D. Bodas and C. Khan-Malek, “Formation of more stable hydrophilic surfaces of pdms by plasma and chemical treatments,” *Microelectronic engineering*, vol. 83, no. 4-9, pp. 1277–1279, 2006.
- [68] M. M. Stanton, R. E. Ducker, J. C. MacDonald, C. R. Lambert, and W. G. McGimpsey, “Super-hydrophobic, highly adhesive, polydimethylsiloxane (pdms) surfaces,” *Journal of colloid and interface science*, vol. 367, no. 1, pp. 502–508, 2012.

- [69] T. Trantidou, Y. Elani, E. Parsons, and O. Ces, “Hydrophilic surface modification of pdms for droplet microfluidics using a simple, quick, and robust method via pva deposition,” *Microsystems & nanoengineering*, vol. 3, no. 1, pp. 1–9, 2017.
- [70] S. Temmel, W. Kern, and T. Luxbacher, “Surface modification of polyethylene by photosulfonation,” *Polymer Surface Modification: Relevance to Adhesion*, vol. 4, p. 157, 2007.
- [71] W. S. Wong *et al.*, “Adaptive wetting of polydimethylsiloxane,” *Langmuir*, 2020.

# Chapter 3

## Effect of gravity on the spreading of a droplet deposited by liquid needle deposition technique <sup>1</sup>

### Abstract

This study represents an experimental investigation, complemented with a mathematical model, to decipher the effect of gravity on the spreading dynamics of a water droplet. For the theoretical discussion, an overall energy balance approach is adopted to explain the droplet spreading under both microgravity ( $\mu g$ ) and terrestrial gravity condition. Besides explaining the mechanism of the droplet spreading under microgravity condition achieved during the parabolic flight, a technique with detailed experimental set-up has also been developed for the successful deposition of droplet. A rational understanding is formulated through experimental investigation and theoretical analysis, which allows us to distinguish the transient variation of the spreading of a droplet, between microgravity and terrestrial gravity condition. The spreading of the droplet is predicted by the non-linear overall energy balance equation, which accounts for the operating parameters in the form of non-dimensional

---

<sup>1</sup>the version of this thesis chapter has been published as Aleksey Baldygin (A.B), Abrar Ahmed (A.A.), Ryan Baily (R.B.), Md Farhad Ismail (M.F.I.), Muhammed Khan (M.K.), Nigel Rodrigues (N.R.), Ali-Reza Salehi (A.R.S.), Megnath Ramesh (M.R.), Sanjay Bhattacharya (S.B.), Thomas Willers (T.W.), Derek Gowanlock (D.G.), and Prashant R. Waghmare (P.R.W.), “Effect of gravity on the spreading of a droplet deposited by liquid needle deposition technique”, npj Microgravity, Volume 9, issue 1, Pages 49, 2023.

groups like Reynolds number (Re), Weber number (We) and Bond number (Bo). To distinctly identify the difference in the drop spreading at terrestrial and microgravity conditions, the Bo with transient gravitational field obtained through the on-board accelerometer is considered. The obtained theoretical results are further corroborated by experimental results which are obtained from the parabolic flight.

### 3.1 Introduction

The fundamentals of capillarity and spreading phenomenon are dictated by the interplay between the interfacial and body forces like surface tension and gravitational force. In the absence of gravity this interfacial force dominates the most of the liquid behaviours. Therefore thorough painstaking research has been conducted to understand the influence of gravity on the interfacial phenomenon. In this endeavour, a considerable amount of literature have been devoted to the effect of gravity on capillary driven phenomena. Referring to the classical theory of capillarity [72], if the characteristic length of a drop is less than a capillary length, gravitational effects can be neglected and hydrostatic pressure rapidly stabilizes across the droplet profile. It leads to a spherical shape being adopted by the droplet in order to obey the Laplace law.

Droplet spreading or wetting is one of the ubiquitous phenomena that is governed by interplay between interfacial forces and has a wide range of industrial applications. In nature, several intriguing phenomena are dictated by the wetting such as, the self-cleaning property of lotus leaves [73], the water strider walking in water surfaces[74], the anti-fogging functionality of mosquito eyes [75], the water collection of the Namib Desert beetle[76], and so on [77–79]. On the other hand, the knowledge of spreading dynamics is a fundamental of many industrial-based applications, including but not limited to inkjet printing[18], bio-sensors[80], spray coating[81], agriculture[82], 3D

printing[83] and many more. Therefore, the understanding of the physics of droplet spreading is crucial for the development of nature-inspired, state-of-art research.

Theoretical explanation on the gravitational effect on the contact angle of a droplet has already been presented by many researchers[84–86]. Fujii et al.[87] developed a drop shape model where the curvature of the drop was a function of gravity. Herzberg and Marian[88] have experimentally investigated that the change in the contact angle does not depend on the drop size, rather it is primarily due to the change in the contact angle hysteresis, however, they did not test their hypothesis on reduced gravity environment. Later on, Good and Koo[89] attempted introducing a hypothetical negative line tension to justify the effect of droplet size on the contact angle variation. Performing meticulous mathematical exercise and rigorous calculation based on Bashforth and Adams [90] scheme, Fuji and Nakae[87] showed that the equilibrium contact angle is unaffected by the gravity.

However, the clarity is still missing, whether the physical and interfacial properties of fluid are affected by the gravitational force or not? Due to the higher expense and accessibility to reduced gravity environment at the International Space Station (ISS), researchers have attempted to simulate the reduce gravity environment instead of going to space with fairly accessible parabolic flights[91] or drop tower facilities[92]. In the case of droplet dynamics, with either ways, unfortunately, drop deposition always remained the biggest engineering challenge, in particular if the drop deposition is achieved during the reduced gravity time span. This time span is a few seconds (2-2.5 seconds) for drop tower and between 15-25 seconds for parabolic flights. Hence, significant efforts have been devoted to engineer drop deposition technique that unaltered the wetting or spreading of the droplet. In the current study, presented by us, we proposed a technique, which circumvents most of the undesirable effects associated with the deposition technique. After the flight campaign we are convinced

that this can be the next generation drop deposition techniques for reduced gravity applications and we have vetted it for the wetting characteristic and drop spreading dynamics applications, where the drop deposition is the key step.

With terrestrial conditions, drop deposition can be achieved using techniques such as drop deposition with the needle facing the substrate[93], drilling substrate [61, 62] and other specific needle-less drop deposition techniques [34–36, 94]. So far, for the reduced gravity applications, majority of studies have drilled the substrate to pump liquid from underneath the substrate, that eventually forms the drop on the substrate[28]. Alternatively, drop is deposited on a surface prior experiencing the reduced gravity and deformation in equilibrated drop shape is studied[95]. In both the circumstances, experimental arrangements were restricted from studying the spreading dynamics, thus instantaneous spreading in reduced gravity environment has not been studied yet. Ababneh et al.[28] experimentally investigated, using parabolic flight, the effect of gravity on the advancing contact angle after depositing the drop before the drop experiences the reduced gravity. In their work, advancing contact angle in the terrestrial gravity is reported  $5^\circ$  larger than that in reduced gravity. Later on, Zhu et al.[96] experimentally investigated the contact angle dependence of an evaporating sessile and pendant drop on the microgravity. However, they have observed that the equilibrium or apparent contact angle of a water droplet on aluminium substrate is decreased by  $15^\circ$  in microgravity[96]. Diana et al.[95] initiated the development of a database of contact angles of sessile droplet under reduced gravity conditions.

Based on the database presented in by Diana et al.[95], two observations can be made, in all of the studies the drop is deposited before the reduced gravity triggers and the measured contact angles are always smaller in magnitude as compared to the terrestrial measurements. From this study it is also evident that the Young-Laplace equation was validated to accurately predict the contact angle in reduced gravity for droplets smaller than capillary length scale; however, it was not adequate to describe

the contact angle for drops larger than capillary length scale. One limitation of this study is the duration of the reduced gravity drop can experience, and is limited to 2.2 seconds. Brutin et al.[97] have witnessed two different contact angles depending on the onset of water droplet generation. If the drop is the already equilibrated before it goes the microgravity, the contact angle can be  $10^\circ$  lower compared to the same drop created under microgravity condition [97].

Despite a fair number of publications have been devoted to the experimental investigation on the variation of physical parameters of a droplet with respect to gravity, a fundamental model describing the droplet spreading phenomenon under reduced gravity condition is still missing from the literature. Additionally, a reliable and reproducible drop deposition technique under reduce gravity condition is yet to be addressed. Thus, our present study addresses a droplet deposition technique functioning under microgravity and proposes a mathematical model, which can predict the spreading of the three-phase contact line diameter of a droplet both under reduced and terrestrial gravity condition. The theoretical model presented here is based on an overall energy balance equation, where dimensionless numbers, such as; the Reynolds number, the Weber number, and the Bond number characterize the droplet spreading. Furthermore, the jet impact analysis is introduced in order to define the initial condition while quantifying the transient variations in the geometrical parameters of a droplet. Finally, we compare our theoretical predictions with the experimental results, obtained in parabolic flight, which was a part of flight campaign sponsored by Canadian Space Agency through FAST Grant that took place in October 2021 at Flight Research Laboratory. The experimental set-up was previously verified in parabolic flight, which was part of inaugural the Canadian Reduced Gravity Experiment Design Challenge (CAN-RGX) flight campaign and results reported here are from recently performed flight campaign.

## 3.2 Results and Discussion

### 3.2.1 Drop Deposition in $\mu g$

The conventional drop deposition such as droplet volume method or sessile droplet method have their limitation in reduce gravity experiment, perhaps they will fail in this case [27]. Droplet weight or volume method[98], where the droplet is detached from the capillary by its own weight, is not a valid choice to deposit droplet on the substrate. The pendant droplet technique, where the drop is brought in the close proximity to the substrate and allowed it to detach from the needle, is also not a viable option as it poses numerous engineering challenges[34]. Moreover for parabolic flight experiments, the time window to perform experiments is between 18-20s, as shown in Figure 3.5 and the “g-jitter” plays a crucial factor while deciding the drop deposition technique[99]. Similarly, for the drop tower, the drop deposition has not been achieved that can work during the reduced gravity time ( $\sim 2.2s$ ) window. To the best of our knowledge, all the previous literature on reduce gravity experiment in parabolic flight or drop tower facility describe generation of droplet on the substrate through the quasi-static addition of mass by pumping a liquid through a hole in the substrate, where the position of the needle is underneath the substrate[28, 61, 95]. However, pumping liquid by a needle through the punctured substrate has major drawbacks, as it is sensitive to the injection mass flow rate and the appropriate ratio between the drop and needle diameter. If the injection mass flow rate is high enough then there will be formation of jet from the needle instead of a droplet[96]. On the other hand, if the injection of mass flow rate is low, it will grow at drop-medium interface rather spreading at the three phase contact line and the evaporation of liquid can also take place during the slower drop generation [100]. Considering all the adverse effects of existing drop deposition method in microgravity, a jet-based drop deposition method, also known as liquid needle method [36, 57, 101], is proposed here. In liquid needle drop deposition technique, a very thin jet ( $100\mu m$ ) of constant flow

rate that can pump out the fluid through jetting at constant jet velocity up to  $25 \mu l s^{-1}$  [57, 101]. It is proven that, on terrestrial conditions, a reproducible sessile drop volumes with same equilibrium contact angles can be produced with this deposition technique [57, 101]. It is also proven that if the ratio of the diameter of the jet to the diameter of the drop is 0.2 or less, the adverse effect of kinetic energy [57, 101] on the reproducibility of the recently advanced contact angle can be minimized [100]. Therefore, considering all the shortcomings of traditional droplet deposition techniques and other approaches, we have decided to extend the utility of a jet based drop deposition technique [36, 101] to deposit or generate the droplet onto the substrate under reduced gravity condition.

It is noteworthy to mention that a numerous piezoelectric and pneumatic drop on demand (DOD) generators are available in the market. However, all the commercially available DOD generators are developed for pharmaceutical or ink-jet applications where the inherent kinetic energy due to the impacting droplets is significantly higher. To the best of our knowledge none of the existing devices are ideal for the droplet deposition and wetting characteristic due to the inherent kinetic energy with ejecting fluid that contribute towards the erroneous contact angles [36, 57, 101]. Additionally, commercially available pneumatic DOD devices are more prone to generate satellite droplets which is not desirable in the micro gravity environment [102]. Finally, cyclic acceleration ( $2g$  to  $\sim 0g$ ) involved in the parabolic flights and limited space inside the flight cabin mandates the robustness, compactness and requirement of less number of components with minimal energy consumption for a component or device.

Using liquid jet for the purpose of generating a spreading droplet comes with challenges. Usually in order to form a continuous jet, a necessary criteria must be fulfilled such as Rayleigh stability or high Weber number [64, 103, 104]. As mentioned earlier,

the higher kinetic energy might have a considerable influence on the spreading and resultant contact angle. More precisely, if the liquid jet is impacting on a substrate, with significantly higher speed (i.e., kinetic energy and resultant Weber number), the kinetic energy in the drop translates into the formation of the drop and overspreading of drop might be witnessed or in some cases splashing with formations of multiple droplets. As a result, either drop formation cannot be achieved or the measured contact angles with formed drops is incorrect representation of wettability of the substrate. Conversely, if the jet speed is low enough, the break-up of the liquid jet before hitting the substrate can cause the instabilities at the drop medium interface and triggers the air bubble formations inside the drops, resulting in falsified contact angle results. Therefore, the speed at which the jet emanates from the nozzle needs to be controlled carefully in order to get an impeccable wetting results, which in general is cumbersome with the commercial DOD generator.

The liquid needle drop deposition technique[101] is precisely studied to circumvent these unavoidable effects and optimized in such a way that the influence of the kinetic energy on the measured contact angles is negligible. To achieve this, the flow rate of the water is optimized at  $15 \pm 2 \mu l s^{-1}$  that assures a continuous laminar liquid jet emanating from a pressurized dosing systems[36, 57]. This laminar jet is used to generate the sessile drop, as shown in Figure 3.1, where the droplet size is generally one order of in magnitude higher than the jet diameter[36, 57]. As shown in Figure 3.1, the jet spreads radially outward from the point of contact as soon as the liquid jet hits the surface due to the jet's kinetic energy. The continuous mass addition through jet results in the increase in the base diameter and height of the spreading droplet. It is noteworthy to mention that, unlike the single droplet impact scenarios, rapid retraction of the spreading drop at the three phase contact line or other undesirable effects due to resultant capillary waves [101] are restrained during liquid needle drop deposition technique. Hence, we can say that in case of liquid needle deposition

technique, the simultaneous spreading is achieved along with the mass addition via jetting across the drop-medium interface.

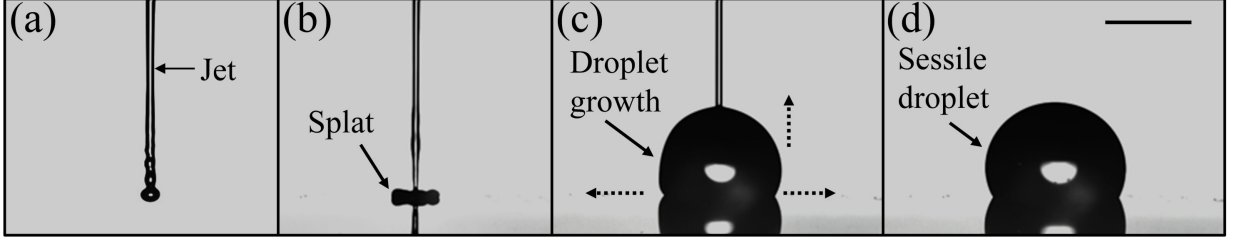


Figure 3.1: **Snapshots representing the formation of a droplet through liquid needle drop deposition technique.** (a) The water jet formation in the air medium, (b) liquid jet impacting on a substrate and forming a splat, (c) droplet growth due to the continuous addition of mass in the form of liquid jet where the horizontal and vertical dotted arrow signs indicate the spreading of base diameter and the increment of droplet height, (d) sessile droplet created by the liquid needle drop technique. The scale bar showed in panel (d) represents  $1mm$ .

The jet parameters used in this study are tuned optimally for a given liquid-surrounding medium in such a way that the magnitude of the momentum imparted on the drop negligibly impacts the later stage drop spreading and resultant equilibrium contact angle. The details of the theoretical understanding are described in the Supplementary Discussion of the paper. Droplet spreading is also influenced by surface energies of the liquid and solid for a given surrounding medium, viscous dissipation within the drop and from the surrounding medium, and gravitational forces. If the operating parameters are not optimized, the jet rebound can be witnessed [105, 106], which we have avoided by optimizing the jetting parameters. After achieving the successful drop deposition, the effect of gravity on droplet spreading and equilibrium shape, in particular, for droplets with larger volume are demonstrated by performing a comparative study. The theoretical model is based on overall energy balance equation and can successfully predict the spreading dynamics while the droplet is forming via jet based deposition system. The detailed derivation and discussion on the model is presented in the Supplementary Discussion section.

### 3.2.2 Dynamics of Drop Spreading

In this flight campaign (funded through FAST) we deposited a drop of different volumes that distinguishes the role of gravity on drop spreading and equilibrated drop shape configurations. Figure 3.4 represents the effect of gravity on the evolution of a  $10\mu\text{l}$  sessile droplet, generated by the liquid needle dosing system. This figure represents the state of a drop, generated by liquid needle drop deposition technique, in three different gravity levels, provided during the parabolic flight. As shown in the Figure 3.4, the microgravity environment stays from  $0-22\text{s}$ . It is to be noted that the drop deposition was initiated, as soon as the microgravity condition started, which was identified by the operator's experience of gravity in relation with the announcements made by the pilot. For the  $10\mu\text{l}$  drop, the opening of the nozzle was closed at  $660\text{ms}$ , that ceased the jetting subsequently. Until this moment, the continuous influx of flow through the drop-medium interface, normal to the advancement of the three phase contact line results in a rapid increasing in the drop base diameter and height. At the onset of the deposition (Supplementary Video 1), the drop grows vertically faster than the spreading along the substrate, hence, the contact angle increase at first for a few milliseconds and then decreases. This can be attributed to the slower rate of spreading at beginning that can be due to several reasons, such as; contact angle hysteresis, roughness of the substrates, jetting parameters, etc. Once the spreading begins, the base diameter and the maximum height of the drop grow until the volume is added to the drop. After the deposition of a required volume, the drop remained stable during the microgravity period but the marginal influence of g-jitter can be witnessed in contact angle variations.

The geometrical profile of the sessile drop, on the copper substrate, while it is going through the  $\mu\text{g}$ ,  $\sim 2\text{g}$ , and  $1\text{g}$  is sequentially numbered in Figure 3.4(a) whereas

the corresponding extracted drop shape is shown in Figure 3.4(b). As a standard operating procedure followed by pilots for such parabolic flights, immediately after the microgravity, the flight goes through a  $45^\circ$  nose down manoeuvre, which results in  $\sim 2g$ . This  $\sim 2g$  or hypergravity period continued from  $22s - 40s$ . From  $23.5s$  to  $27s$ , during this period, the drop base was pinned, however, due to the hypergravity the drop gets compressed and as a result an increase in contact angle is observed. In the event of drop pinning the base diameter remains unchanged, however, the height of the drop and subsequently contact angle will change. When the pinning effect is dominant, the drop profile deviates from spherical cap and resembles to an oblate ellipsoidal cap. From the experimental results presented in Figure 2(a), we can observe that during the  $\mu g$  period, both base diameter and height attains equilibrium at the same instant, one can argue that pinning was minimal. However, in hypergravity ( $\sim 2g$ ), when drop height decreases the base diameter does not increase proportionally, which suggest the pinning of the droplet. For an ideal substrate, the change in the base diameter with constant contact angle can be witnessed. The contact angle attains another maxima ( $\sim 78^\circ$ ) at point 2 as annotated in Figure 3.4 (a), and the corresponding profile of the drop at point 2 can be observed in Figure 3.4 (b). After  $27s$  the base diameter of the drop was increasing, while the height of the drop was decreasing and as a result the contact angle decrement continues until  $40s$ , as indicated by case 3 in Figure 3.4 (a) & (b). The point 3 also marks the end of hypergravity period. After the hypergravity period the flight entered into the  $1g$  period and during  $1g$  period the contact angle remains stable at  $71^\circ$ .

The hydrostatic pressure at the apex and base of a sessile drop is minimum and maximum, respectively. The variation from zero to maximum is a linear function of drop height measured from the apex of the drop [107]. For a given substrate-liquid combination, the hydrostatic pressure increases as the drop volume increases. At the three-phase contact line, the hydrostatic ( $P_H$ ) and capillary pressure ( $P_C$ ) act against

each other. The hydrostatic pressure pushes the drop outward, whereas the capillary pressure attempts to minimize the surface area of the drop. With terrestrial gravity or hyper-gravity, drop with  $Bo > 1$ , the hydrostatic pressure is larger than capillary pressure and the difference grows as the droplet volume increases. During  $2g$  manoeuvre, for larger droplets, the role of hydrostatic pressure is prominent. This can be witnessed by observing the decrease in drop height or bulging out of the droplet. However, a similar argument is invalid in  $\mu g$ . This phenomenon is also well supported by our experimental observation in Figure 2(a). It is evident that under  $2g$  drop height is smaller and in microgravity, it increases, which is the manifestation of pure surface tension driven phenomenon.

During the hypergravity or  $2g$  period, the drop get compressed from apex to the depth of the base due to the higher hydrostatic pressure. As a result the base or spreading diameter increases. From Figure 2(a) we can also observe that during hyper gravity, from  $22s - 23.5s$ , a sudden jump in base dia is observed, which is the manifestation of hydrostatic pressure driven phenomena, because during this hyper-gravity period the hydrostatic pressure is greater than the capillary pressure and as a result we can observe an outward flow along the base diameter.

In order to distinguish the drop behaviour in microgravity from terrestrial gravity, we have presented the figure 3.2. This figure compares the transient variation of physical parameters of the droplet for both the gravity conditions. From the Figure 3.2 (a), a slight difference in the transient variation of base diameter between micro gravity ( $\mu g$ ) and terrestrial gravity ( $1g$ ) condition is observed. Under terrestrial gravity condition, the base diameter is larger than the micro gravity condition while the droplet is forming. It is noteworthy to mention that, the perimeter of the droplet where the three phases: liquid, solid and vapour meet, also called three phase contact line (TPCL), can be quantified based on the droplet base diameter if we make a

well accepted assumption of spherical cap shape. Under microgravity condition the surface tension dominates over the gravity and as a result the droplet tends to form a spherical shape and will minimize the solid-liquid and liquid-air surface area. Thus, in reduced gravity environment for a given drop volume, particularly for the drops having characteristic length larger than capillary length scale, the base diameter or TPCL spreads less as opposed to spreading with earth gravity as shown in Figure 3.4. One can also argue that that contact angle hysteresis more prone in reduce gravity that restricts the drop spreading in pronounced way.

Figure 3.2(b) shows the variation of height with respect to time under  $\mu g$  as well as  $1g$ . A  $10 \mu l$  volume of water droplet was formed on the copper substrate, by the continuous addition of mass in the form of water jet. From Figure 3.4 (b), it is evident that the overall height of the droplet is significantly higher in the micro gravity condition compared to the height in the earth gravity. While the droplet is in microgravity condition, the effects driven by capillary forces are enhanced due to which the droplet tends to stretch along its height rather spreading along the three phase contact line by overcoming the pinning due to the contact angle hysteresis, which is measured as  $38^\circ$ , for the tested substrate. Therefore, the droplet minimizes its base radius and tries to form a sphere over the substrate due to the interfacial forces. In the the drop formation process (Supplementary Video 1), the drop under microgravity tends to grow normal to the three phase contact line; therefore, the height of the drop is higher in the micro gravity conditions. Under microgravity conditions, the drop is more stable than the terrestrial drop deposition, which is evident by the monotonous change in the height vs time plot, as well as it can also be observed that after  $\sim 9s$  the drop stops oscillating in the vertical direction. On the other hand, the change in the drop height is not monotonous in terrestrial gravity. In  $1g$ , after  $\sim 1s$ , the drop height was reducing and it became stable after  $\sim 13s$ . It indicates that under the effect of gravitational field, for drop volume as high as  $10\mu l$ , the competition

between gravity and surface forces allow the drop reaching equilibrium later than the microgravity condition.

The influence of gravity on the advancing contact angle can also be understood from the Figure 3.2 (c). The significant difference of  $8^\circ$  in the contact angle can be easily observed from this figure. During the microgravity, the advancing contact angle is  $74.5^\circ \pm 2^\circ$ , whereas under terrestrial gravity the value of advancing contact angle is  $66^\circ \pm 1.3^\circ$ . The reason behind the higher contact angle, for a specific liquid-substrate combination, can also be explained with the help of Figure 3.2 (b & c). Due to the absence in gravitational effect, the pure surface tension driven phenomenon takes place and as a result the deposited drop in microgravity tends to form a spherical bead to stay at a low energy state by contracting its base diameter and expanding its height. Therefore, a higher value of contact angle is observed in the microgravity condition. On the contrary, inside the gravitational field, the hydrostatic force of the drop is no longer negligible rather for a larger drop it dominates over surface forces and the effect of hydrostatic force causes the drop to spread more and further reduces the contact angle. It has already been demonstrated that due to hydrostatic force the advancing contact angle decreases with the larger drop size, where Bond number is close to unity [108]. In any ideal experimental condition contact angle depends on the measurement conditions, such as, drop size, external forces (e.g. gravity)[108], drop deposition rate[101], characteristics of the solid needle material [94], surface tilt angle [109]. In short it can be said in ideal case, an experimental conditions in which drop based study is conducted does not guarantee that thermodynamic equilibrium is really achieved and as a result one can argue that it is not possible to measure advancing contact angle experimentally. Therefore, in order to distinguish between theoretical and experimentally achieved contact angle, apparent as placed contact angle is introduced[108]. As placed contact angle refers to a contact angle that a drop makes upon being placed gently on a horizontal surface, and after allowing some

time for the drop to equilibrate, and pin to the surface in some metastable position somewhere between theoretical advancing and receding contact angle[108]. Therefore, contact angle resulted from the gravitational effect can be considered as an ‘as placed’ contact angle. It has also been observed that as placed contact angle is lower in magnitude than the true advancing contact angle. The results presented in Figure 3.2 (c) is representing a  $10\mu l$  drop. However, the similar kind of results can also be shown for other volumes, as shown in Supplementary Figure 2.

Again referring to the Figure 3.4 we can observe that in the parabolic flight experiment when the drop is in microgravity period it sustains its low energy states by smaller base radius and larger drop height resulting in a higher contact angle ( $\sim 74^\circ$ ), whereas when the same drop enters into the gravity period the contact angle reduces to  $\sim 68^\circ$ , which is closer to the results observed in Figure 3.2.

Again, the size and shape of the liquid droplet sticking to solid substrate relies on the contact line hysteresis, pinning, and the stress balance at the two interfaces of the droplet, primarily the solid-liquid interface or at the three phase contact line. The balance of the liquid droplet over a surface is effected by gravity effect, surface tension and bulk flow inside the liquid drop. With gravity-effect together with surface tension, i.e., Bond number, induce the bulk flow, which could eventually influence the contact line and free surface shape of the liquid drop.

It is important to note that, under microgravity condition, simulated in drop tower or parabolic flight, the experimental set-up continuously going through vibrations, due to which it experiences a periodic time dependant acceleration, which is also called ‘g-jitter’. Due to the g-jitter or vibration of the plane body, the drop-medium also oscillates randomly. Therefore, in microgravity the experimental reproducibility and corresponding error are higher than on earth observation as observed in most of

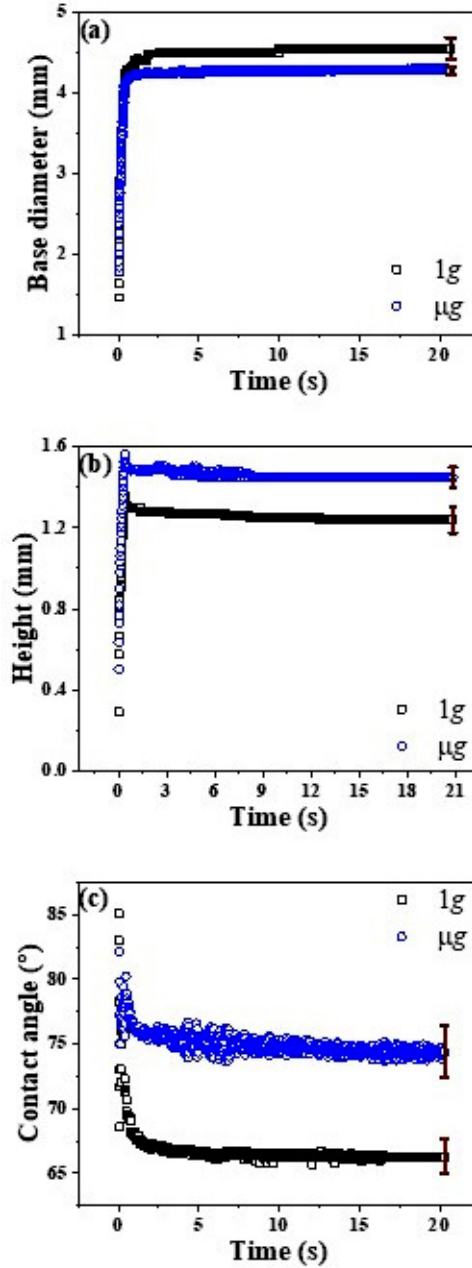


Figure 3.2: Variation of geometrical parameter of drop in  $\mu g$  and  $1g$ . Comparison of (a) drop diameter (b) drop height and (c) contact angle with respect to time between  $\mu g$  and  $1g$ . The error bar presented in the figure imply the highest error in the corresponding dataset.

the literature related to droplet dynamics in reduced gravity environment [28, 95, 110].

## 3.3 Methods

### 3.3.1 Experimental Constraints and Requirements

The choice of equipment used in devising the prototype experimental set-up was a result of constraints and requirements set by the National Research Council of Canada (NRC) in association with Canadian Space Agency (CSA). Size of the prototype was restricted to the dimensions of  $45.7 \times 45.7 \times 45.7 \text{ cm}^3$  to fit within a commercial protective case (Pelican Case Model 0340, Pelican Products Inc.), modified for parabolic flight, and weight of the prototype was  $45\text{kg}$  without the hard case. Power consumption was restricted to  $600\text{W}$  while power supply was provided in 115 VAC 5 Amp format. Batteries used in this experiment were restricted to the dry cell type. The same set-up was used for the ground based experiment. To maintain the same operating conditions from temperature and humidity perspective, special arrangements and efforts were made such as installing the  $18\text{L}$  ( $\sim 5$  Gallon) of desiccants for  $45.7 \times 45.7 \times 45.7\text{cm}^3$  pelican case which ascertain the relative humidity of 4 % – 8%. Finally, during the parabolic flight, the cabin was pressurized to maintain the atmospheric pressure which is similar to the pressure that we have for the ground based experiment. Further, a major constraint was 20 – 23s (typical) microgravity time. Considering the parabolic trajectory of the aircraft (Supplementary Figure 1), constraints due to physical limitations caused procedures to be limited during  $\sim 2g$  manoeuvres, as well as the duration of the flight dictates the endurance limits of the experimenters. A detailed description of parabolic flight trajectory can be found in Supplementary Note 1.

### 3.3.2 Prototype Components

The experimental set-up was assembled using components chosen as result of the aforementioned constraints and requirements. During the event of parabolic trajec-

tory the prototype must be able to deposit a drop, record video of the phenomenon at a frame rate suitable to capture all events, move the substrate to a new position to allow for multiple data points, record the acceleration experienced to confirm the events occurred in micro-gravity and control the humidity during the experiment. An overview of the experiment inside the hard case can be found in Figure 3.3.

The main component of the experimental setup is commercial-off-the-shelf (COTS) the liquid jetting unit, Mobile Surface Analyzer (MSA, KRÜSS Scientific Instruments Inc.). The MSA was modified to accommodate a high-speed camera (UI-3060CP Rev. 2, IDS Imaging Development Systems GmbH). The upgraded camera allows events to be captured at 166 frames per second (fps) at  $1936 \times 1216$  (full frame) and up to 2000 fps at  $96 \times 64$ . For the experiment, 400 frames per second were captured at  $800 \times 200$  (cropped frame).

In this experiments, a commercial electromagnetic, 2/2-way modular microvalve, normally closed has been used as a dispensing nozzle. The microvalve is primarily actuated via electromagnetic force and the internal diameter of the nozzle is  $0.1\text{mm}$ . This nozzle is integral component of the commercially used pressure dosing system or mobile surface analyser (MSA, KRÜSS Scientific Instruments Inc.) and the necessary operating parameters, for efficient functioning of this nozzle, are controlled through The KRÜSS ADVANCE software [101].

Further COTS components include a pair of linear motion stages with built-in controllers (QTY 2 X-LSQ150A, Zaber Technologies Inc.) couple with additional linear motion stage for Z -axis (QTY 1 X-VSR20A, Zaber Technologies Inc.). The XYZ stages reposition substrate between each parabola . To allow the MSA to dispense droplets without contacting the previously formed droplets, a 25 mm section of the MSA base was milled to provide clearance. The data acquisition system (DAQ) system monitors the environment for the period of reduced gravity and gives indication

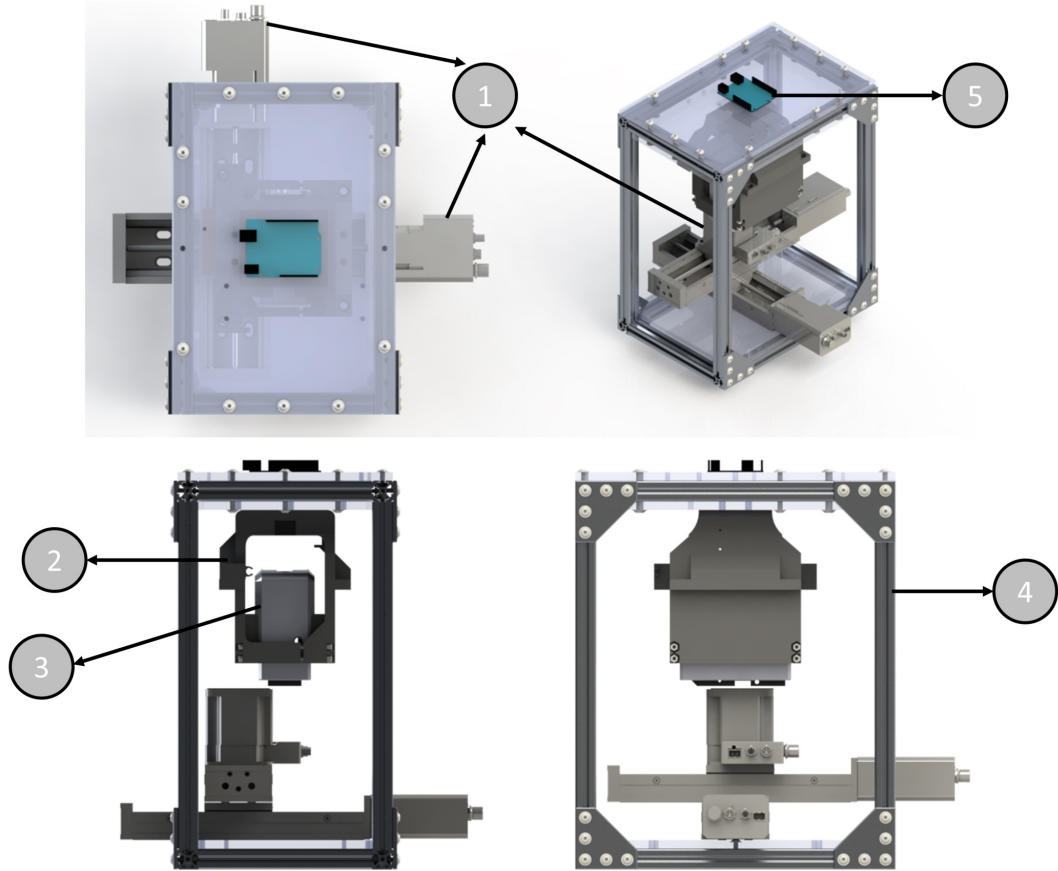


Figure 3.3: Experimental setup. Breakdown of key components: 1 – motorized XYZ stage (QTY 2 X-LSQ150A and QTY 1 X-VSR20A, Zaber Technologies Inc.), 2 – custom 3D printed MSA holder, 3 – pressure dosing system (Mobile Surface Analyzer (MSA), KRÜSS Scientific Instruments, Inc.), 4 – frame with vibration resistant frame mounts (not shown), 5 -accelerometer.

to the operator when the drop should be deposited by using the monitoring command prompt. Accelerations in the X, Y and Z directions as well as quaternion rotations (later converted into Yaw, Pitch and Roll Euler angles) and angular rates (in degree per seconds (dps)) were recorded at 100 Hz throughout the flight and stored in a text-based log-file. Comparing the timestamps of each series of data allows to verify that the events of interest have occurred in the reduced gravity environment. As mentioned earlier, to control the humidity, desiccant packs were loaded into the hard case to absorb the moisture and reduce humidity. A copper (Mirror-Like Multipurpose 110 Copper Sheet, P/N: 9821K31, McMaster Carr) substrates was firmly fixed to the

Z axis using a commercially available thermal paste (Arctic Silver 5, silver compound thermal paste). Copper substrate was functionalized using flaming process, which allowed removal of organic contaminations. Stability of identical substrates and respected surface energy over period of time was verified using polar and non polar liquids (details are provided in Supplementary Methods) .

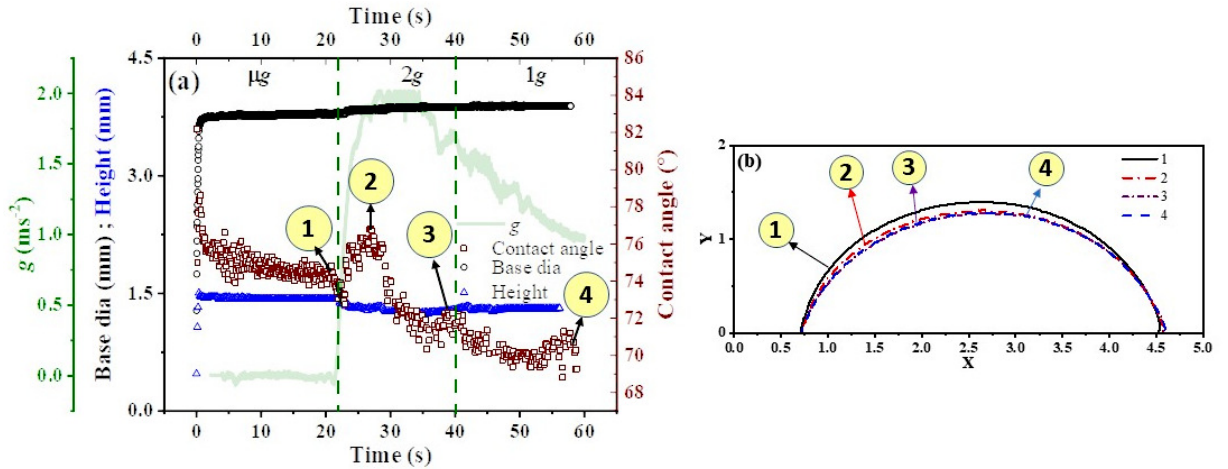


Figure 3.4: Transient variation of droplet shape and wetting properties with respect to different levels of gravity. Panel (a) is the representation of change in drop base diameter, drop height and dynamic contact angle with respect to time at micro-g ( $\mu g$ ),  $2g$  and  $1g$ , while (b) is the representation of change in drop profile, extracted from experimental still images, corresponds to the point 1, 2, 3 and 4 as shown in (a).

### 3.4 Experimental Procedure

The procedure followed to conduct the experiment is divided into 3 phases: Pre-flight, In-flight, and post-flight.

#### Pre-Flight

In preparation for the flight, desiccants were placed in the hard case for minimum of 24 hours before the flight occurred. A measurement of the humidity within the hard case was taken and was found to be in the range of 4% – 8% in the morning before the

flight. Prior to take-off, the software was loaded and the functionality of the devices was tested.

### **In-Flight**

Before the first experimental parabola took place, the log file for the accelerometer was started. Operating the prototype required a strict procedure to be followed due to the sequential g-forces (Supplementary Note 1 and Supplementary Figure 1). During the  $2g$  periods, motor function of the operators diminishes; to avoid strain on the operator and to avoid potential operator error, procedural steps were restricted to the level flight and the microgravity periods. Following the parabola of the Falcon 20 parabolic flight, the in-flight procedure planned as follows. During the level flight and before initial  $2g$  pull (pre-microgravity), operator queues camera recording software and waits for the  $2g$  pull indication then starts camera recording. Drop deposition triggers when microgravity is reached. Directly after remaining  $2g$  pull (post-microgravity), operator stops recording, indexes the drop deposition unit to the next position and changes drop volumes if necessary. This procedure is repeated for each parabola until the end of the flight.

### **Post-Flight**

Once the last parabola has been completed, the log files were stopped, duplicates of the data were stored on an external memory device, and the devices were disconnected from the laptop. The data was then processed later to obtain the results of interest. To process the data, various methods were used from using rudimentary spreadsheet analysis for using sophisticated software to analyse the data. The data from the log files required simple arithmetic operations to produce the data. In this study, we have used two commercial image processing software to measure the geometrical parameter of the droplet, which includes contact angle, height, base diameter and volume. In order to measure the contact angle, axisymmetric drop shape analysis

(ADSA) system has been adopted. ADVANCE (KRÜSS Scientific Instruments Inc.) software has been used to perform the contact angle measurement by adopting tangent droplet method. On the other hand, we used ImagePro (media cybernetics), to quantify the drop radius and height. The outer diameter of the nozzle is considered as a reference for the calibration.

### 3.4.1 Experimental Trails

The crucial factor for the success of this experiment was the deposition of a droplet onto a surface under microgravity conditions. Without this functionality, the experimental set-up would not have been able to produce the anticipated results. Concerns that the droplet may not detach from the dosing orifice existed, but the pressure dosing unit within the MSA was capable of ejecting the droplet. The supply pressure of the MSA created a large enough force for the liquid to properly detach from the dosing unit without any unwarranted effects like formation of the satellite droplets or rebounding of the jet. With the known mass flow rate, jet diameter ( $10\mu m$ ) and measured volume of the droplet we can determine the jet velocity. It is evident that in both the cases, the required drop growth is achieved at the same time for a constant drop volume. This assures us that the jet speed is not significantly altered due to the gravitational effects.

With the Falcon 20, operated for parabolic manoeuvre, 8 parabolas were planned to perform the planned experiments. Figure 3.5 represents the acceleration versus time plot at different coordinates and it is evident that we attained the magnitude of gravity as low as  $2 \times 10^{-5}g$ . From the inset figure we can also get the information about the strength of the periodic time dependant acceleration i.e., g-jitter, the maximum value of which is  $\pm 0.07g$ . For the better prediction from the propose model, this g-jitter profile was used as gravitational acceleration for the theoretical modelling.

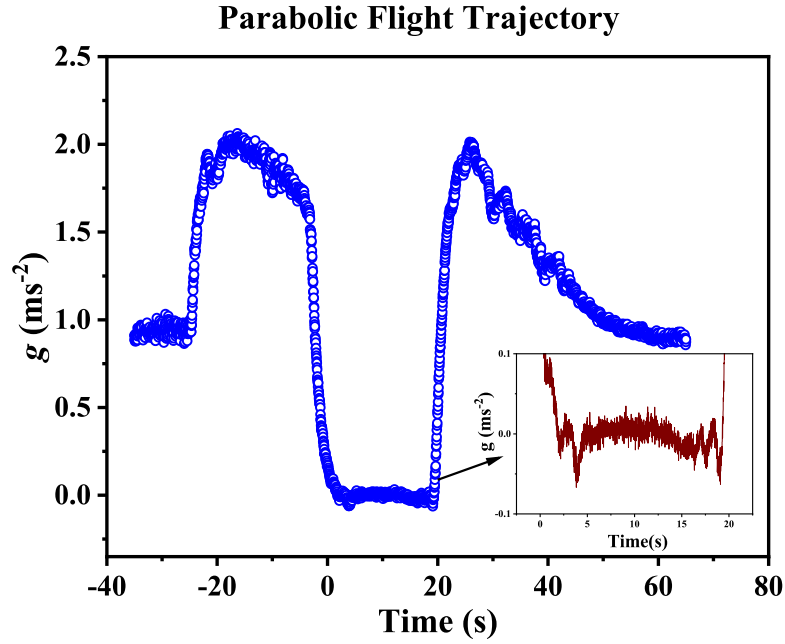


Figure 3.5: Gravitational acceleration profile in parabolic flight. Gravitational acceleration as a function of time at vertical Z axis recorded during flight. In comparison to Z axis acceleration along X and Y axes are negligible and; therefore, we have omitted them. The inset figure represents the gravitational and g-jitter value during the parabolic path of the flight or in microgravity environment.

### 3.5 Mathematical Model

As mentioned earlier, the mechanism of droplet generation via liquid needle is free from solid-needle and droplet interaction. Now considering all of the forces involved in jetting process, we can develop a theoretical model for droplet spreading, based on overall energy balance (OEB) approach as suggested by Erickson et al. [63]. By adopting OEB approach the dimensional form of the governing equation that dictates the spreading of the droplet, deposited by liquid needle drop deposition technique, under gravity can be expressed by equation 3.1, the detailed derivation of which can be found in the Supplementary Discussion section.

$$6\pi\mu_d \ln(\varepsilon^{-1}) \frac{R}{\theta_d} \left( \frac{dR}{dt} \right)^2 + \frac{dm}{dt} \left[ \frac{gRf(\theta_d)}{4} - \frac{v_j^2}{2} \right] + \left[ 2\pi R\sigma_{dm}(2h(\theta_d) - \cos\theta_e) + (m_0 + \frac{dm}{dt})g\frac{f(\theta_d)}{4} - \frac{4\mu_d}{R\rho_m} \frac{dm}{dt} \right] \frac{dR}{dt} = 0 \quad (3.1)$$

In equation 3.1,  $\mu_d$  and  $\mu_m$  is the viscosity of the droplet and surrounding medium, respectively and  $\varepsilon$  is ratio of the microscopic length ( $L_\delta$ ) to macroscopic cut-off length ( $L$ )[63]. In general,  $L_\delta$  may vary between 1  $\mu\text{m}$  to 5  $\mu\text{m}$ , whereas  $L$  can be defined as the characteristic length scale ( $R$ ) of the drop. The advancing (dynamic) and equilibrium contact angle of the droplet can be denoted by  $\theta_d$  and  $\theta_e$ , respectively, and  $f(\theta_d) = \frac{2 - \sin^2\theta_d + 2\cos\theta_d}{(2 + \cos\theta_d)\sin\theta_d}$ , whereas,  $\sigma_{dm}$  is the interfacial tension between drop-medium interface,  $m$  is the total mass of the deposited droplet at any time  $t$ ,  $\rho_m$  is the mass density of the droplet,  $D_j$  is the diameter of the jet and  $v_j$  is the velocity of the impacting jet.

The non-dimensional form of equation 3.1 can also be obtained as depicted in equation 3.2 where the characteristic length and velocity are considered as the jet radius and velocity, respectively.

$$\begin{aligned} & \frac{6 \ln(\varepsilon^{-1}) R^*}{\theta_d \text{Re}} \left( \frac{dR^*}{dt^*} \right)^2 \\ & + \left[ \frac{4R^*}{\text{We}} (2h(\theta_d) - \cos\theta_e) + \frac{f(\theta_d)G(\theta_d)}{24} (R_0^*)^3 \frac{\text{Bo}}{\text{We}} + \frac{k_{h_j} f(\theta_d)}{4} t^* \frac{\text{Bo}}{\text{We}} \right. \\ & \left. + \frac{k_{\mu_m}}{R^*} \frac{8}{\text{Re}} \right] \frac{dR^*}{dt^*} + \frac{dm}{dt} \left[ \frac{f(\theta_d)}{4} R^* \frac{\text{Bo}}{\text{We}} \right] = 0 \end{aligned} \quad (3.2)$$

Here, Reynolds number (Re) is  $\rho_d v_j D_j / \mu_d$ , Webber number (We) is  $\rho_d v_j^2 D_d / \sigma_{dm}$ , and Bond number (Bo) is  $\rho_d g D_j^2 / \sigma_{dm}$ ; also, viscosity ratio ( $k_{\mu_m}$ ) is  $\mu_m / \mu_d$ . Further details of non-dimensional parameters such as  $R^*$ ,  $R_0^*$ , and  $t^*$  can be found in the

Supplementary Discussion.

It is to be noted that, the first term in both equation 3.1 and 3.2 represent the viscous dissipation work, which is based on lubrication approximation theory [111]. However, lubrication approximation applies when equilibrium contact angle is less than  $90^\circ$ . Therefore, for higher contact angle scenario, the boundary layer approximation [112] should be used. For boundary layer approximation the first term in both equations should be replaced by  $\mu_d v_j \pi k_{h_j} \sqrt{\text{Re}} R \frac{dR}{dt}$  and  $\frac{k_{h_j}}{4\sqrt{\text{Re}}} R^* \frac{dR^*}{dt^*}$ , respectively, where,  $k_{h_j} = h_j/D_j$ .

As the governing equation either 3.1 or 3.2 is a non-linear ordinary differential equation, the numerical solution is strongly dependent on the initial condition of the system. We have considered the maximum drop diameter of the droplet,  $R_0$ , at the first onset of the impact on the substrate, i.e., the splat shape of the drop as the initial condition. With the knowledge of droplet impact analysis, the splat shape of the drop can be non-dimensionalised and can be expressed as initial spreading ratio,  $\xi = D_0/D_j = R_0/R_j$ . In the case of an impacting jet, we can assume that at the first instant, the splat-shape drop spreading is obtained with a drop volume equivalent to initial jet volume immediately before impact from the nozzle to the surface. The non-dimensional equation of initial spreading ratio ( $\xi = D_0/D_j$ ) can be calculated for both lubrication and boundary layer approximation, from the energy balance equation, as shown in equation 3.3 and 3.4, respectively. The detailed derivation of initial spreading ratio ( $\xi = D_0/D_j$ ), in case of jet based deposition technique can be found in the Supplementary Discussion.

$$\xi^3 \left[ \frac{9 \ln(\varepsilon^{-1})}{32 \theta_d} + \frac{3 k_{\mu_m} k_{h_j}}{8} \right] \frac{\text{We}}{\text{Re}} + \frac{\xi^2}{4} [1 - \cos \theta_e] - \frac{k_{h_j}}{8} \text{We} - k_{h_j} - \frac{1}{4} k_{h_j}^2 \text{Bo} = 0 \quad (3.3)$$

$$\frac{1}{4} \frac{k_{\mu m}}{k_{h_j}} \frac{We}{Re} \xi^3 + \left[ \frac{We}{8\sqrt{Re}} + \frac{1}{4}(1 - \cos(\theta_e)) \right] \xi^2 - \frac{k_{h_j}}{8} We - \frac{1}{4} k_{h_j}^2 Bo = 0 \quad (3.4)$$

Figure 3.6 compares the theoretical prediction presented in this paper with the experimental observations. From this figure, we can say that considering the error bar our theoretical model can successfully predict the effect of gravity on the spreading of the droplet. Taking a closer look at the Figure 3.6, it can be observed that our theoretical model slightly under predict the drop spreading in microgravity, the reason of which can be attributed to the fact the in the model for the sake of simplicity the effect of g-jitter was ignored.

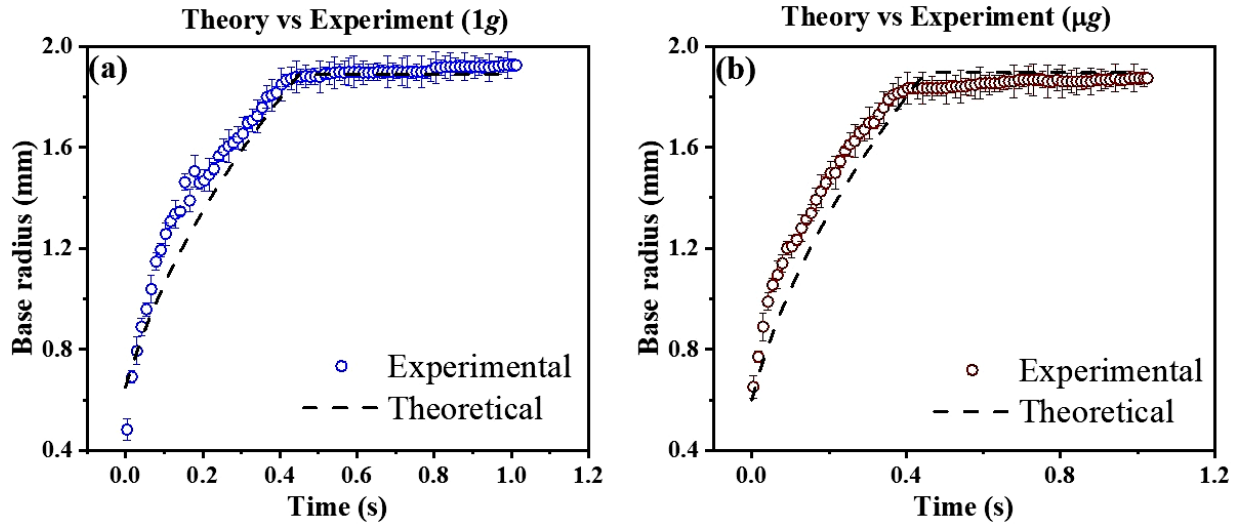


Figure 3.6: Validation of theoretical model with experimental observation. Comparison between theoretical prediction and experimental observation of droplet spreading under (a) terrestrial gravity and (b) reduced gravity environment.

It is noteworthy mention that one of the major assumption in our theoretical model is we assume the drop profile will be a spherical cap. However, the spherical cap assumption depends on the Bond number. The spherical cap assumption is invalid if the Bond number,  $Bo > 1$ . When the  $Bo$  is above unity a transition from a spherical cap to the paddle shape is observed for a sessile drop[113]. From perturbation solution approach it has been observed that the sessile drop profile starts deviating from the

spherical cap once corresponding length of the Bond number is  $0.8 \times l_{\text{cap}}$ [114]. The deviation becomes pronounce once the Bo is corresponding to the  $2.4 \times l_{\text{cap}}$ , at which the drop becomes paddle or splat shape. From the sensitivity analysis it can be shown that the theoretical model presented in this study can predict the physics of drop dynamics until  $\text{Bo} \approx 2$ .

### 3.6 Conclusion

Considering the thorough investigation of the spreading dynamics of a droplet on a solid surface under the effect of terrestrial gravity and microgravity condition, performed in this study, the liquid needle droplet deposition technique is proved to be an ideal drop deposition technique in microgravity. From the experimental investigation, larger droplet height is evident for the microgravity compared to the terrestrial gravity condition. The theoretical model, which has accounted for the viscous force, the surface forces, the wettability of the substrate, and the gravitational force, successfully predicts the transient variation of the base diameter of the droplet. The study presented here can be considered as a potential element for answering some unanswered questions, especially in the field of jetting or material deposition through jetting for reduced gravity applications. With enough resources, it will be possible to extend the study to droplet coalescence and droplet manipulation in reduced gravity condition.

## References

- [18] Y. Son, C. Kim, D. H. Yang, and D. J. Ahn, "Spreading of an inkjet droplet on a solid surface with a controlled contact angle at low weber and reynolds numbers," *Langmuir*, vol. 24, no. 6, pp. 2900–2907, 2008.
- [27] A. Passerone, "Twenty years of surface tension measurements in space," *Microgravity Sci. Technol.*, vol. 23, no. 2, pp. 101–111, 2011.
- [28] A Ababneh, A Amirfazli, and J. Elliott, "Effect of gravity on the macroscopic advancing contact angle of sessile drops," *Can. J. Chem. Eng.*, vol. 84, no. 1, pp. 39–43, 2006.
- [34] P. R. Waghmare, S. Das, and S. K. Mitra, "Drop deposition on under-liquid low energy surfaces," *Soft Matter*, vol. 9, no. 31, pp. 7437–7447, 2013.
- [35] P. R. Waghmare and S. K. Mitra, "Needle-free drop deposition technique for contact angle measurements of superhydrophobic surfaces," *J. Appl. Phys.*, vol. 116, no. 11, p. 114 903, 2014.
- [36] M. Jin, R. Sanedrin, D. Frese, C. Scheithauer, and T. Willers, "Replacing the solid needle by a liquid one when measuring static and advancing contact angles," *Colloid Polym Sci.*, vol. 294, no. 4, pp. 657–665, 2016.
- [57] B. Friedrich, F. Weser, and C. Scheithauer, *Contact angle measurement apparatus*, US Patent 9,816,909, 2017.
- [61] D Li, P Cheng, and A. Neumann, "Contact angle measurement by axisymmetric drop shape analysis (adsa)," *Adv. Colloid Interface Sci.*, vol. 39, pp. 347–382, 1992.
- [62] D. Kwok, R Lin, M Mui, and A. Neumann, "Low-rate dynamic and static contact angles and the determination of solid surface tensions," *Colloids Surf. A Physicochem. Eng. Asp.*, vol. 116, no. 1-2, pp. 63–77, 1996.
- [63] D. Erickson, B. Blackmore, and D. Li, "An energy balance approach to modeling the hydrodynamically driven spreading of a liquid drop," *Colloids Surf. A Physicochem. Eng. Asp.*, vol. 182, no. 1-3, pp. 109–122, 2001.
- [64] B. Bonhoeffer, A. Kwade, and M. Juhnke, "Impact of formulation properties and process parameters on the dispensing and deposition of drug nanosuspensions using micro-valve technology," *J. Pharm. Sci.*, vol. 106, no. 4, pp. 1102–1110, 2017.
- [72] T. Young, "Iii. an essay on the cohesion of fluids," *Philos. Trans. R. Soc. Lond.*, no. 95, pp. 65–87, 1805.
- [73] L. Feng *et al.*, "Super-hydrophobic surfaces: From natural to artificial," *Adv. Mater.*, vol. 14, no. 24, pp. 1857–1860, 2002.
- [74] X. Gao and L. Jiang, "Water-repellent legs of water striders," *Nature*, vol. 432, no. 7013, pp. 36–36, 2004.

- [75] X. Gao *et al.*, “The dry-style antifogging properties of mosquito compound eyes and artificial analogues prepared by soft lithography,” *Adv. Mater.*, vol. 19, no. 17, pp. 2213–2217, 2007.
- [76] A. R. Parker and C. R. Lawrence, “Water capture by a desert beetle,” *Nature*, vol. 414, no. 6859, pp. 33–34, 2001.
- [77] Y. Zheng *et al.*, “Directional water collection on wetted spider silk,” *Nature*, vol. 463, no. 7281, pp. 640–643, 2010.
- [78] P. R. Waghmare, N. S. K. Gunda, and S. K. Mitra, “Under-water superoleophobicity of fish scales,” *Sci. Rep.*, vol. 4, no. 1, pp. 1–5, 2014.
- [79] M. R. Flynn and J. W. Bush, “Underwater breathing: The mechanics of plastron respiration,” *J. Fluid Mech.*, vol. 608, p. 275, 2008.
- [80] X. Yao, Y. Song, and L. Jiang, “Applications of bio-inspired special wettable surfaces,” *Adv. Mater.*, vol. 23, no. 6, pp. 719–734, 2011.
- [81] M Pasandideh-Fard, V Pershin, S Chandra, and J Mostaghimi, “Splat shapes in a thermal spray coating process: Simulations and experiments,” *J. Therm. Spray Technol.*, vol. 11, no. 2, pp. 206–217, 2002.
- [82] M. J. De Ruijter, T. Blake, and J. De Coninck, “Dynamic wetting studied by molecular modeling simulations of droplet spreading,” *Langmuir*, vol. 15, no. 22, pp. 7836–7847, 1999.
- [83] K. Pataky, T. Braschler, A. Negro, P. Renaud, M. P. Lutolf, and J. Brugger, “Microdrop printing of hydrogel bioinks into 3d tissue-like geometries,” *Adv. Mater.*, vol. 24, no. 3, pp. 391–396, 2012.
- [84] B. Pethica and T. Pethlca, “The contact angle eqmhbrmm,” in *Proc. Second Inter. Congress of Surface Activity III, Butterworths Scientific Publ*, 1957, pp. 131–35.
- [85] C. Ward and M. Sasges, “Effect of gravity on contact angle: A theoretical investigation,” *J. Chem. Phys.*, vol. 109, no. 9, pp. 3651–3660, 1998.
- [86] M. Sasges and C. Ward, “Effect of gravity on contact angle: An experimental investigation,” *J. Chem. Phys.*, vol. 109, no. 9, pp. 3661–3670, 1998.
- [87] H. Fujii and H. Nakae, “Effect of gravity on contact angle,” *Philos. Mag. A*, vol. 72, no. 6, pp. 1505–1512, 1995.
- [88] W. J. Herzberg and J. E. Marian, “Relationship between contact angle and drop size,” *J. Colloid Interface Sci.*, vol. 33, no. 1, pp. 161–163, 1970.
- [89] R. J. Good and M. Koo, “The effect of drop size on contact angle,” *J. Colloid Interface Sci.*, vol. 71, no. 2, pp. 283–292, 1979.
- [90] F. Bashforth and J. C. Adams, *An attempt to test the theories of capillarity*. University Press, 1883.
- [91] F. Karmali and M. Shelhamer, “The dynamics of parabolic flight: Flight characteristics and passenger percepts,” *Acta Astronaut.*, vol. 63, no. 5-6, pp. 594–602, 2008.

- [92] P. Von Kampen, U. Kaczmarczik, and H. J. Rath, “The new drop tower catapult system,” *Acta Astronaut.*, vol. 59, no. 1-5, pp. 278–283, 2006.
- [93] J.-C. Baret and M. Brinkmann, “Wettability control of droplet deposition and detachment,” *Phys. Rev. Lett.*, vol. 96, no. 14, p. 146106, 2006.
- [94] P. R. Waghmare, S. Mitra, N. S. K. Gunda, and S. K. Mitra, “Needle-free drop deposition: The role of elastic membranes,” *RSC Adv.*, vol. 5, no. 100, pp. 82374–82380, 2015.
- [95] A. Diana, M. Castillo, D. Brutin, and T. Steinberg, “Sessile drop wettability in normal and reduced gravity,” *Microgravity Sci. Technol.*, vol. 24, no. 3, pp. 195–202, 2012.
- [96] Z.-Q. Zhu *et al.*, “Experimental investigation of pendant and sessile drops in microgravity,” *Microgravity Sci. Technol.*, vol. 22, no. 3, pp. 339–345, 2010.
- [97] D. Brutin, Z. Zhu, O. Rahli, J. Xie, Q. Liu, and L. Tadrist, “Sessile drop in microgravity: Creation, contact angle and interface,” *Microgravity Sci. Technol.*, vol. 21, no. 1, pp. 67–76, 2009.
- [98] O. E. Yildirim, Q. Xu, and O. A. Basaran, “Analysis of the drop weight method,” *Phys. Fluids*, vol. 17, no. 6, p. 062107, 2005.
- [99] A. Bateni, A. Ababneh, J. Elliott, A. Neumann, and A. Amirfazli, “Effect of gravity and electric field on shape and surface tension of drops,” *Adv. Space Res.*, vol. 36, no. 1, pp. 64–69, 2005.
- [100] M. F. Ismail, A. Baldygin, T. Willers, and P. R. Waghmare, “Optical contact angle measurement considering spreading, evaporation and reactive substrate,” *Advances in Contact Angle, Wettability and Adhesion*, vol. 3, pp. 59–79, 2018.
- [101] A. Ahmed, R. Sanedrin, T. Willers, and P. R. Waghmare, “The effect of dynamic wetting pressure on contact angle measurements,” *J. Colloid Interface Sci.*, vol. 608, pp. 1086–1093, 2022.
- [102] S. Banitabaei and A. Amirfazli, “Pneumatic drop generator: Liquid pinch-off and velocity of single droplets,” *Colloids Surf. A Physicochem. Eng. Asp.*, vol. 505, pp. 204–213, 2016.
- [103] L. Rayleigh, “On the instability of jets,” *Proc. London Math. Soc.*, vol. 1, no. 1, pp. 4–13, 1878.
- [104] C. Clanet and J. C. Lasheras, “Transition from dripping to jetting,” *J. Fluid Mech.*, vol. 383, pp. 307–326, 1999.
- [105] F. Celestini, R. Kofman, X. Noblin, and M. Pellegrin, “Water jet rebounds on hydrophobic surfaces: A first step to jet micro-fluidics,” *Soft Matter*, vol. 6, no. 23, pp. 5872–5876, 2010.
- [106] K. Cardin, S. Wang, O. Desjardins, and M. Weislogel, “Rebound of large jets from superhydrophobic surfaces in low gravity,” *Phys. Rev. Fluids*, vol. 6, no. 1, p. 014003, 2021.

- [107] C. Extrand and S. I. Moon, “When sessile drops are no longer small: Transitions from spherical to fully flattened,” *Langmuir*, vol. 26, no. 14, pp. 11 815–11 822, 2010.
- [108] R. Tadmor and P. S. Yadav, “As-placed contact angles for sessile drops,” *J. Colloid Interface Sci.*, vol. 317, no. 1, pp. 241–246, 2008.
- [109] B. Krasovitski and A. Marmur, “Drops down the hill: Theoretical study of limiting contact angles and the hysteresis range on a tilted plate,” *Langmuir*, vol. 21, no. 9, pp. 3881–3885, 2005.
- [110] A. Calvimontes, “The measurement of the surface energy of solids using a laboratory drop tower,” *NPJ Microgravity*, vol. 3, no. 1, pp. 1–14, 2017.
- [111] P.-G. De Gennes, “Wetting: Statics and dynamics,” *RMP*, vol. 57, no. 3, p. 827, 1985.
- [112] S Chandra and C. Avedisian, “On the collision of a droplet with a solid surface,” *Proc R Soc Lond A Math Phys Sci*, vol. 432, no. 1884, pp. 13–41, 1991.
- [113] V. A. Lubarda and K. A. Talke, “Analysis of the equilibrium droplet shape based on an ellipsoidal droplet model,” *Langmuir*, vol. 27, no. 17, pp. 10 705–10 713, 2011.
- [114] D Homentcovschi, J Geer, and T Singler, “Uniform asymptotic solutions for small and large sessile drops,” *Acta Mech.*, vol. 128, no. 3, pp. 141–171, 1998.

# Chapter 4

## Dynamics of jet breakup and subsequent drop formation dynamics as a function of gravity

### Abstract

Three-dimensional (3D) printing offers tremendous potential for space-based manufacturing, particularly in upcoming Mars and Lunar missions. However, the absence of gravity presents significant challenges when it comes to depositing materials onto a 3D printer bed in reduced gravitational environments. Surprisingly, there is a dearth of literature addressing the successful execution of metal 3D printing under space conditions. To tackle this issue, a microgravity-compatible 3D printing prototype equipped with a jet-based deposition mechanism that deposits materials as solid metal particle colloids, could be a potential solution. However, premature dripping of the liquid jet before reaching the printer bed leads to liquid splashes and the formation of bubbles within the deposited material, potentially compromising the strength of the printed object. We conducted numerous successful tests of this jet-based liquid deposition system during 20-second microgravity phases achieved through parabolic flights (a total of 165 times). The quality of the final product was found to be notably influenced by the dynamics of liquid jet breakup in reduced gravity. We observed that when the liquid jet dripped prematurely before reaching the printer bed,

it caused liquid splashes and the formation of bubbles within the deposited material. This could potentially weaken the strength of the printed object. In response to this challenge and to optimize the parameters for successful deposition, we conducted an in-depth investigation into the effects of gravity and surface tension on the dynamics of jet breakup. We employed ultra-high-speed imaging technology (with frame rates of up to 20,000 frames per second) under microgravity, Martian gravity, and terrestrial gravity conditions. Our findings revealed that the breakup length and critical breakup time of the jet depend on the strength of gravity. Furthermore, we developed a theoretical model capable of predicting the size of microdrops formed during jet breakup. This model incorporates an analysis of Rayleigh-Plateau instability and a modified Navier-Stokes equation, integrating parameters such as jet velocity, capillary effects, viscosity, and gravitational acceleration, represented by dimensionless numbers (Froude number, Ohnesorge number and Bond number). Our study extends beyond space-based additive manufacturing, with potential applications in drug delivery through spraying mechanisms, addressing liquid splashing issues during spacecraft tank filling, bio-printing, and various other space-based manufacturing endeavors.

## 4.1 Introduction

A liquid jet is a continuous, elongated stream or column of liquid ejected from a nozzle or orifice under pressure, typically with a specific direction and velocity [115]. Liquid jets are often characterized by their cylindrical or conical shape and can vary in size from microscopic to macroscopic, depending on the application. Micro jet is commonly encountered in various industrial, scientific, and technological contexts, including inkjet printing[116], fuel injection[117], water jet cutting[118], drug delivery [64], micro-fabrication [119], biotechnology[120], additive manufacturing [121], space industry [122] and the study of fluid dynamics[115]. The behaviour and characteristics of a liquid jet depend on factors such as the properties of the liquid, the nozzle design, the velocity of ejection, and environmental conditions.

Within a certain proximity to the nozzle, a continuous liquid jet exhibits a smooth surface, but instability eventually sets in, characterized by asymmetrical variations in the jet's radius along its length. This instability culminates in the fragmentation of the liquid jet into droplets. There are two distinct types of instabilities depending on where they originate and propagate: absolute and convective instabilities. Absolute instability [123], is found to grow over time at a specific point along the jet, typically upstream from the disturbance's point of initiation. On the other hand, convective instability [124] occurs when disturbances are convected only downstream. Convective instability is the more commonly encountered form of instability in our everyday lives and various industrial applications.

The jet breakup caused by convective instabilities can be categorized into five regimes, as described in previous research [64, 125, 126]: dripping, Rayleigh, first wind-induced, second wind-induced, and atomization regimes. In the dripping regime, occurring at very low velocities, capillary forces dominate, leading to periodic droplet emissions from the nozzle. Consequently, the breakup length is nearly zero in this regime. In the Rayleigh regime, a smooth-surfaced laminar jet disintegrates into droplets due to the Rayleigh-Plateau instability. The first wind-induced regime is marked by the transition from laminar to turbulent flow. The jet interacts with the surrounding environment, causing a decrease in the breakup length as the jet velocity increases. In the second wind-induced regime, a turbulent jet interacts with the surrounding air, generating shear forces that create unstable waves on the jet's surface, ultimately leading to jet breakup. In the atomization regime, which occurs at the highest jet velocities, the liquid jet breaks into tiny droplets. The breakup length decreases as the jet velocity increases. It's worth noting that, due to challenges related to human factors and budget constraints associated with conducting experiments in parabolic flight, the study presented here focused its analysis on the Rayleigh regime.

Plateau[127] was the first who rationalised that the fluid thread becomes unstable when the wavelength of a perturbed jet is larger than the radius of the unperturbed cylindrical jet. Plateau further elaborates that capillary instability arises, as a result of interfacial tension, whenever the wavelength of the surface disturbance exceeds the circumference of the cylindrical liquid jet; i.e. capillary instability is caused by long disturbance waves. Rayleigh [103] used rigorous theoretical analysis to show that, from an initially small disturbance, a number of unstable waves may form on the jet surface; the wave that causes the jet to breakup, the "most unstable wave", is that which has the maximum growth rate in amplitude. Since then studies regarding thread instability have evolved to incorporate the effect of the viscosity, shear, elasticity of the bulk phases nozzle design, the velocity of ejection, and environmental conditions.

One of the most crucial outcome of jet break-up phenomenon is the formation of microdroplets due to the disintegrated fluid ligaments. This microdroplets has serious impact on many space applications. In space, cryogenic fuels and fluids like liquid hydrogen and liquid oxygen are essential for various propulsion and life support systems. Cryogenic propellant transfer between vehicles in orbit, so-called a propellant depot, has been investigated to expand the capability of space exploration beyond the Earth orbit[128, 129]. During in-orbit propellant transfer the flow returns to the tank in the form of a spray or an axial jet which contributes to control of the tank pressure and the destratification of liquid temperature layer[130]. Therefore, drop generation upon jet breakup for liquid hydrogen, which is flammable, can pose a serious fire threat to the spacecraft by escaping to the environment. In addition, during the jet based 3D printing, the microdroplets creation upon jet brakup can cause bubble entrapment [131, 132] inside the deposited material, resulting in a weak internal bonding for the manufactured 3D printed product. Therefore, the investigation of the effect of gravity

on the jet breakup dynamics and subsequent drop formation is of utmost important. However, only a handful of literatures have studied both experimental and theoretical analysis of the breakup of jet and microdrop formation in reduced gravity condition.

The initial experiments in reduced gravity were conducted by Vihinen et al. [123], who presented an image illustrating absolute and convective instability in a liquid jet, achieved within NASA Glenn Research Center's 2.2 drop tower. Subsequently, Edwards et al. [133] observed that in reduced gravity, both absolute and convective instabilities led to slower drop formation during jet breakup, but these drops were larger in size compared to those formed under terrestrial gravity conditions. Tomotika [134], while not accounting for gravity and jet inertia, discovered that jet instability was heavily influenced by the ratios of viscosities and densities between the jet and ambient fluids, as well as the Ohnesorge number, a dimensionless parameter representing the ratio of viscous forces to interfacial-tension forces. More recently, Sunol et al. [135], in a microgravity environment simulated within a drop tower, reported on droplets formed during the dripping and jetting regimes. Their study focused on aspects such as droplet size, trajectory, oscillation, and rotation. Notably, they observed a larger drop volume under terrestrial gravity conditions, which contradicted the findings reported by Vihinen et al. [123].

As highlighted in the previous literature review, it is evident that some studies have investigated the phenomenon of drop formation resulting from the breakup of liquid jets in microgravity conditions. However, there is a noticeable absence of comprehensive and consistent investigations concerning the relationship between drop size formation and gravitational forces. This inconsistency in drop formation under both microgravity and Earth gravity conditions can be attributed to two primary experimental limitations. The first limitation stems from the fact that, to the best of our knowledge, most reduced gravity experiments related to drop formation are

carried out in drop tower facilities. These facilities offer only a brief time window, typically around 2 to 4 seconds of microgravity. Within such a short timeframe, achieving and maintaining true microgravity conditions becomes challenging. Additionally, conducting experiments precisely at the desired level of reduced gravity becomes problematic. The second, and arguably the most critical, limitation is the lack of comprehensive documentation of jet breakup dynamics in microgravity using ultra-high-speed imaging techniques, with a minimum frame rate of 10,000 frames per second (FPS).

To address this gap, our present study investigates the phenomenon of jet breakup in three distinct gravity environments: microgravity, Martian gravity, and terrestrial gravity. Microgravity and Martian gravity conditions were simulated during parabolic flight, which provided a minimum of approximately 20 seconds of reduced gravity. Moreover, we captured the intricate dynamics of jet breakup using a frame rate of 18,000 FPS. This high frame rate allowed us to track the entire journey of a drop, from its initial disintegration from the jet to its coalescence with adjacent drops. Consequently, we were able to discern variations in drop size as a function of gravity. In addition to examining the interplay between surface tension and gravitational forces in microgravity, we also investigated the impact of inertial forces resulting from variations in jet exit velocity. This was achieved by systematically altering the jet velocity. Our study specifically focuses on exploring the effect of gravitational and inertial forces on jet breakup length by observing how it varies with Bond and Froude numbers. Furthermore, we have developed a mathematical model that combines Rayleigh-Plateau instability analysis with the modified Navier-Stokes equation. This model accounts for jet velocity, capillary effect, viscosity, and gravitational acceleration, which are represented by dimensionless numbers (Froude number, Ohnesorge number and Bond number).

## 4.2 Experimental Procedure

Detailed explanation of experimental setup can be found in section 3.3.

## 4.3 Theoretical Model

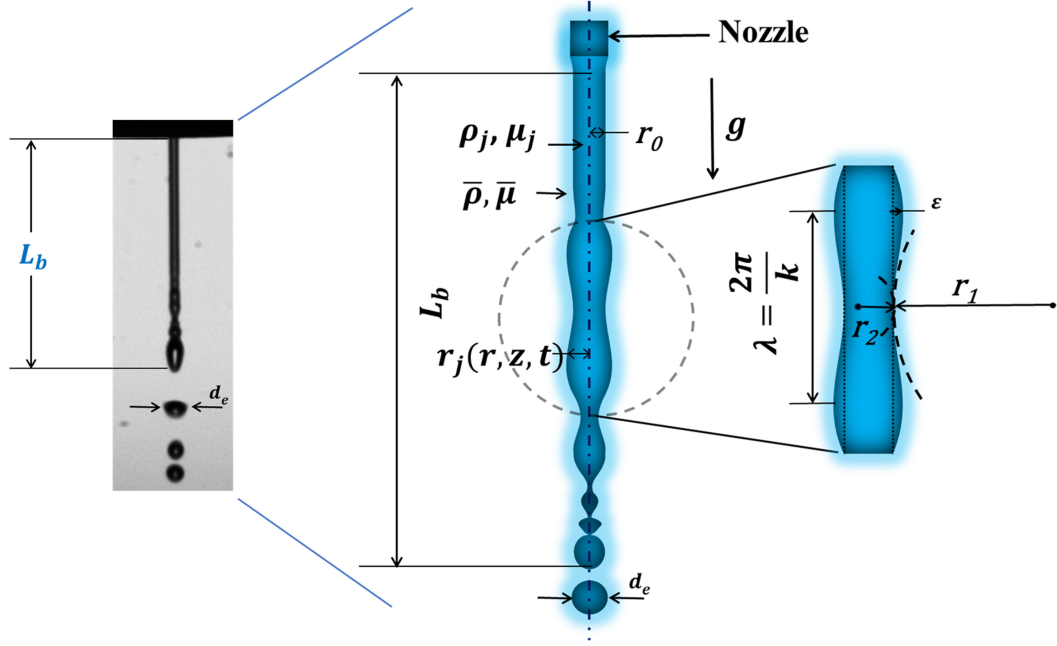


Figure 4.1: Graphical representation of breakup of a liquid jet, emanating from a nozzle, and subsequent drop formation in gravity.

This section represents the mathematical model associated with the influence of gravity on the subsequent drop formation after the microjet breakup as shown in figure 4.1. For this model the liquid jet is assumed to be a Newtonian and incompressible, which is surrounded by a ambient fluid where the density of the ambient fluid is less than the liquid jet. Considering the assumptions the conservation of energy of the falling liquid jet exiting from a nozzle can be written as follows [136],

$$\int_V \frac{d}{dt} \left( \frac{1}{2} \rho_j u_i^2 \right) dV = \int_S \tau_{ij} u_i n_j dS - \int_V \tau_{ij} \epsilon_{ij} dV - \int_V \rho_j g_i u_i dV \quad (4.1)$$

In equation 4.1,  $V$  is the volume of the jet,  $t$  is the time,  $\rho_j$  is the density of the liquid jet,  $u_i$  is the velocity component along the  $i$ th direction,  $S$  is the surface

area of the cylindrical jet,  $n_j$  is the unit normal vector,  $\tau_{ij}$  and  $\epsilon_{ij}$  are the stress and strain rate tensor, respectively, and  $g$  is the gravitational acceleration. Each term in equation 4.1 represents a time rate of change. The first term in the left hand side of equation 4.1 is the rate of change of kinetic energy, while the first term in the right hand side (rhs) represents the rate of work done on the jet by the surface forces, the second term in rhs is the rate of energy dissipation and the last term in the rhs is the rate of work by body force. In this study the gravitational force is considered only as the body force.

It is worthwhile to mention that for a falling jet, subjected to perturbation due to disturbances, we cannot ignore the dynamic behaviour of the jet and surrounding medium interface. Therefore we have to consider the effect of fluid properties of the ambient fluid on the dynamics of jet breakup. The momentum and continuity equation that govern the motion of the surrounding medium are as follows:

$$\frac{\partial \bar{u}}{\partial t} = \frac{1}{\rho} \nabla \bar{P} + \frac{\bar{\mu}}{\rho} \nabla^2 \bar{u} \quad (4.2)$$

and

$$\nabla \cdot \bar{u} = 0 \quad (4.3)$$

Where  $\bar{\square}$  implies the ambient fluid properties and  $P$  and  $\mu$  denote the pressure and viscosity, respectively.

The boundary condition at the interface of jet and ambient fluid can be defined as follows,

$$u_{rs} = \bar{u}_{rs}, u_{zs} = \bar{u}_{zs} \quad (4.4)$$

and

$$\begin{aligned}\tau_{rrs} &= -\bar{P} + 2\bar{\mu} \left( \frac{\partial \bar{u}_r}{\partial r} \right)_s - \sigma \left( \frac{1}{r_1} + \frac{1}{r_2} \right) \\ \tau_{rzs} &= \bar{\mu} \left( \frac{\partial \bar{u}_z}{\partial r} + \frac{\partial \bar{u}_r}{\partial z} \right)_s\end{aligned}\tag{4.5}$$

Where, subscript  $s$  denotes the fluid properties at the jet-ambient fluid interface,  $u_r$  is the radial component of the velocity,  $u_z$  is the axial component of the velocity,  $\sigma$  is the interfacial tension and  $r_1$  and  $r_2$  are the principal radii of curvature of the interface.

The next task in hand would be to find out each and every term in equation 4.1 and then solve for to deduce a dispersion relation for the breakup of liquid jet by following Rayleigh's instability theory [103] .

According to Rayleigh [103] the radius ( $r_s$ ) of a perturbed columnar surface, subjected to infinitesimal varicose perturbation on the substrate can be expressed as,

$$r_j = r_0 + \epsilon e^{\omega t} \cos(kz)\tag{4.6}$$

Where,  $r_0$  is the radius of the undisturbed jet,  $\epsilon$  is the perturbation amplitude which is assumed to be  $\ll r_0$ ,  $\omega$  is the growth rate of instability and  $k = \frac{2\pi}{\lambda}$  is the wave number with  $\lambda$  is the wavelength of the perturbed jet. For the sake of simplicity we will use  $\alpha(t) = \epsilon e^{\omega t}$  in equation 4.6.

For a one dimensional Cosserat fluid jet, the continuity equation can be expressed as follows[137],

$$\frac{\partial}{\partial t}(\pi r_j^2) + \frac{\partial}{\partial t}(\pi r_j^2 u_z) = 0\tag{4.7}$$

Where,  $\pi r_j^2$  is the cross sectional area of the cylindrical liquid jet. Combining continuity equation for a cylindrical jet and the equation 4.7 the approximated expression

for the axial( $u_z$ ) and radial velocity ( $u_r$ ) component of the liquid jet can be written, respectively, as follows,

$$\begin{aligned} u_z &\approx -\frac{2\alpha_t}{kr_0} \sin(kz) \\ u_r &\approx -\frac{r\alpha_t}{r_0} \cos(kz) \end{aligned} \quad (4.8)$$

Where  $\alpha_t = \frac{d\alpha}{dt}$ . Using the information in equation 4.8, using  $dV = r dr dz d\theta$  for cylindrical coordinate system, and  $u_i^2 = u_r^2 + u_z^2$  the kinetic energy term in the left hand side of equation 4.1 can be written as follows,

$$\int_V \frac{d}{dt} \left( \frac{1}{2} \rho_j u_i^2 \right) dV = \frac{1}{2} \rho_j \frac{d}{dt} \left[ \int_0^{r=r_0} \int_0^{z=\frac{2\pi m}{k}} \int_0^{\theta=2\pi} (u_r^2 + u_z^2) r dr dz d\theta \right] = \frac{\rho_j m \pi^2 r_0^3}{2\eta^3} (8 + \eta^2) \dot{\alpha}_t \ddot{\alpha}_t \quad (4.9)$$

Where,  $\eta = kr_0$ , along axial axis integration is performed from  $z = 0$  to  $z = \frac{2\pi m}{k}$ , in which  $m$  is the number of waves along  $z$  axis. Similarly using equation 4.8 the energy dissipation rate in the rhs of the equation of 4.1 can be found. It is worthwhile to recall that for an incompressible liquid the viscous stress and strain rate at a point can be expressed as [136]  $\tau_{ij} = \mu_j \left( \frac{\partial u_r}{\partial u_z} + \frac{\partial u_r}{\partial u_z} \right)$  and  $\epsilon_{ij} = \frac{1}{2} \left( \frac{\partial u_r}{\partial u_z} + \frac{\partial u_r}{\partial u_z} \right)$  and from which the dissipation work can be written as follows,

$$\int_V \tau_{ij} \epsilon_{ij} dV = \frac{1}{2} \mu_j \int_0^{r=r_0} \int_0^{z=\frac{2\pi m}{k}} \int_0^{\theta=2\pi} \left( \frac{\partial u_r}{\partial z} + \frac{\partial u_z}{\partial r} \right)^2 r dr dz d\theta = \frac{\mu_j m \pi^2 r_0}{2\eta} (24 + \eta^2) \dot{\alpha}_t^2 \quad (4.10)$$

By considering z-axis as the axis of symmetry the work done on the jet by surface forces can be written as,

$$\int_S \tau_{ij} u_i n_j ds = \int_S \tau_{rr} u_r n_r dS + \int_S \tau_{rz} u_z n_r dS \quad (4.11)$$

Applying the interface boundary condition from equation 4.4 and 4.5, and substituting them in equation 4.11 we can write,

$$\int_S \tau_{ij} u_i n_j ds = - \int_S \bar{P} u_r ds + \int_S 2\bar{\mu} \left( \frac{\partial \bar{u}_r}{\partial r} \right) ds - \int_S \sigma_{jm} \left( \frac{1}{r_1} + \frac{1}{r_2} \right) u_r ds + \int_S 2\bar{\mu} \left( \frac{\partial \bar{u}_z}{\partial r} + \frac{\partial \bar{u}_r}{\partial z} \right) ds \quad (4.12)$$

Due to the curvature effect in the perturbed jet surface we must consider the Laplace pressure pressure [138, 139], which can be expressed as,  $\sigma_{jm} \left( \frac{1}{r_1} + \frac{1}{r_2} \right)$ , where  $\sigma_{jm}$  is the interfacial tension at the jet and surrounding medium interface and  $r_1$  and  $r_2$  are the inner and outer radii of curvature of the perturbed jet surface, respectively. Using the alternate form of the Rayleigh's perturbed jet radius we can write  $\frac{1}{r_1} = \frac{1}{r_0 + \alpha_t e^{ikz}}$  and after performing binomial expansion we can write the expression for inner radius of curvature the perturbed jet as,

$$\frac{1}{r_1} = \frac{1}{r_0} - \alpha_t \frac{\epsilon}{r_0^2} e^{ikz} \quad (4.13)$$

On the otherhand the outer radius of the curvature is expressed as,  $\frac{1}{r_2} = \frac{r_{zz}}{1 + r_z^2}$ , which can be further simplified to a linearised form by ignoring the higher order  $O(2)$  term and can be expressed as follows,

$$\frac{1}{r_2} \approx \alpha_t k^2 e^{ikz} \quad (4.14)$$

Now with the equation 4.13 and 4.14, the approximated expression for the Laplace pressure can be written as,

$$\sigma_{jm} \left( \frac{1}{r_1} + \frac{1}{r_2} \right) = \frac{\sigma_{jm}}{r_0} - \frac{\sigma_{jm} \alpha_t}{r_0^2} (1 - \eta^2) \cos kz \quad (4.15)$$

However, we are interested only in the unstable part of the perturbed jet for the instability analysis as suggested by Rayleigh [103]. Therefore, for the instability analysis we will consider  $\frac{\sigma_{jm}}{r_0} \approx 0$ . Now combining Rayleigh's approximation, equation 4.8 and 4.15 we can write the surface tension related work term in equation 4.12 as follows,

$$\int_S \sigma_{jm} \left( \frac{1}{r_1} + \frac{1}{r_2} \right) u_r ds = - \frac{2\pi^2 m \sigma_{jm}}{\eta} (1 - \eta^2) \alpha_t \dot{\alpha}_t \quad (4.16)$$

It is essential to note that, in the absence of flow in the base state (undisturbed jet radius), the radial and axial velocities, denoted as  $u_r$  and  $u_z$  respectively, can be regarded as perturbation velocities. Furthermore, under the constraint we previously posited, namely that  $\epsilon \ll r_0$ , it is reasonable to assume that  $\frac{\partial u_i}{\partial r} = \frac{\partial u_i}{\partial z} \approx 0$ . Employing this assumption, and considering the z-axis as the axis of symmetry, we can proceed to simplify Equation 4.2, which constitutes the momentum equation for the surrounding medium. Subsequently, we can separate this equation into distinct radial and axial momentum equations, respectively as follows:

$$\frac{\partial \bar{u}_r}{\partial t} = -\frac{1}{\bar{\rho}} \frac{\partial \bar{P}}{\partial r} + \frac{\bar{\mu}}{\bar{\rho}} \left[ \left( \frac{\partial}{\partial r} \left( \frac{1}{r} \frac{\partial (r \bar{u}_r)}{\partial r} \right) \right) + \frac{\partial^2 \bar{u}_r}{\partial z^2} \right] \quad (4.17)$$

and,

$$\frac{\partial \bar{u}_z}{\partial t} = -\frac{1}{\bar{\rho}} \frac{\partial \bar{P}}{\partial z} + \frac{\bar{\mu}}{\bar{\rho}} \left[ \frac{1}{r} \left( \frac{\partial}{\partial r} \left( r \frac{\partial \bar{u}_z}{\partial r} \right) \right) + \frac{\partial^2 \bar{u}_z}{\partial z^2} \right] \quad (4.18)$$

Choosing the wavelength,  $\lambda$  and the undisturbed jet radius  $r_0$  as the characteristics length scale along axial and radial directions, respectively the non-dimensional form of the equation 4.17 and 4.18 can be written as follows:

$$\frac{\partial \bar{u}_r^*}{\partial t^*} = -\frac{\lambda}{r_0} \frac{\partial \bar{P}^*}{\partial r^*} + \frac{\lambda}{r_0} \frac{1}{\overline{Re}} \left[ \left( \frac{\partial}{\partial r^*} \left( \frac{1}{r^*} \frac{\partial (r^* \bar{u}_r^*)}{\partial r^*} \right) \right) + \frac{r_0^2}{\lambda^2} \frac{\partial^2 \bar{u}_r^*}{\partial z^{*2}} \right] \quad (4.19)$$

and,

$$\frac{\partial \bar{u}_z^*}{\partial t^*} = -\frac{\partial \bar{P}^*}{\partial z^*} + \frac{\lambda}{r_0} \frac{1}{\overline{Re}} \left[ \frac{1}{r^*} \left( \frac{\partial}{\partial r^*} \left( r^* \frac{\partial \bar{u}_z^*}{\partial r^*} \right) \right) + \frac{r_0^2}{\lambda^2} \frac{\partial^2 \bar{u}_z^*}{\partial z^{*2}} \right] \quad (4.20)$$

Where, nondimensional terms can be defined as,  $r^* = r/r_0$ ,  $z^* = z/\lambda$ ,  $\bar{u}_z^* = \bar{u}_z/U$ ,  $\bar{u}_r^* = \bar{u}_r/U$ , while  $U$  is the unperturbed jet velocity,  $P^* = \bar{P}/\bar{\rho}U^2$ , and  $Re = \bar{\rho}Ur_0/\bar{\mu}$  is the Reynolds number. For a low viscous fluid flowing with a lower mass flow rate  $Re \gg 1$ , nondimensional equation in 4.19 and 4.20 can be further simplified

to :

$$\begin{aligned}\frac{\partial \bar{u}_r^*}{\partial t^*} &= -\frac{\lambda}{r_0} \frac{\partial \bar{P}^*}{\partial r^*} \\ \frac{\partial \bar{u}_r}{\partial t} &= -\frac{1}{\bar{\rho}} \frac{\partial \bar{P}}{\partial r}\end{aligned}\tag{4.21}$$

and,

$$\begin{aligned}\frac{\partial \bar{u}_z^*}{\partial t^*} &= -\frac{\partial \bar{P}^*}{\partial z^*} \\ \frac{\partial \bar{u}_z}{\partial t} &= -\frac{1}{\bar{\rho}} \frac{\partial \bar{P}}{\partial z}\end{aligned}\tag{4.22}$$

Since, we are modelling the dynamics of jet breakup in the inviscid flow region we can define a velocity potential  $\phi$ , which can be modelled as,  $u_z = \frac{\partial \phi}{\partial z}$  and equation 4.22 can be written as:

$$\frac{\partial \phi}{\partial t} = -\frac{\bar{P}}{\bar{\rho}}\tag{4.23}$$

As a potential function,  $\phi$  must satisfy the Laplace equation cylindrical coordinate and can be written as follows:

$$\left( \frac{\partial^2}{\partial r^2} + \frac{1}{r} \frac{\partial}{\partial r} + \frac{\partial^2}{\partial z^2} \right) \phi = 0\tag{4.24}$$

Combining equation 4.21, 4.22, 4.24 and continuity equation in cylindrical coordinate system will reveal that the Laplace's equation in equation 4.24 is Bessel's equation [140] and general solution of which can be written as,

$$\phi = C_1 I_0(kr) + C_2 K_0(kr)\tag{4.25}$$

where  $I_0$  and  $K_0$  are the modified Bessel functions of the first and second kind, respectively and  $C_{1,2}$  as integration constants. For the surrounding medium, the general solution must not be dependent on  $I_0$ , since for  $r \rightarrow 0$ ,  $I_0$  diverges, the exact opposite being valid for the jet fluid[141]. Therefore eliminating  $I_0$  from equation 4.25 will give  $\phi = C_2 K_0(kr)$ . Integral constant  $C_2$  can be determined by using the interface boundary condition from equation 4.4 and 4.5, and subsequently substituting the closed

form of  $\phi$  into equation 4.23 will give us the expression for pressure at the interface of the perturbed jet as follows:

$$\bar{P} = \bar{\rho} \frac{\ddot{\alpha}_t K_0(kr)}{k K_I(\eta)} \cos(kz) \quad (4.26)$$

Where  $K_0$  and  $K_I$  are the zeroth and first order modified Bessel functions of second kind. Now the pressure term in equation 4.12 can be written as;

$$\int_S \bar{P} u_r dS = \frac{2\bar{\rho}m\pi^2 r_0^3 K_0(kr)}{\eta^2 K_I(\eta)} \dot{\alpha}_t \ddot{\alpha}_t \quad (4.27)$$

Again using 4.23 and 4.26, we can write the following:

$$\frac{1}{\bar{\rho}} \frac{\partial \bar{P}}{\partial z} = \frac{\eta}{2} \frac{\partial \bar{u}_{zs}}{\partial t} \frac{K_0(kr)}{K_I(\eta)} \quad (4.28)$$

Considering the equation 4.6 and 4.8, the last term in equation 4.1, i.e., the rate of work done dur to gravity can be expressed as follows,

$$\int_V (\rho g u_i dV) = \rho_j g \left[ \int_0^{r=r_0} \int_0^{z=\frac{2\pi m}{k}} \int_0^{\theta=2\pi} (u_r + u_z) r dr dz d\theta \right] = \frac{\pi^2 r_0^2 m \rho_j g \alpha_t \dot{\alpha}_t}{\eta} \quad (4.29)$$

With all the available information we can write the final form of the equation 4.1 dispersion relation which is also our governing equation and can be expressed as,

$$\begin{aligned} & \left[ 1 + \frac{1}{2} \frac{\bar{\rho}}{\rho_j} \frac{\eta}{1 + \frac{\eta^2}{8}} \frac{K_0(\eta)}{K_I(\eta)} \right] \ddot{\alpha}_t + \left[ 3 \frac{\mu}{\rho_j r_0^2} \eta^2 \frac{1 + \frac{\eta^2}{24}}{1 + \frac{\eta^2}{8}} + \frac{\bar{\mu}}{\rho_j r_0^2} \frac{\eta^2}{1 + \frac{\eta^2}{8}} \right] \dot{\alpha}_t \\ & - \left[ \frac{1}{2} \frac{\sigma_{jm}}{\rho r_0^3} \eta^2 \frac{1 - \eta^2}{1 + \frac{\eta^2}{8}} \alpha_t + \frac{1}{4} \frac{g}{r_0} \frac{\eta^2}{1 + \frac{\eta^2}{8}} \right] \alpha = 0 \end{aligned} \quad (4.30)$$

The equation 4.30 can be converted into the nondimensional form of dispersion equation, by dividing the each term by  $1/2 \frac{\sigma_{jm}}{\rho r_0^3}$ , as follows:

$$\left[ 1 + \frac{1}{2} \frac{\bar{\rho}}{\rho_j} \eta \frac{K_0(\eta)}{K_I(\eta)} \right] \Omega^2 + [2Oh_m \eta^2] \Omega - \eta^2 \left[ (1 - \eta^2) + \frac{Bo}{2} \right] = 0 \quad (4.31)$$

Where,  $\Omega = \omega\sqrt{2\rho r_0^3/\sigma_{jm}}$  is the nondimensional variables of our dispersion relation which contains the angular velocity  $\omega$  term while  $Oh_m = \left(3 + \frac{\bar{\mu}}{\mu}\right) \frac{\mu}{\sqrt{\rho r_0 \sigma_{jm}}}$  and  $Bo = \frac{\rho g r_0^2}{\sigma}$  is the modified Ohnesorge and Bond number, respectively.

The jet is unstable whenever  $\Omega > 0$ , which requires  $\eta < 1$ . Under such conditions,  $\frac{K_0(\eta)}{K_I(\eta)} < 1$  and  $\eta \frac{K_0(\eta)}{K_I(\eta)} \ll 1$ . Thus, for liquid jets that satisfy the condition,  $\frac{\bar{\rho}}{\rho_j} < 0$  equation 4.31 will reduce to,

$$\Omega^2 + [2Oh_m\eta^2] \Omega - \eta^2 \left[ (1 - \eta^2) + \frac{Bo}{2} \right] = 0 \quad (4.32)$$

Based on Rayleighs maximum instability theory, the most-unstable wave number can be obtained by applying the condition [103]  $\left. \frac{d\Omega}{d\eta_m} \right|_{\eta=\eta_m} = 0$  to equation 4.32, which can be written as follows:

$$\eta_m = \sqrt{\frac{1 + Bo/2}{2(1 + Oh_m)}} \quad (4.33)$$

In this analysis, we assume that the droplets are spherical with a diameter  $d_e$ . We also assume a constant rate of droplet formation, producing  $N$  droplets over a time interval  $\Delta t$ . The total volume of these  $N$  droplets is given by  $V_1 = N\pi d_e^3/6$ . During the same time interval, the volume of the fluid exiting the orifice in the form of a jet is represented by  $V_2 = \int_{\Delta t} \frac{\pi}{4} d_0^2 u_0 dt = \frac{\pi}{4} d_0^2 u_0 \Delta t$ , where  $d_0$  and  $u_0$  denote the stable jet diameter and bulk-mean jet velocity at the nozzle exit, respectively. From continuity we can write  $V_1 = V_2$ , which will give us the following equation:

$$N\pi d_e^3/6 = \frac{\pi}{4} d_0^2 u_0 \Delta t \quad (4.34)$$

We can assume that each most-unstable disturbance wave produces a single droplet; i.e.,  $u_0 \Delta t = N\lambda_m$ , where  $\lambda_m$ , is the most-unstable wavelength. Thus, equation 4.34 becomes,

$$\frac{d_e}{d_0} = \left( \frac{3\pi}{2\eta_m} \right)^{1/3} \quad (4.35)$$

Where,  $\eta_m = \frac{\pi d_0}{\lambda_m}$ . The stable jet diameter at any point is also a function of nozzle diameter,  $a$  and jet velocity, which can be represented as,  $\frac{d_0}{a} = \left(1 + \frac{2}{Fr} \frac{z}{a}\right)^{-1/4}$ .

Now combining equation 4.1- 4.35 we can express the closed form of nondimensional jet diameter as follows:

$$\frac{d_e}{a} = \left(1 + \frac{2}{Fr} \frac{z}{a}\right)^{-1/4} \left(\frac{3\pi}{\sqrt{2 + Bo}}\right)^{1/3} (1 + Oh_m)^{1/6} \quad (4.36)$$

Equation 4.36 is the approximated final and closed form of our governing equation from which we can express the non dimensional drop diameter after jet break up as a function of Froude ( $Fr$ ), Bond ( $Bo$ ) and modified Ohnesorge ( $Oh_m$ ) number.

## 4.4 Results and Discussion

Figure 4.2 represents the break up dynamics and subsequent drop formation of a laminar liquid jet, emanating from a nozzle with circular orifice of  $0.1mm$ , in both  $\mu g$  and  $1g$ . In both cases the average jet exit velocity was  $0.6 \pm 0.1m/s$ . From both figure 4.1 and 4.2, it is observed that the disturbance is convected only in the downstream direction, which suggests that the instability that we encountered in this experiments is convective instability[123]. In this study the jet velocity is kept between  $0.5 - 1.6 m/s$ , which is high enough to avoid dripping regime but low enough to avoid triggering wind induced regime[64]. This velocity range is crucial for our jet based study as our theoretical model is based on Rayleigh-Taylor instabilities.

In Figure 4.2a, the time series of a jet break up process is illustrated. The jet is formed by injecting liquid through a nozzle parallel to the direction of gravity at a constant velocity. Upon exiting the nozzle, disturbances caused by capillary forces overpowering inertial forces are encountered downstream of the jet. This competition between capillary and inertial forces amplifies perturbations at the interface between

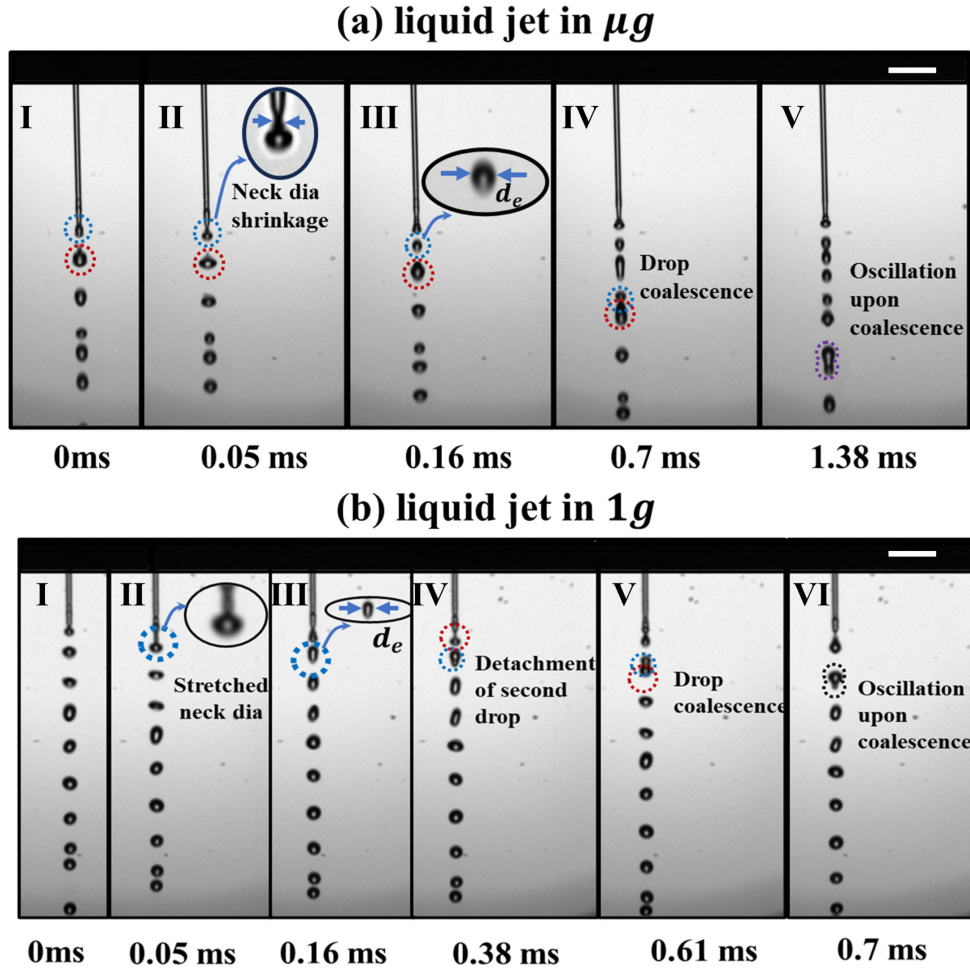


Figure 4.2: Snapshot of jet break up dynamics and subsequent drop formation. (a) Break up of a laminar liquid jet filament in microgravity and (b) breakup of a laminar liquid jet filament in terrestrial gravity. The scale bar in figure (a) and (b) represents 1mm.

the jet and medium. Consequently, as it moves downstream, the diameter of the jet narrows to form a neck attached to a droplet-shaped bulb of liquid which eventually separates from this narrow region to become an individual droplet with size denoted as  $d_e$ . In Figure 4.2a, this disintegrated droplet  $d_e$  can be identified by observing its location within blue dotted circle. The recently created droplet rapidly falls from a time range of  $0.05ms - 0.7ms$ , and eventually at  $0.7ms$  it merges with the previously formed droplet, as indicated by the red dotted circle in figure 4.2a. After coalescing, the newly formed drop continues to fall downward with rapid oscillations.

Figure 4.2b illustrates the influence of gravity on drop formation during the disintegration of a laminar jet. In terrestrial gravity, the initially cylindrical liquid jet undergoes rapid deformation downstream, owing to the interplay of inertial, capillary, and gravitational forces. Panel II in Figure 4.2b demonstrates how the perturbed interface of the jet and surrounding medium experiences stretching due to its accelerated motion in the Earth's gravitational field. This gravitational acceleration transforms the downstream perturbation into a thread, which progressively elongates to a minimal radius before eventually breaking up into a droplet, as indicated by the blue dotted circle in Figure 4.2b. This stretching of the ligament formation within a gravitational field is not a random occurrence. We can also observe a similar elongation of the neck diameter in the subsequent droplet, denoted by the red dotted circle in Panel IV of Figure 4.2b. Following the breakup, the first and second drops, as highlighted by the blue and red dotted circles respectively, coalesce and descend with oscillations.

When we qualitatively compare the dynamics of jet breakup in microgravity with those in terrestrial gravity, Figure 4.2 makes it evident that the entire breakup process occurs significantly faster in a 1g environment. This accelerated motion of the stretched ligament, formed under 1g conditions, leads to an earlier jet breakup. Conversely, in microgravity, where the breakup is primarily driven by capillary forces alone, the jet breakup occurs at a slower pace compared to the conditions experienced under Earth's gravity. More quantitative discussion will be presented in the subsequent discussions.

In this present study, we conducted controlled experiments to investigate the dynamics of jet breakup under three distinct gravitational conditions, namely, microgravity, Martian gravity, and terrestrial gravity. These gravitational scenarios were simulated within the confines of a parabolic flight, facilitating an exploration of fluid

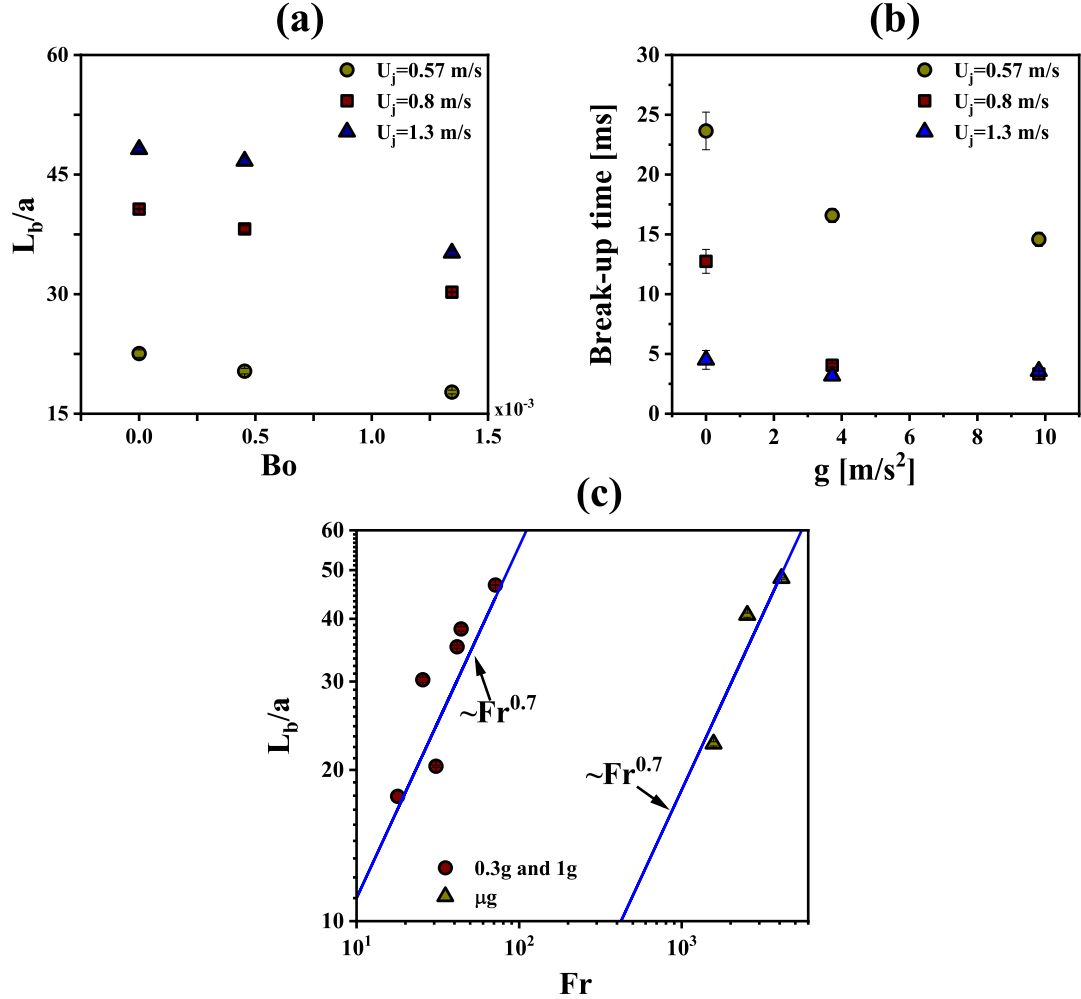


Figure 4.3: Experimental observations of break up length and time as a function of jet velocity, gravitational acceleration and surface forces. (a) Non dimensional break up length as a function of Bond number for varied jet velocity, (b) Total break up time as a function of gravitational acceleration for varied jet velocity and (c) Log-log plot representing the power law relationship for a non dimensional breakup length as a function of Froude number.

behavior under idealized Earth gravity conditions and reduced-gravity environments.

Figure 4.3a offers insight into the interplay of gravitational and inertial forces by illustrating the relationship between the non-dimensional breakup length ( $L_b/a$ ) and the Bond number ( $Bo$ ). The graphical representation in Figure 4.3a unmistakably indicates an inverse proportionality between  $L_b/a$  and the Bond number. Remarkably, this inverse dependency aligns consistently with the observations presented in Figure 4.2.

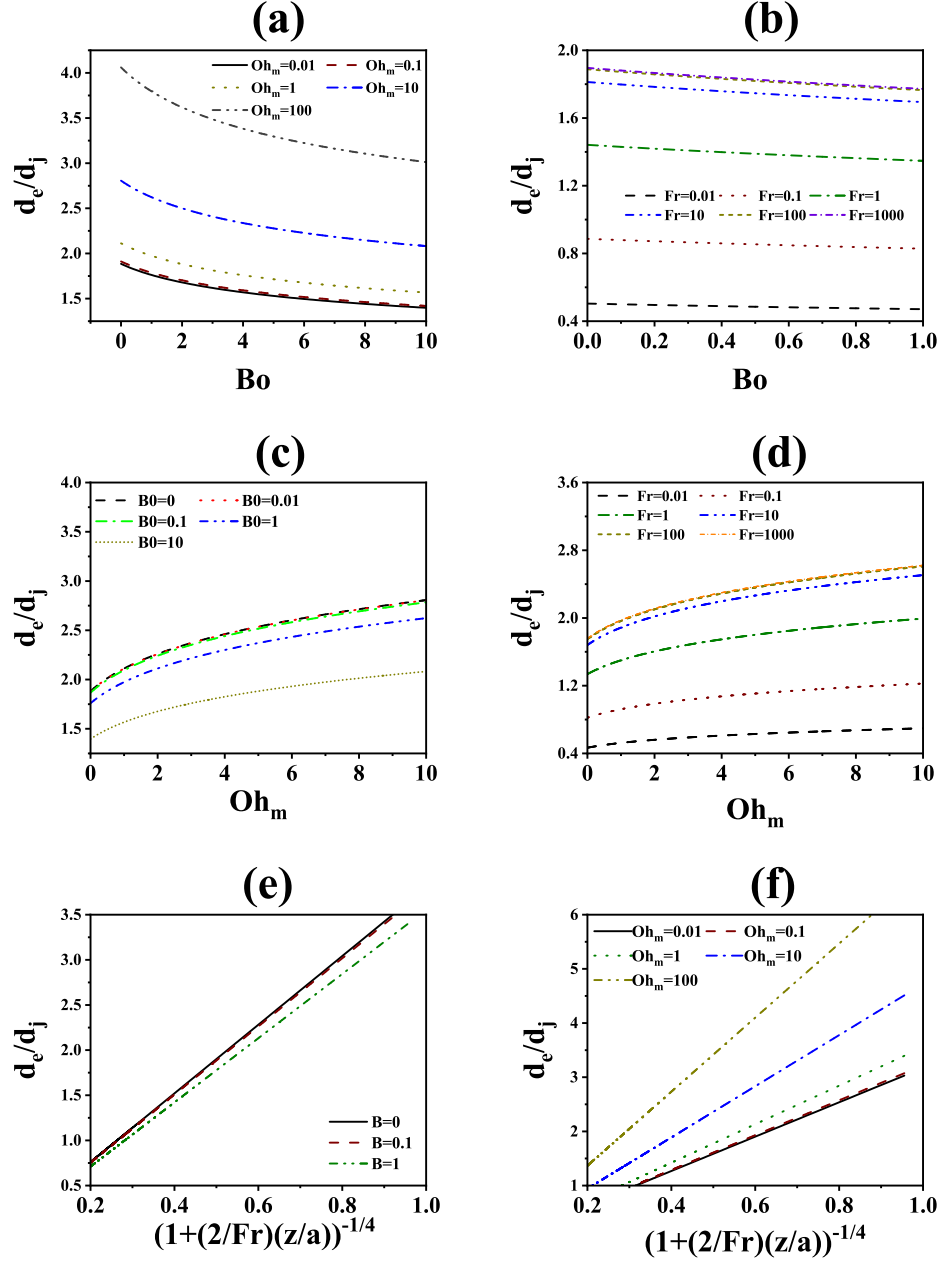


Figure 4.4: Parametric study for the effect of Bond number number ( $Bo$ ), modified Ohnesorge number ( $Oh_m$ ) and modified Froude number  $((1 + 2/Fr)(z/a)^{-1/4})$  on the non dimensional drop size, generated from the laminar jet break up. (a) and (b) represents  $d_e/d_j$  as a function  $Bo$  for varied  $Oh_m$  and  $Fr$ , respectively; (c) and (d) represents  $d_e/d_j$  as a function  $Oh_m$  for varied  $Bo$  and  $Fr$ , respectively; and (e) and (f) represents  $d_e/d_j$  as a function  $(1 + 2/Fr)(z/a)^{-1/4}$  for varied  $Bo$  and  $Oh_m$ , respectively.

Under the microgravity condition, characterized by the absence of gravitational

influence, we observed a decelerated jet breakup process primarily driven by capillary forces. This diminished gravitational effect is further elucidated in Figure 4.3b, which demonstrates that, for a fixed jet velocity, the time required for jet disintegration into micro-droplets is significantly prolonged in a reduced gravitational field. Specifically, it becomes evident that, at lower jet velocities where capillary forces predominate over inertial forces, gravitational acceleration exerts a discernible influence on breakup time. At a velocity of 0.57 m/s, the breakup process takes approximately 25 ms in a microgravity environment, whereas in Martian and Earth gravity, the breakup time reduces to approximately 17 ms and 15 ms, respectively.

A more detailed examination of Figure 4.3a and b reveals that, at higher velocities, specifically at  $U_j = 1.3\text{m/s}$ , the variation in jet breakup dynamics becomes less significant, particularly when comparing Martian and Earth gravity. This phenomenon can be attributed to the dominance of inertial forces over capillary forces in the presence of higher velocities and stronger gravitational fields.

The data presented in Figure 4.3a illustrates a discernible decrease in the non-dimensional breakup length ( $L_b/a$ ) concerning the Bond number ( $Bo$ ), thus revealing an inverse relationship with gravitational force. Conversely, the same figure exhibits an increase in  $L_b/a$  in response to variations in jet velocity or flow rate. Consequently, it is imperative to conduct a comprehensive analysis of the influence exerted by inertial and gravitational forces on the jet breakup length. To achieve this, we propose an examination of the dependence of  $L_b/a$  as a function of the Froude number ( $Fr$ ), which quantifies the ratio of inertial force to gravitational force. It is noteworthy that under Martian and Earth gravity conditions, where the internal nozzle diameter is fixed at 0.1mm,  $Fr$  attains values on the order of approximately  $O(2)$ , whereas in the microgravity environment,  $Fr$  escalates to around  $O(4)$ . In light of these considerations, we present a log-log plot depicting the relationship between  $L_b$  and  $Fr$  in

Figure 4.3c. This representation illuminates that the non-dimensional breakup length adheres to a power-law relationship with respect to  $Fr$ . The slope of the log-log plot is approximately 0.7, signifying that  $L_b/a$  can be expressed as  $L_b/a \sim Fr^{0.7}$ .

The findings presented in Figure 4.2 (a-c) have already established that under reduced gravity conditions, the jet breakup process occurs at a notably slower rate compared to Earth gravity conditions, with jet breakup being approximately 1.5 times slower in reduced gravity. Consequently, the droplets formed during jet breakup in a microgravity environment exhibit larger diameters and volumes when contrasted with their counterparts in Earth gravity. Conversely, within the Earth's gravitational field, the accelerated motion results in the stretching of thinner jet ligaments, thereby promoting a faster jet breakup. Consequently, in Earth gravity, we observe smaller drop diameters. A similar comparative analysis can be extended to the jet breakup dynamics in microgravity and Martian gravity.

Our developed mathematical model, as represented in Equation 4.36, successfully predicts this inversely proportional relationship between non-dimensional drop diameter and gravitational field, a phenomenon evident in Figure 4.4.

Figure 4.4 (a) and (b) illustrate the variation of the ratio of drop diameter to jet diameter ( $d_e/d_j$ ) as a function of Bond Number for various combinations of Ohnesorge number ( $Oh_m$ ) and Froude number ( $Fr$ ), respectively. Figure 4.4 (a) reveals that, for a fixed  $Oh_m$ ,  $d_e/d_j$  exhibits a decreasing trend with respect to the Bond Number ( $Bo$ ), indicative of larger drop formation in reduced gravitational environments. This finding aligns with our experimental observations. Moreover, it is evident from this figure that  $d_e/d_j$  increases in relation to the viscosity ratio between the drop and the surrounding medium. It is important to note that while this relationship may not be readily apparent from our specific experimental setup utilizing a single liquid and

surrounding medium combination, it has been established in previous studies.

Figure 4.4 (b) further demonstrates that our mathematical model accurately predicts the experimental observations presented in Figure 4.3, specifically the increase in drop diameter concerning modified Froude number ( $Fr$ ) and the decrease in diameter with respect to Bond Number ( $Bo$ ).

Upon scrutiny of Figure 4.4 (c) and (d), it becomes evident that, for a constant Bond Number ( $Bo$ ) or modified Froude Number ( $Fr$ ), the non-dimensional jet diameter exhibits an increase relative to the Ohnesorge Number ( $Oh_m$ ). This trend underscores that a higher viscosity ratio between the jet and the surrounding medium fluid corresponds to a larger drop diameter, a conclusion congruent with previously documented analyses.

Furthermore, a meticulous examination of Figure 4.4 hints at a nonlinear variation of  $d_e/d_j$  concerning Bond Number ( $Bo$ ) and Ohnesorge Number ( $Oh_m$ ). In contrast, the relationship between  $d_e/d_j$  and modified Froude Number ( $Fr$ ) appears to follow a linear trend. Importantly, our experimental observations align with these discerned relationships.

Figure 4.5 offers a comprehensive evaluation of the precision of our developed model in comparison to experimental observations pertaining to drop formation during jet breakup under three distinct gravitational conditions: Earth, Martian, and micro-gravity. A careful examination of this figure reveals that our model, as represented by Equation 4.36, consistently predicts experimental data within an acceptable margin of error, typically within  $\pm 10\%$ . It is worth noting, however, that while our developed model accurately forecasts drop diameters for higher jet velocities, it exhibits a slight tendency to overpredict drop diameters at lower jet speeds. This discrepancy

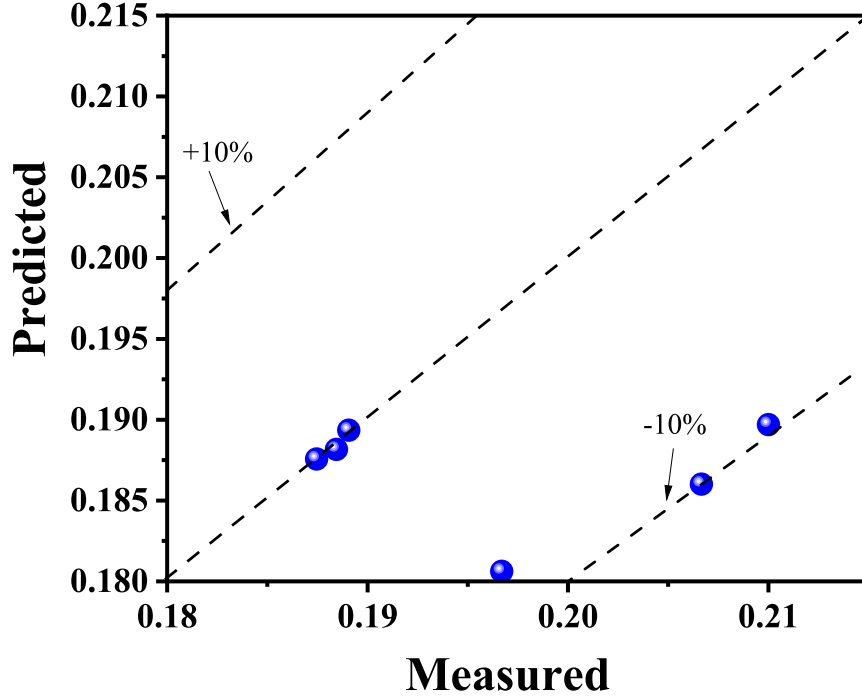


Figure 4.5: Accuracy of the prediction of the developed model at equation 4.36 with the experimental observation. Nondimensional theoretical microdrops diameter is represented by vertical axis, whereas nondimensional experimental microdrop diameter is represented by horizontal axis.

in the model’s performance at lower speeds may be attributed to the linearization of certain nonlinear terms inherent in the mathematical model. Alternatively, it could be connected to the critical Weber number ( $We_{critic}$ ), as elucidated by Clanet [104], since our calculations indicate that  $We_{critic}$  falls within the transitional regime between dripping and jetting, a region known for its potential to exhibit chaotic behavior.

## 4.5 Conclusion

This study delves into the impact of gravity and liquid properties on the dynamics of jet breakup and the subsequent formation of drops. The findings of this investigation hold the potential to enhance the optimization of jetting parameters for space-based 3D printing processes, with the aim of mitigating issues such as liquid splashes and

the formation of bubbles within the deposited material, which could otherwise compromise the structural integrity of the printed objects.

Our research has unveiled significant insights. We've determined that the critical jet breakup length in a liquid-air system exhibits an inverse relationship with gravitational strength and a direct proportionality with jet exit velocity. Additionally, we've observed that jet breakup occurs at a slower rate in reduced gravity. This observation implies that for any jet-based application in space missions, such as the filling of liquid tanks or 3D printing, it is advisable to maintain a jet velocity lower than that under Earth's gravity to prevent unintended jet splashing or bubble formation.

Furthermore, our study has uncovered that, for a given level of gravity, the nondimensional critical jet breakup length ( $L_b/a$ ) follows a power-law relationship with the Froude number, represented as  $L_b/a \sim Fr^{0.7}$ .

Moreover, the mathematical model we have presented not only elucidates the physics behind drop formation during jet breakup by demonstrating a proportional connection with the Ohnesorge number and an inverse relationship with the Bond number, but it can also accurately predict the size of drop diameter upon jet breakup with a margin of error within  $\pm 10\%$ .

## References

- [64] B. Bonhoeffer, A. Kwade, and M. Juhnke, “Impact of formulation properties and process parameters on the dispensing and deposition of drug nanosuspensions using micro-valve technology,” *J. Pharm. Sci.*, vol. 106, no. 4, pp. 1102–1110, 2017.
- [103] L. Rayleigh, “On the instability of jets,” *Proc. London Math. Soc.*, vol. 1, no. 1, pp. 4–13, 1878.
- [104] C. Clanet and J. C. Lasheras, “Transition from dripping to jetting,” *J. Fluid Mech.*, vol. 383, pp. 307–326, 1999.
- [115] J. Eggers and E. Villermaux, “Physics of liquid jets,” *Reports on progress in physics*, vol. 71, no. 3, p. 036 601, 2008.
- [116] G. D. Martin, S. D. Hoath, and I. M. Hutchings, “Inkjet printing—the physics of manipulating liquid jets and drops,” in *Journal of Physics: Conference Series*, IOP Publishing, vol. 105, 2008, p. 012 001.
- [117] S. X. Liu and M. Lu, “Nonlinear evolution and breakup of the cavitating liquid jet surrounded by the rotary compressible air,” Dec. 2019. [Online]. Available: <https://scite.ai/reports/10.1021/acsomega.9b02477>.
- [118] T Nguyen, D. Shanmugam, and J. Wang, “Effect of liquid properties on the stability of an abrasive waterjet,” *International Journal of Machine Tools and Manufacture*, vol. 48, no. 10, pp. 1138–1147, 2008.
- [119] D. Pede, G. Serra, and D. De Rossi, “Microfabrication of conducting polymer devices by ink-jet stereolithography,” *Materials Science and Engineering: C*, vol. 5, no. 3-4, pp. 289–291, 1998.
- [120] M. E. Kuil, J. P. Abrahams, and J. C. Marijnissen, “Nano-dispensing by electrospray for biotechnology,” *Biotechnology Journal: Healthcare Nutrition Technology*, vol. 1, no. 9, pp. 969–975, 2006.
- [121] G. Li, X. Xiao, T. Liu, M. Gu, R. Dai, and W. Liao, “Three-dimensional morphology and contour quality of conductive lines printed by high-viscosity paste jetting,” *Langmuir*, 2023.
- [122] A. Baldygin *et al.*, “Effect of gravity on the spreading of a droplet deposited by liquid needle deposition technique,” *npj Microgravity*, vol. 9, no. 1, p. 49, 2023.
- [123] I Vihinen, A. Honohan, and S. Lin, “Image of absolute instability in a liquid jet,” *Physics of Fluids*, vol. 9, no. 11, pp. 3117–3119, 1997.
- [124] S. Lin and E. Ibrahim, “Instability of a viscous liquid jet surrounded by a viscous gas in a vertical pipe,” *Journal of Fluid Mechanics*, vol. 218, pp. 641–658, 1990.
- [125] R. D. Reitz, *Atomization and other breakup regimes of a liquid jet*. Princeton University, 1978.

- [126] M. L. Cordero, F. Gallaire, and C. N. Baroud, “Quantitative analysis of the dripping and jetting regimes in co-flowing capillary jets,” *Physics of Fluids*, vol. 23, no. 9, 2011.
- [127] J. Plateau, “Experimental and theoretical statics of liquids subject to molecular forces only,” 1873.
- [128] E. Musk, “Making life multi-planetary,” *New Space*, vol. 6, no. 1, pp. 2–11, 2018.
- [129] D. J. Chato, “Cryogenic fluid transfer for exploration,” *Cryogenics*, vol. 48, no. 5-6, pp. 206–209, 2008.
- [130] L. Bolshinskiy, A. Hedayat, L. Hastings, S. Sutherlin, A. Schnell, and J. Moder, “Tank system integrated model: A cryogenic tank performance prediction program,” Tech. Rep., 2017.
- [131] V. Ozbolat, M. Dey, B. Ayan, A. Povilianskas, M. C. Demirel, and I. T. Ozbolat, “3d printing of pdms improves its mechanical and cell adhesion properties,” *ACS Biomaterials Science & Engineering*, vol. 4, no. 2, pp. 682–693, 2018.
- [132] M. Xia, D. Gu, G. Yu, D. Dai, H. Chen, and Q. Shi, “Selective laser melting 3d printing of ni-based superalloy: Understanding thermodynamic mechanisms,” *Science Bulletin*, vol. 61, no. 13, pp. 1013–1022, 2016.
- [133] A. Edwards, B. Osborne, J. Stoltzfus, T. Howes, and T. Steinberg, “Instabilities and drop formation in cylindrical liquid jets in reduced gravity,” *Physics of fluids*, vol. 14, no. 10, pp. 3432–3438, 2002.
- [134] C. Kinoshita, H. Teng, and S. Masutani, “A study of the instability of liquid jets and comparison with tomotika’s analysis,” *International journal of multiphase flow*, vol. 20, no. 3, pp. 523–533, 1994.
- [135] F. Suñol and R. González-Cinca, “Liquid jet breakup and subsequent droplet dynamics under normal gravity and in microgravity conditions,” *Physics of Fluids*, vol. 27, no. 7, 2015.
- [136] P. K. Kundu, I. M. Cohen, and D. R. Dowling, *Fluid mechanics*. Academic press, 2015.
- [137] D. Bogy, “Drop formation in a circular liquid jet,” *Annual Review of Fluid Mechanics*, vol. 11, no. 1, pp. 207–228, 1979.
- [138] A. W. Adamson, A. P. Gast, *et al.*, *Physical chemistry of surfaces*. Interscience publishers New York, 1967, vol. 150.
- [139] P. Ghosh, *Colloid and interface science*. PHI Learning Pvt. Ltd., 2009.
- [140] D. G. Zill, *Advanced engineering mathematics*. Jones & Bartlett Learning, 2020.
- [141] C. Patrascu and C. Balan, “The effect of curvature elasticity on rayleigh–plateau instability,” *European Journal of Mechanics-B/Fluids*, vol. 80, pp. 167–173, 2020.

# Chapter 5

## Measurement of surface free energy in microgravity

### Abstract

This study presents a comprehensive exploration of a theoretical model designed to measure the surface energy of solids under microgravity conditions. While numerous studies have investigated various techniques for determining the surface energy of solids through the use of pairs of liquids based on Young's equation of contact angle, these methods often lack accuracy and are impractical in space-like environments due to safety concerns. In this investigation, we critically examine and validate the sessile drop accelerometry model, specifically developed for measuring the surface free energy of solids in microgravity conditions through the deposition of a single water droplet. This model encompasses a set of governing equations that enable the determination of interfacial energies as a function of changes in the droplet's shape resulting from the release of gravitational energy. To validate and analyze the theoretical model, a sophisticated experimental payload was developed, and a series of rigorous experiments were conducted under both reduced gravity and hypergravity conditions, simulated using parabolic flight. Through theoretical and experimental analyses, we have established a coherent understanding of the influence of the non-dimensional Bond number on the metastable droplet shape and its implications for surface energy measurements.

## 5.1 Introduction

Capillary phenomena, arising from the intricate interplay between interfacial forces and body forces, such as gravitational force, serve as the underlying mechanism for various fundamental phenomena, including Marangoni effects, wetting, spreading, and the behavior of droplets on specific surfaces. These capillary forces, primarily interfacial forces, hold significant relevance in a wide range of industrial processes, such as casting, molding, crystal growth, smelting, refining, brazing, sintering, zone refining, and fiber formation [142]. Furthermore, comprehending the impact of gravitational forces on physical phenomena governed by interfacial or surface tension-driven forces has spurred investigations into a novel realm of research, notably the realm of 3D printing within spacecraft. Consequently, for the past three decades, there has been a growing emphasis on exploring surface and interfacial forces under "zero gravity," microgravity, or the so-called "reduced gravity" conditions [27].

The pioneering work of Miller and Cezairliyan [143] marked the initial measurement of copper's surface tension at elevated temperatures under reduced gravity conditions within a KC-135 parabolic flight. Subsequently, Egry and Szekely [144] introduced an innovative technique for assessing surface tension in space conditions, involving the levitation and oscillation of molten droplets generated by electromagnetic fields. In a later development, Egry et al. [144] extended their model by incorporating formulas proposed by Lord Rayleigh and Lord Kelvin, which establish relationships between the frequency ( $\omega$ ) and damping ( $\Gamma$ ) of oscillations and the surface tension ( $\sigma$ ) and viscosity ( $\eta$ ) of the material, respectively. The governing equations of oscillating levitated droplet method can be expressed as[144],

$$\omega^2 = \frac{32\pi\sigma}{3M} \quad (\text{Raighleigh's formula}) \quad (5.1)$$

and

$$\Gamma = \frac{20\pi a_0 \eta}{3M} \quad (\text{Kelvin's formula}) \quad (5.2)$$

Where,  $M$  and  $a_0$  are the mass and radius of the droplet. it is worth noting that the levitated droplet method exhibits limitations as it is primarily applicable to molten metal droplets. Furthermore, this method is highly sensitive to the amplitude of oscillations, a characteristic that can potentially lead to artificially elevated surface tension values [145]. To address these limitations and to enable investigations under microgravity conditions, Passerone et al. [146] introduced an alternative technique known as capillary pressure tensiometry (CPT). This method is founded on the measurement of capillary pressure across a spherical interface. Under appropriate mechanical quasi-equilibrium conditions, the CPT method adheres to Laplace's equation, which can be mathematically expressed as follows:

$$\Delta P = \frac{2\sigma}{R} \quad (5.3)$$

Where, the pressure differential, denoted as  $\Delta P$ , existing across the interface is quantified using a pressure transducer, while the radius of curvature of the droplet, represented as  $R$ , is either directly determined through imaging or derived through computations based on the volume of liquid injected. It is important to note that the capillary pressure tensiometry (CPT) technique is contingent upon the spherical configuration of the interface, rendering it well-suited for the measurement of interfacial tension between a liquid droplet and a liquid medium. However, it is important to recognize that CPT's applicability is notably confined to scenarios involving microgravity or environments with negligible gravitational influence. In terrestrial gravity conditions, the technique faces substantial limitations attributable to convective effects and interfacial deformations due to gravity, as elucidated by Kovalchuk et al.[147].

It is important to highlight that, in addition to research on surface or interfacial tension measurement, a substantial body of literature has been dedicated to understanding the influence of gravity on various capillary-driven phenomena. Sakai et al.'s [148] theoretical model indicated that gravity can elevate the apparent contact angle on rough surfaces. Furthermore, Ababneh et al. [28] experimentally scrutinized the effect of gravity on the macroscopic advancing contact angle. Their findings revealed that the advancing contact angle in terrestrial gravity exceeds that in reduced gravity by 5 degrees. A comprehensive comparative analysis was conducted by Brutin et al. [97], exploring contact angles and the behavior of sessile droplets formed under both terrestrial gravity (1g) and microgravity ( $\mu g$ ) conditions. Later on, Diana et al. [95] laid the foundation for the establishment of a database encompassing contact angles of sessile droplets in reduced gravity conditions.

In light of the preceding discussions within the extant literature, it is evident that while a significant body of work has been dedicated to measuring surface tension or interfacial tension at liquid-gas or liquid-liquid interfaces, as well as investigating the influence of gravity on contact angles, the measurement of surface free energy pertaining to solid substrates remains relatively unexplored. To the best of our knowledge, Calvimontes [110] stands as the sole contributor to have developed both a model and a technique for effectively measuring the surface energy of a solid surface under reduced gravity conditions. This innovative technique, termed sessile drop accelerometry (SDAcc), has been tested in a laboratory drop tower under reduced gravity, but it is yet to be validated in a microgravity or "zero-g" environment.

Despite the availability of alternative methods for measuring solid surface energy, SDAcc is believed to be the most effective approach under reduced or microgravity conditions. Prominent models in the realm of surface energy have been proposed

by Zisman[50], Owens and Wendt [149], Wu[52], Van Oss, Chaudhury and Good [53], Kwok et al.[54]. Nevertheless, all these surface energy measurement techniques are founded on Young’s model, where wetting of the solid surface by a liquid droplet results from the mechanical equilibrium of three bidimensional tensors acting on the droplet’s contour and the three-phase contact line on the solid substrate. Young’s equation can also be derived from the principle of minimizing the total free energy of the system. This equation can be mathematically expressed as follows:

$$\gamma_{sv} = \gamma_{sl} + \gamma_{lv}\cos\theta_Y \quad (5.4)$$

Where  $\gamma_{sv}$ ,  $\gamma_{sl}$  and  $\gamma_{lv}$  represent the interfacial tensions per unit length of the solid-vapor, solid-liquid, and liquid-vapor contact lines respectively, i.e., the surface tensions, and  $\theta_Y$  is the Young’s equilibrium contact angle. The interfacial tension in solid vapour phase can also be named as surface energy.

Nevertheless, the applicability of Young’s model for measuring contact angles on the nanoscale [150] and on flexible surfaces [151] raises questions about its validity. Young’s equation, moreover, fails to consider the influence of gravity on the shape of liquid droplets, while gravity significantly affects the interface shape of droplets. This gravitational impact on the contact angle and the behavior of the three-phase contact line has been demonstrated through parabolic arc flight and microgravity drop tower experiments [28, 95, 97].

Under microgravity conditions, liquid droplets experience a swift decrease in hydrostatic pressure due to the negligible gravitational force. Consequently, in microgravity, the minimal effect of gravity coupled with the dominance of surface tension prompts droplets to adopt a spherical shape. Consequently, the three-phase contact line has minimal contact with the solid surface. Given the significant role of gravity in interfacial tension and surface energy measurements, conventional techniques may

prove inadequate under reduced gravity conditions. Hence, we propose the Sessile Drop Accelerometry (SDAcc) method for simultaneously measuring interfacial tension of liquid droplets and the surface energy of solid substrates.

A pivotal advantage of the Sessile Drop Accelerometry (SDAcc) method, as opposed to conventional approaches, is its elimination of the need for a priori knowledge of interfacial tension at the solid-liquid interface. Instead, this innovative method permits the measurement of interfacial tension alongside the surface energy of the solid substrate, requiring solely the knowledge of surface tension, liquid droplet density, and volume as input parameters. Additionally, the SDAcc model offers another substantial advantage – the requirement of just one type of liquid droplet (either polar or nonpolar) to measure surface free energy. In contrast, conventional methods demand the use of both polar (e.g., water) and nonpolar (e.g., Diiodomethane) droplets. It is worth emphasizing that employing toxic fluids like Diiodomethane in space-like environments is impractical and poses significant health and safety concerns for space crews. Given the limitations and challenges inherent in traditional techniques for assessing interfacial tension and surface energy, we strongly advocate the SDAcc method as a more suitable approach for measuring the surface free energy of solid substrates, especially in microgravity conditions.

Nevertheless, the reliability of the Sessile Drop Accelerometry (SDAcc) model remains a subject of uncertainty due to the absence of microgravity data. Previously, this model underwent validation solely under reduced gravity conditions for a mere 2-second duration, a period provided by a drop tower facility. Such a brief timeframe presents significant challenges for adequately assessing droplet behavior. Furthermore, a notable limitation of SDAcc is its validation exclusively on hydrophobic surfaces, leaving the validation of surface free energy data associated with hydrophobic surfaces incomplete. Consequently, this study embarks on a rigorous investigation

into the validity of the SDAcc model. This investigation entails experimental assessments conducted under 20 seconds of microgravity conditions, encompassing multiple metastable stages experienced by the droplet as it transitions from terrestrial gravity to microgravity. In addition we have also validated the model for high energy and low energy surfaces.

## 5.2 Experimental procedure

Detailed explanation of experimental setup can be found in section 3.3.

## 5.3 Theoretical Model

A surface or an interface can be characterised by a thermodynamic quantity which is the surface works,  $w$  required to create a new area,  $\Omega$  of surface or interface at a constant temperature,  $T$ ; volume,  $V$  and chemical potential of a component  $i$ ,  $\mu_i$ . Therefore, the reversible specific work required to form a unit area of surface or interface can be expressed as the following equation,

$$\gamma = \frac{dw}{d\Omega} \quad (5.5)$$

Now, we can consider a system which is not influenced by any form of external work such as, electrical, magnetic, gravitational etc. Considering this situation, the terms associated with the general Maxwell relations in thermodynamics can be expressed as the following equations,

$$dE = TdS - PdV + \sum_{i=1}^{\infty} \mu_i dN_i + \gamma d\Omega \quad (5.6)$$

$$dH = TdS - VdP + \sum_{i=1}^{\infty} \mu_i dN_i + \gamma d\Omega \quad (5.7)$$

$$dA = -SdT - PdV + \sum_{i=1}^{\infty} \mu_i dN_i + \gamma d\Omega \quad (5.8)$$

$$dG = -SdT + VdP + \sum_{i=1}^{\infty} \mu_i dN_i + \gamma d\Omega \quad (5.9)$$

Where,  $E$ ,  $H$ ,  $A$  and  $G$  are the internal energy, enthalpy, Helmholtz free energy and Gibbs free energy, respectively while  $S$  and  $P$  are the entropy and pressure of the system, respectively and  $N_i$  is the number of molecules of the component  $i$ .

It is noteworthy to mention that the result of the formation of new interface is an increase in the free energy of the system. If a bulk phase of a solid surface is cleaved and separated into two newly formed solid surfaces, then the nature of the immediate environment of freshly formed surfaces will affect the actual excess surface free energy of the system. If the surfaces are in contact with a vacuum, there are, naturally, no atoms or molecules present to interact with the exposed units. Those units, therefore, can be considered to have bare areas that represent a high energy situation relative to the bulk. When in contact with an adjacent fluid phase (liquid or gas), surface units can interact to some extent with the fluid phase and thereby lose some of the excess energy they have gained by virtue of their position. The greater the interaction between surface units and the adjacent phase, the greater the reduction in excess surface energy. From a practical standpoint, the surface excess can also be considered to be the amount of  $i$  adsorbed at the interface.

Liquid-vapor interfaces generally exhibit simpler adsorption characteristics (in principle, at least) than those containing solid surfaces, because in liquid surfaces, the complications arising due to specific structures and surface heterogeneity can be ignored. Before beginning the discussion on adsorption phenomena, it is customary to discuss about the classical adsorption theory - the Gibbs dividing surface and the Gibbs adsorption isotherm. The Gibbs approach to determining (or at least estimating) the concentration of components in the interfacial region can be described by

considering a system containing a substance  $i$  in one or both of two phases  $\alpha$  and  $\beta$ . Let's consider a uniform unit concentration of substance  $i$ ,  $C_i^\alpha$  and  $C_i^\beta$  throughout the phase  $\alpha$  and  $\beta$  with volume  $V_\alpha$  and  $V_\beta$ , respectively. Therefore, the total amount of substance  $i$ ,  $n_i$  can be expressed by the following equation,

$$n_i = C_i^\alpha V_\alpha + C_i^\beta V_\beta \quad (5.10)$$

However, since the local value of  $C_i$  varies while going through the interface, there will generally be a different concentration of  $i$  present in the interfacial region than that indicated by equation 10 and in general the concentration of adsorbed molecules at the top layer of a surface or interface is greater than the other layer. That difference, defined as the surface excess amount of  $i$  ( $N_i$ ) and is given by,

$$N_i = n_i - C_i^\alpha V_\alpha + C_i^\beta V_\beta \quad (5.11)$$

Gibbs's approach was to define a hypothetical surface called Gibbs dividing surface which is also called the interface as a two dimensional plane in which the concentration of one phase component becomes zero. According to Gibbs's approach if the surface excess molecules  $dN_i$  flowing in and out from the newly created surface of area  $d\Omega$  resulting in a concentration profiles can lead to surface excess of component  $i$  as the following,

$$\Gamma_i = \frac{dN_i}{d\Omega} \Rightarrow \sum_{i=1}^{\infty} \mu_i dN_i = \sum_{i=1}^{\infty} \mu_i \Gamma_i d\Omega \quad (5.12)$$

Now substituting equation 12 into the equations (6-9) we can derive the following energy terms,

$$\begin{aligned}
(dE)_V &= TdS + \sum_{i=1}^{\infty} \mu_i \Gamma_i d\Omega + \gamma d\Omega \\
(dA)_{T,V} &= \sum_{i=1}^{\infty} \mu_i \Gamma_i d\Omega + \gamma d\Omega \\
(dG)_{T,P} &= \sum_{i=1}^{\infty} \mu_i \Gamma_i d\Omega + \gamma d\Omega
\end{aligned} \tag{5.13}$$

Where, the subscript implies the constant parameter in the system. Now, if we are to consider a single-component system i.e.  $\Gamma_i = 0$ , given that there is no significant change in density of the phase near the newly formed surface or interface. Therefore, considering equation 13 for a single-component system specific surface energies can be expressed as the following equations:

$$\begin{aligned}
\left(\frac{dE}{d\Omega}\right)_V &= TdS + \gamma d\Omega \\
\left(\frac{dA}{d\Omega}\right)_{T,V} &= \gamma d\Omega \\
\left(\frac{dG}{d\Omega}\right)_{T,P} &= \gamma d\Omega
\end{aligned} \tag{5.14}$$

Although, from equation 14 it is evident that under constant pressure, temperature, volume and entropy specific surface energy, specific surface Helmholtz energy and specific surface Gibbs free energy is not different, in general, Helmholtz free energy is preferred over the other energies in case of surface energy because pressure is more a constant parameter than volume.

Now we can consider a system where the initial condition is defined as configuration  $o$ . The term configuration refers to a state in which the droplet is at rest in a position of stable or metastable equilibrium. In the initial condition we considered an infinitesimal distance between the droplet and the surface as shown in Figure 5.1a. We assume no external body force is acting on the droplet including the gravitational force. Due to the absence of gravity the droplet will try to minimise its surface area

by forming a sphere. If  $r_0$  is the radius of the spherical droplet at the initial configuration  $o$ , then the area of the droplet can be expressed as,  $\Omega_0 = 4\pi r_0^2$ . While the system under consideration is still unaffected by the external body force, the droplet spreads spontaneously on the surface due to the work developed by the surface energy of the system. The final destination of the spreading droplet is the configuration  $\kappa$  where the droplet stops further spreading on the surface and forms a spherical dome in the liquid gas interfacial region as shown in Figure 5.1b. In the configuration  $\kappa$ , the droplet forms new interfacial areas in the liquid-solid and liquid-vapor interfaces which can be represented as  $\Omega_{sl}$  and  $\Omega_{sV}$ .

By considering equation 14, the transient variation of the Helmholtz energy of a single component system, passing from any configuration  $i$  to the configuration  $j$ ,  $\Delta A_{ij}$ , at constant volume and temperature can be expressed as the following equation,

$$\Delta A_{ij} = \Delta \sum (\gamma\Omega)_j - \Delta \sum (\gamma\Omega)_i \quad (5.15)$$

Where,  $\gamma$  is the specific surface work required to form a new surface area  $\Omega$ . Equation 15 is the representation of the ideal wetting process in the absence of gravity where the net change of Helmholtz energy during the wetting process between configuration  $o$  and  $\kappa$  is zero i.e.  $A_\kappa = A_o$ . However, in reality  $A_\kappa$  will be slightly greater than  $A_o$  because a part of the available surface energy will be lost in the form of entropy during the wetting process. For the time being we will consider the ideal model for spontaneous spreading and expanding equation 15 with respect to all the associated interface we can get the following equation,

$$\Delta A_{o\kappa} = \gamma_{lv}\Omega_{lv}^\kappa + \gamma_{sl}\Omega_{sl}^\kappa + \gamma_{sv}(\Omega_{sv}^0 - \Omega_{sv}^\kappa) - \gamma_{lv}\Omega_{lv}^o - \gamma_{sv}\Omega_{sv}^o = 0 \quad (5.16)$$

By rearranging the equation 16 and eliminating the like terms we can come up with the following equation,

$$\gamma_{sl} - \gamma_{sv} = \kappa\gamma_{lv} \quad (5.17)$$

Where,  $\kappa = \frac{\Omega_{lv}^o - \Omega_{lv}^\kappa}{\Omega_{sl}^\kappa}$  is dimensionless parameter which is independent of the size of the droplet while the droplet is unaffected by the gravity. This  $\kappa$  factor differentiate the SDACC model from Young's model given in equation 1. Young's equation is dependent on the  $\cos\theta_Y$  term which applies only to the three phase contact line of the droplet from here we cannot extract the information associated with the change in shape of the droplet. On the other hand,  $\kappa$  factor includes all the interfaces of the three dimensional system from which we can calculate the effect of gravity on the droplet profile which also effects the surface energy of the system.

Until equation 17, we have discussed about the spontaneous spreading of droplet unaffected by the gravity. Now, we will consider a new system with the initial configuration,  $G$ , where the droplet is in equilibrium condition resting on a solid and flat surface under the effect of terrestrial gravity. Due to the effect of gravity the surface tension of the droplet is no longer the only dominating force and due to the interplay between gravity and surface tension the droplet is flattened on the surface as shown in Figure 5.1c. In case of free falling condition created by parabolic flight or drop tower, theoretically there will be no effect of gravitational field on the droplet along with the surface. Now the droplet will reach a new configuration  $\kappa'$ , where the gravity is switched off due to free fall and the additional energy which flattens the drop under gravity effect will be released. As a result in  $\kappa'$  configuration the receding of the droplet takes place by the decrements of solid-liquid interfacial areas and the droplet will deformed into a sphere due to the influence of interfacial energies. Under the free fall the droplet has to perform mechanical work,  $W_m$  in order to change its shape, which can be expressed as the following equation,

$$W_m = W_p + W_s \quad (5.18)$$

Where,  $W_p$  is the work associated with the movement of the center of gravity of the droplet in the upward direction and  $W_s$  is the work necessary to move the three phase contact line of the droplet during the receding of the droplet. For a droplet with volume  $V$ , density  $\rho$  and the center of gravity  $Z_{cG}$  and  $Z_{c\kappa'}$  at the configuration  $G$  and  $\kappa'$ , respectively, the  $W_p$  and  $W_s$  can be represented by the following equations,

$$W_p = \rho V a_f (Z_{c\kappa'} - Z_{cG}) \quad (5.19)$$

$$W_s = \tau (\Omega_{sl}^{\kappa'} - \Omega_{sl}^G) \quad (5.20)$$

Where,  $a_f = +g$  is the acceleration of the particles inside the droplets under the free fall and  $\tau$  is the tension required to move three phase contact line of the droplet while receding.

Again, the mechanical work done by the droplet during the free fall can be also expressed in terms of the difference between the Helmholtz free energy of the droplet at configurations  $G$  and  $\kappa'$ . Therefore,

$$\begin{aligned} W_m &= - \Delta A \\ &= A'_{\kappa} - A_G \\ &= \gamma_{lv} (\Omega_{lv}^{\kappa'} - \Omega_{lv}^G) + \gamma_{sl} (\Omega_{sl}^{\kappa'} - \Omega_{sl}^G) + \gamma_{sv} (\Omega_{sv}^o - \Omega_{sl}^{\kappa'} - \Omega_{sv}^o + \Omega_{sl}^G) \end{aligned} \quad (5.21)$$

When the droplet will be at the equilibrium then the energy released by the droplet and the work done by the droplet will be equal. Therefore, combining equations (18-21) and rearranging the like terms we will get the following equations,

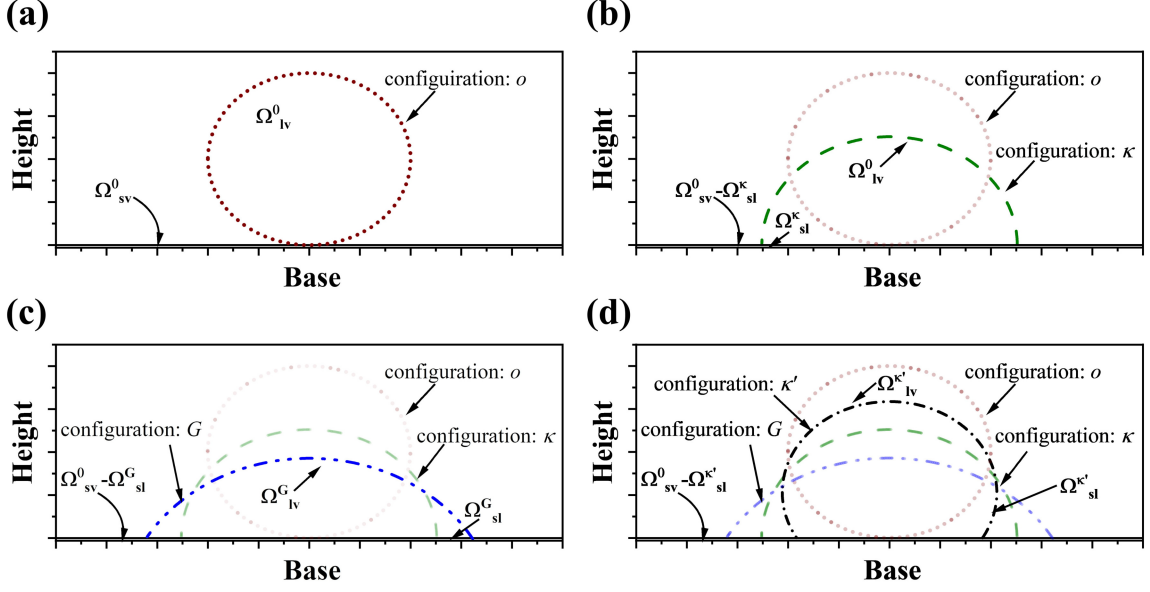


Figure 5.1: Wetting phenomenon unaffected by gravity and after switching off gravity. (a) In the absence of gravity, the spherical drop of the state  $A_o$  which (b) spontaneously spreads on the surface and reaches the state  $A_\kappa$ . By the free fall, in state  $A_G$  the energy that the terrestrial gravitational field is using to deform the droplet at (c) is released, letting the droplet reach a new equilibrium state  $A_\kappa$  only governed by the interfacial energies (d), which shape is a spherical dome.

$$(\gamma_{sl} - \gamma_{sv} + \tau)(\Omega_{sl}^{\kappa'} - \Omega_{sl}^G) = -\gamma_{lv}(\Omega_{lv}^{\kappa'} - \Omega_{lv}^G) - \rho V a_f (Z_{c\kappa'} - Z_{cG}) \quad (5.22)$$

During the dewetting process of the droplet contour due to the free fall, the droplet must do work to overcome the tension  $\tau$  to recede on the solid surface i.e. to create a new solid surface. The tension,  $\tau$  is also equivalent to the surface energy of the solid as it is associated with creating a new solid surface. Therefore, we can say that,

$$\tau = -\gamma_s \quad (5.23)$$

Now considering equations (22-23) we can write the following equation which relates all the interfacial energies with the interfacial areas, acceleration of the droplet particles at the free fall and the density of the droplet,

$$\gamma_{sl} - 2\gamma_{sv} = \frac{-\rho V a_f (Z_{ck'} - Z_{cG}) - \gamma_{lv} (\Omega_{lv}^{\kappa'} - \Omega_{lv}^G)}{(\Omega_{sl}^{\kappa'} - \Omega_{sl}^G)} \quad (5.24)$$

Equation 17 and 24 formed a system of equations solving which we can determine the surface energy of solid and surface tension at solid-liquid interface while the surface tension of the liquid, its density, and the drop volume is an input parameter. However, by combining equation 17 with the equation 24 we can also write the following equation where we can directly get the surface energy of the solid without solving the systems of equations,

$$\gamma_{sv} = \kappa \gamma_{lv} + \frac{\rho V a_f (Z_{ck'} - Z_{cG}) + \gamma_{lv} (\Omega_{lv}^{\kappa'} - \Omega_{lv}^G)}{(\Omega_{sl}^{\kappa'} - \Omega_{sl}^G)} \quad (5.25)$$

For equation 17 or 25 the  $\kappa$  factor can be calculated from the interfacial areas  $\Omega_{lv}^o$ ,  $\Omega_{lv}^{\kappa}$  and  $\Omega_{sl}^{\kappa}$ , which can be obtained by the drop volume. For equation 24 the values of interfacial areas at configuration  $G$ , corresponding to the drop resting in equilibrium under the effects of gravity, can be obtained from the very first frames of the video before starting the free fall. The drop centers of mass  $Z_{cG}$  and  $Z_{ck'}$  can also be calculated from the initial images. Before, starting solving the governing equations and performing all the measurements it is important to note that for the current SDACC model we have assumed there is a negligible difference between configurations  $\kappa$  and  $\kappa'$ . However, configuration  $\kappa$  is the idealised scenarios where the droplet spreads spontaneously that results in stable equilibrium while the configuration  $\kappa'$  represents the dewetting of the droplet under the free fall, a condition which is a metastable equilibrium but very close to stable equilibrium. Any drop shape analysis method, symmetry of a droplet is a crucial parameter. For two dimensional measurement method the wetting needs to be isotropic or other words the droplet shape should be axisymmetric, otherwise complex three dimensional analysis of the droplet geometry needs to be performed.

In order to theoretically calculate the solid-liquid and liquid-air interfacial areas the following sets of equations need to be considered [113, 152], nomenclatures of which can be found in Figure 5.2.

For spherical cap geometry as shown in Figure 5.2a, the following equations are needed to be considered:

$$R = \sqrt{h(2b - h)} \quad (5.26)$$

$$V = \frac{\pi}{6}h(3R^2 + h^2) \quad (5.27)$$

$$\Omega_{sv} = \pi(R^2 + h^2) \quad (5.28)$$

$$\Omega_{sl} = \pi R^2 \quad (5.29)$$

For the oblate spheroid as shown in Figure 5.2b, the following equations are needed to be considered,

$$R = b\sqrt{1 - (1 - \frac{h}{c})^2} \quad (5.30)$$

$$V = \frac{\pi}{3}b^2c(\frac{h}{c})^2(3 - \frac{h}{c}) \quad (5.31)$$

$$\Omega_{lv} = \pi bc\frac{b}{c} - (1 - \frac{h}{c})\sqrt{[1 + \epsilon^2(1 - \frac{h}{c})^2] +} \quad (5.32)$$

$$\frac{1}{\epsilon}(\text{arsinh}(\epsilon) - \text{arsinh}[\epsilon(1 - \frac{h}{c})]) \quad (5.33)$$

$$\Omega_{sl} = \pi b^2[1 - (1 - \frac{h}{c})^2] \quad (5.34)$$

## 5.4 Discussion

The variation of solid-liquid, solid-vapor and liquid -vapor interfacial areas of a spreading droplet from the hypothetical configuration  $o$  to configuration  $\kappa$  has been represented in Figure 5.3. This plot has been generated from the simulated results of a 20  $\mu L$  droplet spreading on a solid surface. We have considered all the formulae given

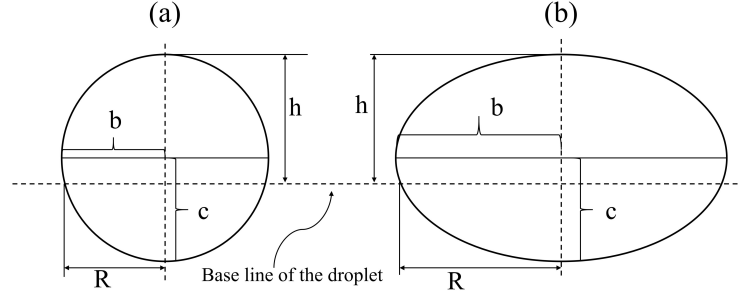


Figure 5.2: Probable droplet shape profile while the droplet is not effected by the gravity and effected by the gravity. Under the so called (a) weightlessness condition i.e. no effect of gravity the droplet will form a spheroidal shape and (b) when the droplet is affected by the gravity it will form an oblate shape.

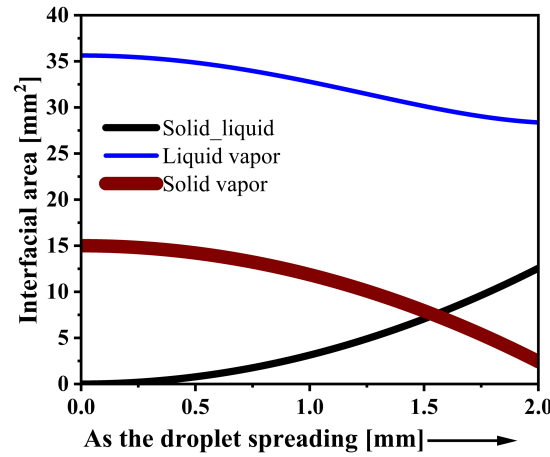


Figure 5.3: Change in interfacial areas as a function of droplet base radius, from the hypothetical configuration  $o$  to the configuration  $\kappa'$ , by assuming  $\kappa = \kappa'$ . This figure represents the change in solid-liquid, solid-vapor and liquid-vapor interfacial areas while the droplet is spreading spontaneously.

in equation 26-27. From this figure it can be seen that with the spreading of the droplet on a solid surface the solid-liquid interfacial area is increasing whereas, the liquid-vapor and solid-vapor interfacial areas are decreasing. The graphical result supports the fact that when a droplet touches a solid surface then with the expense of liquid-vapor interfacial area, the solid-vapor interfacial area has been destroyed to form the new solid-liquid interfacial areas and this process continues while the droplet spreads on the solid surface.

Figure 5.4 shows the schematic representation of the energetic changes of a sys-

tem while a drop spontaneously and ideally wets a solid surface without the effect of gravity. If our previous assumption, i.e., configuration  $\kappa = \kappa'$ , still sustains then we can quantify the idealised spontaneous wetting of the droplet without the effect of gravity. The decrements of the Helmholtz energy of the system due to the transformation of the water-air interface into the solid-water interface facilitates the idealized spontaneous wetting in the absence of gravity. The solid-air interface also contributes to building the solid-liquid interface. As mentioned earlier the spontaneous wetting process starts from configuration  $o$  and finishes at configuration  $\kappa$ . From Figure 5.4 it can also be seen that the total Helmholtz free energy of the system decreases up to a minimum threshold value and then it starts increasing. Actually, the wetting process could end at the configuration  $d'$  as indicated by the inflection point of Figure 5.4, where the Helmholtz energy between two configurations stop changing. However, while the wetting between  $o$  and  $d'$  takes place, a fraction of energy of the system is momentarily stored inside the liquid due to the morphological restructuring of the molecules. That stored energy of the system increases the internal energy of the drop, i.e.,  $A_o - A_{d'} = T\Delta S = \Delta E$ . This internal energy supply the work necessary to continue wetting from  $d'$  up to the equilibrium configuration  $\kappa$ . At the configuration  $\kappa$ , the Helmholtz energy of the system recovers the value of the initial configuration  $o$ , which implies, no work has been done on the system, nor has it done any work on its surroundings as the wetting continues from  $o$  to  $\kappa$ . However, in a real process, a part of the available surface energy will be lost in the form of entropy during wetting without the gravitational effect. Therefore,  $A_\kappa$  will be slightly smaller than  $A_o$ . This fact tells us that during the wetting process, at  $\kappa$  configuration we cannot recover the configuration  $o$ .

Now, in order to demonstrate the non dimensional number that governs the system we have non-dimensionalised the equation 25 with respect to the liquid-vapor interfacial tension,  $\gamma_{lv}$ , which gives us the following dimensionless equation,

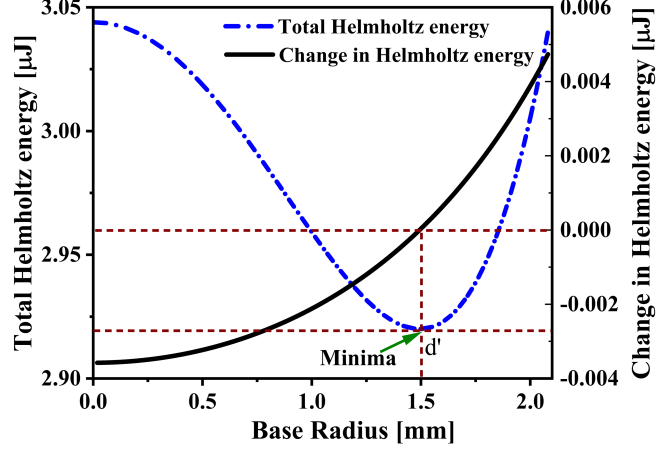


Figure 5.4: Variation of Helmholtz free energy of the system during the spontaneous wetting of droplet on a solid surface without the effect of gravity.

$$\gamma_{sv}^* = \kappa + \frac{4}{3}Bo \frac{\pi R_o(z_{c\kappa'} - z_{cG})}{\Omega_{sl}^{\kappa'} - \Omega_{sl}^G} + \frac{\Omega_{lv}^{\kappa'} - \Omega_{lv}^G}{\Omega_{sl}^{\kappa'} - \Omega_{sl}^G} \quad (5.35)$$

Where,  $\gamma_{sv}^* = \frac{\gamma_{sv}}{\gamma_{lv}}$  and  $R_o$  is the radius of the spherical droplet at the initial configuration  $o$ . In equation 28,  $\kappa$  factor is a dimensionless term which can be calculated from equation 17.  $\kappa$  resembles to but not equal to the  $\cos\theta_Y$  term of the Young's equation which is represented as a function of interfacial areas. In other words, we can say that the parameter  $\kappa$  represents the wettability of the substrate. The most important non dimensional parameter in equation 28 is the Bond number which represents the ratio of the gravitational force to surface tension force. The Bond number can be expressed by the following equation,

$$B_o = \frac{\Delta\rho g R^2}{\gamma_{lv}} \quad (5.36)$$

Where,  $\Delta\rho$  is the density difference between the liquid and the vapor,  $g$  is the gravity,  $R$  is the wetting radius and  $\gamma_{lv}$  is the liquid-vapor interfacial tension. Bond number represents the interplay between surface tension and gravitational force. Now

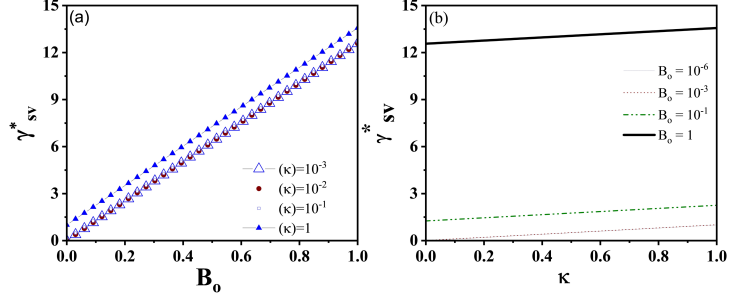


Figure 5.5: Sensitivity analysis of the non dimensional governing equation. (a) Variation of  $\gamma_{sv}^*$  as a function of  $B_o$  while the  $\kappa$  factor is varying and (b) Variation of  $\gamma_{sv}^*$  as a function of  $\kappa$  while the  $B_o$  is varying

in order to shed light on the dominance of non dimensional numbers we perform a detailed sensitivity analysis, results of which can be seen in Figure 5.5. From Figure 5.5a it can be seen that with the increasing of  $\kappa$  factor the  $\gamma_{sv}^*$  is increasing with respect to Bond number. However, negligible change is observed in  $\gamma_{sv}^*$  until  $\kappa = 10^{-1}$  and at  $\kappa = 1$  a slight change can be observed. Whereas, from Figure 5.5b, which represents the increment of  $\gamma_{sv}^*$  as a function of  $\kappa$  with respect to Bond number,  $B_o$ , we can observe that for a slight change in the order of magnitude of  $B_o$  a significant change occurs to  $\gamma_{sv}^*$ . Therefore, from Figure 5.5 it is evident that in SDAcc method the measurement of surface energy of a solid is more sensitive to the Bond number than the wettability of the substrate or other non dimensional parameter. Physically, it also makes sense as gravity is the primary concern in our theoretical model as well as the considered system.

The limitation of the application of the model presented here can be categorised into two segments such as; theoretical and experimental. The theoretical constraints regarding SDACC method is basically build upon the assumptions that we have made throughout the mathematical modeling. The equation 17 which is one of the major equations in our systems of governing equation where  $\kappa$  is a parameter considered to be independent on the drop size. However, the dependence of  $\kappa$  factor on droplet size is strongly dependent on the balance between the surface tension of the liquid

droplet and the gravity forces. Without the effect of any externally imposed body force, size of a droplet depends on two governing forces: the liquid surface tension which helps the droplet to minimise its surface area to form a sphere and the gravitational force which tends to distort that contour of the droplet curvature by flattening the droplet. The equilibrium shape of the droplet under the effect of the gravity is ensured by the balance between the surface tension and the gravity. If the volume is small enough then the surface tension will dominate by rendering the gravity effect negligible which will make the formulation of equation 24 too difficult. On the other hand, if the volume of the droplet is large enough that the gravity of the droplet will diminish the effect of surface tension by facilitating the effect of mass and viscosity of the droplet over the interfacial forces. In the extremely gravity dominant cases, the inertia of the drop initiate larger vibrations during the energy release process, which renders the droplet shape almost impossible to detect. Therefore finding an optimal volume of the droplet for surface energy measurement under reduce gravity is of greater concern. Considering the equation of Bond number, i.e., equation 29, the maximum threshold of capillary length of any liquid droplet will be increased in micro-gravity and therefore, it will give us a freedom to test larger ranges of volume.

Basically, the whole discussion on the limitation of the theoretical model with respect to the interplay between the gravitational force and surface tension can be explained from the phase plot presented in Figure 5.6. Figure 5.6a represents the variation of surface energy with respect to the Bond number and  $\kappa$  factor, which is a function the interfacial forces. From Figure 5.6a we can also observe that for a certain pairs of  $\kappa$  and  $B_o$  the mathematical model presented in equation 28 is not valid which is represented by the invalid regime because in this region the surface energy value becomes negative which is not realistic. Now Figure 5.5b is similar to Figure 5.6a , however, Figure 5.6b represents the phase plot under microgravity condition. For the microgravity phase plot there is no invalid regime. However, if we compare

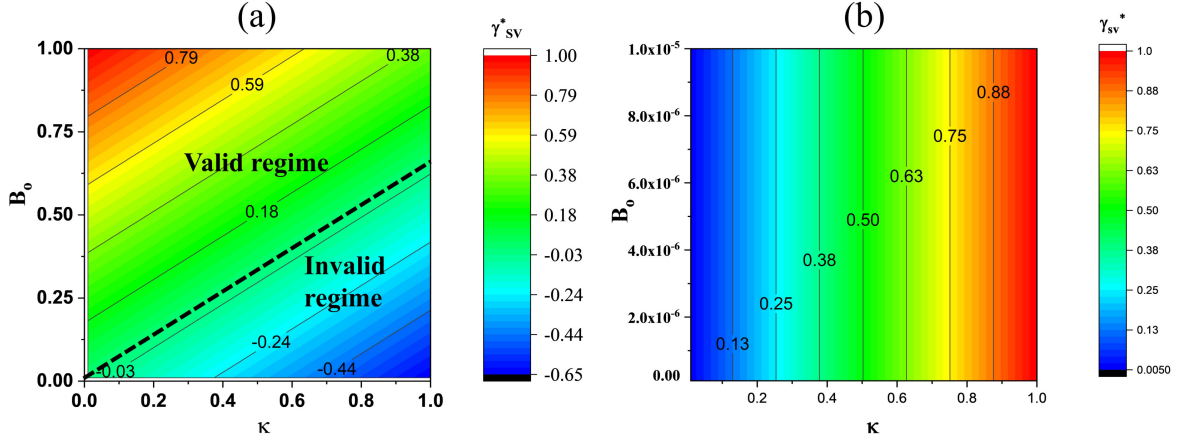


Figure 5.6: Phase plot of the non dimensional governing equation showing the variation of non dimensional surface energy with respect to  $B_o$  and  $\kappa$ . In (a) both the  $B_o$  and  $\kappa$  are restricted between 0 to 1 as beyond which there is no such physical meaning. The black dotted line separates theoretically valid region from the invalid one. Whereas, (b) represents the the interplay of surface forces and gravity forces under microgravity condition as the Bond number is constrained in microscale.

Figure 5.5a and Figure 5.5b, we can see that under the microgravity condition, for a slight change in  $\kappa$  factor the change in surface energy is higher in Figure 5.5, which clearly shows the domination of surface forces under low gravity field because as given in equation 17,  $\kappa$  is a function of interfacial forces. Therefore, besides showing the limitation of the theory the phase plot presented in Figure 5.6 also represents the validation of theory.

Again combining the discussions on the sensitivity analysis and the phase plot, it is evident that Bond number i.e. the gravity is the primary factor which effects the surface energy measurement of the substrate. In order to comment on the effect of Bond number on the droplet shape and to check the validity of the theoretical model we have also run simulations to generate various droplet shapes under different gravity conditions. Figure 5.7 shows the simulated results of droplet shape under zero gravity and hypergravity condition. For the simulation we have solved non-linear Adam-Bashforth equation [90, 153] for a sessile droplet resting on a solid

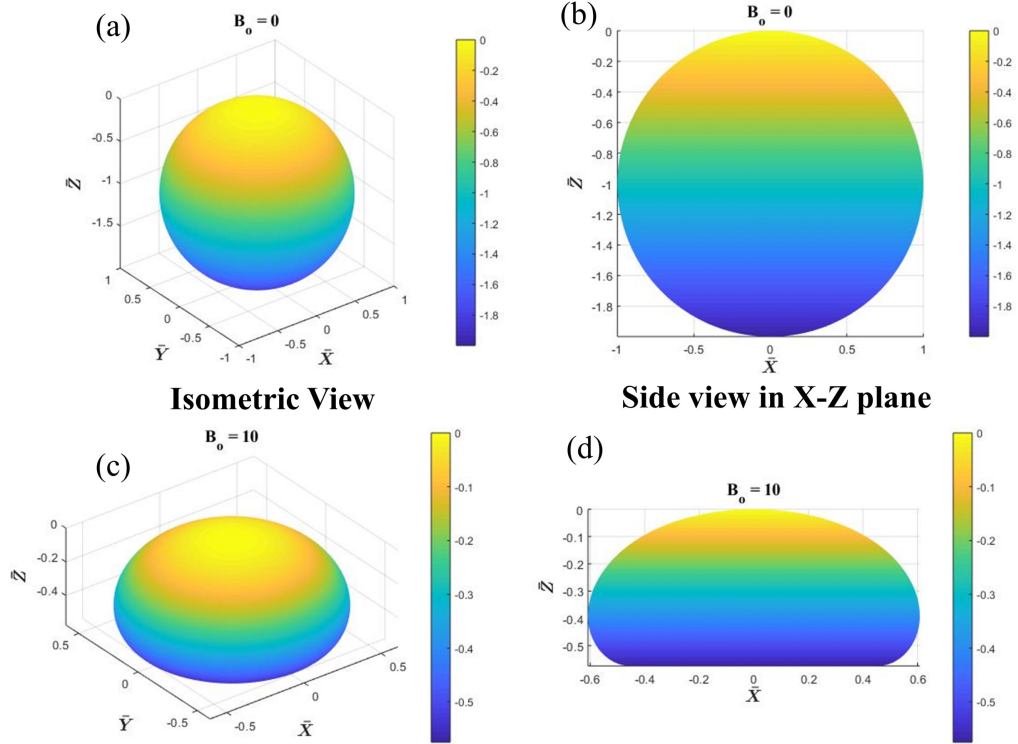


Figure 5.7: Simulated results of droplet shape under different gravity conditions. All the droplet shapes have been generated by solving the Adam-Bashforth equation through a fourth order Runge-Kutta scheme. (a) and (b) represents the isometric and side view in x-z plane of a complete spherical droplet, respectively when  $B_o = 0$ , whereas, (c) and (d) represents the isometric and side view in x-z plane of an oblate droplet when  $B_o = 10$ , respectively.

surface. A classical fourth order Runge-Kutta(RK4) method [154, 155] has been used by converting the non-linear Adam-Bashforth equation into a system of three coupled ordinary differential equations.[90] A detailed Matlab code for the numerical analysis has been provided in the Appendix. From Figure 5.7a, we can observe that at zero gravity the droplet forms a complete sphere whereas under hypergravity condition i.e.,  $B_0 = 10$ , the droplet forms an oblate shape. Due to the effect of gravity, the droplet is compressed along its height by forming an oblate spheroid. In Figure 5.7,  $\bar{X}$ ,  $\bar{Y}$ ,  $\bar{Z}$  represents the nondimensional length along the x, y and z axes, respectively.

## 5.5 Results

The major experimental constraint regarding the measurement of surface energy under reduced gravity condition is the creation of gravity less condition. According to the available literature, two methods can be found for droplet experimentation under reduced gravity condition, such as, free falling drop tower[92] and parabolic flight. [91] However, regardless of the method, the experimental prototype while free falling faces ‘g-jitter’ i.e. lateral and longitudinal vibration which makes it difficult to capture the exact moment when the droplet will be at configuration  $G$ ,  $\kappa$  or  $\kappa'$ . Hence, in order to minimise the effect of ‘g-jitter’, the high speed imaging tools have been used to ensure that the exact moment of either of the configurations have not been missed.

It is noteworthy to mention that so far, only Calvimontes [110] has investigated the surface energy measurement under reduced gravity condition while the magnitude and duration of reduced gravity were  $+0.0884g$  and  $600ms$ , respectively. However, it is always desirable to analyse the surface force driven phenomena under zero or at least micro-gravity condition. Moreover, longer duration of microgravity was also desired to attain metastable state of the drop. Again, referring to the same literature of Calvimontes; so far only the surface energy of hydrophobic surfaces has been measured with SDAcc model. Therefore in the presented study we have used parabolic flight trajectory to simulate the microgravity to ensure where the duration of  $\mu g$  was  $\approx 20s$ , which is  $\sim 30$  times higher than the time utilised by earlier study[110]. We have also measure the surface free energy for both low and high energy surfaces.

Figure 5.8 illustrates the evolution of a liquid drop’s profile on a superhydrophobic surface with low energy characteristics, as it undergoes a parabolic flight trajectory. The parabolic maneuver, akin to an elliptical arc, unfolds in a zero-gravity flight environment, comprised of three distinctive phases: the parabola pull-up ( $2g$ ), the

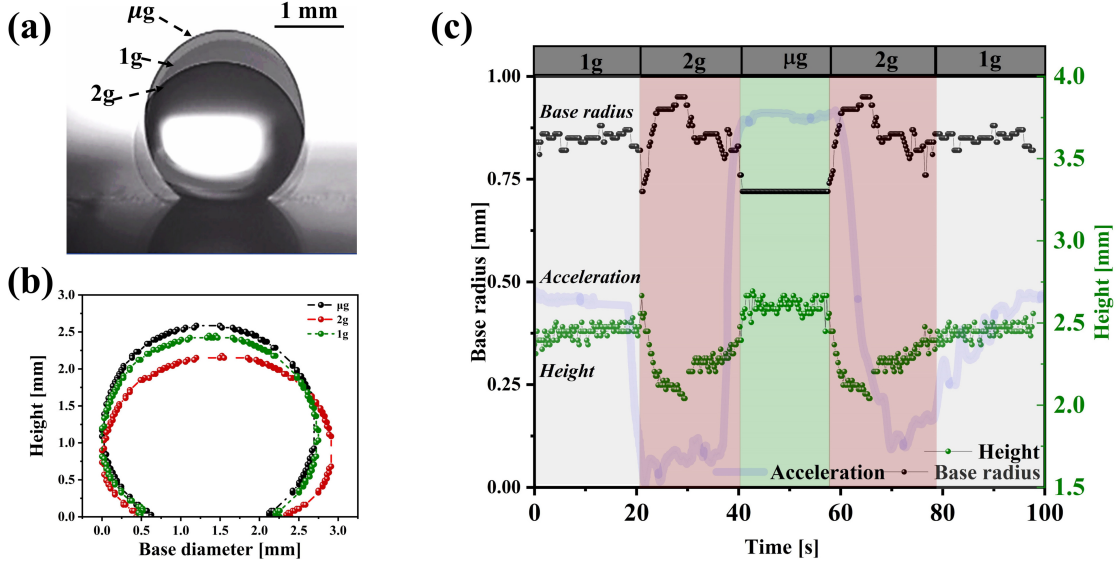


Figure 5.8: Experimental evidence of drop profile change on Superhydrophobic (chemically functionalised) copper substrate as a function of gravity. (a) Snapshot of compression of drop height as the gravity is increased, (b) Drop profile under various gravitational level where the coordinates are extracted from real images as shown in a, (c) Transient variation of base radius and drop height where the transparent lineplot shows the corresponding acceleration profile during the parabolic flight.

parabola ( $\mu g$ ), and the parabola pull-out (2g). Consequently, a drop deposited during this parabolic maneuver experiences a sequence of gravitational conditions, starting with 1g, followed by 2g,  $\mu g$ , another 2g phase, and concluding with 1g.

Within the scope of this study, we have explored three distinct metastable states of deposited drops, each corresponding to one of the following gravitational conditions: 1g, 2g, and  $\mu g$ . The findings, as depicted in Figure 5.8a and 5.8c, reveal that the drop assumes varying shapes in response to these different gravitational magnitudes. Specifically, the drop experiences compression and takes on an oblate shape under 2g conditions, leading to increased spreading on the solid surface. Conversely, under microgravity ( $\mu g$ ), the drop assumes a prolate ellipsoid or spherical form.

Figure 5.8b provides a graphical representation of the transient changes in the drop's basal radius and height, with a shaded line indicating the concurrent accelera-

tion profile. This figure effectively illustrates the synchronous variation in the drop's geometric parameters on a low-energy surface in relation to the acceleration profile. It is observed that during the hypergravity period from 20s to 40s, the basal radius or the three-phase contact line of the drop advances significantly due to the excessive hydrostatic forces acting upon the contact line. Simultaneously, the drop's height is compressed as a result of additional hydrostatic forces on the drop's contour. It is essential to note that turbulence during the hypergravity phase leads to contact line movement on the smooth, low-energy surface. Therefore, in the calculation of interfacial areas, special consideration is given to the segment of the data where there is no acceleration jitter, as evident between 30s and 33s in Figure 5.8c.

Between 40s and 60s, the drop enters a microgravity regime, and upon reaching this state, it releases energy, resulting in the retraction of its three-phase contact line and an increase in its height. This stage corresponds to the experimental configuration denoted as  $\kappa = \kappa'$ . Subsequently, from 58s to 78s, the drop returns to the hypergravity environment, where it reverts to the oblate shape. This is the configuration referred to as  $G$  in the experiment. Remarkably, it is noted that during both hypergravity conditions, the drop's shape remains consistent on the smooth, low-energy surface, as evidenced in Figure 5.8c.

Figure 5.9 presents the various metastable stages of a drop and its transient behavior in response to gravity when deposited on a hydrophilic or high-energy surface. In contrast to the low-energy surface depicted in Figure 5.8, the hydrophilic substrate results in minimal changes in the drop's base diameter relative to the significant changes in its height, as evidenced in Figure 5.9a and 5.9b. This negligible alteration in drop radius can be attributed to the phenomenon of drop pinning on the substrate. The occurrence of this pinning effect is further substantiated by the stick and slip motion observed in the drop's contact line during gravity transitions, as depicted in

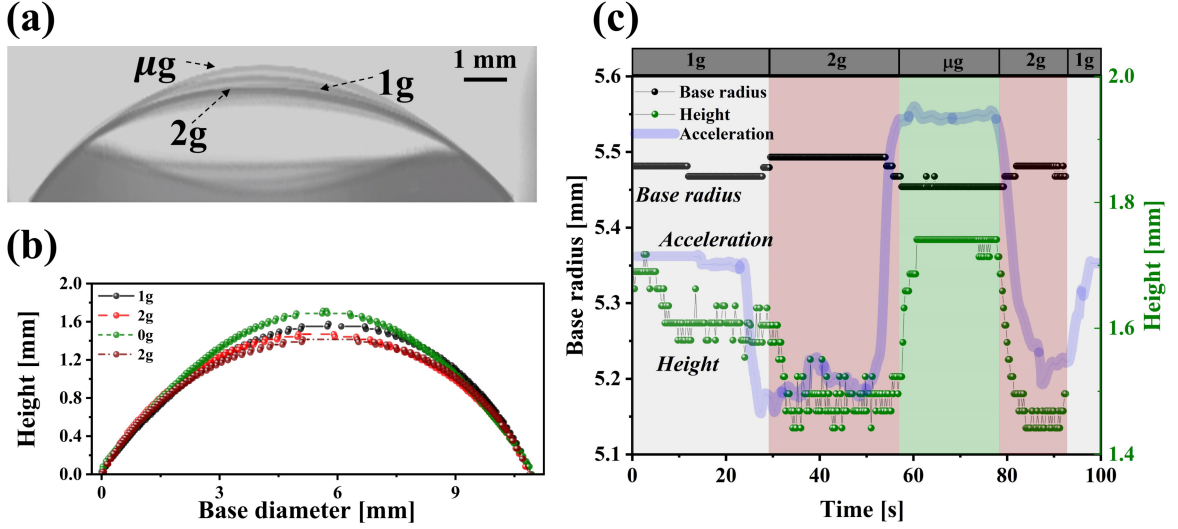


Figure 5.9: Experimental evidence of drop profile change on hydrophilic copper substrate as a function of gravity. (a) Snapshot of compression of drop height as the gravity is increased, (b) Drop profile under various gravitational level where the coordinates are extracted from real images as shown in a, (c) Transient variation of base radius and drop height where the transparent lineplot shows the corresponding acceleration profile during the parabolic flight.

Figure 5.9c. During the first hypergravity phase, spanning from 32s to 58s, the drop undergoes compression along its height due to the heightened hydrostatic pressure. Subsequently, between 60s and 80s, the drop enters a  $\mu\text{g}$  period, during which the absence of gravity and the predominance of capillary forces lead to an increase in the drop's height. The microgravity period aligns with our experimental configuration " $\kappa = \kappa''$ ", followed by the subsequent hypergravity period denoted as configuration " $G''$ ".

Figure 5.10 represents the surface free energy, calculated by solving the system of equation as shown in equation 17 and 25, which is also called SDAcc model. Later on, we have also included the established and classical model represented by OWRRK model, where we used a polar liquid drop and a nonpolar liquid drop to measure the surface free energy of solid. Form the side by side comparison in Figure 5.10, there was a negligible difference in SFE value measured by SDAcc and OWRRK model.

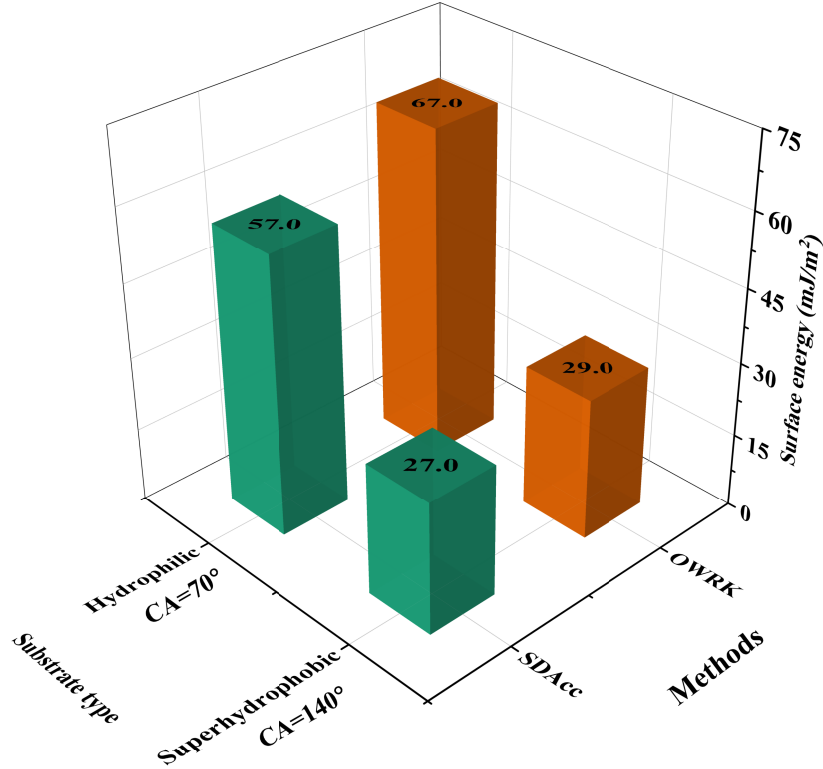


Figure 5.10: Comparison of surface free energy of solid surfaces measured by SDAcc model and classical Two component (OWRK) method.

Whereas, for low energy surface the SFE value was  $62\text{mN/m}$  and  $69\text{mN/m}$ , measured by SDAcc and OWRK model, respectively. From this it is evident SDAcc model can also successfully predicted the SFE for hydrophilic surfaces.

## 5.6 Conclusions

In this report, a mathematical model is presented for the measurement of the solid-vapor and solid-liquid interfacial energies under micro-gravity condition while the interfacial energies are function of the change in droplet contour due to the release of stored gravitational energy. The mathematical model consists of a set of governing equations, which represents the surface energy of a solid as a function of gravitational force and an unique nondimensional parameter  $\kappa$ , that makes the interfacial energies free from the apparent contact angle measurements. In contrast to the Young's model

the presented model is not dependent on the balance of bi-dimensional tensors on the three phase contact line, rather the presented model is based on the thermodynamic equilibrium of the interfaces. From the phase plot of the non dimensional governing equation of the system and from the numerical analysis, it is seen that the presented model can successfully predict the interplay between the surface tension and gravitational force under micro-gravity condition. The evaluation method of surface energies presented in this paper facilitates the possibilities for the development of new surface characterization procedures while submitting the solid-liquid-gas system into an artificially generated force fields.

## References

- [27] A. Passerone, “Twenty years of surface tension measurements in space,” *Microgravity Sci. Technol.*, vol. 23, no. 2, pp. 101–111, 2011.
- [28] A Ababneh, A Amirfazli, and J. Elliott, “Effect of gravity on the macroscopic advancing contact angle of sessile drops,” *Can. J. Chem. Eng.*, vol. 84, no. 1, pp. 39–43, 2006.
- [50] H. Fox and W. Zisman, “The spreading of liquids on low energy surfaces. i. polytetrafluoroethylene,” *Journal of Colloid Science*, vol. 5, no. 6, pp. 514–531, 1950.
- [52] S. Wu, “Calculation of interfacial tension in polymer systems,” in *Journal of Polymer Science Part C: Polymer Symposia*, Wiley Online Library, vol. 34, 1971, pp. 19–30.
- [53] C. J. van Oss, M. Chaudhury, and R. J. Good, “Monopolar surfaces,” *Advances in colloid and interface science*, vol. 28, pp. 35–64, 1987.
- [54] D. Kwok, A Leung, C. Lam, A Li, R Wu, and A. Neumann, “Low-rate dynamic contact angles on poly (methyl methacrylate) and the determination of solid surface tensions,” *Journal of colloid and interface science*, vol. 206, no. 1, pp. 44–51, 1998.
- [90] F. Bashforth and J. C. Adams, *An attempt to test the theories of capillarity*. University Press, 1883.
- [91] F. Karmali and M. Shelhamer, “The dynamics of parabolic flight: Flight characteristics and passenger percepts,” *Acta Astronaut.*, vol. 63, no. 5-6, pp. 594–602, 2008.
- [92] P. Von Kampen, U. Kaczmarczik, and H. J. Rath, “The new drop tower catapult system,” *Acta Astronaut.*, vol. 59, no. 1-5, pp. 278–283, 2006.
- [95] A. Diana, M. Castillo, D. Brutin, and T. Steinberg, “Sessile drop wettability in normal and reduced gravity,” *Microgravity Sci. Technol.*, vol. 24, no. 3, pp. 195–202, 2012.
- [97] D. Brutin, Z. Zhu, O. Rahli, J. Xie, Q. Liu, and L. Tadrist, “Sessile drop in microgravity: Creation, contact angle and interface,” *Microgravity Sci. Technol.*, vol. 21, no. 1, pp. 67–76, 2009.
- [110] A. Calvimontes, “The measurement of the surface energy of solids using a laboratory drop tower,” *NPJ Microgravity*, vol. 3, no. 1, pp. 1–14, 2017.
- [113] V. A. Lubarda and K. A. Talke, “Analysis of the equilibrium droplet shape based on an ellipsoidal droplet model,” *Langmuir*, vol. 27, no. 17, pp. 10 705–10 713, 2011.
- [142] J. L. Margrave, “Determination of thermophysical properties of liquid metals at high temperatures by levitation methods,” *Materials Science and Engineering: A*, vol. 178, no. 1-2, pp. 83–88, 1994.

- [143] A. Miiller and A Cezairliyan, “A dynamic technique for measuring surface tension at high temperatures in a microgravity environment,” *International Journal of Thermophysics*, vol. 11, no. 4, pp. 663–674, 1990.
- [144] I. Egry, G. Lohoefer, E. Schwartz, J. Szekely, and P. Neuhaus, “Surface tension measurements on liquid metals in microgravity,” *Metallurgical and Materials Transactions B*, vol. 29, no. 5, pp. 1031–1035, 1998.
- [145] H Soda, A McLean, and W. Miller, “The influence of oscillation amplitude on liquid surface tension measurements with levitated metal droplets,” *Metallurgical Transactions B*, vol. 9, no. 1, pp. 145–147, 1978.
- [146] A. Passerone, L. Liggieri, N. Rando, F. Ravera, and E. Ricci, “A new experimental method for the measurement of the interfacial tension between immiscible fluids at zero bond number,” *Journal of colloid and interface science*, vol. 146, no. 1, pp. 152–162, 1991.
- [147] V. Kovalchuk *et al.*, “Capillary pressure studies under low gravity conditions,” *Advances in colloid and interface science*, vol. 161, no. 1-2, pp. 102–114, 2010.
- [148] H. Sakai and T. Fujii, “The dependence of the apparent contact angles on gravity,” *Journal of colloid and interface science*, vol. 210, no. 1, pp. 152–156, 1999.
- [149] D. Owens and R. Wendt, *J. of applied polym*, 1969.
- [150] K.-H. Chu, R. Xiao, and E. N. Wang, “Uni-directional liquid spreading on asymmetric nanostructured surfaces,” *Nature materials*, vol. 9, no. 5, p. 413, 2010.
- [151] Y. Liu, J. Wang, and X. Zhang, “Accurate determination of the vapor-liquid-solid contact line tension and the viability of young equation,” *Scientific reports*, vol. 3, p. 2008, 2013.
- [152] G. Whyman and E. Bormashenko, “Oblate spheroid model for calculation of the shape and contact angles of heavy droplets,” *Journal of colloid and interface science*, vol. 331, no. 1, pp. 174–177, 2009.
- [153] J. Padday, “Surface and colloid science,” *Vol. I, edited by Egon Matkijevic, Pub: Wiley-Interscience*, 1969.
- [154] P. Moin, *Fundamentals of engineering numerical analysis*. Cambridge University Press, 2010.
- [155] S. C. Chapra *et al.*, *Applied numerical methods with MATLAB for engineers and scientists*. New York: McGraw-Hill, 2012.

# Chapter 6

## Geometric similarities in asymmetric droplet freezing under reduced gravity environment

### Abstract

This study investigates the asymmetric drop freezing phenomenon on cooled surfaces in microgravity, terrestrial gravity and hypergravity. This study is crucial to quantify the height of a deposited material after solidification which is an important parameter for 3D printing in space. Based on our experimental and proposed theoretical study, we show that existing symmetric drop assumption is not accurate enough to quantify the shape of an asymmetric drop. Further comparison with the existing heat transfer model and symmetric drop approach for drop freezing, reveals that our proposed two triangle model outperforms the existing model in terms of accurately predict the solidified drop height. Our experimental observation indicates that the ice to liquid water drop height ratio is always constant in terrestrial, reduced and hypergravity. Our derived expression for height ratio can successfully predict the experimental observation for both asymmetric and symmetric drop freezing scenario as well as during the freezing of molten parafin wax, volume of which is decreasing upon cooling.

## 6.1 Introduction

The need for a deeper understanding of freezing dynamics has become more pressing due to safety concerns related to ice accretion[156]. Consequently, there has been a notable increase in research on icephobic coatings with improved surface properties to tackle this issue [157–159]. Numerous studies have investigated the mechanisms underlying liquid freezing and subsequent solidification of droplets with tip formation[156, 160–162]. The theoretical investigation of the symmetric drops is well studied and corroborated with the experimental studies. But the reliability of such a theoretical model is not validated for freezing the asymmetric drop shapes, particularly with varied gravitational fields. It is confirmed by several studies [163, 164], the difference in density between the solid and liquid phases, i.e., water and ice, leads to a volumetric change, causing the freezing front to extend beyond the liquid-gas interface and resulting in the creation of what is referred to as a “pointy ice drop” [163, 164]. Despite the surface tension’s tendency to prevent pointed edges, the density contrast between the liquid and solid phases gives rise to a cusped singularity [163, 165]. The minor deviations in the tip angle can provide valuable insights into specific liquid properties, such as liquid purity [166].

Asymmetric droplet freezing is encountered more frequently in real-life applications than symmetric droplet freezing. The dynamics of drop solidification through freezing play a crucial role in numerous space-related applications, encompassing freeze drying for food preservation, 3D printing for manufacturing, and bioprinting, among others. These processes rely on the controlled solidification of droplets to achieve desired outcomes, making a comprehensive understanding of freezing dynamics essential for optimizing and advancing these applications in space environments. Thus, a generalized droplet freezing model that accommodates both symmetric and asymmetric freezing is essential. Furthermore, it is crucial to assess whether existing models,

such as the heat transfer model [160], the two-circle approach [167], and the average contact angle approach [168], can accurately predict the deformation of asymmetric droplets.

In the context of droplet freezing, the release of latent heat during front propagation plays a pivotal role in shaping the final droplet form. This is due to the relatively higher heat transfer to the cold substrate compared to the heat released into the surrounding ambient air [169]. Notably, the shape and orientation of the propagating ice front can be maneuvered by the shape of the three-phase contact line [170]. In addition to this, Starostin et al. [165] demonstrated that the shape of the frozen droplet can be controlled by modulating the heat flux at the solid base, even in the case of asymmetric droplets, where the direction of heat flux influences the tip position, preserving the tip angle’s universal behaviour.

The “two-triangle approach” was proposed, based on scaling and theoretical analysis, which successfully quantified the shapes of both symmetric and asymmetric frozen droplets. In this letter, we further elaborate on the proposed two-triangle approach. We validate the theory through an experimental analysis conducted under varying magnitudes of gravitational fields, including microgravity, martian gravity, terrestrial gravity, and hypergravity. A comparison is made between our two-triangle approach and the existing heat transfer theory and the symmetric droplet approach derived from the average contact angle theory. These approaches are assessed in terms of determining the drop height ratio, defined as the ratio between the final droplet height and the initial liquid droplet height ( $h_i/h_w$ ), and validated using experimental data. Remarkably, we observe universal behavior in the height ratio, independent of gravitational acceleration, droplet symmetry, and fluid density ratio.

## 6.2 Experimental Procedure

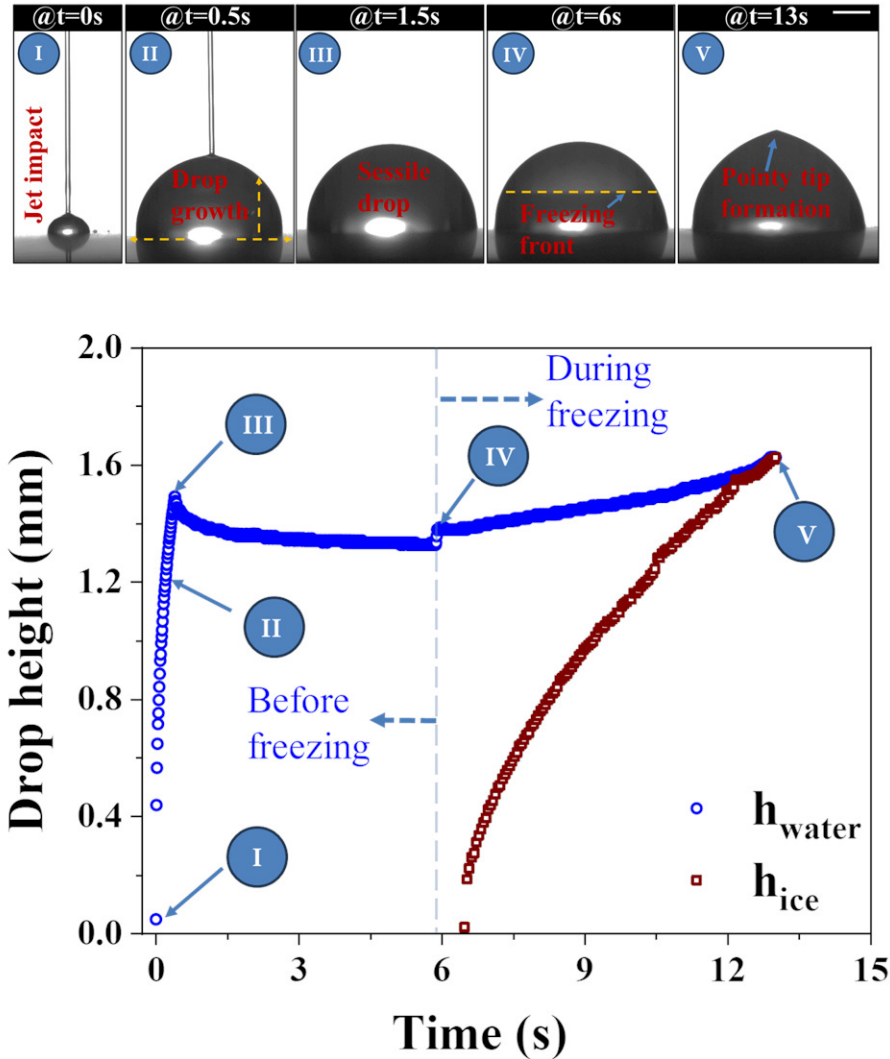


Figure 6.1: Graphical representation of drop freezing dynamics via liquid needle drop deposition techniques.

In this investigation, we conducted a comprehensive series of experiments to explore the freezing of droplets deposited on various metal substrates in Earth and microgravity. The droplets were carefully observed and analyzed from a side view, as illustrated in Figure 6.1. Employing a pressurized dosing system, we deposited water droplets of different volumes ( $3\mu\text{L}$ ,  $6\mu\text{L}$ ,  $10\mu\text{L}$ ,  $15\mu\text{L}$ , and  $20\mu\text{L}$ ) onto four distinct metal substrates (aluminum, brass, copper, and titanium). The pressurized dosing system facilitated droplet formation through a stable liquid jet, as demonstrated in

Figure 6.1. In this study, we utilized deionized water, which was degasified by removing dissolved gases using a vacuum pump. The substrates were carefully flamed and cleaned to ensure minimal contact angle hysteresis while the droplets spread. For the details of drop deposition relevant experimental setup, please refer to our previous study [101].

To ensure precise control over experimental conditions, all tests were conducted within a carefully regulated liquid-cooled temperature-controlled environment (TC40, Krüss), maintaining temperatures between  $^{\circ}\text{-5C}$  to  $^{\circ}\text{-15C}$ . After the droplet deposition, we induced asymmetry by tilting the substrate at specific angles within the range of  $^{\circ}\text{0-}^{\circ}\text{90}$ . Freezing of the droplets occurred at approximately  $^{\circ}\text{-15C}$  upon achieving the desired  $\Delta\theta$  (tilting angle).

For contact angle quantification, a maximum experimental uncertainty of  $\pm 1.5^{\circ}$  was observed, and each case underwent a minimum of three sets of experiments to ensure the repeatability of the experiment. High-speed imaging was conducted using an integrated imager with capturing frequency of  $400\text{Hz}$ . To facilitate accurate observations, we deliberately maintained a higher than usual saturation of the camera's field of view, ensuring the visualization of the solid-liquid interface of the droplets without compromising essential curvature details of spreading droplet.

Moreover, we conducted reduced gravity experiments by enclosing the entire experimental setup within a pelican case ( $47.5\text{cm}\times 47.5\text{cm}\times 47.5\text{cm}$ ). This setup was subsequently installed in a parabolic flight that simulated microgravity, Martian gravity, and hypergravity. The parabolic flight facility, provided by the Flight Research Laboratory in Ottawa, Canada, enabled the desired gravitational fields for 20-23 seconds. All the experiments performed with parabolic flights are for symmetric drops since tilting the substrate during parabolic maneuvers was an engineering challenge.

A detailed description of the parabolic flight maneuvers with relevant acceleration profiles and experimental setup can be found in our prior studies [122].

### 6.3 Theoretical Model

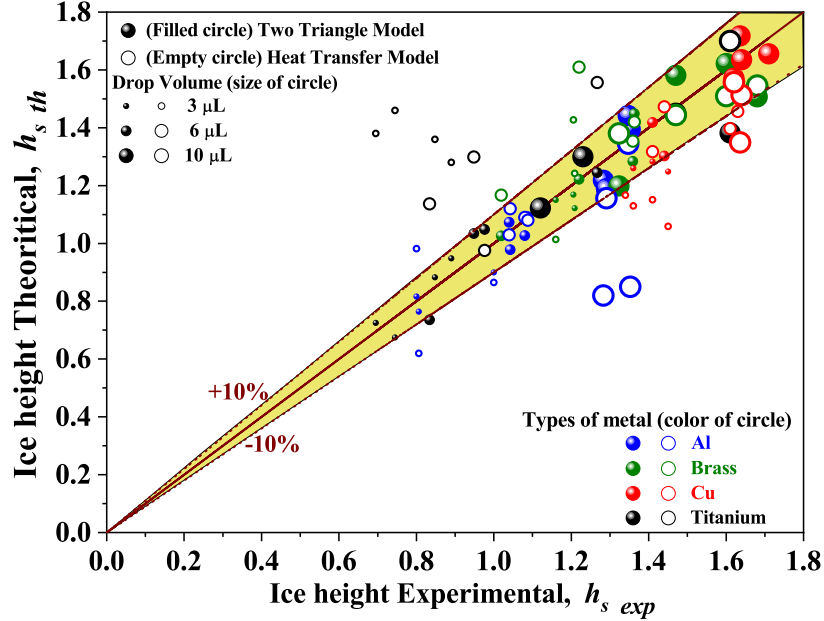


Figure 6.2: Asymmetric drop maximum height ( $h_i$ ) prediction: We compare the two triangle approach and heat transfer model with our experimental results. Filled and empty circles represent the two triangle and heat transfer approach respectively. We investigate the asymmetric drop freezing with four different metals for three different drop volume as mentioned in the figure

Our experimental evaluations in this study consistently measured the tip angle ( $2\alpha$ ) as  $130^\circ \pm 8^\circ$ , regardless of the droplet’s symmetry when frozen. To ensure generality and maintain consistency, we will adopt a fixed value of  $2\alpha = 130^\circ$  throughout this study. It is worth mentioning that the tip cone angle  $2\alpha = 130^\circ$  similar to the constant tip angle value of  $139^\circ \pm 8^\circ$ , as reported by Marin et al. [171] for symmetric droplets. The relationship suggested by Schetnikov et al [164] for density ratio and the ratio between the volumes of unfrozen and frozen liquid is used in the current study to determine the theoretical tip angle. Refer to supplementary material for

detailed explanation.

Given our consideration of asymmetric droplets due to the difference in the base contact angles, it is crucial to recognize that the shape of the three-phase contact line can not be assumed to be a circle. As described in the experimental section, this configuration was achieved with the tiled table where the larger and smaller contact angles with goniometric measurements represent the advancing receding contact angles, respectively. It is essential to note that in a typical contact angle hysteresis study, the advancing and receding angles are usually defined on the onset droplet sliding on the tilted substrate. However, in this study, to articulate the asymmetry in drop shape, we strictly avoided the sliding of the droplets; therefore, the advancing and receding contact angles defined in this study do not represent contact angle hysteresis.

It is well understood and documented that the tip angle is the function of the density ratio of the liquid and solid phases, irrespective of the drop shape[164]. This has been confirmed by the conservation mass approach, but the height of the frozen droplet necessitates the consideration of the shape of the droplets. For asymmetric droplets, it can be achieved by assuming the average contact angles also labelled as heat transfer, but this assumption deviates significantly from the experimental results. With the knowledge of liquid droplet shape and the universality in the tip cone angle, the proposed two-triangle approach predicts the height of the frozen droplets correctly, as depicted in Fig. 6.2. This compares the predictions of the two-triangle approach and the heat transfer model in determining the final height of the frozen drops. This comparative analysis encompasses four distinct metal substrates: Aluminium, Brass, Copper, and Titanium. Additionally, the study considers water droplets with volumes of  $3\mu\text{L}$ ,  $6\mu\text{L}$ , and  $10\mu\text{L}$ . We can also get the freezing time required for achieving the maximum height of any frozen water droplet using heat transfer model. Thus, if the experimental and theoretical time based on the heat transfer model is  $t_{exp}$  and

$t_{th}$  respectively we can define the non-dimensional time as  $t^* = t_{exp}/t_{th}$ , which is the abscissa of the Figure 6.2.

It can be observed that the two-triangle approach (solid symbols in Fig. 6.2) can predict the frozen droplet height within  $\pm 10\%$ , regardless of the thermal properties of the substrate and the volume of the drop corresponding to the capillary length scale. The heat transfer model prediction constitutes the thermophysical properties of the system, primarily the thermal conductivity of the substrate, and from Fig. 6.2 the model predicts well for the substrate with higher thermal conductivity within  $\pm 10\%$ . However, for substrates with lower thermal conductivity, the model fails to predict as seen for the case of 3 and 6  $\mu\text{L}$  droplets on titanium substrates.

In Figure 6.2 the Titanium has the lowest thermal conductivity and we can observe that almost all of the calculated freezing height from heat transfer model deviates more than  $\pm 30\%$ . It is noteworthy to mention that the heat transfer model only consider the thermal properties of the substrate and drops. The wetting properties such as surface energies, contact angle and other associated geometrical properties has been ignored by the heat transfer model. At lower thermal conductivity the wetting properties of the substrate dominates the freezing dynamics of the drop.

Another major comparison between two triangle approach and the heat transfer model is the quantification of freezing dynamics for an asymmetric drop. Due to the geometrical parameter considered in two-triangle approach it is possible to quantify the tip shifting from symmetric to asymmetric configuration. However, with the heat transfer model it is not possible to do so.

The two-triangle method employs the advancing contact angle, denoted as  $\theta_A$ , and the receding contact angle, denoted as  $\theta_R$ , of the asymmetric frozen droplet to gen-

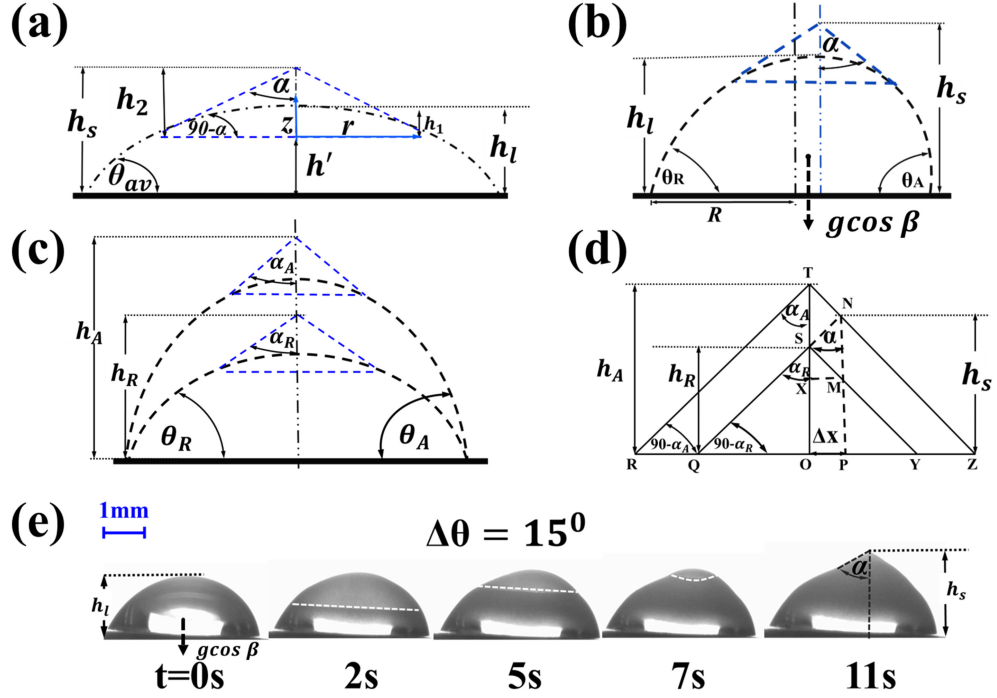


Figure 6.3: Maximum height measurement of asymmetric drop (a) Parameters involved for theoretical modeling for symmetric drop approach having initial contact angle  $\theta_{av}$ ;  $h_s$  and  $h_l$  are the maximum height of droplet in solid and liquid phase respectively,  $r$  and  $z$  are the radius and height of the solid liquid interface at any time respectively;  $h'$  is the height of frozen part at any time,  $h_1$  is the unfrozen part at that time and  $h_2$  is the final frozen part of the remaining height  $h_1$  of the droplet. (b) Asymmetric drop having different initial contact angles i.e. advancing  $\theta_A$  and receding  $\theta_R$  contact angle with universal tip angle  $2\alpha$ . (c) Two superimposed symmetric droplet having initial contact angles of the asymmetric drop i.e.  $\theta_A$  and  $\theta_R$  ( $\theta_A > \theta_R$ ). Based on this two different contact angles we find two different corresponding heights of  $h_A$  and  $h_R$  respectively but due to the tip angle universality of drop freezing we observe  $\alpha_A = \alpha_R = \alpha$ . (d) Theoretical basis of the two-triangle approach for predicting asymmetric drop parameters: the approach indicates that  $h_A < h_s < h_R$  with the assumption of  $\alpha_A = \alpha_R = \alpha$  based on the experimental observation. (e) Experimental observation of asymmetric drop freezing at different time for  $\Delta\theta = \theta_A - \theta_R = 15^\circ$ . Here, we observe the value of tip angle,  $2\alpha = 130^\circ$ . A position vector representing the center of mass of the asymmetric drop is shown in (b) and (e).

erate two isosceles triangles. Figure 6.3 illustrates these triangles, constructed with heights  $h_A$  and  $h_R$ , corresponding to the advancing and receding contact angles, respectively. The original height of the frozen asymmetric droplet is represented by  $PN$ .

By superimposing these two isosceles triangles, we can determine the height of the

asymmetric frozen droplet, denoted as  $h_s$ , and the location of the tip shift, denoted as  $\Delta X$ , from the symmetric to asymmetric droplet.

Figure 6.3(d) is the representation of two superimposed isosceles triangles based on the information from the asymmetric droplet given in Figure 6.3(b). From figure 6.3(d) we can deduce the following geometrical parameter of an asymmetric frozen droplet:

$\triangle TRZ$  and  $\triangle SQY$  are the two superimposed isosceles triangle based on the advancing and receding contact angle respectively, where normal  $TO$  connecting the tips of the both triangles.  $90 - \alpha_A$  and  $90 - \alpha_R$  are the base angles of  $\triangle TRZ$  and  $\triangle SQY$ , respectively. Height of the  $\triangle TRZ$  is  $OT = h_A$  and height of the  $\triangle SQY$  is  $OS = h_R$ . Based on the previous information the expression for tip shifting,  $OP = MX = \Delta X$  can be determined by the following equation,

$$\begin{aligned} MX &= SM \sin \alpha = \frac{h_A - h_R}{2 \cos \alpha} \sin \alpha \\ \therefore \Delta X &= \frac{h_A - h_R}{2} \tan \alpha \end{aligned} \quad (6.1)$$

Finally the expression of the height,  $h_s$  of the frozen asymmetric droplet can be derived from the following equation,

$$\begin{aligned} h_s &= PN = MN + PM = (h_A - h_R) + \frac{3}{2}h_R - \frac{1}{2}h_A \\ \therefore h_s &= \frac{h_A + h_R}{2} \end{aligned} \quad (6.2)$$

The detailed derivation of equation 6.1 and 6.2 can be found in the supplementary notes.

The solid height of the droplet can also be predicted by the heat transfer model. This model is based on parameters associated with heat and mass transfer, unlike the two-triangle approach, which comprises the geometrical parameters. The primary

assumption of the heat transfer model is the one-dimensional heat transfer process at the solid-liquid interface [160]. In this approach, both heat and mass have also been assumed to be conserved during the solidification process. This implies that there is no evaporation or addition of liquid as a result of condensation occurring during the freezing of the droplet. We assume a quasi-steady state for the heat conduction during the ice layer propagation, meaning that the amount of heat that the solid portion of the droplet releases must be equal to the latent heat released from the liquid part of the droplet during the phase change. After some simplification and integration (see the Supplementary Material for a detailed description), we can obtain the final form of the height ( $h_s$ ) of the frozen drop as a function of solid thermal conductivity ( $k$ ), solid density ( $\rho_s$ ), latent heat of the fusion  $L$ , the difference in temperature  $\Delta T$  and the freezing time ( $t$ ):

$$h_s = z = \sqrt{\frac{2k\Delta T}{\rho_s L} t} \quad (6.3)$$

Symmetrical drop theory is derived by taking the average contact angle approach, where, average contact angle  $\theta_{av} = (\theta_A + \theta_R)/2$ . Using  $\theta_{av}$ , a symmetric drop is drawn as shown in Figure 1(a). During the final stages of freezing, it is assumed that a cone shape is formed on top of the spherical cap whose volume will be filled when the remaining liquid is converted to ice [164].  $h_1$  &  $h_2$  are acquired from this conical shape.

Let  $V$  be the volume of any corresponding height  $h$ . Thus, from Figure 6.3(a) we can derive the expression of the solid-to-liquid drop volume ratio as follows:

$$\frac{V(h_l)}{V(h_s)} = \frac{V(h_l)}{V(h_l) - V(h_1) + V(h_2)} = \nu = 0.92 \quad (6.4)$$

Defining and adding all the values in Eq.6.4. We can rewrite the general form as

follows:

$$\frac{h_s}{h_l} = 1 + \left[ \sqrt[3]{\frac{\frac{1}{\nu} - 1}{(\tan\alpha)^2 - f(\alpha)(\tan\alpha)^3}} \right] \frac{f(\theta_{av})^{\frac{1}{3}}}{\tan\frac{\theta_{av}}{2}} \quad (6.5)$$

Thus, equation 6.5 is the representation of the height ratio of ice and water, indicating that  $h_s/h_l \geq 1$  for all the cases as long as  $\nu \leq 1$ .

The detailed derivation of equation 6.4 and 6.5 can be found in the supplementary note.

## 6.4 Results and discussion

For the operating condition (substrate thermal conductivity ranging from 20 to 400  $Wm^{-1}K^{-1}$ , temperature upto  $-15^\circ C$  and water drop) that we have used, we can observe an universality in the ratio of frozen drop height( $h_s$ ) to the liquid drop height( $h_l$ ), i.e.,  $h_s/h_l$ . Regardless of substrate properties and the freezing rate, the experimentally observed  $h_s/h_l$  is  $1.25 \pm 0.04$  as shown in Figure 6.4(a). From this observation it is evident that for a certain density ratio the solid to liquid height ratio always remains same.  $h_s/h_l$  calculated from two triangle approach is  $\sim 1.27$  whereas,  $h_s/h_l$  is  $\sim 1.5$  when calculated from symmetric drop approach. From this analysis we can argue that though both two triangle and symmetric drop approach can predict the freezing drop height closer to the observed height, the two triangle approach is better in predicting the frozen drop height.

In Figure 6.4(b), it is evident that the ratio  $h_s/h_l$  remains independent of the strength of the gravitational field. To achieve these results, we conducted experiments in various gravitational conditions, including microgravity, Martian gravity, terrestrial gravity, and hypergravity. The experiments were facilitated by a parabolic flight, during which we observed the freezing height ratio on a cold copper substrate.

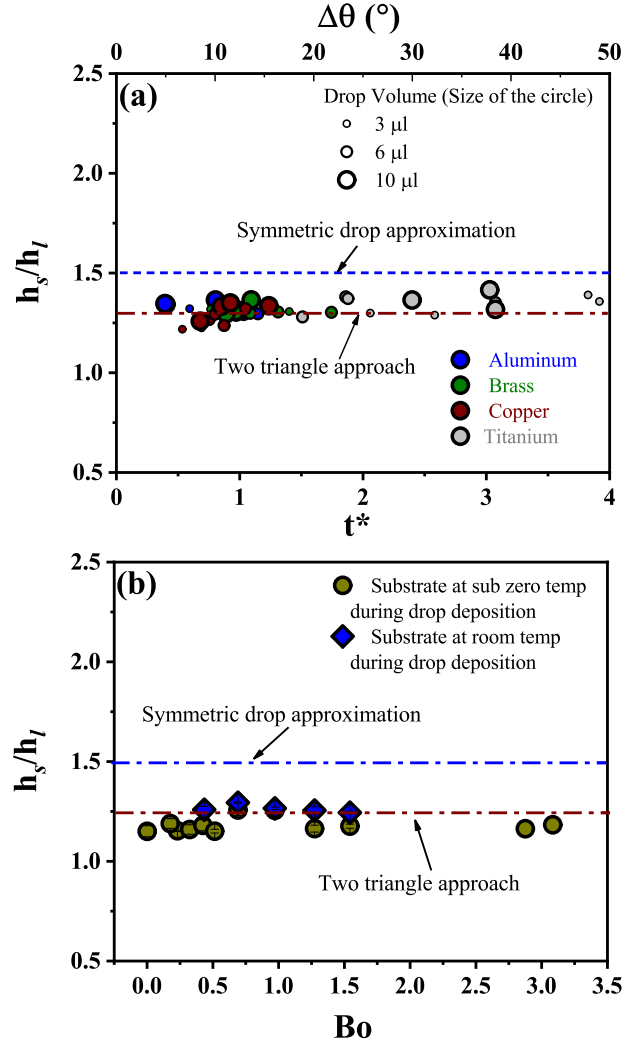


Figure 6.4: (a)Ice ( $h_s$ ) to water  $h_l$  height ratio for symmetric and asymmetric drop. For contact angle difference  $\leq 50^\circ$ , this height ratio varies within 1.2 and 1.6. We develop new theory based on the asymmetric drop assumption (average contact angle) and compare the results with two triangle one along with the experimental observations. Within our experimental range, the two triangle approach suggest the height ratio of 1.2 while new symmetric drop model suggest 1.5. (b)Ice ( $h_s$ ) to water  $h_l$  height ratio for symmetric and asymmetric drop as a function of gravitational field which can be represented by a non-dimensional Bond number.

To demonstrate the interplay between surface forces and gravitational field, we presented the height ratio as a function of the Bond number, which represents the ratio of gravitational force to surface forces. Remarkably, Figure 6.4(b) indicates that

$h_s/h_l$  remains constant regardless of the strength of gravity.

However, due to time constraints during the parabolic flight experiments, we deposited the droplet on an already cooled copper substrate at subzero temperature. Under this condition, we observed  $h_s/h_l \sim 1.2$ . In contrast, in terrestrial gravity when we deposited the drop on an already cooled substrate at subzero temperature and then initiated the freezing process, we observed a slightly different value of  $h_s/h_l \sim 1.25$ . Regardless of the specific operating conditions, it is evident from the results that the two-triangle approach effectively predicts the magnitude of  $h_s/h_l$ .

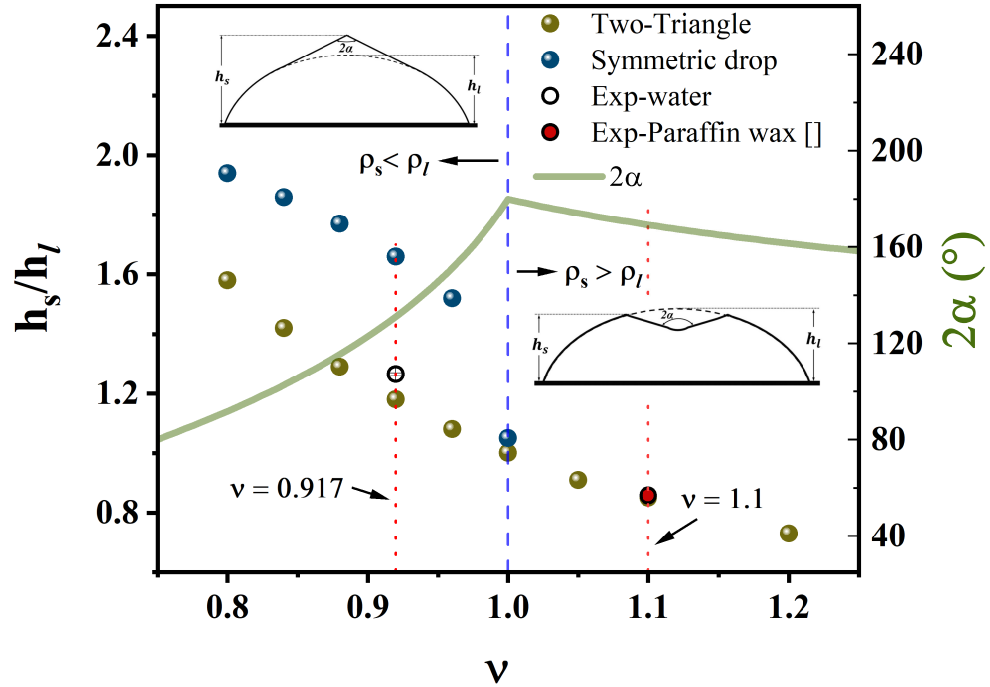


Figure 6.5: Solid-liquid height ratio for different density ratio predicted by Two-triangle and symmetric drop approach. Green line indicated the Tip cone angle for corresponding density ratios. Blue dashed line separates the plot at  $\nu = 1$  representing the symmetric drop limitation. The images inscribed in the plot shows the tip formation when  $\nu < 1$  and a cusp formation when  $\nu > 1$ . The red dotted line highlights the height ratios predicted by both the models, experimental and the respective Tip angle for the case of water.

The Figure 6.5 illustrates theoretical depiction of the non-dimensional solid-liquid height ratio of a droplet relative to its density ratio  $\nu$ , using both the two-triangle and symmetric drop approaches. From the figure it is evident that the symmetric drop model tends to overestimate the drop height ratio compared to the two-triangle approach. This discrepancy can be confirmed from the case of water ( $\nu = 0.917$ ). Both models predict that the decrease of height ratio with the increase of the density ratio. It is crucial to note that for density ratio of 1, the symmetric drop approach diverges, indicating a limitation in its applicability. To overcome this limitation, a value of  $\nu$  slightly less than one is shown in the figure. In contrast, the proposed two-triangle approach has the advantage of accurately predicting the height ratio for  $\nu \geq 1$ . The two-triangle approach provides reasonable agreement of height ratio with experimental data, especially at higher density ratios. This is confirmed for the case of paraffin wax ( $\nu = 1.1$ ), where the height ratio estimated using the two-triangle approach is compared against experimental measurements from the work of Pritam et al[172]. This highlights the predictive capability of the proposed two-triangle method in capturing droplet behavior across a wider range of density ratios.

The tip angle ( $2\alpha$ ) for different density ratios is plotted in Fig 6.5 using the relationship discussed earlier. An increasing trend in the value of  $2\alpha$  can be observed as long as  $\rho_s$  is less than  $\rho_l$ , until  $\nu$  reaches 1. However, once  $\rho_s$  surpasses  $\rho_l$ , a downward trend becomes evident. The schematic diagrams inscribed in the Fig signifies the formation of a tip when  $\nu < 1$  and a dimple when  $\nu > 1$  [163, 172]. The  $2\alpha$  for water and paraffin are 131 and 168 respectively which are in reasonable agreement with the literature [170–172]

## 6.5 Conclusion

Our research findings indicate that there is a specific value for the ratio of the height of the ice to water drop, which is approximately  $\sim 1.2$ . According to our theoretical assumption, this ratio depends solely on the contact angle and density ratio. Our

proposed two-triangle method allows us to predict the universal height ratio with an error margin of  $\pm 10\%$ . Additionally, we have demonstrated that the heat transfer model does not accurately predict frozen drop height, while the symmetric drop approach can only predict symmetric drop height. Further analysis also confirms that this universality in solid-to-liquid height ratios holds true under different levels of gravity (reduced gravity or hypergravity), as accurately predicted by our proposed two-triangle model.

## References

- [101] A. Ahmed, R. Sanedrin, T. Willers, and P. R. Waghmare, “The effect of dynamic wetting pressure on contact angle measurements,” *J. Colloid Interface Sci.*, vol. 608, pp. 1086–1093, 2022.
- [122] A. Baldygin *et al.*, “Effect of gravity on the spreading of a droplet deposited by liquid needle deposition technique,” *npj Microgravity*, vol. 9, no. 1, p. 49, 2023.
- [156] W. Kong and H. Liu, “A theory on the icing evolution of supercooled water near solid substrate,” *International Journal of Heat and Mass Transfer*, vol. 91, pp. 1217–1236, 2015.
- [157] H. Sojoudi, M. Wang, N. Boscher, G. H. McKinley, and K. K. Gleason, “Durable and scalable icephobic surfaces: Similarities and distinctions from superhydrophobic surfaces,” *Soft matter*, vol. 12, no. 7, pp. 1938–1963, 2016.
- [158] T. M. Schutzius *et al.*, “Physics of icing and rational design of surfaces with extraordinary icephobicity,” *Langmuir*, vol. 31, no. 17, pp. 4807–4821, 2015.
- [159] V. Hejazi, K. Sobolev, and M. Nosonovsky, “From superhydrophobicity to icephobicity: Forces and interaction analysis,” *Scientific reports*, vol. 3, no. 1, pp. 1–6, 2013.
- [160] D. Anderson, M. G. Worster, and S. Davis, “The case for a dynamic contact angle in containerless solidification,” *Journal of crystal growth*, vol. 163, no. 3, pp. 329–338, 1996.
- [161] J.-P. Delplanque and R. Rangel, “An improved model for droplet solidification on a flat surface,” *Journal of materials science*, vol. 32, no. 6, pp. 1519–1530, 1997.
- [162] M Stiti, G. Castanet, A Labergue, and F Lemoine, “Icing of a droplet deposited onto a subcooled surface,” *International Journal of Heat and Mass Transfer*, vol. 159, p. 120 116, 2020.
- [163] J. H. Snoeijer and P. Brunet, “Pointy ice-drops: How water freezes into a singular shape,” *American Journal of Physics*, vol. 80, no. 9, pp. 764–771, 2012.
- [164] A. Schetnikov, V. Matiunin, and V. Chernov, “Conical shape of frozen water droplets,” *American Journal of Physics*, vol. 83, no. 1, pp. 36–38, 2015.
- [165] A. Starostin, V. Strelnikov, L. A. Dombrovsky, S. Shoval, O. Gendelman, and E. Bormashenko, “Effect of asymmetric cooling of sessile droplets on orientation of the freezing tip,” *Journal of Colloid and Interface Science*, vol. 620, pp. 179–186, 2022.
- [166] F. Boulogne and A. Salonen, “Drop freezing: Fine detection of contaminants by measuring the tip angle,” *Applied Physics Letters*, vol. 116, no. 10, p. 103 701, 2020.

- [167] A. ElSherbini and A. Jacobi, “Liquid drops on vertical and inclined surfaces: Ii. a method for approximating drop shapes,” *Journal of colloid and interface science*, vol. 273, no. 2, pp. 566–575, 2004.
- [168] M. Santos, S Velasco, and J. White, “Simulation analysis of contact angles and retention forces of liquid drops on inclined surfaces,” *Langmuir*, vol. 28, no. 32, pp. 11 819–11 826, 2012.
- [169] J. E. Castillo, Y. Huang, Z. Pan, and J. A. Weibel, “Quantifying the pathways of latent heat dissipation during droplet freezing on cooled substrates,” *International Journal of Heat and Mass Transfer*, vol. 164, p. 120 608, 2021.
- [170] M. F. Ismail and P. R. Waghmare, “Universality in freezing of an asymmetric drop,” *Applied Physics Letters*, vol. 109, no. 23, p. 234 105, 2016.
- [171] A. G. Marin, O. R. Enriquez, P. Brunet, P. Colinet, and J. H. Snoeijer, “Universality of tip singularity formation in freezing water drops,” *Physical review letters*, vol. 113, no. 5, p. 054 301, 2014.
- [172] P. K. Roy, S. Shoval, N. Shvalb, L. A. Dombrovsky, O. V. Gendelman, and E. Bormashenko, “Apple-like shape of freezing paraffin wax droplets and its origin,” 2023.

# Chapter 7

## Freezing of a magnetic liquid under the effect of magnetic field

### Abstract

The study, presented here, critically investigates the solidification rate of a water-based magnetic fluid, which is responsive to magnetic field. Solidification of droplet via freezing is ubiquitous in nature and affects several aspects of our daily lives and many industrial applications. However, a little is known about a comprehensive model that can predict the freezing or solidification rate of a colloidal droplet while the freezing occurs under the influence of an external body forces other than gravity. In this study, we present a generalized governing equation to describe a magnetic droplet freezing on solid substrate. This model accounts for the strength of the actuating field, physical properties of liquid and ice (solid), in addition to the associated interfacial and surface energies and curvature of the droplet. The mathematical model formulated here is based on the mass, momentum and energy conservation equation, which eventually deduced to an equation similar to the lubrication equation accounting for the phase change and solidification velocity as a function of magnetic field strength. The solution of the governing equation via scaling analysis will offer us a mechanism to control the solidification rate of the colloidal droplet, infused with metal nanoparticles, by tuning the magnetic field strength, which we also observed experimentally. Apart from academic interest, this study is essential to freeze casting

and additive manufacturing of metallic and organic objects consisting of magnetic nanoparticles. In such processes, solidification rate of a colloidal droplet dictates the pore morphology as well as the strength of the green body.

## 7.1 Introduction

The freezing or solidification of droplets is a widely observed phenomenon with diverse industrial applications in fields such as aerospace[173], wind turbine[174], manufacturing[175], and medical science[176]. The formation of ice through drop freezing can also present significant risks to power plants[177] and the aviation industry[178]. In manufacturing, particularly in freeze casting, the rate of freezing or solidification of colloidal solutions directly influences the pore morphology and overall strength of the final products[179]. Given the widespread occurrence of this phenomenon and its relevance to various industrial applications, it is of utmost importance to comprehend and control the solidification of liquid droplets using external forces.

Researchers have conducted comprehensive studies to better understand the icing mechanism, resulting in a thorough understanding of the morphology of freezing drops and the formation of tip singularity during the freezing process of a drop [170, 171, 180, 181]. Additionally, numerous studies have focused on the functionalization of surfaces through the creation of micro/nanostructured patterns to prevent frost formation and passively control freezing time[182, 183]. However, active control of freezing dynamics through substrate treatment is not feasible as the surface structure cannot be changed while the drop is freezing. Alternatively, active manipulation of freezing can be achieved using external forces such as electric or magnetic fields. Although there have been several investigations on the morphology of drops under electromagnetic fields, only a limited number of studies have explored the active manipulation of drop freezing through electromagnetic fields, which only investigated the freezing of a static drop.

This letter explores the impact of a magnetic field on the solidification process of a water-based magnetic fluid, also referred to as a water-based ferrofluid. The ferrofluid consists of iron oxide nanoparticles dispersed in a colloidal suspension. Our investigation involves formulating a set of governing equations that enable the prediction of the dynamics involved in the simultaneous freezing and spreading of a ferrofluid droplet under the influence of a magnetic field.

Notably, the freezing dynamics of magnetic fluids combined with magnetowetting have not been adequately addressed in existing literature. Therefore, our model addresses this research gap by taking into account the strength of the magnetic field, the physical properties of the liquid and solid (ice), as well as interfacial and surface energies, and the curvature of the droplet.

Through experimental analysis, we have successfully demonstrated that our developed model accurately predicts the physics behind the freezing behavior of a deforming ferrofluid droplet when subjected to a magnetic field. This study holds significant importance in the field of freeze casting, as it provides a means to control the solidification time using a magnetic field. This capability ultimately contributes to maintaining the desired strength and pore morphology of the resulting solidified material.

## 7.2 Theoretical modelling

- The mathematical model considers a copper substrate that is uniformly cooled, as illustrated in 7.1, for the freezing of a ferrofluid droplet under the influence of a vertically oriented magnetic field. The liquid-vapor interface, representing the liquid phase of the partially solidified drop, is denoted by  $h$ , while the propagating length

of the solid-liquid interface is represented by  $s$ . The substrate on which the drop is deposited, solidified, and reaches an equilibrium contact angle,  $\theta_E$ , is maintained at a constant temperature,  $T_f$ , from the bottom side. The thickness and the thermal conductivity of the substrate is denoted by  $d_W$  and  $k_W$ , respectively .

Since the model focuses on phase change during magneto wetting, it takes into account the different physical properties of each phase present, namely, density, thermal conductivity, and heat capacity, which differ for the liquid water and solid ice phases. Furthermore, the model aims to predict both the deformation of the droplet under a magnetic field and the evolution of the freezing front. The model will be derived from the classical Navier-Stokes (N.S.) equations, which will be coupled with the physical parameters dependent on the magnetic field.

We can consider ferrofluid to be an incompressible liquid that deforms according to the conservation of mass and momentum equations, which can be described by the Navier-Stokes (N.S) equations:

$$\vec{\nabla} \cdot \vec{v} = 0 \tag{7.1}$$

$$\rho_l \left( \frac{\partial v}{\partial t} + (v \cdot \nabla)v \right) = -\nabla \rho + \eta \nabla^2 v + \mu_0 M \nabla H - \rho_l g \tag{7.2}$$

In these equations,  $\rho_l$  represents the density of the ferrofluid,  $v$  denotes the velocity,  $\eta$  stands for the ferrofluid's viscosity,  $\mu_0$  represents the magnetic permeability of free space,  $g$  is the acceleration due to gravity,  $M$  represents the magnetization of the fluid, and  $H$  represents the magnetic field. To simplify the model, we assume that the change in viscosity of the ferrofluid with respect to magnetic field is negligible.

If we consider the drop-substrate system in a hydrophilic configuration, the lubrication approximation can be applied. This approximation assumes that the base

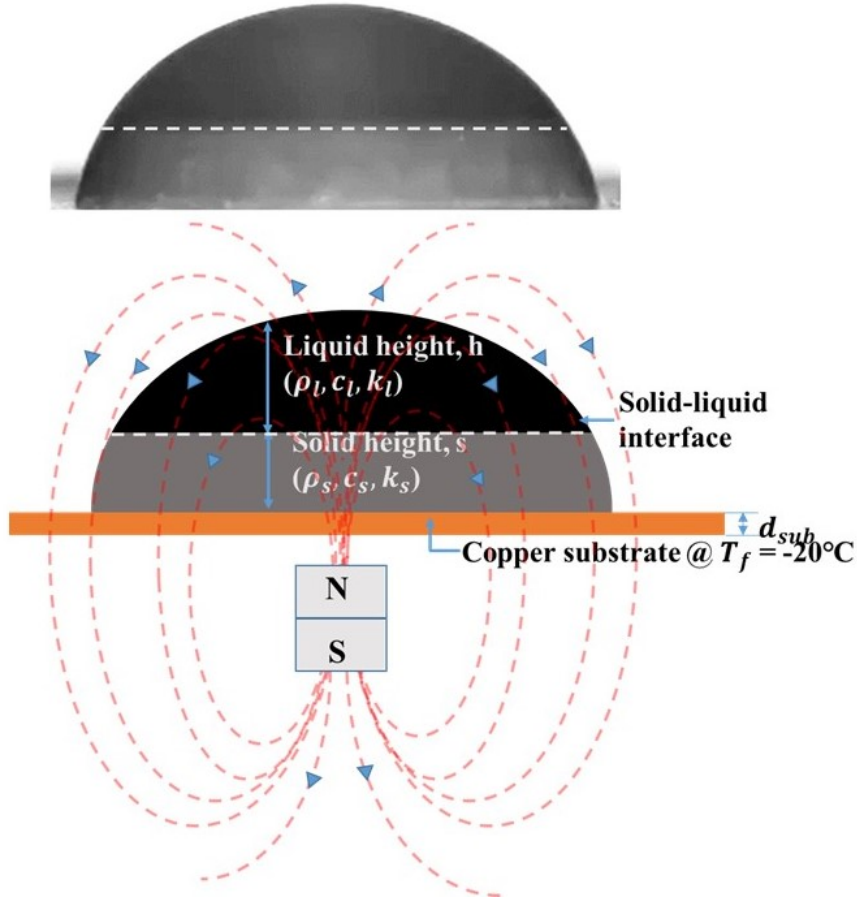


Figure 7.1: Water based ferrofluid drop freezing on a copper substrate at  $-20^{\circ}\text{C}$ . Figure (a) is the still image captured from camera sensor and figure (b) is the schematics for the notation used in the theoretical modelling.

diameter of the deposited drop ( $\sim L$ ) is much larger than the height of the same drop ( $\sim H$ ). Consequently, by defining the characteristic length scale associated with the  $x$  direction as  $L$  and the characteristic length scale associated with the  $y$  direction as  $H$ , as well as considering the characteristic velocity associated with the  $x$  and  $y$  components of velocity as  $V$ , it can be shown that the inertia term in the Navier-Stokes equation becomes negligible during a steady-state drop configuration, i.e.  $\rho_l \left( \frac{\partial v}{\partial t} + (v \cdot \nabla)v \right) = 0$ . Thus, the continuity equation and the Navier-Stokes equation can be simplified as follows[184, 185]:

$$\tilde{\nabla} \cdot u + \frac{\partial w}{\partial z} = 0 \quad (7.3)$$

$$-\tilde{\nabla} p + \eta \frac{\partial^2 u}{\partial z^2} + \mu_0 M \tilde{\nabla} H + \rho_l g = 0 \quad (7.4)$$

$$-\frac{\partial p}{\partial z} + \mu_0 M \frac{\partial H}{\partial z} = 0 \quad (7.5)$$

Where,  $\tilde{\nabla} = \left( \frac{\partial}{\partial x}, \frac{\partial}{\partial y} \right)$ .

By integrating equation 7.5 with respect to  $z$ , the expression for pressure can be derived as  $P = \mu_0 M H + C_1$ , where  $C_1$  represents the integrating constant. To determine the value of  $C_1$ , the Young-Laplace boundary condition is applied at the liquid-air interface, specifically at  $z = h + s$  where  $P = P(s + h)$ . This yields  $C_1 = P(s + h) - \mu_0 M H$ . With this comprehensive information, the pressure can now be expressed as follows:

$$P = P(s + h) \quad (7.6)$$

Now if we consider disjoining and atmospheric pressure along with the Young-Laplace pressure we can write the pressure expression as follows[181],

$$\mathbb{P} = P(s + h) = \gamma^M \kappa + P_0 - \mathbb{I} \quad (7.7)$$

Here,  $\gamma^M$  represents the effective surface tension of the magnetic liquid, which is influenced by a magnetic field.  $\kappa$  denotes the radius of curvature of the drop,  $P_0$  represents atmospheric pressure, and  $\mathbb{I}$  represents the disjoining pressure. Notably, the effective surface tension  $\gamma^M$  incorporates both the effects of the applied magnetic field and the shape factor that governs the morphology of the magnetic drop [60]. Therefore, the expression for  $\gamma^M$  encompasses both magnetic terms and the shape factor, contributing to the characterization of the magnetic drop's shape. Hence,  $\gamma^M$  can be expressed as follows:

$$\gamma^M = \gamma_{lv} \left\{ \frac{\chi}{3(1 + N\chi)Bo_m + s/2} \right\} \quad (7.8)$$

In the above equation, the magnetic Bond number, denoted as  $Bo_m$ , is a dimensionless parameter defined as the ratio of the magnetic force to the interfacial tension. It can be calculated using the formula  $Bo_m = \frac{B^2 D}{2\mu_0 \gamma_{lv}}$ , where  $B$ ,  $\chi$ ,  $\mu_0$ ,  $N$ ,  $D$ , and  $\gamma_{lv}$  represent the magnetic field, initial magnetic susceptibility of the fluid, magnetic permeability in free space, demagnetizing factor, diameter of the equivalent spherical drop, and liquid-vapor interfacial tension, respectively. The magnetic susceptibility ( $\chi$ ) can be obtained from the fluid supplier, and the constant  $\mu_0$  is defined as  $4\pi \times 10^{-7}$ . The demagnetizing factor ( $N$ ) can be determined from relevant literature sources [186, 187].

An additional parameter in equation 7.8 is the shape factor ( $s$ ), which depends on the direction of the magnetic field and the magnetic characteristics of the fluid, whether paramagnetic or diamagnetic. The shape factor describes the oblate, prolate, or spherical shape of the magnetic drop [60]. For a prolate ellipsoid ( $L > D$ ), the shape factor is given by  $s = \frac{\sin^{-1}q}{q} + k$ , while for an oblate ellipsoid ( $D > L$ ), it is given by  $\frac{\sinh^{-1}q}{q} + k$ , where  $k = D/L$  represents the aspect ratio of the drop. Here,  $q = \sqrt{1 - \frac{D^2}{L^2}}$  and  $\sqrt{\frac{D^2}{L^2} - 1}$  correspond to the eccentricity of the prolate and oblate ellipsoid, respectively [188]. In the absence of a magnetic field, it can be shown that the shape factor for a spherical drop is  $s = 2$  [60].

By substituting the pressure influenced by the magnetic field from equation 7.7 into equation 7.4 and subsequently integrating with respect to  $z$ , the following equation can be obtained,

$$-\tilde{\nabla}\mathbb{P}z + \eta \frac{\partial u}{\partial z} + \mu_0 M \tilde{\nabla} H z + \rho_l g z = C_1 \quad (7.9)$$

Integrating equation 7.9 again we will get,

$$-\tilde{\nabla}\mathbb{P} \frac{z^2}{2} + \eta u + \mu_0 M \tilde{\nabla} H \frac{z^2}{2} + \rho_l g z = C_1 + C_2 z \quad (7.10)$$

Here,  $C_1$  and  $C_2$  represent the integrating constants. At this juncture, the expression for the velocity profile can be deduced by applying the no-slip boundary condition at the liquid-air interface, specifically at  $z = 0, u = 0$  in equation 7.9. Additionally, it is also considered that there is no shear stress at the tip of the frozen droplet, i.e., at  $z = h + s, \frac{\partial u}{\partial z} = 0$  in equation 7.10.

$$u = \frac{-1}{\eta} \left[ (-\tilde{\nabla}\mathbb{P} + \mu_0 M \tilde{\nabla}H + \rho_l g) (z - s) \left( \frac{z - s}{2} - h \right) \right] \quad (7.11)$$

Now, knowing the velocity field  $u$ , it is possible to derive the expression for average velocity  $U$  over the thickness of the liquid portion,  $h$ , of the solidified droplet, i.e.,  $U = \frac{1}{h} \int_s^{s+h} u dz$ , as follows,

$$U = \frac{h^2}{3\eta} \left[ -\tilde{\nabla}\mathbb{P} + \mu_0 M \tilde{\nabla}H + \rho_l g \right] \quad (7.12)$$

With the expression of velocity field in liquid phase,  $u$ , integrating the continuity equation, i.e., equation 7.1 with respect to  $z$  from  $z = s$  to  $z = s + h$ , followed by applying the Leibniz integral rule while the integral limits are variable, we find, following equation,

$$\int_s^{s+h} \tilde{\nabla} \cdot \mathbf{u} dz = \tilde{\nabla} \cdot \int_s^{s+h} \mathbf{u} dz - \left[ u \cdot \tilde{\nabla}(h + s) \Big|_{s+h} - \mathbf{u} \cdot \tilde{\nabla}s \Big|_s \right] \quad (7.13)$$

From the definition of average velocity,  $U$  over the liquid thickness,  $h$  of a freezing drop we also know,  $\int_s^{s+h} u dz = Uh$ , and from equation 7.13 we will have,

$$\int_s^{s+h} \tilde{\nabla} \cdot \mathbf{u} dz = \tilde{\nabla} \cdot (Uh) - \left[ u \cdot \tilde{\nabla}(h + s) \Big|_{s+h} - \mathbf{u} \cdot \tilde{\nabla}s \Big|_s \right] \quad (7.14)$$

Once again considering no slip boundary condition at the liquid ice interface, i.e., at  $z = s$ ,  $u|_s = 0$  equation 7.14 can be expressed as,

$$\int_s^{s+h} \tilde{\nabla} \cdot \mathbf{u} dz = \tilde{\nabla} \cdot (Uh) - u \cdot \tilde{\nabla}(h+s) \Big|_{s+h} \quad (7.15)$$

Applying the kinematic boundary condition at the top of the droplet can be expressed as,

$$w \Big|_{s+h} = \frac{d}{dt}(h+s) = \frac{\partial}{\partial t}(h+s) + u \tilde{\nabla}(h+s) \quad (7.16)$$

Substituting equation 7.15 and 7.16 in equation 7.3 the expression for the vertical freezing front velocity,  $w|_s$  under the effect of magnetic field can be derived,

$$\frac{\partial}{\partial t}(h+s) + \tilde{\nabla} \cdot (hU) = w|_s \quad (7.17)$$

It is possible to deduce the final form of the speed of the solidification front by applying conservation of mass at the liquid-solid interface. Thus at the liquid-solid interface we can write,

$$\rho_l(v_l - v_i) \cdot n = \rho_s(v_s - v_i) \cdot n \quad (7.18)$$

In equation 7.18,  $v_l$  is the velocity of the liquid phase which has only components in  $z$  direction, i.e,  $v_l = w$  due to the no-slip boundary condition at the liquid-solid interface ( $u = v = 0$ ). On the otherhand,  $v_i = \frac{\partial s}{\partial t}$  is the freezing front velocity and we can assume the velocity of the solid phase,  $v_s = 0$ . Therefore the equation 7.18 can be simplified as follows,

$$w|_s = \left(1 - \frac{\rho_s}{\rho_l}\right) \frac{\partial s}{\partial t} \quad (7.19)$$

Finally, substituting equation 7.19 into 7.17 will give us the first governing which represents the drop deformation during the freezing under magnetic field strength,

$$\frac{\partial h}{\partial t} + \tilde{\nabla} \cdot (hU) = -\frac{\rho_s}{\rho_l} \frac{\partial s}{\partial t} \quad (7.20)$$

Where, the average velocity  $U$  of the freezing droplet is determined by the magneto-capillary action, as depicted in Equation (7.12). Notably, Equation (7.20) represents the lubrication equation associated with the magnetic field-assisted phase change of a ferrofluid droplet. In this equation, the transformation of a liquid ferrofluid droplet into a solidified state under the influence of a magnetic field is governed by the ratio of ice and liquid densities in the ferrofluid.

To incorporate the thermal effect into the model, the conservation of energy at the liquid-solid (liquid-ice) interface must be considered. During the freezing process, conduction and phase change are assumed to occur at the interface. Hence, the energy conversion equation at the liquid-ice interface can be expressed as follows:

$$\rho_l H_l v_i - k_l \nabla T = \rho_s H_s v_i - k_s \nabla T \quad (7.21)$$

In equation 7.21,  $v_i = \frac{\partial s}{\partial t}$  represents the interface velocity or the freezing front velocity. Additionally,  $k_l$  and  $k_s$  denote the thermal conductivity of the liquid and solid phases, respectively. The enthalpies at the liquid and solid phases can be defined as  $H_l = C_l T_f$  and  $H_s = C_s T_f + L_f$ , where  $C_l$  and  $C_s$  represent the specific heat of the liquid and solid phases, respectively. Moreover,  $L_f$  and  $T_f$  correspond to the latent heat of fusion and the temperature during the phase change. By substituting the values of  $v_i$ ,  $H_l$ , and  $H_s$ , the simplified form of Equation (7.21) can be expressed as follows:

$$[\rho_s L_f + (\rho_s C_s - \rho_l C_l) T_f] \frac{\partial s}{\partial t} = k_s \frac{\partial T_s}{\partial z} - k_l \frac{\partial T_l}{\partial z} \quad (7.22)$$

For water-based ferrofluid used in this study, it can be assumed that  $(\rho_s C_s - \rho_l C_l) \ll \rho_s L_f$ . This allows us to simplify Equation (7.22) by considering  $(\rho_s C_s - \rho_l C_l) \approx 0$ . To solve Equation (7.22), we need to determine the expression for each term on the right-hand side using known or measured values.

The heat flux at the liquid-ice interface ( $z = s$ ) can be considered as,

$$Q_s = -k_s \frac{\partial T_s}{\partial z} \quad (7.23)$$

Now if we consider the thermal boundary condition at the liquid-ice interface, i.e., at  $z = s$ ,

$$T_l = T_s = T_{eq} \quad (7.24)$$

where  $T_{eq}$  is the equilibrium or melting point temperature at the liquid-ice interface. In the context of freezing a ferrofluid droplet with dimensions within the capillary length scale, it is essential to account for interfacial energy and the influence of curvature deformation under a magnetic field. Considering the capillary condensation effect or the impact of confinement on the solid-liquid transition at the liquid-ice interface becomes crucial [189, 190]. This effect is captured by the Gibbs-Thomson effect at the interface. The equilibrium or melting point temperature  $T_{eq}$  at the interface, as depicted in Equation (7.24), can be expressed as follows,

$$T_l = T_s = T_{eq} = T_m \left( 1 - \frac{\gamma^M \kappa}{\rho_s L_f} \right) \quad (7.25)$$

Where  $\gamma^M$  is the effective interfacial tension under the effect of magnetic field and  $\kappa$  is the radii of the curvature at the liquid-ice interface.

However, to accurately quantify the heat flux in the solid region of a freezing droplet, it is insufficient to know only the equilibrium temperature. Additional information is needed, including the thermal resistance of the substrate ( $D_{sub}/k_{sub}$ ),

the thermal resistance of the solid ice ( $s/k_s$ ), and the thermal contact resistance  $r_c$  between the liquid and the substrate at  $z = 0$ . By considering the equilibrium temperature at the interface and incorporating the aforementioned thermal resistances, we can derive the expression for the heat flux in the solid region of the freezing droplet as follows:

$$Q_s = -k_s \frac{\partial T_s}{\partial z} = -k_s \frac{T_{eq} - T_{sub}}{D_{sub}k_s/k_{sub} + s + k_s r_c} \quad (7.26)$$

In equation 7.26,  $T_{sub}$ , is temperature at the bottom of the substrate.

We can solve the heat transfer equation to find the heat flux for the liquid phase,  $Q_l = -k_l \frac{\partial T_l}{\partial z}$ . The heat transfer equation for the liquid phase of a freezing drop can be expressed as follows:

$$\rho_l C_{pl} w_s \frac{\partial T_l}{\partial z} = k_l \frac{\partial^2 T_l}{\partial z^2} \quad (7.27)$$

Substituting the expression for  $w_s$  from equation 7.19 into equation 7.27 we can get the modified Laplace equation for the temperature field distribution inside the liquid phase as follows:

$$\frac{\rho_l C_{pl}}{k_l} \left(1 - \frac{\rho_s}{\rho_l}\right) \frac{\partial s}{\partial t} \frac{\partial T_l}{\partial z} = \frac{\partial^2 T_l}{\partial z^2} \quad (7.28)$$

It is to be noted that  $\frac{\rho_l C_{pl}}{k_l}$  can be expressed as  $1/\alpha_l$ , where  $\alpha_s$  is the thermal diffusivity of the liquid phase. If we are considering the heat transfer between the liquid and surrounding air then from the Newton's law of cooling we can write,

$$-k_l \frac{\partial T_l}{\partial z} = h_T (T - T_a) \quad (7.29)$$

Now equation 7.28 is a second order partial differential equation and hence we require two boundary conditions to solve for temperature distribution  $T_l$  in the liquid

phase. Therefore, using equation 7.24 and 7.29 as the boundary conditions for solving equation 7.28, we can find the following expression,

$$Q_l = -k_l \frac{\partial T_l}{\partial z} = \frac{-\Phi k_l h_T (T_a - T_{eq})}{h_T (e^{\Phi h} - 1) + \Phi k_l e^{\Phi h}} \quad (7.30)$$

Where,  $\Phi = \left( \frac{\rho_l - \rho_s}{\rho_l \alpha_l} \right) \frac{\partial s}{\partial t}$ .

Finally substituting equation 7.26 and 7.30 into 7.22 we can get the another expression for the freezing front velocity,

$$\rho_s L_f \frac{\partial s}{\partial t} = -k_s \frac{T_{eq} - T_{sub}}{D_{sub} k_s / k_{sub} + s + k_s r_c} - \frac{\Phi k_l h_T (T_a - T_{eq})}{h_T (e^{\Phi h} - 1) + \Phi k_l e^{\Phi h}} \quad (7.31)$$

Equation (7.31) represents the second governing equation, which incorporates the thermal effect on the freezing ferrofluid droplet under a magnetic field. By examining both Equation (7.20) and Equation (7.31), we can observe that there are two unknowns, namely  $h$  and  $s$ . These two variables are coupled non-linear partial differential equations (PDEs), requiring an extensive numerical scheme for their solution. However, solving these equations is beyond the scope of this paper. Our focus here is to establish the correlation between the magnetic field and thermal effects on the solidification of a colloidal metal solution. Therefore, in the subsequent discussion, we will elucidate the relationship between various parameters using scaling analysis.

To further simplify the mathematical analysis we can consider the droplet is symmetric in the  $X - Y$  plane. Therefore, we can write the simplified version of the equation 7.20 as follows,

$$\frac{\partial h}{\partial t} + \frac{\partial}{\partial x}(hU) = -\frac{\rho_s}{\rho_l} \frac{\partial s}{\partial t} \quad (7.32)$$

The coordinate  $x$  can be scaled by drop initial radius  $R_0$  and hence, set  $x \sim R_0$ . Similarly identifying the appropriate length scale for  $h$  and  $s$ , which is the final height of the drop after freezing,  $H_f$ , we can write  $h \sim H_f$  and  $s \sim H_f$ . So from equation 7.32 we can write,

$$\frac{H_f}{t_c} \sim \frac{\gamma^M}{3\eta}(1 - \rho^*) \quad (7.33)$$

Where,  $t_c$  is the time scale concerned with the drop deformation under magnetic field and  $\rho^* = \frac{\rho_s}{\rho_l}$ . We can also scale  $\gamma^M$  as  $\frac{\gamma_{lv} \left\{ \frac{\chi}{3(1 + N\chi)Bo_m + s/2} \right\}}{H_f}$  by considering the interface curvature  $\kappa \sim 1/H_f$ . Again rescaling the freezing height as  $H_f \sim R_0$  we can get the expression for time scale for drop deformation under lubrication approximation,

$$t_c \sim \frac{\eta R_0}{\gamma_{lv} Bo'_m (1 - \rho^*)} \quad (7.34)$$

$$\text{Where, } Bo'_m = \frac{3(1 + N\chi)Bo_m + s/2}{\chi}.$$

Again neglecting the second term in 7.31 and setting the denominator of the 1st term as the initial radius or height of the drop,  $\sim R_0$ , and  $T_{eq} - T_f \sim \Delta T$  we can get the second time scale associated with freezing,

$$t_f \sim \frac{\rho_s L_f R_0^2}{k_s \Delta T} \quad (7.35)$$

The two characteristic times are relevant since the modelling is concerned with the freezing of a (deformable) droplet, as opposed to a static object. Only  $t_f$  would have been relevant if the freezing had to be performed on a static configuration such as in the case of the Stefan problem. Therefore, we introduce  $t_{sc}$ , which combines the two time scales for the modelling of the freezing droplet and defines it as the product

between the two characteristic times as,

$$t_{sc} \sim \sqrt{\frac{\eta\rho_s L_f R_0^3}{\gamma_{lv} B o'_m (1 - \rho^*) k_s \Delta T}} \quad (7.36)$$

The equation 7.36 can also be used for overall freezing height of the drop by replacing  $R_0$  with the final freezing height  $H_f$ , which results in  $h \sim t^{2/3}$ . Rescaling  $R_0$  with the final freezing height  $h_f$  in the the equation 7.36, we can develop a relationship between the non-dimensional freezing height,  $h^* = h/h_f$  with the nondimensional freezing time,  $t^* = t/t_c$  and from which we can get the following relation,

$$h^* \sim t^{*2/3} \quad (7.37)$$

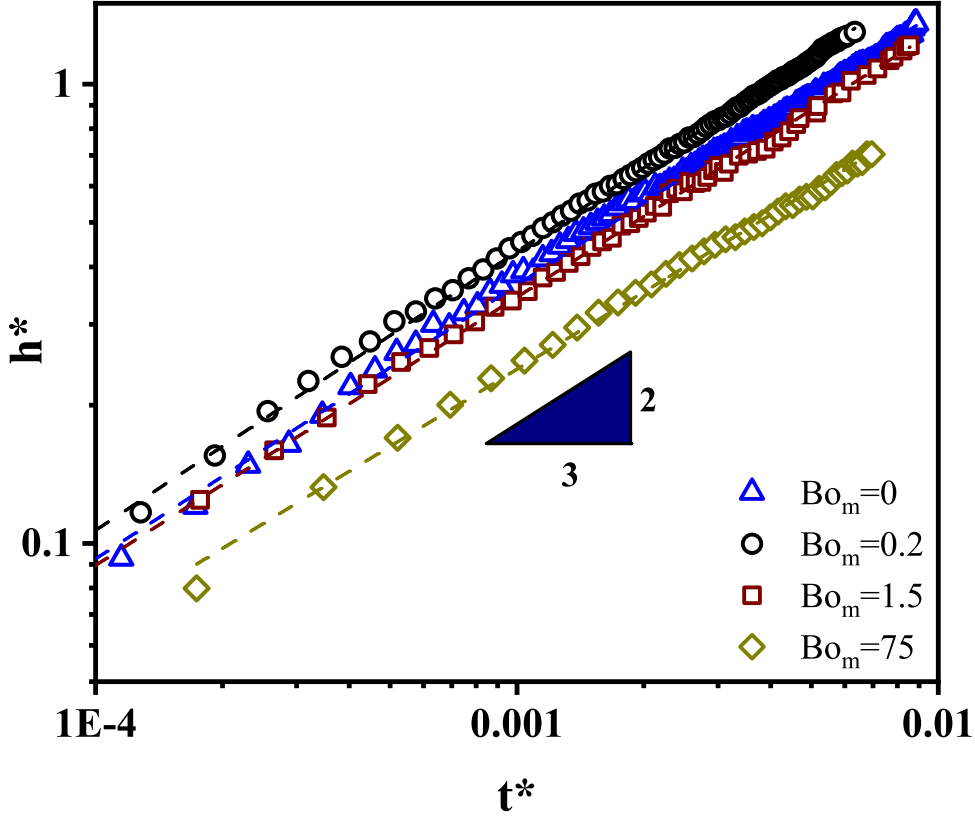


Figure 7.2: Relation between the nondimensional freezing height and the nondimensional time. The freezing height is nondimensionalised by the final freezing height whereas the freezing time is nondimensionalised by the magnetic freezing time scale.

The propagation of non dimensional freezing front height was indeed observed, in Figure 7.2, to obey the scaling law as expected from equation 7.37. The experimental

nondimensional freezing height versus nondimensional solidification time is providing an exponent of  $2/3$ , which is in good agreement with equation 7.37. The scaling law that we observed and theoretically derived is different from other studies [173] where the freezing height can be scaled as the square root of the time. It is due to the fact that the model presented here accounts for the freezing front height while the drop is deforming under the effect of magnetic field, as opposed to the scenario where a static sessile drop is freezing.

### 7.3 Results and discussion

The time scale presented in equation 7.36 justifies the physics behind the freezing of a deforming drop under magnetic field as it involves both magnetoviscous capillary time scale,  $t_c$  shown in equation 7.34, and the time scale associated with freezing,  $t_f$ , as shown in equation 7.35.  $t_c$  accounts for the deformation of a droplet due to magnetowetting whereas  $t_f$  accounts for the propagation of freezing front of a deforming drop. It is to be noted that by scaling, during magnetowetting the freezing of a drop does not directly follow Stefan problem, rather part of it follows lubrication approximation,  $h_f \sim t_c[\gamma v / B\sigma'_m(1 - \rho^*)]$ , whereas other part of it follows the Stefan case,  $h_f \sim t_f^{1/2}[k_s \Delta t / (\rho_s L_f)]$ . Therefore, we can argue the time scale we developed here justifies the experimental results that can be observed from figure 7.2. For a millimetric drop deformation under the magnetic field strength of  $\sim 500mT$  and the temperature difference of  $20K$ , the typical duration of freezing of a ferrofluid drop,  $t_{sc}$ , which can be evaluated from equation is of the order of  $1 - 9ms$ , with good agreement with total solidification time that we observed from our experiment.

By carefully rearranging the parameters in equation 7.36, we can also perform a nondimensional analysis. From the equation 7.36 we can deduce that the total solidification time,  $t_{f,total}$ , for a deforming ferrofluid drop under magnetic field is inversely

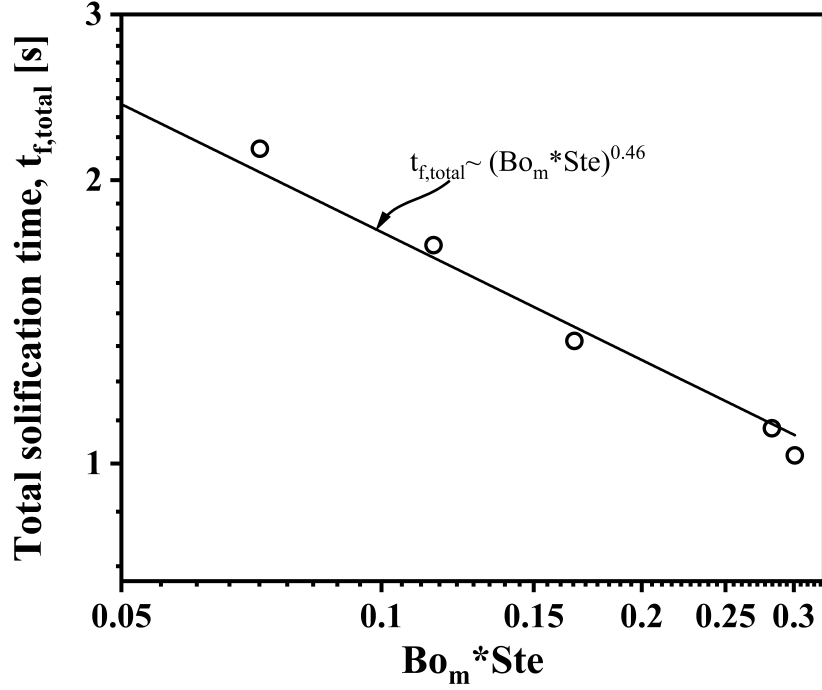


Figure 7.3: Freezing time vs magnetic Bond number

proportional to the square root of the product of effective magnetic Bond number,  $Bo'_m$  and the Stefan Number,  $Ste$ , i.e.,

$$t_{f,total} \propto (Bo'_m Ste)^{-0.5} \quad (7.38)$$

We also observe this inversely proportional relationship during our experiment, which is reported in figure 7.3. Again, we claim that the data are fairly well described by the relationship deduced in equation 7.38. The exponent found from the linear fit in log-log plot presented in figure 7.3 is  $-0.46 \pm 0.04$ , which is in good agreement with the equation 7.38, which predicts  $-0.5$  for this exponent.

Again paying a careful attention to the equation 7.36, we can deduce a linear but inversely proportional relationship between total solidification time and the particle concentration, which is also a linear function of ferrofluid density,  $t_{f,total} \sim \rho^*$ . This relationship is also valid as observed from experimental data presented in figure 7.4, which also depicts a linear relationship with a negative slope between the  $t_{f,total}$  and

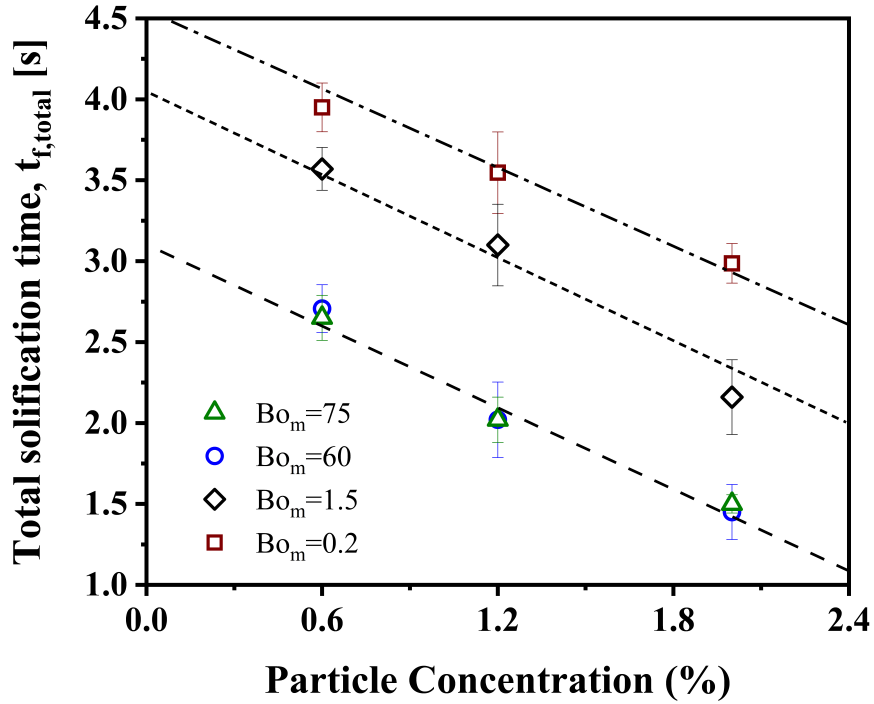


Figure 7.4: Response of concentration of particles to the applies magnetic field strength.

$\rho^*$ . When ferrofluid with higher concentration of iron nanoparticles is in a certain magnetic field then it solidified faster than the ferrofluid with lower concentration under a same magnetic field strength. Higher particle concentration ensures more spreading under a magnetic field which results in lower height of the drop, so does the directional solidification time along the drop height.

## 7.4 Conclusion

In conclusion, this study has provided valuable insights into the role of magnetic fields in the freezing dynamics of colloidal solutions. We have successfully deduced the magnetic field-assisted freezing time scale, shedding light on the critical parameters that influence the solidification process. One of the key findings of our research is the ability to control the total solidification time through the manipulation of magnetic fields. By increasing the strength of the magnetic field, we can significantly reduce the

rate at which the material undergoes solidification and vice-versa is also true. This control opens up new possibilities for tailoring the properties of solidified materials in various applications. Furthermore, our investigation has revealed a compelling relationship between freezing height ( $h_f$ ) and time ( $t$ ), characterized by  $h_f \sim t^{2/3}$ . This power-law scaling offers a fundamental understanding of how freezing height evolves over time in the presence of magnetic fields, providing a basis for predicting and optimizing the freezing process. Lastly, we have explored the solidification rate as a function of particle concentration and magnetic field strength. This analysis has unveiled the intricate interplay between these parameters and their impact on the rate of solidification. Such insights are critical for the precise engineering of materials with desired properties, particularly in applications where control over solidification is paramount. These findings have the potential to advance various fields, from materials science to additive manufacturing, by offering innovative methods for controlling and optimizing the solidification of colloidal solutions.

## References

- [60] A. Ahmed, B. A. Fleck, and P. R. Waghmare, “Maximum spreading of a ferrofluid droplet under the effect of magnetic field,” *Phys. Fluids*, vol. 30, no. 7, p. 077102, 2018.
- [170] M. F. Ismail and P. R. Waghmare, “Universality in freezing of an asymmetric drop,” *Applied Physics Letters*, vol. 109, no. 23, p. 234105, 2016.
- [171] A. G. Marin, O. R. Enriquez, P. Brunet, P. Colinet, and J. H. Snoeijer, “Universality of tip singularity formation in freezing water drops,” *Physical review letters*, vol. 113, no. 5, p. 054301, 2014.
- [173] H. Zhang *et al.*, “Active control of the freezing process of a ferrofluid droplet with magnetic fields,” *Applied Thermal Engineering*, vol. 176, p. 115444, 2020.
- [174] N Dalili, A. Edrisy, and R. Carriveau, “A review of surface engineering issues critical to wind turbine performance,” *Renewable and Sustainable energy reviews*, vol. 13, no. 2, pp. 428–438, 2009.
- [175] K. P. Cooper, “Layered manufacturing: Challenges and opportunities,” *MRS Online Proceedings Library (OPL)*, vol. 758, pp. LL1–4, 2002.
- [176] M. B. Adali, A. A. Barresi, G. Boccardo, and R. Pisano, “Spray freeze-drying as a solution to continuous manufacturing of pharmaceutical products in bulk,” *Processes*, vol. 8, no. 6, p. 709, 2020.
- [177] K. Mensah and J. M. Choi, “Review of technologies for snow melting systems,” *Journal of Mechanical Science and Technology*, vol. 29, no. 12, pp. 5507–5521, 2015.
- [178] F. T. Lynch and A. Khodadoust, “Effects of ice accretions on aircraft aerodynamics,” *Progress in Aerospace Sciences*, vol. 37, no. 8, pp. 669–767, 2001.
- [179] S. Deville, “Freeze-casting of porous ceramics: A review of current achievements and issues,” *Advanced Engineering Materials*, vol. 10, no. 3, pp. 155–169, 2008.
- [180] S. Jung, M. K. Tiwari, N. V. Doan, and D. Poulikakos, “Mechanism of supercooled droplet freezing on surfaces,” *Nature communications*, vol. 3, no. 1, pp. 1–8, 2012.
- [181] M. Tembely and A. Dolatabadi, “A comprehensive model for predicting droplet freezing features on a cold substrate,” *Journal of Fluid Mechanics*, vol. 859, pp. 566–585, 2019.
- [182] L. Mishchenko, B. Hatton, V. Bahadur, J. A. Taylor, T. Krupenkin, and J. Aizenberg, “Design of ice-free nanostructured surfaces based on repulsion of impacting water droplets,” *ACS nano*, vol. 4, no. 12, pp. 7699–7707, 2010.
- [183] P. Hao, C. Lv, and X. Zhang, “Freezing of sessile water droplets on surfaces with various roughness and wettability,” *Applied physics letters*, vol. 104, no. 16, p. 161609, 2014.

- [184] A. Oron, S. H. Davis, and S. G. Bankoff, “Long-scale evolution of thin liquid films,” *Reviews of modern physics*, vol. 69, no. 3, p. 931, 1997.
- [185] Y. A. Cengel, *Fluid mechanics*. Tata McGraw-Hill Education, 2010.
- [186] K. M. Krishnan, *Fundamentals and applications of magnetic materials*. Oxford University Press, 2016.
- [187] J. Osborn, “Demagnetizing factors of the general ellipsoid,” *Physical review*, vol. 67, no. 11-12, p. 351, 1945.
- [188] G. J. Tee, “Surface area of ellipsoid segment,” Department of Mathematics, The University of Auckland, New Zealand, Tech. Rep., 2005.
- [189] H. K. Christenson, “Confinement effects on freezing and melting,” *Journal of Physics: Condensed Matter*, vol. 13, no. 11, R95, 2001.
- [190] C Alba-Simionesco *et al.*, “Effects of confinement on freezing and melting,” *Journal of Physics: Condensed Matter*, vol. 18, no. 6, R15, 2006.

# Chapter 8

## Conclusions, Recommendations, & Future Work

### 8.1 Concluding remarks

This thesis introduced a jet-based material delivery technique for 3D printing in microgravity settings. The research presented in this thesis delves into the impact of capillary-driven phenomena on three fundamental phases of 3D printing in microgravity: material delivery, multilayer mass addition, and solidification. Furthermore, the analysis provided in this thesis offers insights for optimizing the parameters related to jet-based 3D printing, ensuring the successful printing of desired materials in microgravity without jeopardizing structural integrity. The following conclusions can be drawn from this thesis:

- Our jet-based material delivery technique has been confirmed as the ideal method for delivering liquid or ink-based materials in microgravity conditions. We have successfully validated this technique through numerous 20-second microgravity phases achieved during parabolic flights, totalling 165 parabolas, all with a one hundred percent success rate.
- Furthermore, we have illustrated that the influence of dynamic wetting pressure is negligible on the proposed jet-based material delivery technique, thereby guaranteeing a material delivery process unaffected by external forces. This

method ensures that in a microgravity environment, the ultimate destination of the deposited material is the printer bed.

- In this research presented in this thesis, we have conducted a comprehensive investigation into the dynamics of jet breakup as a function of gravity. This analysis has the potential to significantly improve the optimization of jetting parameters for space-based 3D printing processes, effectively mitigating issues such as liquid splashing and the formation of bubbles within the deposited material due to jet breakup phenomena. Our experimental observations have revealed that the jet breaks at a slower rate in reduced gravity conditions. Additionally, our findings have unveiled a critical non-dimensional jet breakup length that exhibits an inverse relationship with the Bond number and a proportional variation with the Froude number, represented as  $L_b/a \sim Fr^{0.7}$ . Furthermore, we have developed a mathematical model that provides insights into the jetting regime, highlighting that drops generated as a consequence of jet breakup are larger in size in reduced gravity conditions. This model demonstrates its capacity to predict the size of drop diameter upon jet breakup with a remarkable degree of accuracy, within a margin of error of  $\pm 10\%$ .
- To measure the extent of material spreading on a printer bed and the gap between two successive depositions, we have introduced a theoretical model grounded in the overall energy balance equation. This model takes into consideration viscous, surface, inertial, and gravitational forces. Notably, this model effectively forecasts the transient variations in the spread of deposited material on a substrate. From this investigation, we can conclude that under reduced gravity conditions, deposited liquid exhibits less spreading compared to terrestrial gravity.
- Our proposed sessile drop accelerometry model demonstrates the capability to accurately predict the surface energy of a solid using just a single drop.

This advancement eliminates the need for using toxic nonpolar liquids like Diiodomethane in microgravity conditions, which contrasts with conventional methods for measuring solid surface energy, such as the FOWKES and OWRK methods.

- During our examination of material solidification, we introduced a theoretical method for gauging the height of the solidified material. This "two triangle approach" not only provides an accurate prediction of drop height but also unveils the universality of the solid-to-liquid height ratio, approximately  $\sim 1.27$ . Significantly, the accuracy of this model surpasses that of contemporary methods like heat transfer and average contact angle techniques. Notably, this model reveals a universal behavior in the height ratio that remains independent of gravitational acceleration, drop symmetry, and fluid density ratio.
- Finally, to showcase the feasibility of metal 3D printing using colloidal metal solutions, we conducted an examination of the freezing dynamics of a colloidal solution containing magnetically responsive particles. Our findings indicate that we can control the freezing time by adjusting the magnetic field strength and particle concentration. Both theoretical and experimental evidence supports the conclusion that higher magnetic field strength and increased particle concentration lead to a quicker solidification of the deposited material..

## 8.2 Future work and recommendations

Based on the outcomes presented in this thesis, we have successfully demonstrated the feasibility of material deposition using a jet-based deposition system in a microgravity environment. This study has provided insights into calculating parameters such as the nozzle-to-printer bed distance, nozzle or substrate movement during multilayer mass addition, and the influence of printer bed surface properties on deposited material. Furthermore, we have illustrated how external forces like gravitational and magnetic

forces can be used to manipulate the solidification of deposited material.

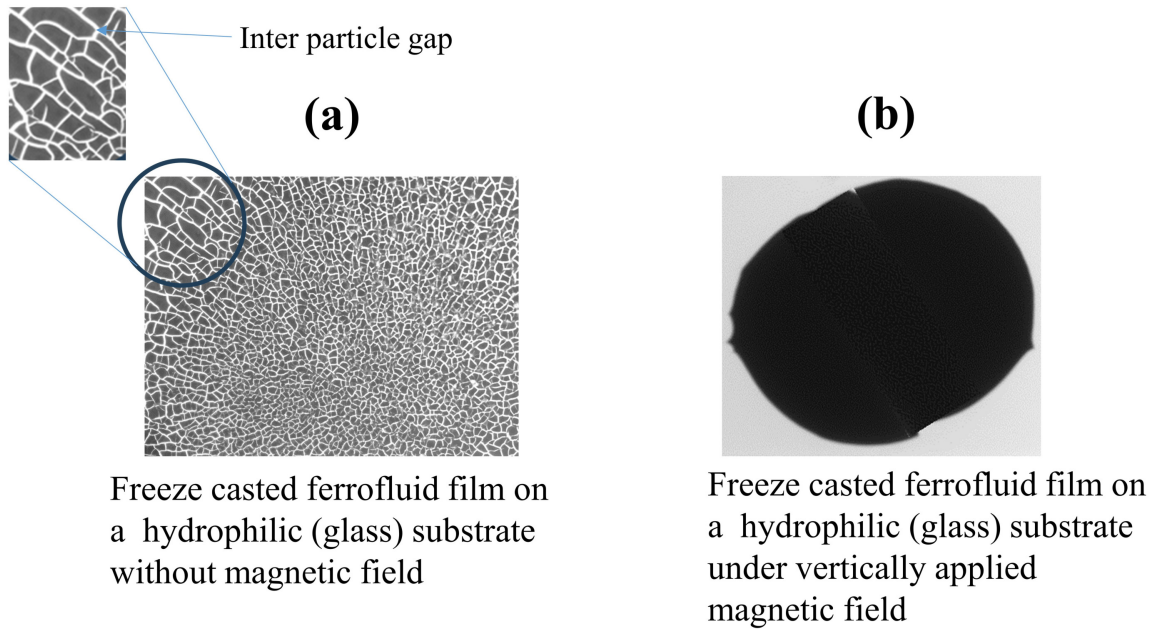


Figure 8.1: Effect of magnetic field on the interparticle spacing of a freeze dried ferrofluid film. (a) A ferrofluid film (with a solid loading of 6%) deposited on a glass substrate in the absence of a magnetic field, and (b) a ferrofluid film (6% solid loading) deposited on a glass substrate subjected to a vertically applied magnetic field of  $150mT$

Moreover, we have scrutinized the impact of a magnetic field on the internal structure of a solidified metallic entity derived from a deposited substance subsequent to the process of freeze casting. Figure 8.1 illustrates an amplified depiction of a solidified ferrofluid film post freeze casting, with the material deposited on a hydrophilic glass substrate. In Figure 8.1a, a detailed view of a ferrofluid droplet (with a solid loading of 6%) on a glass substrate is presented in the absence of a magnetic field. Conversely, Figure 8.1b exhibits a magnified view of a ferrofluid droplet (6% solid loading) on a glass substrate subjected to a vertically applied magnetic field of  $150mT$ . Analysis of Figure 8.1 reveals that in the absence of a magnetic field, particles exhibit a lack of interconnection, resulting in a noticeable increase in interparticle spacing. This larger interparticle gap can be ascribed to both the low concentration of iron parti-

cles and the limited presence of binder elements within the ferrofluid. Conversely, in the presence of a magnetic field, the absence of interparticle gaps is evident, ensuring the internal cohesion and strength of the solidified structure. Given these findings, we propose further investigation into the synergistic influence of particle loading and various binder materials in conjunction with the impact of a magnetic field on the three-dimensional (3D) printing of metallic objects in microgravity conditions.

While this thesis comprehensively covered the fundamentals of all stages associated with 3D printing in reduced gravity, it is worth noting that the heat treatment or curing process of a freeze-casted material in microgravity remains unexplored in this thesis. We were able to 3D print a iron dome with our proposed method of metal 3D printing with freeze casting as shown in Figure 8.2a . However, the obtained sample was so brittle, as shown in Figure 8.2b, as the proper heat-treatment process was not utilised. Therefore, future research efforts should prioritize the study of curing freeze-casted materials in a microgravity environment. Subsequently, after curing the freeze-casted object, the primary objectives should include characterizing the printed object through compression and tensile testing, as well as investigating the internal structure of the object using scanning electron microscopy (SEM) techniques.



Figure 8.2: (a) Freeze casted iron dome (b) Freeze casted object shattered into pieces due to the lack of heat treatment.

Building upon this understanding of surface tension-driven phenomena in 3D print-

ing processes under reduced gravity conditions, the next crucial step should involve the development of a miniaturized freeze casting system integrated with a freeze dryer, the current deposition unit, and a furnace unit for curing. A 3D design of a deposition unit with XYZ traverse system with a thermal unit is shown in the Figure 8.3.

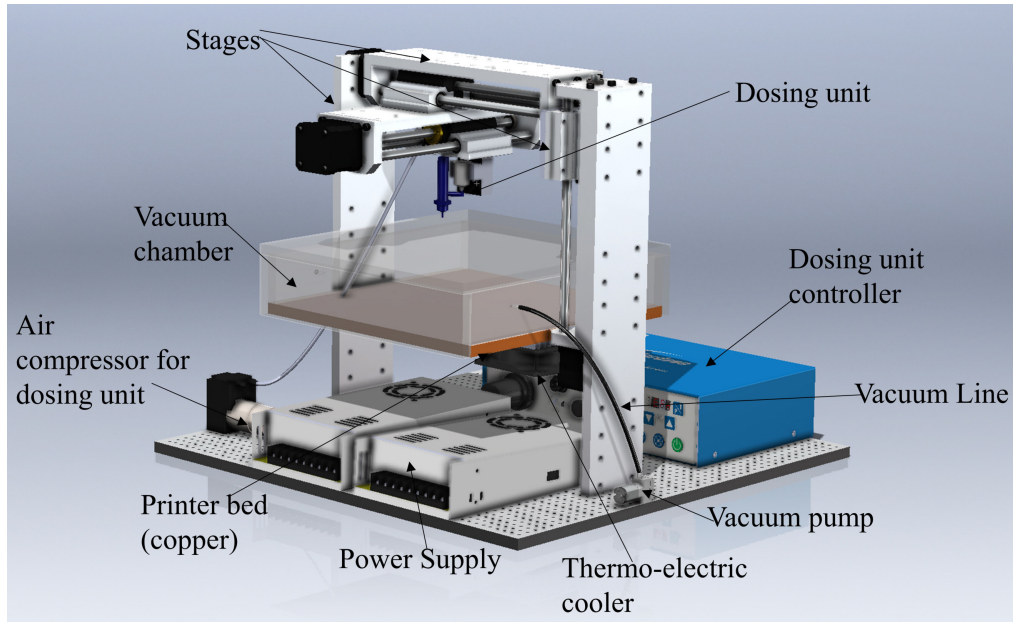


Figure 8.3: Proposed design of 3D printer unit jetting unit with thermal unit and freeze drying unit.

# Bibliography

- [1] A. A. Siddiqi, *Beyond Earth: A chronicle of deep space exploration, 1958-2016*. National Aeronautics & Space Administration, 2018, vol. 4041.
- [2] N. NASA, “Strategic plan,” *National Aeronautics and Space Administration*, 2018.
- [3] A. Barton, N. Wong, and D. Webber, “The google lunar xprize—past, present and future,” in *Proceedings of the 13th Reinventing Space Conference*, Springer, 2018, pp. 75–82.
- [4] T. Prater *et al.*, “Summary report on phase i results from the 3d printing in zero g technology demonstration mission, volume i,” 2016.
- [5] T. Prater, N. Werkheiser, F. Ledbetter, D. Timucin, K. Wheeler, and M. Snyder, “3d printing in zero g technology demonstration mission: Complete experimental results and summary of related material modeling efforts,” *The International Journal of Advanced Manufacturing Technology*, vol. 101, pp. 391–417, 2019.
- [6] C. Buchanan and L. Gardner, “Metal 3d printing in construction: A review of methods, research, applications, opportunities and challenges,” *Engineering Structures*, vol. 180, pp. 332–348, 2019.
- [7] S. Das, D. L. Bourell, and S. Babu, “Metallic materials for 3d printing,” *Mrs Bulletin*, vol. 41, no. 10, pp. 729–741, 2016.
- [8] A. Ambrosi and M. Pumera, “3d-printing technologies for electrochemical applications,” *Chemical society reviews*, vol. 45, no. 10, pp. 2740–2755, 2016.
- [9] S. H. Ko, J. Chung, N. Hotz, K. H. Nam, and C. P. Grigoropoulos, “Metal nanoparticle direct inkjet printing for low-temperature 3d micro metal structure fabrication,” *Journal of Micromechanics and Microengineering*, vol. 20, no. 12, p. 125 010, 2010.
- [10] S. Hong, C. Sanchez, H. Du, and N. Kim, “Fabrication of 3d printed metal structures by use of high-viscosity cu paste and a screw extruder,” *Journal of electronic materials*, vol. 44, pp. 836–841, 2015.
- [11] S. V. Murphy and A. Atala, “3d bioprinting of tissues and organs,” *Nature biotechnology*, vol. 32, no. 8, pp. 773–785, 2014.
- [12] A. Ribeiro *et al.*, “Assessing bioink shape fidelity to aid material development in 3d bioprinting,” *Biofabrication*, vol. 10, no. 1, p. 014 102, 2017.

- [13] J. H. Chung *et al.*, “Bio-ink properties and printability for extrusion printing living cells,” *Biomaterials Science*, vol. 1, no. 7, pp. 763–773, 2013.
- [14] T. Prater *et al.*, “Analysis of specimens from phase i of the 3d printing in zero g technology demonstration mission,” *Rapid Prototyping Journal*, vol. 23, no. 6, pp. 1212–1225, 2017.
- [15] K. N. Prabhu, P. Fernades, and G. Kumar, “Effect of substrate surface roughness on wetting behaviour of vegetable oils,” *Materials & design*, vol. 30, no. 2, pp. 297–305, 2009.
- [16] A. Eifert, D. Paulssen, S. N. Varanakkottu, T. Baier, and S. Hardt, “Simple fabrication of robust water-repellent surfaces with low contact-angle hysteresis based on impregnation,” *Advanced Materials Interfaces*, vol. 1, no. 3, p. 1300138, 2014.
- [17] M. Sakai, T. Yanagisawa, A. Nakajima, Y. Kameshima, and K. Okada, “Effect of surface structure on the sustainability of an air layer on superhydrophobic coatings in a water- ethanol mixture,” *Langmuir*, vol. 25, no. 1, pp. 13–16, 2009.
- [18] Y. Son, C. Kim, D. H. Yang, and D. J. Ahn, “Spreading of an inkjet droplet on a solid surface with a controlled contact angle at low weber and reynolds numbers,” *Langmuir*, vol. 24, no. 6, pp. 2900–2907, 2008.
- [19] J. Perelaer, C. E. Hendriks, A. W. de Laat, and U. S. Schubert, “One-step inkjet printing of conductive silver tracks on polymer substrates,” *Nanotechnology*, vol. 20, no. 16, p. 165303, 2009.
- [20] H. Yang and P. Jiang, “Self-cleaning diffractive macroporous films by doctor blade coating,” *Langmuir*, vol. 26, no. 15, pp. 12598–12604, 2010.
- [21] M Rauscher and S Dietrich, “Wetting phenomena in nanofluidics,” *Annu. Rev. Mater. Res.*, vol. 38, pp. 143–172, 2008.
- [22] Z. Keshavarz-Motamed, L. Kadem, and A. Dolatabadi, “Effects of dynamic contact angle on numerical modeling of electrowetting in parallel plate microchannels,” *Microfluidics and Nanofluidics*, vol. 8, no. 1, p. 47, 2010.
- [23] J. S. Marin Quintero and P. R. Waghmare, “Sessile drop response to a single wave electrokinetic excitation,” *Physics of Fluids*, vol. 32, no. 12, p. 122102, 2020.
- [24] Y. Guo, H. S. Patanwala, B. Bognet, and A. W. Ma, “Inkjet and inkjet-based 3d printing: Connecting fluid properties and printing performance,” *Rapid Prototyping Journal*, 2017.
- [25] L. Li, W. Kang, and D. Ye, “A contact angle measurement method for the droplets in ewod-based chips,” in *2007 2nd IEEE International Conference on Nano/Micro Engineered and Molecular Systems*, IEEE, 2007, pp. 1071–1075.
- [26] A. Mata, A. J. Fleischman, and S. Roy, “Characterization of polydimethylsiloxane (pdms) properties for biomedical micro/nanosystems,” *Biomedical microdevices*, vol. 7, no. 4, pp. 281–293, 2005.

- [27] A. Passerone, “Twenty years of surface tension measurements in space,” *Microgravity Sci. Technol.*, vol. 23, no. 2, pp. 101–111, 2011.
- [28] A. Ababneh, A. Amirfazli, and J. Elliott, “Effect of gravity on the macroscopic advancing contact angle of sessile drops,” *Can. J. Chem. Eng.*, vol. 84, no. 1, pp. 39–43, 2006.
- [29] T. Huhtamäki, X. Tian, J. T. Korhonen, and R. H. Ras, “Surface-wetting characterization using contact-angle measurements,” *Nature protocols*, vol. 13, no. 7, pp. 1521–1538, 2018.
- [30] A. Marmur, “Measures of wettability of solid surfaces,” *Eur. Phys. J. Special Topics*, vol. 197, no. 1, pp. 193–198, 2011.
- [31] A. Marmur, C. Della Volpe, S. Siboni, A. Amirfazli, and J. W. Drelich, “Contact angles and wettability: Towards common and accurate terminology,” *Surf. Innov.*, vol. 5, no. 1, pp. 3–8, 2017.
- [32] D. Cwikel, Q. Zhao, C. Liu, X. Su, and A. Marmur, “Comparing contact angle measurements and surface tension assessments of solid surfaces,” *Langmuir*, vol. 26, no. 19, pp. 15 289–15 294, 2010.
- [33] G. Wolansky and A. Marmur, “The actual contact angle on a heterogeneous rough surface in three dimensions,” *Langmuir*, vol. 14, no. 18, pp. 5292–5297, 1998.
- [34] P. R. Waghmare, S. Das, and S. K. Mitra, “Drop deposition on under-liquid low energy surfaces,” *Soft Matter*, vol. 9, no. 31, pp. 7437–7447, 2013.
- [35] P. R. Waghmare and S. K. Mitra, “Needle-free drop deposition technique for contact angle measurements of superhydrophobic surfaces,” *J. Appl. Phys.*, vol. 116, no. 11, p. 114 903, 2014.
- [36] M. Jin, R. Sanedrin, D. Frese, C. Scheithauer, and T. Willers, “Replacing the solid needle by a liquid one when measuring static and advancing contact angles,” *Colloid Polym Sci.*, vol. 294, no. 4, pp. 657–665, 2016.
- [37] J. W. Drelich, “Contact angles: From past mistakes to new developments through liquid-solid adhesion measurements,” *Advances in colloid and interface science*, vol. 267, pp. 1–14, 2019.
- [38] R. M. Podhajny, “Material science-astm d-5946-96, an astm-approved water contact angle test method for quantifying the level of corona treated films, is reported to be a more accurate alternative to the dyne,” *Paper Film and Foil Converter*, vol. 71, no. 6, pp. 26–27, 1997.
- [39] A. Designation, “D 724 89: Standard test method for surface wettability of paper (angle of contact method),” *Annual Book of ASTM Standards*, vol. 15, p. 60,
- [40] DIN, “Coating materials — wettability — part 2: Determination of the free surface energy of solid surfaces by measuring the contact angle,” *DIN 55660-2*, 2011.

- [41] E. DIN, *828: Klebstoffe–benetzbarkeit–bestimmung durch messung des kontaktwinkels und der kritischen oberflächenspannung fester oberflächen*, 1997.
- [42] J. Drelich, “Guidelines to measurements of reproducible contact angles using a sessile-drop technique,” *Surface innovations*, vol. 1, no. 4, pp. 248–254, 2013.
- [43] G. F. Teletzke, L. Scriven, and H. T. Davis, “Gradient theory of wetting transitions,” *Journal of Colloid and Interface Science*, vol. 87, no. 2, pp. 550–571, 1982.
- [44] A. Bussonnière, A. Antkowiak, F. Ollivier, M. Baudoin, and R. Wunenburger, “Acoustic sensing of forces driving fast capillary flows,” *Physical Review Letters*, vol. 124, no. 8, p. 084502, 2020.
- [45] H.-M. Kwon, A. T. Paxson, K. K. Varanasi, and N. A. Patankar, “Rapid deceleration-driven wetting transition during pendant drop deposition on superhydrophobic surfaces,” *Physical review letters*, vol. 106, no. 3, p. 036102, 2011.
- [46] J. M. Kolinski, L Mahadevan, and S. M. Rubinstein, “Lift-off instability during the impact of a drop on a solid surface,” *Physical review letters*, vol. 112, no. 13, p. 134501, 2014.
- [47] M. R. Rahman, H. N. Mullagura, B. Kattamalalawadi, and P. R. Waghmare, “Droplet spreading on liquid–fluid interface,” *Colloids and Surfaces A: Physicochemical and Engineering Aspects*, vol. 553, pp. 143–148, 2018.
- [48] J. M. Kolinski, L Mahadevan, and S. Rubinstein, “Drops can bounce from perfectly hydrophilic surfaces,” *EPL (Europhysics Letters)*, vol. 108, no. 2, p. 24001, 2014.
- [49] R Shuttleworth and G. Bailey, “The spreading of a liquid over a rough solid,” *Discussions of the Faraday Society*, vol. 3, pp. 16–22, 1948.
- [50] H. Fox and W. Zisman, “The spreading of liquids on low energy surfaces. i. polytetrafluoroethylene,” *Journal of Colloid Science*, vol. 5, no. 6, pp. 514–531, 1950.
- [51] D. K. Owens and R. Wendt, “Estimation of the surface free energy of polymers,” *Journal of applied polymer science*, vol. 13, no. 8, pp. 1741–1747, 1969.
- [52] S. Wu, “Calculation of interfacial tension in polymer systems,” in *Journal of Polymer Science Part C: Polymer Symposia*, Wiley Online Library, vol. 34, 1971, pp. 19–30.
- [53] C. J. van Oss, M. Chaudhury, and R. J. Good, “Monopolar surfaces,” *Advances in colloid and interface science*, vol. 28, pp. 35–64, 1987.
- [54] D. Kwok, A Leung, C. Lam, A Li, R Wu, and A. Neumann, “Low-rate dynamic contact angles on poly (methyl methacrylate) and the determination of solid surface tensions,” *Journal of colloid and interface science*, vol. 206, no. 1, pp. 44–51, 1998.

- [55] I. Fraunhofer *et al.*, “Droplet-based additive manufacturing of hard metal components by thermoplastic 3d printing (t3dp),” *Journal of Ceramic Science and Technology*, vol. 8, no. 1, pp. 155–160, 2016.
- [56] S. Basu, A. K. Agarwal, A. Mukhopadhyay, and C. Patel, *Droplet and spray transport: paradigms and applications*. Springer, 2018.
- [57] B. Friedrich, F. Weser, and C. Scheithauer, *Contact angle measurement apparatus*, US Patent 9,816,909, 2017.
- [58] M Pasandideh-Fard, Y. Qiao, S. Chandra, and J. Mostaghimi, “Capillary effects during droplet impact on a solid surface,” *Phys. Fluids*, vol. 8, no. 3, pp. 650–659, 1996.
- [59] T. Mao, D. C. Kuhn, and H. Tran, “Spread and rebound of liquid droplets upon impact on flat surfaces,” *AIChE Journal*, vol. 43, no. 9, pp. 2169–2179, 1997.
- [60] A. Ahmed, B. A. Fleck, and P. R. Waghmare, “Maximum spreading of a ferrofluid droplet under the effect of magnetic field,” *Phys. Fluids*, vol. 30, no. 7, p. 077102, 2018.
- [61] D Li, P Cheng, and A. Neumann, “Contact angle measurement by axisymmetric drop shape analysis (adsa),” *Adv. Colloid Interface Sci.*, vol. 39, pp. 347–382, 1992.
- [62] D. Kwok, R. Lin, M Mui, and A. Neumann, “Low-rate dynamic and static contact angles and the determination of solid surface tensions,” *Colloids Surf. A Physicochem. Eng. Asp.*, vol. 116, no. 1-2, pp. 63–77, 1996.
- [63] D. Erickson, B. Blackmore, and D. Li, “An energy balance approach to modeling the hydrodynamically driven spreading of a liquid drop,” *Colloids Surf. A Physicochem. Eng. Asp.*, vol. 182, no. 1-3, pp. 109–122, 2001.
- [64] B. Bonhoeffer, A. Kwade, and M. Juhnke, “Impact of formulation properties and process parameters on the dispensing and deposition of drug nanosuspensions using micro-valve technology,” *J. Pharm. Sci.*, vol. 106, no. 4, pp. 1102–1110, 2017.
- [65] T. Deng *et al.*, “Nonwetting of impinging droplets on textured surfaces,” *Applied Physics Letters*, vol. 94, no. 13, p. 133109, 2009.
- [66] P. Goel, S. Kumar, J. Sarkar, and J. P. Singh, “Mechanical strain induced tunable anisotropic wetting on buckled pdms silver nanorods arrays,” *ACS applied materials & interfaces*, vol. 7, no. 16, pp. 8419–8426, 2015.
- [67] D. Bodas and C. Khan-Malek, “Formation of more stable hydrophilic surfaces of pdms by plasma and chemical treatments,” *Microelectronic engineering*, vol. 83, no. 4-9, pp. 1277–1279, 2006.
- [68] M. M. Stanton, R. E. Ducker, J. C. MacDonald, C. R. Lambert, and W. G. McGimpsey, “Super-hydrophobic, highly adhesive, polydimethylsiloxane (pdms) surfaces,” *Journal of colloid and interface science*, vol. 367, no. 1, pp. 502–508, 2012.

- [69] T. Trantidou, Y. Elani, E. Parsons, and O. Ces, “Hydrophilic surface modification of pdms for droplet microfluidics using a simple, quick, and robust method via pva deposition,” *Microsystems & nanoengineering*, vol. 3, no. 1, pp. 1–9, 2017.
- [70] S. Temmel, W. Kern, and T. Luxbacher, “Surface modification of polyethylene by photosulfonation,” *Polymer Surface Modification: Relevance to Adhesion*, vol. 4, p. 157, 2007.
- [71] W. S. Wong *et al.*, “Adaptive wetting of polydimethylsiloxane,” *Langmuir*, 2020.
- [72] T. Young, “Iii. an essay on the cohesion of fluids,” *Philos. Trans. R. Soc. Lond.*, no. 95, pp. 65–87, 1805.
- [73] L. Feng *et al.*, “Super-hydrophobic surfaces: From natural to artificial,” *Adv. Mater.*, vol. 14, no. 24, pp. 1857–1860, 2002.
- [74] X. Gao and L. Jiang, “Water-repellent legs of water striders,” *Nature*, vol. 432, no. 7013, pp. 36–36, 2004.
- [75] X. Gao *et al.*, “The dry-style antifogging properties of mosquito compound eyes and artificial analogues prepared by soft lithography,” *Adv. Mater.*, vol. 19, no. 17, pp. 2213–2217, 2007.
- [76] A. R. Parker and C. R. Lawrence, “Water capture by a desert beetle,” *Nature*, vol. 414, no. 6859, pp. 33–34, 2001.
- [77] Y. Zheng *et al.*, “Directional water collection on wetted spider silk,” *Nature*, vol. 463, no. 7281, pp. 640–643, 2010.
- [78] P. R. Waghmare, N. S. K. Gunda, and S. K. Mitra, “Under-water superoleophobicity of fish scales,” *Sci. Rep.*, vol. 4, no. 1, pp. 1–5, 2014.
- [79] M. R. Flynn and J. W. Bush, “Underwater breathing: The mechanics of plas-tron respiration,” *J. Fluid Mech.*, vol. 608, p. 275, 2008.
- [80] X. Yao, Y. Song, and L. Jiang, “Applications of bio-inspired special wettable surfaces,” *Adv. Mater.*, vol. 23, no. 6, pp. 719–734, 2011.
- [81] M Pasandideh-Fard, V Pershin, S Chandra, and J Mostaghimi, “Splat shapes in a thermal spray coating process: Simulations and experiments,” *J. Therm. Spray Technol.*, vol. 11, no. 2, pp. 206–217, 2002.
- [82] M. J. De Ruijter, T. Blake, and J. De Coninck, “Dynamic wetting studied by molecular modeling simulations of droplet spreading,” *Langmuir*, vol. 15, no. 22, pp. 7836–7847, 1999.
- [83] K. Pataky, T. Braschler, A. Negro, P. Renaud, M. P. Lutolf, and J. Brugger, “Microdrop printing of hydrogel bioinks into 3d tissue-like geometries,” *Adv. Mater.*, vol. 24, no. 3, pp. 391–396, 2012.
- [84] B. Pethica and T. Pethlca, “The contact angle eqmhbrmm,” in *Proc. Second Inter. Congress of Surface Activity III, Butterworths Scientific Publ*, 1957, pp. 131–35.

- [85] C. Ward and M. Sasges, “Effect of gravity on contact angle: A theoretical investigation,” *J. Chem. Phys.*, vol. 109, no. 9, pp. 3651–3660, 1998.
- [86] M. Sasges and C. Ward, “Effect of gravity on contact angle: An experimental investigation,” *J. Chem. Phys.*, vol. 109, no. 9, pp. 3661–3670, 1998.
- [87] H. Fujii and H. Nakae, “Effect of gravity on contact angle,” *Philos. Mag. A*, vol. 72, no. 6, pp. 1505–1512, 1995.
- [88] W. J. Herzberg and J. E. Marian, “Relationship between contact angle and drop size,” *J. Colloid Interface Sci.*, vol. 33, no. 1, pp. 161–163, 1970.
- [89] R. J. Good and M. Koo, “The effect of drop size on contact angle,” *J. Colloid Interface Sci.*, vol. 71, no. 2, pp. 283–292, 1979.
- [90] F. Bashforth and J. C. Adams, *An attempt to test the theories of capillarity*. University Press, 1883.
- [91] F. Karmali and M. Shelhamer, “The dynamics of parabolic flight: Flight characteristics and passenger percepts,” *Acta Astronaut.*, vol. 63, no. 5-6, pp. 594–602, 2008.
- [92] P. Von Kampen, U. Kaczmarczik, and H. J. Rath, “The new drop tower catapult system,” *Acta Astronaut.*, vol. 59, no. 1-5, pp. 278–283, 2006.
- [93] J.-C. Baret and M. Brinkmann, “Wettability control of droplet deposition and detachment,” *Phys. Rev. Lett.*, vol. 96, no. 14, p. 146106, 2006.
- [94] P. R. Waghmare, S. Mitra, N. S. K. Gunda, and S. K. Mitra, “Needle-free drop deposition: The role of elastic membranes,” *RSC Adv.*, vol. 5, no. 100, pp. 82374–82380, 2015.
- [95] A. Diana, M. Castillo, D. Brutin, and T. Steinberg, “Sessile drop wettability in normal and reduced gravity,” *Microgravity Sci. Technol.*, vol. 24, no. 3, pp. 195–202, 2012.
- [96] Z.-Q. Zhu *et al.*, “Experimental investigation of pendant and sessile drops in microgravity,” *Microgravity Sci. Technol.*, vol. 22, no. 3, pp. 339–345, 2010.
- [97] D. Brutin, Z. Zhu, O. Rahli, J. Xie, Q. Liu, and L. Tadrist, “Sessile drop in microgravity: Creation, contact angle and interface,” *Microgravity Sci. Technol.*, vol. 21, no. 1, pp. 67–76, 2009.
- [98] O. E. Yildirim, Q. Xu, and O. A. Basaran, “Analysis of the drop weight method,” *Phys. Fluids*, vol. 17, no. 6, p. 062107, 2005.
- [99] A. Bateni, A. Ababneh, J. Elliott, A. Neumann, and A. Amirfazli, “Effect of gravity and electric field on shape and surface tension of drops,” *Adv. Space Res.*, vol. 36, no. 1, pp. 64–69, 2005.
- [100] M. F. Ismail, A. Baldygin, T. Willers, and P. R. Waghmare, “Optical contact angle measurement considering spreading, evaporation and reactive substrate,” *Advances in Contact Angle, Wettability and Adhesion*, vol. 3, pp. 59–79, 2018.

- [101] A. Ahmed, R. Sanedrin, T. Willers, and P. R. Waghmare, “The effect of dynamic wetting pressure on contact angle measurements,” *J. Colloid Interface Sci.*, vol. 608, pp. 1086–1093, 2022.
- [102] S. Banitabaei and A Amirfazli, “Pneumatic drop generator: Liquid pinch-off and velocity of single droplets,” *Colloids Surf. A Physicochem. Eng. Asp.*, vol. 505, pp. 204–213, 2016.
- [103] L. Rayleigh, “On the instability of jets,” *Proc. London Math. Soc.*, vol. 1, no. 1, pp. 4–13, 1878.
- [104] C. Clanet and J. C. Lasheras, “Transition from dripping to jetting,” *J. Fluid Mech.*, vol. 383, pp. 307–326, 1999.
- [105] F. Celestini, R Kofman, X. Noblin, and M. Pellegrin, “Water jet rebounds on hydrophobic surfaces: A first step to jet micro-fluidics,” *Soft Matter*, vol. 6, no. 23, pp. 5872–5876, 2010.
- [106] K. Cardin, S. Wang, O. Desjardins, and M. Weislogel, “Rebound of large jets from superhydrophobic surfaces in low gravity,” *Phys. Rev. Fluids*, vol. 6, no. 1, p. 014003, 2021.
- [107] C. Extrand and S. I. Moon, “When sessile drops are no longer small: Transitions from spherical to fully flattened,” *Langmuir*, vol. 26, no. 14, pp. 11 815–11 822, 2010.
- [108] R. Tadmor and P. S. Yadav, “As-placed contact angles for sessile drops,” *J. Colloid Interface Sci.*, vol. 317, no. 1, pp. 241–246, 2008.
- [109] B. Krasovitski and A. Marmur, “Drops down the hill: Theoretical study of limiting contact angles and the hysteresis range on a tilted plate,” *Langmuir*, vol. 21, no. 9, pp. 3881–3885, 2005.
- [110] A. Calvimontes, “The measurement of the surface energy of solids using a laboratory drop tower,” *NPJ Microgravity*, vol. 3, no. 1, pp. 1–14, 2017.
- [111] P.-G. De Gennes, “Wetting: Statics and dynamics,” *RMP*, vol. 57, no. 3, p. 827, 1985.
- [112] S Chandra and C. Avedisian, “On the collision of a droplet with a solid surface,” *Proc R Soc Lond A Math Phys Sci*, vol. 432, no. 1884, pp. 13–41, 1991.
- [113] V. A. Lubarda and K. A. Talke, “Analysis of the equilibrium droplet shape based on an ellipsoidal droplet model,” *Langmuir*, vol. 27, no. 17, pp. 10 705–10 713, 2011.
- [114] D Homencovschi, J Geer, and T Singler, “Uniform asymptotic solutions for small and large sessile drops,” *Acta Mech.*, vol. 128, no. 3, pp. 141–171, 1998.
- [115] J. Eggers and E. Villermaux, “Physics of liquid jets,” *Reports on progress in physics*, vol. 71, no. 3, p. 036 601, 2008.
- [116] G. D. Martin, S. D. Hoath, and I. M. Hutchings, “Inkjet printing-the physics of manipulating liquid jets and drops,” in *Journal of Physics: Conference Series*, IOP Publishing, vol. 105, 2008, p. 012 001.

- [117] S. X. Liu and M. Lu, “Nonlinear evolution and breakup of the cavitating liquid jet surrounded by the rotary compressible air,” Dec. 2019. [Online]. Available: <https://scite.ai/reports/10.1021/acsomega.9b02477>.
- [118] T Nguyen, D. Shanmugam, and J. Wang, “Effect of liquid properties on the stability of an abrasive waterjet,” *International Journal of Machine Tools and Manufacture*, vol. 48, no. 10, pp. 1138–1147, 2008.
- [119] D. Pede, G. Serra, and D. De Rossi, “Microfabrication of conducting polymer devices by ink-jet stereolithography,” *Materials Science and Engineering: C*, vol. 5, no. 3-4, pp. 289–291, 1998.
- [120] M. E. Kuil, J. P. Abrahams, and J. C. Marijnissen, “Nano-dispensing by electrospray for biotechnology,” *Biotechnology Journal: Healthcare Nutrition Technology*, vol. 1, no. 9, pp. 969–975, 2006.
- [121] G. Li, X. Xiao, T. Liu, M. Gu, R. Dai, and W. Liao, “Three-dimensional morphology and contour quality of conductive lines printed by high-viscosity paste jetting,” *Langmuir*, 2023.
- [122] A. Baldygin *et al.*, “Effect of gravity on the spreading of a droplet deposited by liquid needle deposition technique,” *npj Microgravity*, vol. 9, no. 1, p. 49, 2023.
- [123] I Vihinen, A. Honohan, and S. Lin, “Image of absolute instability in a liquid jet,” *Physics of Fluids*, vol. 9, no. 11, pp. 3117–3119, 1997.
- [124] S. Lin and E. Ibrahim, “Instability of a viscous liquid jet surrounded by a viscous gas in a vertical pipe,” *Journal of Fluid Mechanics*, vol. 218, pp. 641–658, 1990.
- [125] R. D. Reitz, *Atomization and other breakup regimes of a liquid jet*. Princeton University, 1978.
- [126] M. L. Cordero, F. Gallaire, and C. N. Baroud, “Quantitative analysis of the dripping and jetting regimes in co-flowing capillary jets,” *Physics of Fluids*, vol. 23, no. 9, 2011.
- [127] J. Plateau, “Experimental and theoretical statics of liquids subject to molecular forces only,” 1873.
- [128] E. Musk, “Making life multi-planetary,” *New Space*, vol. 6, no. 1, pp. 2–11, 2018.
- [129] D. J. Chato, “Cryogenic fluid transfer for exploration,” *Cryogenics*, vol. 48, no. 5-6, pp. 206–209, 2008.
- [130] L. Bolshinskiy, A Hedayat, L. Hastings, S. Sutherlin, A. Schnell, and J. Moder, “Tank system integrated model: A cryogenic tank performance prediction program,” Tech. Rep., 2017.
- [131] V. Ozbolat, M. Dey, B. Ayan, A. Povilianskas, M. C. Demirel, and I. T. Ozbolat, “3d printing of pdms improves its mechanical and cell adhesion properties,” *ACS Biomaterials Science & Engineering*, vol. 4, no. 2, pp. 682–693, 2018.

- [132] M. Xia, D. Gu, G. Yu, D. Dai, H. Chen, and Q. Shi, “Selective laser melting 3d printing of ni-based superalloy: Understanding thermodynamic mechanisms,” *Science Bulletin*, vol. 61, no. 13, pp. 1013–1022, 2016.
- [133] A. Edwards, B. Osborne, J. Stoltzfus, T Howes, and T. Steinberg, “Instabilities and drop formation in cylindrical liquid jets in reduced gravity,” *Physics of fluids*, vol. 14, no. 10, pp. 3432–3438, 2002.
- [134] C. Kinoshita, H Teng, and S. Masutani, “A study of the instability of liquid jets and comparison with tomotika’s analysis,” *International journal of multiphase flow*, vol. 20, no. 3, pp. 523–533, 1994.
- [135] F. Suñol and R. González-Cinca, “Liquid jet breakup and subsequent droplet dynamics under normal gravity and in microgravity conditions,” *Physics of Fluids*, vol. 27, no. 7, 2015.
- [136] P. K. Kundu, I. M. Cohen, and D. R. Dowling, *Fluid mechanics*. Academic press, 2015.
- [137] D. Bogy, “Drop formation in a circular liquid jet,” *Annual Review of Fluid Mechanics*, vol. 11, no. 1, pp. 207–228, 1979.
- [138] A. W. Adamson, A. P. Gast, *et al.*, *Physical chemistry of surfaces*. Interscience publishers New York, 1967, vol. 150.
- [139] P. Ghosh, *Colloid and interface science*. PHI Learning Pvt. Ltd., 2009.
- [140] D. G. Zill, *Advanced engineering mathematics*. Jones & Bartlett Learning, 2020.
- [141] C. Patrascu and C. Balan, “The effect of curvature elasticity on rayleigh–plateau instability,” *European Journal of Mechanics-B/Fluids*, vol. 80, pp. 167–173, 2020.
- [142] J. L. Margrave, “Determination of thermophysical properties of liquid metals at high temperatures by levitation methods,” *Materials Science and Engineering: A*, vol. 178, no. 1-2, pp. 83–88, 1994.
- [143] A. Miiller and A Cezairliyan, “A dynamic technique for measuring surface tension at high temperatures in a microgravity environment,” *International Journal of Thermophysics*, vol. 11, no. 4, pp. 663–674, 1990.
- [144] I. Egry, G. Lohoefer, E. Schwartz, J. Szekely, and P. Neuhaus, “Surface tension measurements on liquid metals in microgravity,” *Metallurgical and Materials Transactions B*, vol. 29, no. 5, pp. 1031–1035, 1998.
- [145] H Soda, A McLean, and W. Miller, “The influence of oscillation amplitude on liquid surface tension measurements with levitated metal droplets,” *Metallurgical Transactions B*, vol. 9, no. 1, pp. 145–147, 1978.
- [146] A. Passerone, L. Liggieri, N. Rando, F. Ravera, and E. Ricci, “A new experimental method for the measurement of the interfacial tension between immiscible fluids at zero bond number,” *Journal of colloid and interface science*, vol. 146, no. 1, pp. 152–162, 1991.

- [147] V. Kovalchuk *et al.*, “Capillary pressure studies under low gravity conditions,” *Advances in colloid and interface science*, vol. 161, no. 1-2, pp. 102–114, 2010.
- [148] H. Sakai and T. Fujii, “The dependence of the apparent contact angles on gravity,” *Journal of colloid and interface science*, vol. 210, no. 1, pp. 152–156, 1999.
- [149] D. Owens and R. Wendt, *J. of applied polym*, 1969.
- [150] K.-H. Chu, R. Xiao, and E. N. Wang, “Uni-directional liquid spreading on asymmetric nanostructured surfaces,” *Nature materials*, vol. 9, no. 5, p. 413, 2010.
- [151] Y. Liu, J. Wang, and X. Zhang, “Accurate determination of the vapor-liquid-solid contact line tension and the viability of young equation,” *Scientific reports*, vol. 3, p. 2008, 2013.
- [152] G. Whyman and E. Bormashenko, “Oblate spheroid model for calculation of the shape and contact angles of heavy droplets,” *Journal of colloid and interface science*, vol. 331, no. 1, pp. 174–177, 2009.
- [153] J. Padday, “Surface and colloid science,” *Vol. I, edited by Egon Matkijevic, Pub: Wiley-Interscience*, 1969.
- [154] P. Moin, *Fundamentals of engineering numerical analysis*. Cambridge University Press, 2010.
- [155] S. C. Chapra *et al.*, *Applied numerical methods with MATLAB for engineers and scientists*. New York: McGraw-Hill, 2012.
- [156] W. Kong and H. Liu, “A theory on the icing evolution of supercooled water near solid substrate,” *International Journal of Heat and Mass Transfer*, vol. 91, pp. 1217–1236, 2015.
- [157] H. Sojoudi, M. Wang, N. Boscher, G. H. McKinley, and K. K. Gleason, “Durable and scalable icephobic surfaces: Similarities and distinctions from superhydrophobic surfaces,” *Soft matter*, vol. 12, no. 7, pp. 1938–1963, 2016.
- [158] T. M. Schutzius *et al.*, “Physics of icing and rational design of surfaces with extraordinary icephobicity,” *Langmuir*, vol. 31, no. 17, pp. 4807–4821, 2015.
- [159] V. Hejazi, K. Sobolev, and M. Nosonovsky, “From superhydrophobicity to icephobicity: Forces and interaction analysis,” *Scientific reports*, vol. 3, no. 1, pp. 1–6, 2013.
- [160] D. Anderson, M. G. Worster, and S. Davis, “The case for a dynamic contact angle in containerless solidification,” *Journal of crystal growth*, vol. 163, no. 3, pp. 329–338, 1996.
- [161] J.-P. Delplanque and R. Rangel, “An improved model for droplet solidification on a flat surface,” *Journal of materials science*, vol. 32, no. 6, pp. 1519–1530, 1997.

- [162] M Stiti, G. Castanet, A Labergue, and F Lemoine, “Icing of a droplet deposited onto a subcooled surface,” *International Journal of Heat and Mass Transfer*, vol. 159, p. 120 116, 2020.
- [163] J. H. Snoeijer and P. Brunet, “Pointy ice-drops: How water freezes into a singular shape,” *American Journal of Physics*, vol. 80, no. 9, pp. 764–771, 2012.
- [164] A. Schetnikov, V. Matiunin, and V. Chernov, “Conical shape of frozen water droplets,” *American Journal of Physics*, vol. 83, no. 1, pp. 36–38, 2015.
- [165] A. Starostin, V. Strelnikov, L. A. Dombrovsky, S. Shoval, O. Gendelman, and E. Bormashenko, “Effect of asymmetric cooling of sessile droplets on orientation of the freezing tip,” *Journal of Colloid and Interface Science*, vol. 620, pp. 179–186, 2022.
- [166] F. Boulogne and A. Salonen, “Drop freezing: Fine detection of contaminants by measuring the tip angle,” *Applied Physics Letters*, vol. 116, no. 10, p. 103 701, 2020.
- [167] A. ElSherbini and A. Jacobi, “Liquid drops on vertical and inclined surfaces: Ii. a method for approximating drop shapes,” *Journal of colloid and interface science*, vol. 273, no. 2, pp. 566–575, 2004.
- [168] M. Santos, S Velasco, and J. White, “Simulation analysis of contact angles and retention forces of liquid drops on inclined surfaces,” *Langmuir*, vol. 28, no. 32, pp. 11 819–11 826, 2012.
- [169] J. E. Castillo, Y. Huang, Z. Pan, and J. A. Weibel, “Quantifying the pathways of latent heat dissipation during droplet freezing on cooled substrates,” *International Journal of Heat and Mass Transfer*, vol. 164, p. 120 608, 2021.
- [170] M. F. Ismail and P. R. Waghmare, “Universality in freezing of an asymmetric drop,” *Applied Physics Letters*, vol. 109, no. 23, p. 234 105, 2016.
- [171] A. G. Marin, O. R. Enriquez, P. Brunet, P. Colinet, and J. H. Snoeijer, “Universality of tip singularity formation in freezing water drops,” *Physical review letters*, vol. 113, no. 5, p. 054 301, 2014.
- [172] P. K. Roy, S. Shoval, N. Shvalb, L. A. Dombrovsky, O. V. Gendelman, and E. Bormashenko, “Apple-like shape of freezing paraffin wax droplets and its origin,” 2023.
- [173] H. Zhang *et al.*, “Active control of the freezing process of a ferrofluid droplet with magnetic fields,” *Applied Thermal Engineering*, vol. 176, p. 115 444, 2020.
- [174] N Dalili, A. Edrisy, and R. Carriveau, “A review of surface engineering issues critical to wind turbine performance,” *Renewable and Sustainable energy reviews*, vol. 13, no. 2, pp. 428–438, 2009.
- [175] K. P. Cooper, “Layered manufacturing: Challenges and opportunities,” *MRS Online Proceedings Library (OPL)*, vol. 758, pp. LL1–4, 2002.

- [176] M. B. Adali, A. A. Barresi, G. Boccardo, and R. Pisano, “Spray freeze-drying as a solution to continuous manufacturing of pharmaceutical products in bulk,” *Processes*, vol. 8, no. 6, p. 709, 2020.
- [177] K. Mensah and J. M. Choi, “Review of technologies for snow melting systems,” *Journal of Mechanical Science and Technology*, vol. 29, no. 12, pp. 5507–5521, 2015.
- [178] F. T. Lynch and A. Khodadoust, “Effects of ice accretions on aircraft aerodynamics,” *Progress in Aerospace Sciences*, vol. 37, no. 8, pp. 669–767, 2001.
- [179] S. Deville, “Freeze-casting of porous ceramics: A review of current achievements and issues,” *Advanced Engineering Materials*, vol. 10, no. 3, pp. 155–169, 2008.
- [180] S. Jung, M. K. Tiwari, N. V. Doan, and D. Poulikakos, “Mechanism of supercooled droplet freezing on surfaces,” *Nature communications*, vol. 3, no. 1, pp. 1–8, 2012.
- [181] M. Tembely and A. Dolatabadi, “A comprehensive model for predicting droplet freezing features on a cold substrate,” *Journal of Fluid Mechanics*, vol. 859, pp. 566–585, 2019.
- [182] L. Mishchenko, B. Hatton, V. Bahadur, J. A. Taylor, T. Krupenkin, and J. Aizenberg, “Design of ice-free nanostructured surfaces based on repulsion of impacting water droplets,” *ACS nano*, vol. 4, no. 12, pp. 7699–7707, 2010.
- [183] P. Hao, C. Lv, and X. Zhang, “Freezing of sessile water droplets on surfaces with various roughness and wettability,” *Applied physics letters*, vol. 104, no. 16, p. 161 609, 2014.
- [184] A. Oron, S. H. Davis, and S. G. Bankoff, “Long-scale evolution of thin liquid films,” *Reviews of modern physics*, vol. 69, no. 3, p. 931, 1997.
- [185] Y. A. Cengel, *Fluid mechanics*. Tata McGraw-Hill Education, 2010.
- [186] K. M. Krishnan, *Fundamentals and applications of magnetic materials*. Oxford University Press, 2016.
- [187] J. Osborn, “Demagnetizing factors of the general ellipsoid,” *Physical review*, vol. 67, no. 11-12, p. 351, 1945.
- [188] G. J. Tee, “Surface area of ellipsoid segment,” Department of Mathematics, The University of Auckland, New Zealand, Tech. Rep., 2005.
- [189] H. K. Christenson, “Confinement effects on freezing and melting,” *Journal of Physics: Condensed Matter*, vol. 13, no. 11, R95, 2001.
- [190] C Alba-Simionesco *et al.*, “Effects of confinement on freezing and melting,” *Journal of Physics: Condensed Matter*, vol. 18, no. 6, R15, 2006.
- [191] R. E. Sonntag, C. Borgnakke, G. J. Van Wylen, and S. Van Wyk, *Fundamentals of thermodynamics*. Wiley New York, 1998, vol. 6.
- [192] F Brochard-Wyart and P. De Gennes, “Dynamics of partial wetting,” *Adv. Colloid Interface Sci.*, vol. 39, pp. 1–11, 1992.

# Appendix A: Chapter 2

## A.1 Supplementary figure for Chapter 2

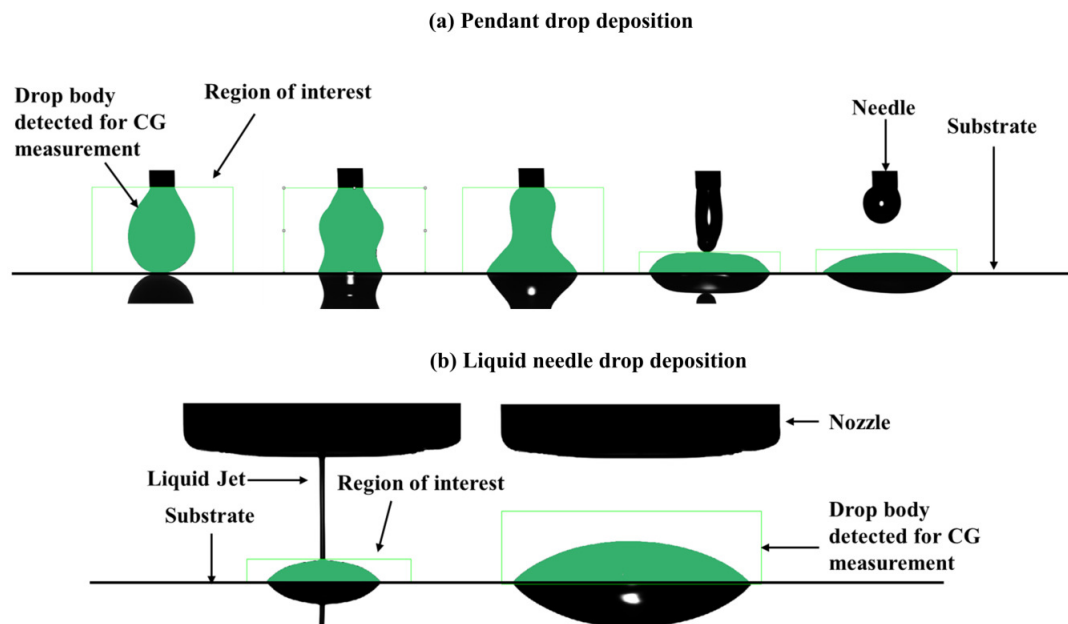


Figure A.1: Center of gravity detection method for the (a) pendant drop and (b) liquid needle drop deposition technique.

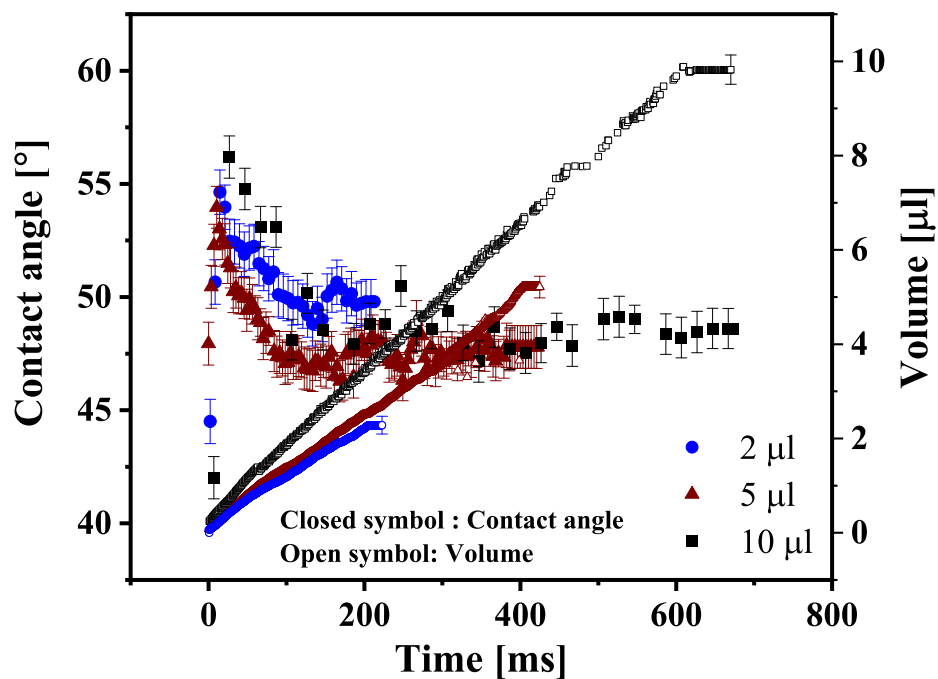


Figure A.2: Transient variation of contact angle (left axis) and volume (right axis) for  $2\mu\text{l}$ ,  $5\mu\text{l}$  and  $10\mu\text{l}$  DIM drop on aqua regia treated glass substrate deposited via liquid needle drop deposition system. For the clarity purpose, for volume data, only the average error bar is presented at the end.

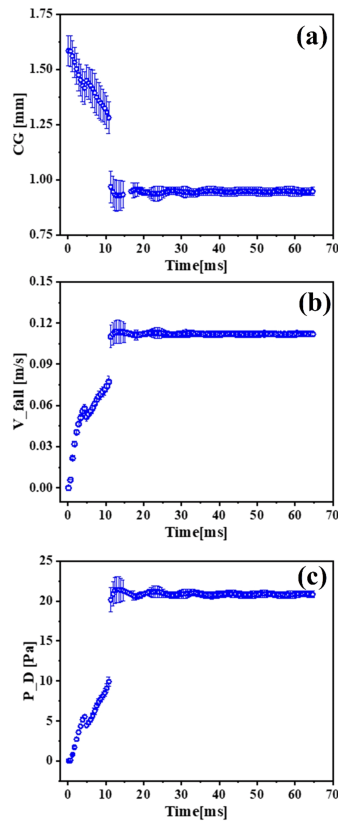


Figure A.3: Supplementary figure for variation of dynamic wetting pressure with respect to center of gravity in case of pendant drop deposition technique.

# Appendix B: Chapter 4

## B.1 Derivation of mathematical model for spreading of a drop deposited by liquid needle drop deposition technique

### Drop spreading via jet deposition

In case of liquid needle droplet deposition technique the energy imparted by the impinging jet is transformed into internal energy, surface energy, and gravitational energy, in addition to the resistance offered by the medium viscosity and viscous dissipation within the spreading droplet. The energy transferred from the impinging jet to the spreading drop results in equation B.1 as follows:

$$\frac{dE_{in}}{dt} = \frac{d}{dt}(E_{system} + E_s + E_g) + \frac{d}{dt}(W_{vd} + W_{mv}) \quad (B.1)$$

Where,  $E_{in}$ ,  $E_{system}$ ,  $E_s$  and  $E_g$  is the incoming energy available in the liquid jet, the internal energy in the spreading droplet, the surface energy and the gravitational potential energy, respectively, whereas,  $W_{vd}$  and  $W_{mv}$  is the work due to viscous dissipation and the work associated with medium viscosity, respectively.

It is to be noted that the kinetic energy of the jet is the only incoming energy,  $E_{in}$  to the system. Considering the mass of the incoming liquid as  $m$  and velocity of the impacting jet as,  $v_j$ , the rate of change of incoming energy transfer can be expressed as,

$$\frac{dE_{in}}{dt} = \frac{v_j^2}{2} \frac{dm}{dt} \quad (B.2)$$

The internal energy of the spreading droplet is the combination of enthalpy [191] and the kinetic energy of the jet. If we assume the overall system as isobaric and isothermal system, then from order of magnitude analysis it can be demonstrated that the overall change in the enthalpy is negligible [63]. on the other hand, the internal kinetic energy induced due to the impingement of the jet on the liquid-medium interface can be ignored since the drop surface area is remarkably greater than the liquid jet cross sectional area. Therefore, as both the enthalpy and internal kinetic energy are negligible, the internal energy in the system can be considered as constant. As a result, in equation B.1 the transient change in  $E_{system}$  can be ignored.

The total surface energy of the system can be defined considering the surface energies of the three interfacial phases, *i.e.*, liquid-solid (drop-substrate), liquid-fluid (drop-medium) and solid-fluid (substrate-medium) which suggests  $E_s = \sigma_{ds}A_{ds} - \sigma_{sm}A_{sm} + \sigma_{dm}A_{dm}$ , where,  $\sigma$  and  $A$  represent the surface energy and area for respective interfaces and subscripts  $d$ ,  $s$  and  $m$  denotes the drop, solid and the surrounding medium, respectively. With a spherical drop shape assumption the rate of change of surface energy can be expressed as,

$$\frac{dE_s}{dt} = 2\pi R\sigma_{dm}[2h(\theta_d) - \cos\theta_e]\frac{dR}{dt} \quad (\text{B.3})$$

where,  $h(\theta_d) = \frac{1 - \cos\theta_d}{\sin^2\theta_d}$  and  $\theta_d$  and  $\theta_e$  are the advancing (dynamic) and equilibrium contact angle, respectively.

During droplet growth, due to the continuous addition of mass, the change in the mass and the change in the center of gravity of the depositing droplet the consideration of the gravitational forces become mandatory. For an infinitesimal increase of mass,  $\Delta m$ , if the center of gravity is shifted by  $\Delta z$ , the change in gravitational potential energy can be expressed as,  $\Delta E_g = g[(m + \Delta m)(z + \Delta z) - mz]$ . After eliminating

the negligible products ( $\Delta m \cdot \Delta z \approx 0$ ) the rate of change in potential energy can be expressed as,  $\frac{dE_g}{dt} = g \left[ m \frac{dz}{dt} + z \frac{dm}{dt} \right]$ , where the total mass of the system can be obtained as  $m = m_0 + \int_a^b \frac{dm}{dt} dt$ . Now considering all the terms the expression for the rate of change in the gravitational potential energy can be expressed as,

$$\frac{dE_g}{dt} = g \left[ m \left( \frac{3f(\theta_d)}{4} \frac{dR}{dt} \right) + \frac{R}{4} f(\theta_d) \frac{dm}{dt} \right] \quad (\text{B.4})$$

where,  $f(\theta_d) = \frac{2 - \sin^2 \theta_d + 2 \cos \theta_d}{(2 + \cos \theta_d) \sin \theta_d}$ .

The viscosity of the surrounding medium can play a crucial role in confining the spreading of the droplet. During liquid needle droplet deposition, due to the continuous addition of mass, the surrounding medium get displaced by the increase in drop volume. Therefore, additional work has been done by the surrounding medium on the drop-medium interface. The rate of work due to medium viscosity can be quantified as,  $\frac{dw_{mv}}{dt} = \tau V dA$ , where  $\tau$  is the shear stress which acts normal to the surface,  $dA$ , due to the drop spreading velocity,  $V = dR/dt$ . The shear stress at the drop boundary, i.e. at the liquid-medium interface, can be defined as  $\tau = 2\mu_m \left( \frac{\partial u}{\partial r} \right)_{r=R}$ , where,  $\mu_m$  is the medium viscosity and  $u$  is the velocity by which the surrounding medium is getting displaced. If we consider a lamina of fluid outside the drop at a distance  $r$ , where  $r > R$ , and implement the mass conservation between surrounding medium and the droplet, one can obtain the velocity of the surrounding medium adjacent to the drop boundary as,  $u = \frac{R^2}{r^2} \frac{dR}{dt}$ . The resultant rate of work due to medium viscosity can be represented as,

$$\frac{dw_{mv}}{dt} = \left[ \frac{4\mu_m}{R} \frac{dR}{dt} \frac{1}{\rho_m} \right] \frac{dm}{dt} \quad (\text{B.5})$$

If we are to consider the internal motion of the liquid layers inside a droplet, the consideration of viscous dissipation force is inevitable. Depending on the magnitude of the contact angle, two models have been adopted by the researchers: lubrication

approximation [111, 192] or boundary layer approximation [112]. De Gennes predicted the viscous dissipation work based on lubrication approximation. For hydrodynamic drop spreading when the contact angle of the droplet is less than  $90^\circ$ , we follow the De Gennes approach. Based on the lubrication model [111, 192], the viscous force per unit length of the three-phase contact line can be expressed as,  $F_v = \frac{3\mu_d}{\theta_d} \ln\left(\varepsilon^{-1} \frac{dR}{dt}\right)$ , where  $\theta_d$  is the instantaneous dynamic contact angle,  $\mu_d$  is the viscosity of the droplet and  $\varepsilon$  is the ratio of the microscopic length ( $L_\delta$ ) to macroscopic cut-off length ( $L$ ). In general,  $L_\delta$  may vary between  $1 \mu m$  to  $5 \mu m$  whereas  $L$  can be defined as the horizontal length scale ( $R$ ) of the drop [63]. The viscous dissipation work of the circular three phase contact line is  $2\pi R F_v$ . Therefore, the rate of viscous dissipation work over the three-phase contact line can be expressed as [111, 192],

$$\frac{dw_{vd}}{dt} = 6\pi\mu_d \ln(\varepsilon^{-1}) \frac{R}{\theta_D} \left(\frac{dR}{dt}\right)^2 \quad (\text{B.6})$$

On the other hand, as an alternative to lubrication approximation, boundary layer approach can be taken into consideration for predicting the viscous dissipation for drop-substrate combination of higher contact angle. Boundary layer approximation for viscous dissipation model was suggested by Chandra et al.[112]. Based on the boundary layer approximation model the viscous dissipation work is approximated as,  $w_v = \int_a^b \phi \Omega t_c$ . [36, 60, 112], where  $\phi$  is the viscous dissipation which can be approximated as,  $\phi = \mu_d \left(\frac{\partial v_i}{\partial x_k} + \frac{\partial v_k}{\partial x_i}\right) \frac{\partial v_i}{\partial x_k} = \mu_d v_j^2 / \delta^2$ , where  $\delta = \frac{2D_j}{\sqrt{Re}}$  is the characteristic length scale of the droplet,  $\Omega = \pi R^2 \delta$  is the volume of the droplet and  $t_c = h_j / v_j = k_{h_j} D_j / v_j$ . Therefore, considering the boundary layer approximation, the work done due to viscous dissipation per unit time, over the three-phase contact line, can be expressed as,

$$\frac{dw_{vd}}{dt} = \mu_d v_j \pi k_{h_j} \sqrt{Re} R \frac{dR}{dt} \quad (\text{B.7})$$

Now, considering the lubrication approximation model for the maximum wetting

scenario, combining equation B.1 to B.6, we can form the following governing equation for the drop spreading for liquid needle drop deposition technique,

$$\begin{aligned}
6\pi\mu_d \ln(\varepsilon^{-1}) \frac{R}{\theta_D} \left(\frac{dR}{dt}\right)^2 + [2\pi R\sigma_{dm}(2h(\theta_d) - \cos\theta_e) \\
+ (m_0 + \frac{dm}{dt})g\frac{f(\theta_d)}{4} - \frac{4\mu_m}{R\rho_m} \frac{dm}{dt}] \frac{dR}{dt} \\
+ \frac{dm}{dt} \left[\frac{gRf(\theta_d)}{4} - \frac{v_j^2}{2}\right] = 0
\end{aligned} \tag{B.8}$$

Whereas, considering the boundary layer approximation theory in case of the minimum wetting scenario, combining equation B.1 to B.5 and B.7, we can form the following governing equation for the drop spreading for liquid needle drop deposition technique,

$$\begin{aligned}
\mu_d v_j \pi k_{h_j} \sqrt{Re} R \frac{dR}{dt} + \left[2\pi R\sigma_{dm}(2h(\theta_d) - \cos\theta_e) \right. \\
+ (m_0 + \frac{dm}{dt})g\frac{f(\theta_d)}{4} - \frac{4\mu_m}{R\rho_m} \frac{dm}{dt}] \frac{dR}{dt} \\
+ \left[\frac{gRf(\theta_d)}{4} - \frac{v_j^2}{2} \frac{dm}{dt}\right] = 0
\end{aligned} \tag{B.9}$$

The non-dimensional form of governing equation can be expressed as the following equation B.10 (a) and B.10(b), for lubrication and boundary layer approximation, respectively.

$$\begin{aligned}
\frac{6\ln(\varepsilon^{-1})}{\theta_d} \frac{R^*}{Re} \left(\frac{dR^*}{dt^*}\right)^2 + \left[\frac{4R^*}{We}(2h(\theta_d) - \cos\theta_e) + \frac{f(\theta_d)G(\theta_d)}{24}(R_0^*)^3 \frac{Bo}{We} + \frac{k_{h_j}f(\theta_d)}{4} t^* \frac{Bo}{We} \right. \\
+ \left. \frac{k_{\mu_m}}{R^*} \frac{8}{Re}\right] \frac{dR^*}{dt^*} + \frac{dm}{dt} \left[\frac{f(\theta_d)}{4} R^* \frac{Bo}{We}\right] = 0
\end{aligned} \tag{B.10a}$$

$$\begin{aligned}
\frac{k_{h_j}}{4\sqrt{Re}} R^* \frac{dR^*}{dt^*} + \left[\frac{4R^*}{We}(2h(\theta_d) - \cos\theta_e) + \frac{f(\theta_d)G(\theta_d)}{24}(R_0^*)^3 \frac{Bo}{We} + \frac{k_{h_j}f(\theta_d)}{4} t^* \frac{Bo}{We} \right. \\
+ \left. \frac{k_{\mu_m}}{R^*} \frac{8}{Re}\right] \frac{dR^*}{dt^*} + \frac{dm}{dt} \left[\frac{f(\theta_d)}{4} R^* \frac{Bo}{We}\right] = 0
\end{aligned} \tag{B.10b}$$

Where,  $Re = \rho_d v_j D_j / \mu_d$ ,  $We = \rho_d v_j^2 D_j / \sigma_{dm}$ , and  $Bo = \rho_d g D_j^2 / \sigma_{dm}$  are Reynolds number, Weber number and Bond number, respectively; also,  $k_{\mu_m} = \mu_m / \mu_d$ ,  $R^* = \frac{R}{D_j/2}$ ,  $R_0^* = \frac{R_0}{D_j/2}$ ,  $t^* = \frac{t}{D_j/v_j}$  and  $G(\theta_d) = \frac{2 - 3 \cos(\theta_d) + \cos^3(\theta_d)}{\sin^3(\theta_d)}$ .

### Initial condition

The spreading of the droplet or the transient variation of the droplet base radius can be predicted by numerically solving (e.g. 4th order Runge Kutta (RK4) method) either form of the equation 3.2, with corresponding contact angle value and appropriate initial boundary condition. For this study we have chosen the drop radius at the moment when the jet makes the first impact on the substrate, i.e., the splat shape of the droplet. Here, we assume that the volume of the splat shape droplet is equivalent to the volume of the liquid jet before the impact.

To determine the initial spreading diameter of the splat, we can further employ the energy balance equation, *i.e.* the energy available in the jet (kinetic energy) before deposition and the energy transferred (surface energy, viscous dissipation work and work done due to medium viscosity) to form the splat droplet shape (initial drop shape). The kinetic energy of the impacting jet can be calculated as,  $\frac{1}{2} m v_j^2$ . We can define the surface energy considering the splat shape as,  $\frac{\pi}{4} D_0^2 \sigma_{dm} (1 - \cos \theta_e)$ . Considering De Genne's approximation [111, 192] the viscous dissipation work can be calculated as,  $6\pi \mu_d \ln(\varepsilon^{-1}) \frac{R}{\theta_d} \left( \frac{dR}{dt} \right)^2$ . Here, we can approximate the change in radius and time as  $dR \approx D_0/2$  and  $dt \approx t_c$ . The time required for the droplet to form splat shape ( $t_c$ ) can be readily used from the traditional droplet impact analysis [58]. Finally, the work due to medium viscosity considering the elemental area of the splat can be approximated as  $\frac{3\pi k_{\mu_M} k_{h_j} D_0^3 We}{8 D_j Re}$ .

Thus, the non-dimensional equation for the initial spreading ratio ( $\xi = D_0/D_j$ ) is:

$$\xi^3 \left[ \frac{9 \ln(\varepsilon^{-1})}{32\theta_d} + \frac{3k_{\mu_M} k_{h_j}}{8} \right] \frac{We}{Re} + \frac{\xi^2}{4} [1 - \cos \theta_e] - \frac{k_{h_j} We}{8} - k_{h_j} = 0 \quad (\text{B.11})$$

Again, by replacing only the viscous dissipation work, approximated by lubrication model, with the boundary layer approximation, we can write the non-dimensional energy balance equation for the splat formation as,

$$\frac{1}{4} \frac{k_{\mu_M} We}{k_{h_j} Re} \xi^3 + \left[ \frac{We}{8\sqrt{Re}} + \frac{1}{4} (1 - \cos(\theta_e)) \right] \xi^2 - \frac{k_{h_j} We}{8} = 0 \quad (\text{B.12})$$

## B.2 How parabolic flight works

Parabolic flights generate gravity free conditions in an aircraft by following a parabolic trajectory . They provide a microgravity environment for scientists to conduct research without reaching the outer space but only for 20-25 seconds. During a parabolic or zero gravity flight the aircraft makes a parabolic manoeuvre to achieve a state of weightlessness for minimum 10 seconds to maximum 22 seconds. The parabolic manoeuvre or ellipse arc during a Zero G flight is divided into three stages: the parabola pull-up, the parabola, and the parabola pull-out as shown in figure.

Before performing a parabolic manoeuvre, the aircraft needs to be at the 6000m while it is in the horizontal flight mode as well as the aircraft needs to gradually gain a speed of 800 – 900km/h before the pull up stage.

During the pull up stage, the pilot lifts the nose of the aeroplane upward from its horizontal position to an angle of 45°. The pull up stage lasts for 20 seconds while the whole aircraft system experiencing a pull of 1.8 times that of gravity on Earth.

As the aircraft travel upwards during the pull up stage, the pilot gradually reducing the speed from 800 – 900km/h to 685km/h. Approximately at an altitude of 7800m

the aircraft enters the parabolic trajectory, as shown in figure, during which it is in free fall for 22 seconds.

During the pull out stage the nose of the plane is tilted back to downward to  $45^\circ$  and during this period the pilot gradually start increasing the flight speed until the plane level off. Whole system in the aeroplane again experience a pull of 1.8 times that of gravity on Earth.

### B.3 Treatment of copper substrate

Copper substrates used in the study underwent routine testing for historical changes in surface free energy (SFE) using a portable goniometer (Mobile Surface Analyzer (MSA), Krüss Scientific Instruments Inc.) equipped with polar and nonpolar liquids, such as water and diiodomethane (DIIM). As shown in the Table B.1 CUCL (Copper cleaned) is a copper substrate cleaned with isopropanol and distilled water. CUCLF(Copper cleaned flamed) undergoes the same treatment with the addition of a flaming step at the end of the process. W1 and W16 stand for week number 1 and 16, respectively, since a substrate has been treated with the flame.

Substrate Type	W-CA [°]	DIIM-CA [°]	SFE [mN/m]	Polar part [mN/m]	Dispersive part [mN/m]
CUCL	91.61	69.29	26.51	3.24	23.27
CUCLF	33.42	31.15	69.02	25.27	43.74
CUCLF-W1	48.42	35.73	59.81	18.15	41.66
CUCLF-W16	59.91	35.74	53.46	11.17	41.69

Table B.1: Table depicting the water contact angle (W-CA), diiodomethane contact angle (DIIM-CA), surface free energy (SFE), polar and dispersive part of variously treated copper substrate.

It can be seen from the results that a significant increase in both polar and dis-

persive parts can be achieved using the flaming process. The dispersive part exhibits insignificant change over sixteen (16) weeks unlike the polar part that reduced by nearly fifty-five (55) percent.

# Appendix C: Nomenclature

## C.1 Chapter 2

$P_D$  : Dynamic wetting pressure,

$P_C$  : Capillary pressure,

$V_{fall}$ : velocity of the falling drop,

$\rho$ : density,

$\Delta$ : displacement of drop's center of gravity,

$\lambda$ : wavelength of the capillary wave,

$\gamma_{LV}$ : Liquid vapour interfacial tension

## C.2 Chapter 3

$V$ : volume of the jet,

$t$  : time,

$\rho_j$  : density of the liquid jet,

$u_i$  : velocity component along the  $i$ th direction,

$S$  : surface area of the cylindrical jet,

$n_j$  : unit normal vector,

$\tau_{ij}$  stress rate tensor

$\epsilon_{ij}$  : strain rate tensor, respectively,

$g$  : the gravitational acceleration,

$\bar{\square}$ : the ambient fluid properties,

$P$  :Pressure,  
 $\mu$  :viscosity,  
 $u_r$  : radial component of the velocity,  
 $u_z$  : axial component of the velocity,  
 $\sigma$  : interfacial tension,  
 $r_1, r_2$  : principal radii of curvature of the interface,  
 $r_s$  : radius of a perturbed columnar surface,  
 $r_0$  : radius of the undisturbed jet,  
 $\epsilon$  : perturbation amplitude,  
 $\omega$  : growth rate of instability,  
 $k$  : wave number,  
 $\lambda$  : wavelength of the perturbed jet,  
 $\sigma_{jm}$ : interfacial tension at the jet medium interface,  
 $I_0$  :modified Bessel functions of the first,  
 $K_0$  :modified Bessel functions of the second kind,  
 $\omega$ : angular velocity,  
 $Oh$  : Ohnesorge number,  
 $Fr$  : Froude number,  
 $Bo$  : Bond number,  
 $d_e$  : diameter of the drop originated from jet break up,  
 $a$  : nozzle inner diameter,  
 $L_b$  : jet breakup length,

### **C.3 Chapter 4**

(Re) : Reynolds number ,  
 (We): Webber number ,  
 (Bo) : Bond number,

$(k_{\mu_m})$ : viscosity ratio ,  
 $\mu_d$  droplet,  
 $\mu_m$  : viscosity of the surrounding medium,  
 $L_\delta$ : microscopic length,  
 $L$  : macroscopic cut-off length ,  
 $\theta_d$ : dynamic CA,  
 $\theta_e$ : equilibrium CA,  
 $\rho_m$  : mass density of the droplet,  
 $D_j$  : diameter of the jet,  
 $v_j$  : velocity of the impacting jet,  
 $h_j$ : height of the jet,  
 $v_j$ : velocity of the jet,  
 $D_j$ : diameter of the jet,  
 $\xi = D_0/D_j = R_0/R_j$ : Maximum spreading ratio,  
 $l_{cap}$ : capillary length,

## C.4 Chapter 5

$\omega$  : frequency,  
 $\Gamma$ : damping of the oscillations,  
 $\sigma$  : surface tension,  
 $\eta$ : viscosity,  
 $M$ : Mass of the drop,  
 $a_0$ : radius of the drop,  
 $\gamma_{sv}$ :interfacial tensions per unit length of the solid-vapor,  
 $\gamma_{sl}$ : interfacial tensions per unit length of the solid-liquid,  
 $\gamma_{lv}$  : interfacial tensions per unit length of the liquid-vapor interface,  
 $\theta_Y$  : Young's contact angle,

$E$ : internal energy,  
 $H$ : enthalpy,  
 $A$ : Helmholtz free energy,  
 $G$ : Gibbs free energy,  
 $\mu_i$ : chemical potential of the  $i$ th component,  
 $V$ : volume,  
 $S$ : entropy,  
 $P$ : Pressure,  
 $W$ : work,  
 $Z$ : Center of gravity,  
 $\tau$ : tension,

## C.5 Chapter 6

$2\alpha$ : tip angle,  
 $h_l$ : height of the liquid phase of the drop,  
 $h_s$ : height of the solid phase of the drop,  
 $\theta_A$ : advancing CA,  
 $\theta_R$ : receding CA,  
 $k$ : thermal conductivity,  
 $L$ : latent heat of fusion,  
 $T$ : temperature,  
 $Bo$ : Bond number,  
 $\nu$ : liquid to solid density ratio,

## C.6 Chapter 7

$\rho_l$ : density of the ferrofluid,

$v$  : velocity,

$\eta$ : ferrofluid's viscosity,

$\mu_0$  :magnetic permeability of free space,

$g$  : acceleration due to gravity,

$M$  : magnetization of the fluid, and  $H$  represents the magnetic field,

$Bo_m$ : magnetic Bond number,

$\gamma^M$  :effective surface tension of the magnetic liquid,

$\kappa$  :radius of curvature of the drop,

$P_0$  :atmospheric pressure,

$\Pi$  : disjoining pressure,

$\chi$ : magnetic susceptibility,

$L$ : Latent heat,

$Ste$ : Stefan number